STRUT-AND-TIE MODELING OF TWO-DIMENSIONAL REINFORCED CONCRETE STRUCTURAL ELEMENTS

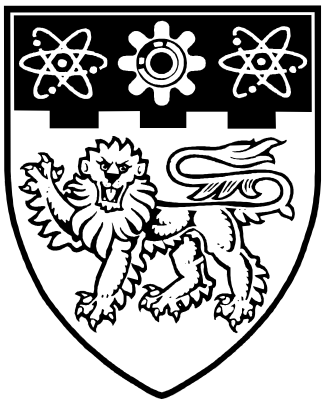

ZHAO YIWEN

SCHOOL OF CIVIL & ENVIRONMENTAL ENGINEERING
NANYANG TECHNOLOGICAL UNIVERSITY

March 2005

Strut-and-Tie Modeling of Two-Dimensional Reinforced Concrete Structural Elements

Zhao Yiwen

School of Civil & Environmental Engineering

A thesis submitted to the Nanyang Technological University
in fulfilment of the requirements for
the Degree of Master of Engineering

March 2005

ABSTRACT

Nowadays, many current concrete design codes have already utilized a strut-and-tie method as a design tool especially for the shear problem and elements with sophisticated stress conditions. The strut-and-tie method has normally been used for the ultimate limit-state design, where little has been said about the stiffness and deformation. Thus, this thesis focused on the applicability of truss models and the strut-and-tie method to the analysis and design of reinforced concrete beams and structural walls with opening that had complicated internal stress flow and to develop a design procedure for these beams and walls based on such models. This research also tried to derive more rigorous analysis not only for the strength of the elements, but also for deformation of the elements.

The first part of the thesis is about the analysis of reinforced concrete beams subjected to shear with the truss model analogy. A modified truss model incoprorating concrete contribution in shear was developed and analyzed. A theoretically based approach, which is able to calculate the strut angles in a variable angle truss model, was proposed. This approach was derived from the analysis using the principle of virtual work in which stiffness and deformation was readily defined.

The second part of the thesis is about the strut-and-tie analysis of reinforced concrete walls with openings. An experimental program of three reinforced concrete walls with openings was conducted to understand the structural behavior in detail. As a consequence of the findings, two different types of strut-and-tie models were defined to analyze the wall specimens. Lastly, a systematic design approach was proposed based on the two strut-and-tie models.

ACKNOWLEDEMENTS

The research work presented in this thesis was conducted at the School of Civil and Environmental Engineering of Nanyang Technological University (NTU) under the auspices of Seismic Design of Structural Walls with Openings Research Program. The author would like to thank NTU for providing the research scholarship during his candidature in this research program.

The author wishes to express his sincere gratitude to Dr. Li Bing, supervisor of this project for his professional guidance, invaluable advice and endless support.

In addition, the author would like to express his thanks the technicians from the Heavy Structure Laboratory of CEE for their helpful assistance in the experimental work, without whom this work certainly could not been done.

This acknowledgement would not be complete without mentioning the contributions of his fellow research students at NTU. They are Wu Hui, Tan Hai Yang, Wu Yiming and Rong Haicheng. Their constructive suggestions, fruitful discussions, as well as technical supports had made this project a most memorable one.

Finally, the special thanks must go to his parents and Miss Wang Jing for their continuous encouragement and support.

TABLE OF CONTENTS

LIST OF FIGURES

CHAPTER 2

CHAPTER 3

CHAPTER 5

CHAPTER 6

LIST OF TABLES

CHAPTER 2

CHAPTER 3

CHAPTER 4

CHAPTER 5

LIST OF SYMBOLS

a	shear span length or depth of the equivalent rectangular compressive stress block or maximum aggregate size in millimeter
$a^{'}$	depth of the transformed equivalent rectangular compressive tress block
A_{cm}	sectional area of concrete compression chord
A_g	gross sectional area of reinforced concrete beam
A_s	sectional area of longitudinal reinforcement
A_{sc}	sectional area of shear reinforcement converted from concrete contribution
A_{sm}	sectional area of concrete diagonal strut
A_{sl}	sectional area of shear reinforcement as defined in Eurocode EC2
A_{st}	sectional area of shear reinforcement
A_v	effective sectional area for shear of reinforced concrete beam
b_w	beam total sectional width
$b^{"}$	width of confined core measured to outside of stirrups
c	depth of concrete compressive stress block
c_x	distance to longitudinal reinforcement
c_y	distance to shear reinforcement
C_c	resultant of concrete compression force
C_s	resultant of reinforcement compression force
d	depth of the beam taken from the extreme compression fiber to the centroid of the outermost layer of tension reinforcement
d_{bx}	bar diameter of longitudinal reinforcement
d_{by}	bar diameter of shear reinforcement
DF	Ductility factor
E_c	modulus of elasticity for concrete

E_s	modulus of elasticity for steel
f_c	concrete compressive strength
f_c'	cylinder compressive strength of concrete
$f_{cu}^{'}$	cube compressive strength of concrete
f_s	Stress of reinforcement
f_y	yield strength of reinforcement
h	height of truss model or strut-and-tie model
K	stiffness of a typical truss unit in cracked concrete
jd	flexural lever arm
l	updated shear span length
l_b	critical strut length
M	bending moment
n	modular ratio of E_s/E_c
P_i	the horizontal load at the middle of the top beam associated with the nominal flexure strength being reached at the critical sections of the walls
s	spacing of shear reinforcement
s_{mx}	indicator of the crack control characteristics of the longitudinal reinforcement
s_{my}	indicator of the crack control characteristics of the shear reinforcement
s_x	spacing of longitudinal reinforcement
s_θ	average crack width over the cracked surface
T	resultant tensile force
v_c	shear stress transferred across the crack
V_c	concrete contribution to shear strength
V_s	truss contribution to shear strength
V_{MTM}	shear capacity of modified truss model by Ramirez and Breen [R1]
w	crack width

Z	slope of descending branch for confined concrete in the stress-stain relationship
α	drift angle of a typical truss unit
Δ	deformation of a typical truss unit or displacement of reinforced concrete element
Δ_y	yield displacement
ε_1	principle compressive strain in concrete
ε_2	principle tensile strain in concrete
ε_c	strain of the extreme compression fiber of concrete
ε_s	strain in tension reinforcement
ε_s'	strain in compression reinforcement
ε_x	strain in x-direction
ε_y	strain in y-direction
μ	ductility factor
θ	crack angle
ρ_s	Bottom longitudinal reinforcement ratio
ρ_s'	Top longitudinal reinforcement ratio
ρ_{st}	Shear reinforcement ratio
ρ_{sv}	Ratio of volume of shear reinforcement to volume of concrete core measured to outside of stirrups
ρ_w	Ratio of area of longitudinal reinforcement to beam effective sectional area

CHAPTER 1

INTRODUCTION

1.1 Background

Nowadays, the basic ideas of designing reinforced concrete structural elements are directed by rules in various codes. Such codes of practice often have simplified and exaggerated design rules, which are not properly understood by designers. A few problems have arisen as a result. Especially, there are inaccuracies in the available models to treat shear in design stages. Also, it is unsatisfactory to rely on simplified and empirical approaches for the design of critical regions of a structure such as those with static and geometric discontinuities.

To make such inaccurate and unsatisfactory rules unnecessary, many researchers have been working on a generalization of the strut-and-tie approach for the design of structural concrete. This approach was initially introduced by Ritter [R4] and Morsch [M8] early in the twentieth century, further refined and expanded by Rausch [R2], Turlimann [L1, L2, M9, T1, T2], Schlaich [S1, S2, S3], Marti [M1, M2, M3, M4, M5, M6], Collins [A2, C3, V1, V2], and etc. Until now, most design codes have adopted truss model analogy, which is a simpler form of strut-and-tie model, as the shear design tool. However, the mechanism for shear transfer is not properly reflected. It is known that pure truss mechanism by shear reinforcement only definitely underestimates the shear strength. The shear carried by concrete must be taken into consideration. The shear carried by concrete, named as concrete contribution frequently, is treated rather empirically. In many current concrete design codes [A1, E3, A7] the formulas given for concrete contribution are derived from regression analysis of experimental data. Lack of analytical model in this part limits the application and understanding of the shear design equations. Even in the truss mechanism of shear reinforcement, there is argument about the angle of inclination. Assumption of $45°$ is questioned.

On the other hand, there is a consistent push to use the strut-and-tie method to investigate the mechanisms of complicated reinforced concrete structures or structural elements, such as corbels, pile caps, shear walls, and etc. The resulting models have been successful in examining the performance of these elements regarding both structural strength and even ductility. Thus the great potential of the strut-and-tie method have been exhibited, but the rationale that supports the development of the strut-and-tie model for a specific type of structural element is often very vague. Consequently, the further use of these models into design works may be confusing.

The current design philosophy is based on the ultimate limit state design approach; engineers are more interested in the final ultimate strength of structural element rather than the whole behavior throughout the loading process. This approach simplifies the design procedure and ignores the deformation property. Hence, it is necessary to develop a truss model and strut-and-tie model which is capable of predicting the strength reasonably well and explaining the behavior at any stage of the structure under loadings. This research utilizes a truss model as rational approach for use in the analysis and design of reinforced concrete beams and structural walls with openings.

1.2 Objectives and Scopes of Research

To date, the understanding of the behavior of reinforced concrete structures and members is not complete. This thesis is part of on going investigation at NTU to advance the level of understanding of reinforced concrete beams and structural walls with openings. This thesis focused on the applicability of truss models and the strut-and-tie method to the analysis and design of reinforced concrete beams and structural walls with opening that had complicated internal stress flow and to develop a design procedure for these beams and walls based on such models.

1.3 Organization of Thesis

This thesis is divided into six chapters. Chapter 1 provides an introduction to the background, objective and scope of this research. Chapter 2 presents a literature review

of development and current research of the truss model and the strut-and-tie model. Then the review focuses on the shear design provisions of various national codes and standard and a few shear design models suggested by other researchers. In Chapters 3, reinforced concrete beams under a monotonic loading condition are analyzed by the modified truss models for strength and load-displacement response. Chapter 4 is dedicated to a theoretical approach to determine strut angles of a variable angle truss model for reinforced concrete beams subjected to shear. Chapter 5 presents the experimental program on reinforced concrete walls with openings. Analytical works associated with the experimental program is conducted in Chapter 6. Conclusions and recommendations based on the work completed in the research at NTU are presented in Chapter 7.

CHAPTER 2

LITERATURE REVIEW

2.1 Introduction

Design or analysis of reinforced concrete structures is not a simple task due to the presence of vast unknowns. Designer and researchers have worked out many theories to facilitate the design and analysis process. Among all these theories, the truss model analogy is a very important and rational approach for the design of reinforced concrete structures. The basis of this idea of the truss model analogy concept involves utilizing concrete blocks as struts to resist compression and reinforcing bars as ties to carry tension. Then the concrete compressive struts and the steel tensile ties form a truss mechanism to resist the applied loads. Designers have been using this concept intuitively for many years. Systematic researches looking into truss models have been performed in the last few decades resulting in the development of several truss model theories dealing with the fundamental behavior of reinforced concrete, particularly with the effect of shear and torsion. Beyond that, a strut-and-tie model concept has been established towards a unified design approach. However, at present, the strut-and-tie model tends to be only specialized as a kind of truss model applied in the complex non-flexural regions of reinforced concrete elements [H4, H5].

In this chapter, historical development of the truss and the strut-and-tie models will be reviewed first. An understanding of the fundamental basis of the strut-and-tie model is given. Next, this chapter will also look into current research status with the truss and the strut-and-tie models. In particular, shear design with truss model will be reviewed in greater details including various design codes.

2.2 Development of the Truss Model and the Strut-and-Tie Model

In the beginning, civil engineers already recognized the ideas of using concrete to carry compressive forces and steel reinforcement to carry tensile forces. These ideas were further developed by Ritter [R4] and Morsch [M8] into a concept of truss analogy for the analysis of reinforced concrete beams subjected to shear and bending. This truss analogy concept, based on relevant experimental observations, assumed that parallel inclined cracks formed in the reinforced concrete beams at failure, and that the concrete blocks between adjacent cracks could carry the inclined compressive forces, and hence acted as diagonal struts. This led to the realisation that a truss like action that could be achieved through longitudinal reinforcement representing the tensile chords and concrete representing the compressive chords on either side of the beam. Stirrups provided the vertical tensile ties joining the longitudinal chords. For simplicity, the concrete struts were assumed to be inclined at $45°$ corresponding to the first shear cracking angle. At this stage, this model was known as the "$45°$-Angle Truss Model" (**Figure 2.1**).

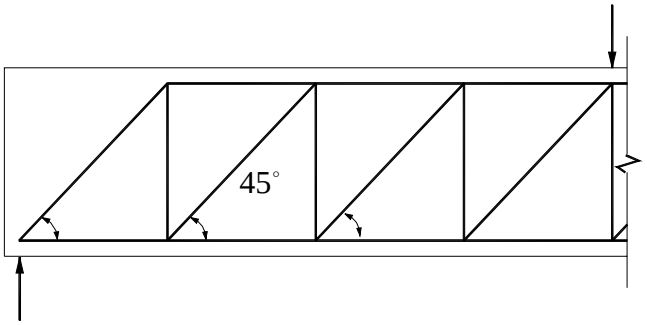

Figure 2.1: $45°$-angle truss model

The truss analogy concept was extended in the late 1920s by Rausch [R2] as a means of designing reinforced concrete beams under torsion. Rausch found that a reinforced concrete beam with closed ties running around all faces could effectively resist torsion by means of a "space-truss" action. He then visualized reinforced concrete beam with inclined cracks forming in each face, spiralling around the beam with the surface concrete between the inclined cracks acting as inclined struts in all faces. This extended space truss provided a practical method for the design of the torsion members.

Before the 1960s, the European Concrete Code required that the full shear force to be carried only by the transverse shear reinforcement in the web. After conducting a major experimental program, Leonhardt [L3] found that concrete has an important role in resisting the shear force even in beams with very thin web. And the stress in the stirrups was less than those predicted by the $45°$-Angle Truss Model, which meant that concrete struts could inclined at an angle smaller than $45°$. Thus, Leonhardt [L3] proposed a truss model with a variable angle of inclination for the compression struts, which was called the "Variable Angle Truss Model". Parallel to Leonhardt [L3], Paulay [P3] utilized the "Variable Angle Truss Model" in defining the contribution of truss action in the thin webbed coupling beam (as **Figure 2.2**).

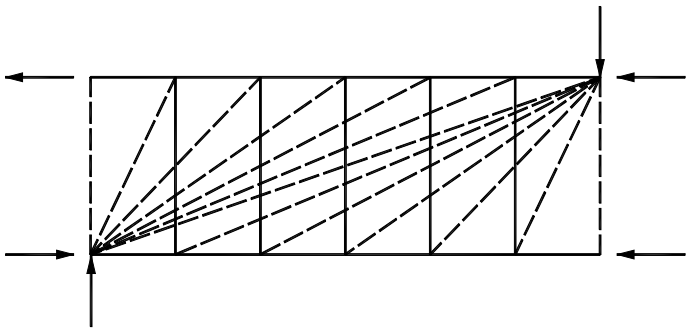

Figure 2.2: Variable angle truss model [P3]

The truss model was further modified by using the Theory of Plasticity [N1]. Nielson [N1] derived the Lower Bound Theorem and Upper Bound Theorem of the Theory of Plasticity. Applications of the two theorems to reinforced concrete beams by truss analogy concept were able to predict strut angles with their respective assumptions and formulations. Details of the Theory of Plasticity will be reviewed in a later section. In the 1970s, the Theory of Plasticity also helped to promote application of the limit analysis methods capable of predicting failure-conditions in the truss model approach. Elfgren [E1] developed a truss model titled the "compression stress field theory". This theory was based on the equilibrium condition and assumed that both the longitudinal and the transverse steel yield at the ultimate load stage. Based on the Theory of Plasticity, Lampert and Thurlimann [L1, L2] studied beams subjected to torsion and flexure using a variable angle space truss approach. Thurlimann *et al* [T2] extended the

work to cover warping torsion as well as combined flexure, shear, and torsion. Thurlimann's space truss model became the basis of the shear and torsion design method adopted in the 1978 CEB-FIP design code [C2].

Before 1972, the truss model severely overestimated the shear and torsion strength owing to the stress state of the concrete struts at failure was assumed to be at the uniaxial compression strength of standard concrete cylinder. This situation changed with Robinson and Demorieux's work [R5, R6]. They observed that a reinforced concrete element under shear is actually subjected to a two-dimensional stress condition. The strength from the principal compression direction along the strut was found to be softened by the principal tension in the perpendicular direction. This softened stress was referred to as the "effective stress of concrete". After that, a number of researchers worked on this effective stress of concrete and many sets of factor have been proposed from different considerations. A full picture of effective stress of concrete for struts will be given in a later section.

Vecchio and Collins [V1] proposed the first softened stress-strain curve of concrete in compression to determine the "effective stress". Combining the softened stress-strain curve of concrete with Mohr's stress and strain circles, they developed a "Compression Field Theory" to predict the behavior of reinforced concrete elements. This theory was further modified in an attempt to derive the "contribution of concrete" [V2], which was called the "Modified Compression Field Theory (MCFT)". In 2000, a disturbed stress field model (DSFM) was proposed by Vecchio [V3] again to redress the two main weaknesses in the MCFT computational model; i.e. the enforced alignment of the principal stress and strain directions and the handling of shear stresses on crack surfaces. New sets of equilibrium, compatibility, and constitutive relations were formulated accordingly, and alternative crack slip models were discussed in the model. The proposed theory was shown to yield improved simulation of responses in specific situations where the MCFT was found to produce inaccuracies.

Based on the equilibrium, compatibility and the constitutive laws of material, a truss model called “softened truss model” was also developed by Hsu [H3, H4, H5] and Pang and Hsu [P1]. And a unified theory was proposed for the behavior of reinforced concrete structures subjected to bending, axial load and torsion [H4]. In 1996, Hsu [H5] proposed a unified approach that covered all four basic actions (bending, axial load, shear, and torsion) in structural concrete elements. This approach was based on the angle of inclination of the concrete struts, the scope of applications, and the three fundamental principles of the mechanics of the materials (stress equilibrium, stain compatibility, and the constitutive laws of materials). It tried to cover all rational reinforced concrete theories developed to date. Six models, including a strut-and-tie model, a Bernoulli compatibility truss model, an equilibrium (plasticity) truss model, a Mohr compatibility truss model, a softened truss model, and a fixed-angle softened-truss model were provided in his study.

Marti [M1, M2, M3, M4, M5] made an effective attempt to promote the application of consistent equilibrium and ultimate strength approaches (limit analysis concept) to the design and detailing of reinforced concrete beams using truss models. In addition, Marti [M5] provided a comprehensive synthesis of the truss model approaches and related theories to be used in the detailing and dimensioning of the required structural concrete elements. In his work, a set of basic tools, which include struts and ties, nodes, fans, and arches, was described. Marti proposed that the dimensioning of the concrete, as well as the distributions and the detailing of the reinforcement, must be determined by developing and drawing to scale truss models on the basis of actual stress fields. These could be achieved through possible equilibrium systems of the internal forces in both the concrete and reinforcement when subjected to ultimate loads. Based on experimental results, Marti also proposed an average value of concrete compressive strength in the struts and nodes. After reviewing the recent developments in the strut-and-tie model, the limit analysis approaches, and the compression field, Marti [M6] emphasized that the strut-and-tie models and the stress field considerations should be part of the toolbox of every designer.

Schlaich *et al* [S1, S2, S3] applied the truss model approach to cover all types of structures in the form of strut-and-tie systems. They [S2] thought that the most basic strut-and-tie model would compose of uniaxially stressed tension ties representing either normal or prestressed reinforcement, uniaxially stressed concrete compression struts, and joint regions referred as nodal zones at points where three or more struts meet, or where a combination of three or more struts, ties and external forces meet. Importantly, they defined the B-regions and D-regions in any reinforced or prestressed concrete structure, with the B-region representing the beam region where Bernoulli's beam theory holds while the D-regions representing the disturbed region where simple method of flexural analysis does not hold. Since the strain distribution is significantly nonlinear in the D-regions, they suggested that the strut-and-tie system should be used as a primary load carrying mechanism. In the B-regions, truss models such as Morsch's truss and Thurlimann's refined truss model could be applicable. Thus, the whole reinforced or prestressed concrete members could be analyzed through truss models.

2.3 General Principles of the Strut-and-Tie Model

2.3.1 B-regions and D-regions

In a reinforced concrete beam under pure bending, the concrete strains in a typical cross-section are longitudinal with transverse tensile cracks forming when the tensile strength of the concrete is reached. This follows the fundamental assumption that plane sections before bending remain plane after bending. However, this pattern of flexural behavior is disturbed in various regions of a real reinforced concrete beam. Thus, any structure or structural element can be divided into regions according to their state of stresses. Those regions of a structure in which Bernoulli's hypothesis of plane distribution of strain can be applied have been referred as B-regions by Schlaich [S1, S2], where B may be taken to stand for Beam or for Bernoulli. In these regions if the concrete remains uncracked, the stresses are calculated using the bending theory for linear elastic material. For the cracked B-regions the truss models or the standard methods in various codes can be applied.

Those regions where the strain distribution is significantly non-linear, for example near concentrated loads, corners, bends, openings and other discontinuities, are call D-regions. D stands for Discontinuity or Disturbance of detail. In these regions, the standard methods are not applicable in principle.

Hsu [H4, H5] expanded the concept of B-regions and D-regions and renamed them main regions and local regions respectively. According to Hsu, a main region is the one where the stresses and strains are distributed so regularly that they can be easily expressed mathematically. That is the stresses and strains in the main regions are governed by simple equilibrium and compatibility conditions. In contrast, a local region is one where the stresses and strains are so disturbed and irregular that they are not amenable into mathematical solutions. In particular, compatibility conditions are difficult to apply.

An advantage of dividing a structure into B-regions and D-regions is that the attention of the designer is focused on the potentially weak spots that require special attention in design and detailing. However, not much accuracy is necessary in determining the dividing sections between B-regions and D-regions. These sections can be assumed to lie approximately in a distance *h* from the geometrical discontinuity or the concentrated load, where *h* is equal to the depth of the adjacent B-region. This assumption is justified by Saint-Venant's principle that the static or geometrical discontinuity, or combination of the two, is of limited extent.

2.3.2 Modeling procedure

Strut-and-tie models are applicable both for B-regions and D-regions. However, according to the different stress and strain distribution, appropriate models to be used in D-regions or B-regions should be carefully selected to give a more accurate representation of the flows of the stresses in the structure. Therefore a systematic approach should be developed for modeling in general cases. With that in mind, the modeling process can be divided into the following steps:

(1) Determine the B-regions and D-regions of the structures or structural elements;

As already mentioned above, structures or structural elements need to be broken up into B-regions and D-regions for the application of different strut-and-tie models. But only an approximation is required.

(2) Construct alternative strut-and-tie models;

In general, the standard truss models can be used in B-regions and the special strut-and-tie models can be developed for D-regions to accommodate the behavior there. Schlaich *et al* [S1] recommended the use of elastic analysis as a basis for defining the strut-and-tie model. That is a stress analysis may be necessary. If the results of a linear-elastic analysis are not available, the models can be developed using the "load-path method".

(3) Identify appropriate model;

There may be several possible strut-and-tie models for a structure or structural element, so it is sometimes necessary to carefully select the appropriate model. In many cases, particularly for service loads, the most appropriate strut-and-tie model is the one in which

$$\sum F_i l_i \varepsilon_{mi} = \text{minimum} \qquad (2\text{-}1)$$

where F_i = force in member i,

l_i = length of member i,

ε_i = mean stain of member i.

The left-hand expression in the Equation (2-1) represents the sum of the work done by the internal forces in the struts and ties. It means the model should use the load paths with the least forces and deformations. As the ties are more likely to deform than the struts, it is only necessary to consider the tensile ties in this particular equation. However in seismic design, criteria based on the maximum energy absorption capacity

or maximum displacement without substantial decrease of strength must be chosen [Y1].

(4) Detail the model.

The basic elements of a strut-and-tie model include:

(a) A strut which represents the resultant of a parallel or fan-shaped compressive stress field; and

(b) A tie which represents the resultant of forces in the reinforcement or in a concrete tensile zone; and

(c) Nodes which are confined regions of concrete in which the compressive strut forces are balanced by the anchored reinforcement or other struts.

When coming to the detailing, a structural analysis must be carried out in order to determine the shear forces and maximum moments which are used to dimension each member and region. The indispensable requirement for any model developed is to satisfy the needs for equilibrium, compatibility, and the strength and deformation properties. This implies that the structures are modeled according to the lower bound Theory of Plasticity [N1]. However, these requirements cannot always be fulfilled rigorously, and modifications are often introduced.

2.3.3 Lower-bound plastic theorem

In any mechanical consideration, three relationships, namely the equilibrium equation, the constitutive relation, and the compatibility equation, must be satisfied. However, a limit analysis for a lower bound solution only needs the equilibrium equation and boundary conditions to be fulfilled. The strut-and-tie model, by selecting a suitable arrangement for calculating the forces upon the struts and ties, obtains discrete distributions of stress fields which satisfy only the equilibrium equations and the

boundary conditions. So, the strut-and-tie method is in fact a lower bound plastic theory approach. The developed stresses in a stress field, any position below yield or at yield, are termed as admissible stresses.

However, there are limitations in applying this Theory of Plasticity [N1]. As the structural concrete permits only limited plastic deformation, it is always necessary to check whether ductility behavior is guaranteed. The strut-and-tie models have to be chosen in such a way so that the deformation capacity is not exceeded at any point before the assumed state of stress is reached.

2.3.4 Stress field and load path method

In the preceding section, it was noted that a small number of forces were used to represent the continuous stress distributions of the real structure in the strut-and-tie models. Hence, it is very important to know the properties of the stress fields. In 1987, Schlaich *et al* [S3] suggested three typical configurations to cover most of compressive stress fields:

(1) Fans-shaped field;

The fan-shaped (**Figure 2.3 (a)**) stress field is an idealization of a stress field with negligible curvature. This field can occur where a force is introduced and channeled through an element that is itself fan-shaped. There is no transverse tensile stress field existing in the fans, which differentiates it from the bottle-shaped field.

(2) Bottles-shaped field;

A bottle-shaped stress field (**Figure 2.3 (b)**) occurs wherever a distributed stress field is balanced by a narrower, more concentrated stress field. The concentrated compressive stress trajectories splaying out from the end results in the stress state that compression into the bottleneck and tension further away. In any bottle-shaped field there are associated transverse tensile stresses, which have to be carried, either by the concrete in

tension, or by specially introduced transverse reinforcements.

(3) Prisms-shaped field.

The prism-shaped field (**Figure 2.3 (c)**) is the simplest compressive stress field. Without any narrowing or splaying of the stress trajectories, there are no associated transverse tensile stresses induced in the concrete. The compressive field in a simple compressive strut is the prismatic or parallel stress field.

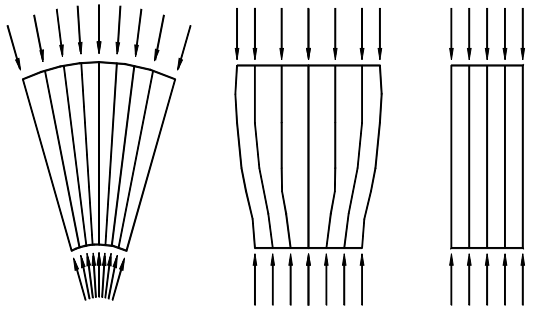

(a) Fan-shaped (b) Bottle-shaped (c) Prismatic-shaped

Figure 2.3: Types of compression stress fields

It should be noted that both fan-shaped and bottle-shaped struts could be reduced to prism-shaped struts. Normally, there is no special advantage in using fan- or bottle-shaped struts. Prism-shaped struts are more practical and adequate.

In the strut-and-tie models, the struts and ties condense the real stress fields' by-products through straight lines and concentrate their curvature in nodes. A load path method has been provided by Schlaich *et al* [S1, S2] to orient the struts and ties. The basic idea of the load-path method is to balance the by-products of the stress diagram action at one border in a region with their counterparts at the other border, as well as any loads applied within the region. Load paths are then used to connect the forces from the opposite borders, with diversions made as necessary at nodes by means of transverse ties and struts. An elastic analysis can help to find out the load path of structures to develop the appropriate strut-and-tie models.

2.3.5 Strength of struts

In any design codes for reinforced concrete structures, a partial safety factor of material is always applied to the characteristic cylinder strength f_c'. This partial safety factor allows for the effect of the difference between the strength of concrete in cylinders and in the actual structures.

$$f_{ce}^{'} = \phi f_c^{'} \tag{2-2}$$

where ϕ =the partial safety factor of material.

In normal flexural moment design theory, in which the uniaxial compression of concrete is assumed to prevail, ϕ can be taken as 0.85.

Even with the partial material factor being applied to the compressive strength of concrete, various researches still find that truss model and strut-and-tie model overestimate the shear and torsion stiffness of reinforced concrete elements. This is because the compressive strength of any concrete strut is affected by the presence of transverse stresses. In the case of biaxial or triaxial compression, the compressive strength can be substantially enhanced. On the other hand, a transverse tensile stress field reduces the compressive strength of the strut. The effective compressive strength of the concrete is also reduced by the presence of cracks and inclined reinforcing bars. In general, the effective compressive strength can be chosen as some portion of the concrete cylinder compressive strength:

$$f_{ce} = \xi f_{ce}^{'} \tag{2-3}$$

where ξ = the effective factor which is less than unit,

f_{ce} = the effective compressive strength of the concrete struts.

Many researches have been conducted in efforts to determine the limiting concrete compressive strength of struts. A lot of efficiency factor have been proposed for this purpose. Su and Chandler [S5] summarized most of these efficiency factors and gave **Table 2.1** below with some being added in this thesis. Other than those listed in the

table, Nielsen *et al* [N1] proposed the following empirical relationship for the efficiency factor based on plasticity analysis of shallow beams.

$$\xi = (0.7 - \frac{f_c'}{200}) \quad f_c' \leq 60\,\text{MPa} \tag{2-4}$$

This equation implied that the efficiency factor is simply a function of concrete strength and does not take account of the effect of cracks in the struts.

Based on the experimental results of tested large panels subjected to uniform stress and strain fields, Hsu [H4] derived an equation to determine the concrete effective factor:

$$\xi = \frac{0.9}{\sqrt{1 + 600\xi_r}} \tag{2-5}$$

where ξ_r = the tensile strain.

Simplified values for practical design have also been proposed by researchers. Marti [M3] has suggested that the maximum compression stress within a general diagonal compression strut be limited by the ratio:

$$\frac{f_{ce}}{f_c'} \leq 0.6 \tag{2-6}$$

Table 2.1: Effective strength level for concrete struts [S5]

Source	Efficiency factor ξ
Uncracked struts with uniaxial state of compressive stress	
Schlaich [S1,S2]	0.85
Muttoni, Schwartz & Thurliman [M9]	$20\alpha \quad \left(\alpha = \left(\frac{f_c'}{20}\right)^{\frac{2}{3}}\right)$
Rogowsky & MacGregor [R7]	0.85
Alshegeir & Ramirez [A3]	0.80-0.95
Warwick & Foster [W2]	0.85
Foster & Gilbert [F1]	0.85
Cracks parallel to the struts with normal crack width	
Schlaich [S1, S2]	0.8
Muttoni, Schwartz & Thurliman [M9]	$0.8\times 20\alpha \quad \left(\alpha = \left(\frac{f_c'}{20}\right)^{\frac{2}{3}}\right)$
Alshegeir & Ramirez [A3]	0.75
Warwick & Foster [W2]	$1.25 - \frac{f_c'}{500} - 0.72\left(\frac{a}{d}\right) + 0.18\left(\frac{a}{d}\right)^2 \le 0.85$
Foster & Gilbert [F1]	$\frac{1}{1.14 + 0.75\left(\frac{a}{d}\right)^2} \le 0.85$
Cracks skewed to the struts with severe crack width	
Schlaich [S1, S2]	0.6
Muttoni, Schwartz & Thurliman [M9]	$0.6\times 20\alpha \quad \left(\alpha = \left(\frac{f_c'}{20}\right)^{\frac{2}{3}}\right)$
Alshegeir & Ramirez [A3]	0.5
Warwick & Foster [W2]	$1.25 - \frac{f_c'}{500} - 0.72\left(\frac{a}{d}\right) + 0.18\left(\frac{a}{d}\right)^2 \le 0.85$
Foster & Gilbert [F1]	$\frac{1}{1.14 + 0.75\left(\frac{a}{d}\right)^2} \le 0.85$
Minimum strength of struts	
Warwick & Foster [W2]	$0.53 - \frac{f_c'}{500}$
Warwick & Foster [F1]	$\frac{1}{1.14 + 0.75\left(\frac{a}{d}\right)^2} \le 0.85$

The Canadian Concrete Code (1984) [C1] recommends that the effective concrete compressive strength of a concrete strut be taken as:

$$f_{ce} = \frac{\lambda \phi_c f_c'}{0.8 + 170\varepsilon_1} \geq \lambda \phi_c f_c' \qquad (2\text{-}7)$$

where λ = factor which depends on the concrete density, namely

1.0 for normal weight concrete,

0.85 for semi-light weight concrete, and

0.75 for light weight concrete.

ϕ_c = material factor for concrete=0.6,

ε_1 = principal tensile strain at right angles to the direction of the strut.

The parameter ε_1 accounts for the fact that the effective strength of a strut decreases when the tensile strains produced by the action of transverse reinforcement exist perpendicular to the direction of the compressive force**.** **Figure 2.4 (a)** shows a compression field with some reinforcement in the x direction. The strut is inclined at an angle θ to the reinforcement. ε_1 is the principle tensile strain at right angles to the strut and ε_2 is the principal compressive strain in the direction of the strut. The strain ε_1 is determined from the strain compatibility in the region where reinforcement action as tensile ties crossed the compressive strut. From the Mohr's circle of strain in **Figure 2.4 (b)** ε_1 is given by the expression:

$$\varepsilon_1 = \varepsilon_x + \frac{\varepsilon_x + \varepsilon_2}{\tan^2 \theta} \qquad (2\text{-}8)$$

If ε_x is replaced by the strain ε_s in the tension tie, and assuming that the compressive strain in the concrete strut when its strength if reached is 0.002, then

$$\varepsilon_1 = \varepsilon_s + \frac{\varepsilon_s + 0.002}{\tan^2 \theta} \qquad (2\text{-}9)$$

where ε_s may be the yield strain of the reinforcement

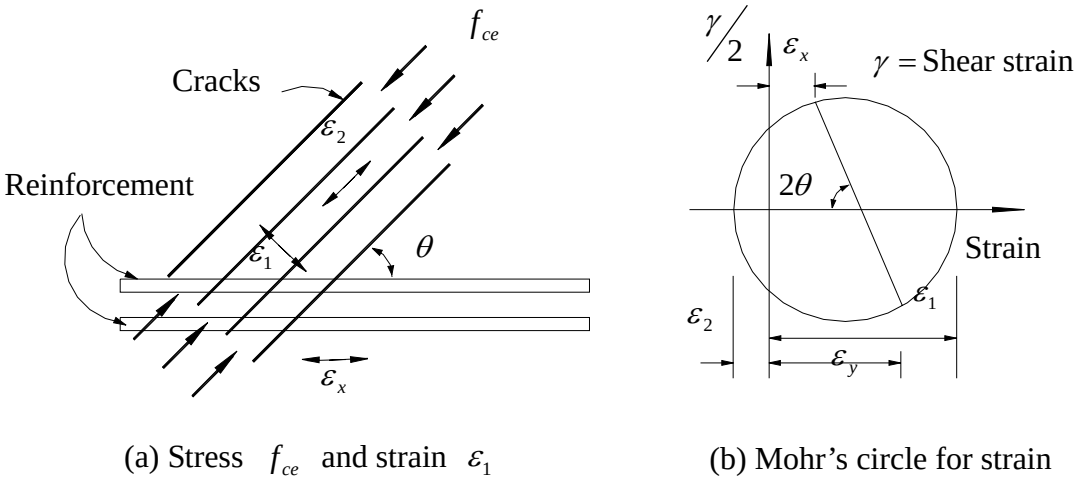

(a) Stress f_{ce} and strain ε_1 (b) Mohr's circle for strain

Figure 2.4: Strains in the cracked compressive concrete strut [C1]

2.4 Advanced Applications of the Strut-and-Tie Model

In the past twenty years, the truss model, as well as the strut-and-tie model, has been used extensively as a mechanical tool in reinforced concrete structures. Classically, shear design is always concentrated on the truss model analogy. A lot of shear design models have been developed and some are implemented into design codes. In the mean while, strut-and-tie models are specially used to investigate complex D-regions of reinforced concrete structures and structural elements such as deep beams and beam-column joints. Researchers have put some efforts into examining the performance of structural elements with the strut-and-tie models regarding structural strength, ductility etc. Some have also touched on the investigation of structural members under reversal cyclic loadings. Consequently, a number of strut-and-tie models of different forms have been thesised and the analysis results of these models are fairly well. The great potential of strut-and-tie models has been exhibited. In this part of thesis, application of strut-and-tie model will be focused.

Kim and Mander [K2, K3] performed extensive investigations in two truss models: the Constant Angle Truss Model and the Variable Angle Truss Model. They applied the Variable Angle Truss Model concept to the strut-and-tie model of coupling beams and developed a full set of mathematical formulations that was capable of predicting the

strength as well as the load-deformation response. In their study, the critical crack angle and the reinforcement stresses and strains could be worked out with reasonable accuracy to the experiment. Also, they considered the concrete contribution in shear and used tensile stress of concrete to effectively model this contribution. The effects from axial load were also included in the strut-and-tie model. Kim and Mander [K3] provided a very good methodology and a mechanical method to solve strut-and-tie model for shear and axial load by mathematical means. However, their formulation was limited to only coupling beams, which had a number of special properties. This concept of mathematical method can be implemented into general solution of reinforced concrete beams under shear.

Future more, a plane strut-and-tie model was developed by Hong [H1] in 1996 for the limited purpose of explaining the failure modes involving bond strength. This model clarified the bond transfer and its dependence on the effects of factors such as the geometry, the reinforcement details, the material strengths of considered structural elements and its state of stress, which was influenced by supports and loading conditions. Therefore, compatible failure mechanisms such as bar development failure and anchorage failure could be incorporated in the strut-and-tie model. The model also provided a rational design methodology and a basis for the revision of the current design provisions regarding bar cutoff.

Adebar *et al* [A2] also used strut-and-tie models to improve the design of pile caps. It was found that they could describe more accurately the behavior of deep pile caps. The influence of the amount and the horizontal distribution of longitudinal reinforcement were emphasized in the models. This had been neglected by ACI-318 [A1] procedures for the shear design of pile caps.

Xiao *et al* [X1] used strut-and-tie model and yield-line theories for the seismic assessment and retrofit of bridge column footings. In their study, different strut-and-tie models were developed for investigating force transfer in the pre-cracking and post-cracking footing respectively. This model concept was also adopted for the

seismic design and assessment of concrete bridge joints by Sritharan *el al* [S4].

Hwang et al [H6, H7] proposed the softened strut-and-tie models to predict the shear strength of the exterior and interior reinforced concrete beam-column joints for seismic resistance. The concept of this model was also used to predict the shear strength of reinforced concrete deep beams and squat walls [H8, H9]. Every predicted result showed a reasonable agreement with the corresponding experimental result.

Sritharan *et al* [S4] presented monotonic non-linear analysis of reinforced concrete knee joints and bridge portal frames using strut-and-tie models. They developed a set of formulas to describe the behavior of concrete struts and reinforcing steel ties at both the B-regions and D-regions for rectangular and circular beam-column sections. In this presentation, analytical charts for beam and column members were designed to assist the formulation of strut-and-tie models upon the section force. In their analysis, the strut-and-tie models were rather complicated in the joint region to capture the action of the compressive forces entering this region and to divert the flexural compressive stress path and to connect it with the column longitudinal reinforcement. Reinforcement lapping and clamping length was also considered in the analysis. This monotonic non-linear analysis showed good correlation between the observed response in laboratory and strut-and-tie model regarding the ultimate strength of the elements.

Some attempts to develop strut-and-tie models allowing the cyclic hysteretic response of the reinforced concrete structure have been made. In 1996, Kim [K2] developed a CIST (Cyclic Inelastic Strut-and-Tie) model for the analysis of Paulay's [P3, P4] coupling beam "specimen 312". Satisfactory agreement between the theory and the experiment was shown although the concrete strength decay was not considered in the analysis. A cyclic strut-and-tie model was developed by To *et al* [T3] to investigate the reinforced beam under reversed cyclic loading in 2000. The results were found to satisfactorily match the experimentally measured force-displacement response.

Ito *et al* [I1, I2] developed a latticed model based on the modified truss theory to

capture the shear failure mechanism in a simple way. By considering compressive and tensile stress field, a concrete section was modeled by flexural compression and tension member, the diagonal compression and tension member, and an arch member. By adopting the arch member, which was different from the traditional truss model, it was possible to express the redistribution of stress in each member after the yielding of the shear reinforcement. The lattice model was applied in the analysis of reinforced concrete columns subjected to reverse cyclic loading. Although the lattice was a complexity in its form of truss formulation, it predicted the load-displacement relationship of columns under cyclic loading quite accurately.

2.5 Shear Design with the Truss Model or the Strut-and-Tie Model

2.5.1 Shear design provisions in codes

ACI 318-02 (American Concrete Institute Building Code, 2002)

The ACI code [A1] adopts the $45°$ truss model with an additional term for concrete contribution. So the nominal shear resistance is:

$$V_n = V_c + V_s \tag{2-10}$$

where V_c = shear carried by the concrete,

V_s = shear carried by the stirrups based on the $45°$ truss.

The shear carried by concrete V_c is the sum of three mechanisms:

V_{cz} the shear carried by the compression zone of uncracked concrete,

V_{ay} the shear carried by aggregate interlocking, and

V_d the shear carried by the dowel action of longitudinal reinforcement.

A few researchers attempted to measure the magnitudes of the three mechanisms during experiments; however, only qualitative results were obtained [P2]. The ACI code [A1] considers the three mechanism as a whole and assumes that V_c is equal to the shear

strength of a beam without stirrups, which in turn, is taken equal to the load at which inclined cracking occurs:

$$V_c = \left(0.16\sqrt{f_c^{'}} + 17.2\rho_w \frac{V_u d}{M_u} \right) b_w d \le 0.3\sqrt{f_c^{'}} b_w d \qquad (2\text{-}11)$$

where ρ_w = longitudinal reinforcement ratio,

M_u = factored moment at section,

$\frac{M_u}{V_u d}$ = the shear span to effective depth ration $\frac{a}{d}$,

b_w = web width.

This equation was first introduced to design code by ACI-ASCE Committee 326 in 1962 and is still in use now. This V_c equation was derived from regression analysis of experimental data and only approximately true when the strut angle is assumed to be $45°$. In the design philosophy of ACI code [A1], V_c will approaches 0 as the struts angle approaches $30°$.

The calculation of V_s is based on $45°$ truss model. Therefore, the number of stirrups spaced at s crossed by a crack is $\frac{d}{s}$. Assuming all stirrups yield at failure, the shear carried by stirrups V_s is:

$$V_s = \frac{A_{st} f_y d}{s} \qquad (2\text{-}12)$$

where A_{st} = cross sectional area of stirrups,

f_y = yielding strength of stirrups,

d = beam effective depth.

Eurocode EC2 Part 1

In Eurocode EC2 Part 1 [E3], two shear design methods are given for reinforced concrete beams. They are:

1) the Standard Method, which combines a concrete contribution term and a shear reinforcement concrete based on $45°$ truss model,
2) the Variable Strut Inclination Method.

The standard method is the traditional approach which is similar to ACI 318-95 [A1]. The Variable Strut Inclination Method is partly derived from the Theory of Plasticity by Nielsen [N1]. This design code revolves around three quantities: V_{Rd1}, V_{Rd2}, and V_{Rd3}.

V_{Rd1} refers to the shear capacity of a concrete beam without shear reinforcement and is determined from an empirical formula:

$$V_{Rd1} = \tau_{rd} k(1.2 + 40\rho_l) b_w d \tag{2-13}$$

where τ_{rd} = basic design shear strength = $0.25 f_{ctk\,0.05}$,

$f_{ctk\,0.05}$ = the lower 5% characteristic tensile strength = $0.7 f_{ctm}$,

f_{ctm} = mean value of the tensile concrete strength = $0.30(f_{ck})^{\frac{2}{3}}$,

f_{ck} = characteristic cylinder compressive strength of concrete,

k = 1.0 for beams where more than 50% of the bottom reinforcement is curtailed; or

= $(1.6 - d) \geq 1.0$,

$\rho_l = \dfrac{A_{sl}}{b_w d} \leq 0.02$.

The above equation can be simplified to the following equation:

$$V_{Rd1} = 0.0525k(f_{ck})^{\frac{2}{3}}(1.2 + 40\rho_l) b_w d \tag{2-14}$$

An enhancement factor can be applied to V_{Rd1} if the beam is loaded by a concentrated load at a distance greater or equal to $2d$ from the face of the support. This factor is given as:

$$\beta = \frac{2.5d}{x} \quad (1.0 \le \beta \le 5.0) \tag{2-15}$$

V_{Rd2} is the shear capacity of a beam when web crushing occurs according to the Theory of Plasticity prior to yielding of shear reinforcement. The maximum V_{Rd2} value that can be attained is limited by the effective stress in the compressive struts such that:

$$V_{Rd2}(\max) = 0.5 v f_{cd} b_w (0.9d) \tag{2-16}$$

where f_{cd} = design value of concrete cylinder compressive strength, which equals the characteristic cylinder strength at 28 days,

v = the efficiency factor = $0.7 - \frac{f_{ck}}{200} \ge 0.5$.

For the purpose of analysis, f_{ck} is assumed to be equal to f_{cd}.

The difference between the Standard Method and the Variable Strut Inclination Method is in the determination of the shear resistance V_{Rd3}. The detailed methods will be illustrated below.

Standard Method

The standard method is similar to the provisions of ACI 318-95 [A1] with the total shear resistance given as:

$$V_{Rd3} = V_{cd} + V_{wd} \tag{2-17}$$

where V_{cd} = concrete contribution and is taken as equal to V_{Rd1},

$V_{wd} = \dfrac{A_{sw} f_{ywd}}{s} 0.9d$,

A_{sw} = cross-sectional area of shear reinforcement,

f_{ywd} = yielding stress of shear reinforcement.

The formula for V_{Rd3} can be written as:

$$V_{Rd3} = \beta\left(0.0525k\left(f_{ck}\right)^{\frac{2}{3}}\left(1.2+40\rho_l\right)b_w d\right) + \frac{A_{sw} f_{ywd}}{s} 0.9d \le V_{Rd2}(\max) \tag{2-18}$$

Variable Strut Inclination Method

The Variable Strut Inclination Method is based on a truss model with an angle θ chosen within the range of

1) $0.4 < \cot\theta < 2.5$ for beams with constant longitudinal reinforcement,
2) $0.5 < \cot\theta < 2.0$ for beams with curtailed longitudinal reinforcement.

The shear resistance based on the crushing of the compressive strut is:

$$V_{Rd2} = \frac{b_w (0.9d) \nu f_{cd}}{\cot\theta + \tan\theta} \tag{2-19}$$

The shear resistance based on a truss model with shear reinforcement yielding is:

$$V_{Rd3} = \frac{A_{sw} f_{ywd}}{s} (0.9d) \cot\theta \tag{2-20}$$

A limitation from the Theory of Plasticity [N1] is placed on the effectiveness of the

shear reinforcement such that:

$$\frac{A_{sw} f_{ywd}}{b_w s} \le 0.5 v f_{cd} \tag{2-21}$$

In design, the applied shear force is set to equal to V_{Rd2} to obtain the largest value of $\cot\theta$, which corresponds to the smallest amount of shear reinforcement. The amount of shear reinforcement is then found from the equation for V_{Rd3}. For analysis, a solution can only be found by equating V_{Rd3} to V_{Rd2}. The solution for θ can be found from:

$$\cot\theta \le \sqrt{\left(\frac{v f_{cd}}{\rho_{sw} f_{ywd}} - 1 \right)} \tag{2-22}$$

After solving for $\cot\theta$, the shear resistance V_{Rd3} can be calculated.

Canadian Standard CSA A23.3-94

The Canadian Standard CSA A23.3-94 [C1] provides two alternative methods for shear design of reinforced concrete beams: the General Method and the Simplified Method. The General Method is essentially the Modified Compression Field Theory [V2]. It is formulated in the form of concrete contribution plus shear reinforcement contribution. However, the General Method has a variable angle truss model. The Simplified Method is the traditional method of concrete contribution plus shear reinforcement. It is based on the $45°$ truss model assumption.

The General Method

The General Method for shear design in flexural regions is based on the Modified Compression Field Theory [V2]. The shear resistance for a section is:

$$V_{rg} = V_{cg} + V_{sg} \le 0.25\phi_c f_c' b_w d_v \qquad (2\text{-}23)$$

where V_{cg} = concrete contribution,

V_{sg} = shear reinforcement contribution.

The limit on V_{rg} is intended to prevent concrete crushing in the web prior to yielding of the transverse reinforcement. In the above equation,

$$V_{cg} = 1.3\lambda\phi_c\beta\sqrt{f_c'}\, b_w d_v \qquad (2\text{-}24)$$

where λ = factor accounting for low density concrete,

ϕ_c = material factor for concrete = 0.60,

β = factor accounting for shear resistance of cracked concrete,

f_c' = specified compressive strength of concrete,

b_w = effective web width,

d_v = lever arm of resisting flexural moment $\ge 0.9d$.

$$V_{sg} = \frac{\phi_s A_v f_y d_v (\cot\theta + \cot\alpha)\sin\alpha}{s} \qquad (2\text{-}25)$$

where ϕ_s = material factor for steel = 0.85,

A_v = area of shear reinforcement with spacing s,

f_y = specified yield strength of reinforcement,

θ = angle of inclination of diagonal compressive stresses to the longitudinal axis,

α = angle of inclined stirrups to the longitudinal axis,

s = spacing of shear reinforcement.

The factor β and the angle θ are given in the table below for sections with

transverse shear reinforcement.

Table 2.2: Values of β and θ for sections with shear reinforcement [C1]

$\frac{v_f}{\lambda\phi_c f_c'}$		Longitudinal strain ε_x						
		≤ 0.0000	≤ 0.00025	≤ 0.0005	≤ 0.00075	≤ 0.0010	≤ 0.0015	≤ 0.0020
≤ 0.050	β	0.405	0.290	0.208	0.197	0.185	0.162	0.143
	θ	27.0°	28.5°	29.0°	33.0°	36.0°	41.0°	43.0°
≤ 0.075	β	0.405	0.250	0.205	0.194	0.179	0.158	0.137
	θ	27.0°	27.5°	30.0°	33.5°	36.0°	40.0°	42.0°
≤ 0.100	β	0.271	0.211	0.200	0.189	0.174	0.143	0.120
	θ	23.5°	26.5°	30.5°	34.0°	36.0°	38.0°	39.0°
≤ 0.125	β	0.216	0.208	0.197	0.181	0.167	0.133	0.112
	θ	23.5°	28.0°	31.5°	34.0°	36.0°	37.0°	38.0°
≤ 0.150	β	0.212	0.203	0.189	0.171	0.160	0.125	0.103
	θ	25.0°	29.0°	32.0°	34.0°	36.0°	36.5°	37.0°
≤ 0.200	β	0.203	0.194	0.174	0.151	0.131	0.100	0.083
	θ	27.5°	31.0°	33.0°	34.0°	34.5°	35.0°	36.0°
≤ 0.250	β	0.191	0.167	0.136	0.126	0.116	0.108	0.104
	θ	30.0°	32.0°	33.0°	34.0°	35.5°	38.5°	41.5°

The use of the above table requires the knowledge of the maximum longitudinal strain ε_x. Due to the effects of a bending moment and a shear force, ε_x can be estimated as:

$$\varepsilon_x = \frac{0.5\left(N_f + V_f \cot\theta\right) + \frac{M_f}{d_v}}{E_s A_s} \qquad (2\text{-}26)$$

where N_f = factored axial load normal to cross-section,

V_f = factored shear force at section,

M_f = factored moment at section (positive),

E_s = modulus of elasticity of reinforcement,

A_s = area of reinforcement in tension zone.

The Simplified Method

The Simplified Method for shear also determines shear resistance as the sum of a concrete contribution and a shear reinforcement contribution.

$$V_r = V_c + V_s \le V_c + 0.8\lambda\phi_c\sqrt{f_c'}b_w d \tag{2-27}$$

The shear reinforcement contribution is:

$$V_s = \frac{\phi_s A_v f_y d}{s} \quad (\theta = 45° \text{ and } \alpha = 90°) \tag{2-28}$$

where A_v = the cross-sectional area of shear reinforcement,

d = effective depth of section.

For members having either at least the minimum amount of transverse shear reinforcement or an effective depth not exceeding 300 mm, the concrete contribution can be calculated as:

$$V_c = \frac{1.3}{6}\lambda\phi_c\sqrt{f_c'}b_w d \tag{2-29}$$

For members with effective depths greater than 300 mm and with transverse shear reinforcement less than the minimum requirement, the concrete contribution is:

$$V_c = \left(\frac{260}{1000 + d}\right)\lambda\phi_c\sqrt{f_c'}b_w d \le 0.10\lambda\phi_c\sqrt{f_c'}b_w d \tag{2-30}$$

European CEB-FIP Model Code (1990)

Although CEB-FIB Model Code [C2] can be directly used by designer, it is mainly intended as a model for various national and international codes. Therefore, it adopts a more theoretical approach than typical national codes. The CEB-FIB Model Code [C2] for shear design uses a variable angle truss model, where the angle of strut inclination varies between 18.4° and 45° ($3 \ge \cot\theta \ge 1$) to the longitudinal axis. Specially, no concrete contribution term is required in this code. In essence, this model code is an

equilibrium model for shear and strain compatibility may not be satisfied. For concrete struts under compression:

$$\frac{V_{Sd}}{\sin\theta} = f_{cd2} b_w z \cos\theta \tag{2-31}$$

where V_{Sd} = design shear load,

f_{cd2} = reduced concrete compression strength due to transverse tension,

b_w = web width,

z = shear depth.

For transverse shear reinforcement in tension:

$$V_{Sd} = \frac{A_{Sw} f_{yd}}{s} z \cot\theta \tag{2-32}$$

where A_{Sw} = area of transverse shear reinforcement,

f_{yd} = design yield strength of transverse shear reinforcement,

s = spacing of transverse shear reinforcement.

So for the CEB-FIB model code [C2], the shear resistance is provided by the transverse shear reinforcement only.

As from Equation (2-31), concrete compressive strength is reduced in the struts due to the existence of transverse tensile stress field. For cracking parallel to the direction of the compressive strut, this reduction in strength can be taken as:

$$f_{cd2} = \frac{f_{cd}}{1 + k\frac{\varepsilon_1}{\varepsilon_0}} \tag{2-33}$$

where f_{cd} = concrete design compressive strength,

k = coefficient which depends on surface roughness and diameter of bars For medium deformed bars, $k = 0.1$,

ε_0 = concrete tensile strain (about 0.002) at maximum compressive stress,

ε_1 = smeared tensile strain of cracked reinforced concrete perpendicular to applied compression.

If cracks are not parallel to the compressive stress in the struts, the compressive stress

has to be transferred across cracks by a combination of concrete friction and dowel action. This results in a further reduction of concrete strength. This reduction is greatest when cracks are at 45° to the compressive stresses, and smallest when they are parallel to each other.

Moreover, this model code specifies the nominal concrete shear strength for members without transverse shear reinforcement as:

$$\tau_c = (1.6 - d)(1 + 50\rho)\tau_{RD} \tag{2-34}$$

where d = section depth,

ρ = the flexural reinforcement ratio,

τ_{RD} = proportional to $(f_{ck})^{\frac{2}{3}}$,

f_{ck} = 28-day cube strength of concrete.

Australia Standard AS 3600 (1994)

The shear design equations in Australia Standard AS 3600 [A7] are based on a variable angle truss model. Shear resistance is also made up of concrete contribution and shear reinforcement contribution:

$$V_u = V_{uc} + V_{us} \le 0.2 f_c' b_v d_0 \tag{2-35}$$

where V_u = shear resistance,

V_{uc} = concrete contribution,

V_{us} = shear reinforcement contribution,

f_c' = concrete compressive strength,

b_v = effective web width,

d_0 = distance fro the extreme compression fiber to the centroid of the outermost layer of longitudinal tensile reinforcement.

The maximum shear capacity specified is to avoid web crushing failure when a large amount of shear reinforcement is used.

The formula for the concrete contribution is similar to a statistically derived expression by Zsutty [Z1]. V_{uc} according to AS 3600 [A7] is:

$$V_{uc} = \beta_1 \beta_2 \beta_3 b_v d_0 \left(\frac{A_{st} f_c^{'}}{b_v d_0} \right)^{\frac{1}{3}} \tag{2-36}$$

where $\beta_1 = 1.1\left(1.6 - \frac{d_0}{1000}\right) \geq 1.1$ (accounts for size factor of a section),

$\beta_2 = 1.0$ when no axial load (account for axial load effects),

$\beta_3 = \frac{2d_0}{a}$ $1.0 \leq \beta_3 \leq 2.0$ (account for the presence of a large concentrated load near a support),

a = the distance of the concentrated load from the support,

A_{st} = cross-sectional area of longitudinal tensile reinforcement.

For vertical transverse shear reinforcement, AS 3600 [A7] gives its contribution as:

$$V_{us} = \frac{A_{sv} f_{sy.f} d_0 \cot\theta_v}{s} = \rho_t f_{sy.f} b_v d_0 \cot\theta_v \tag{2-37}$$

where A_{sv} = cross-sectional area of shear reinforcement,

$f_{sy.f}$ = yield stress of shear reinforcement,

θ_v = angle of inclination of the concrete compressive strut,

s = spacing of the shear reinforcement,

ρ_t = shear reinforcement ratio.

AS 3600 [A7] also stipulates that a minimum amount of shear reinforcement to be used before it is effective for shear contribution:

$$A_{st.\min} = \frac{0.35 b_v s}{f_{sy.f}} \tag{2-38}$$

In AS 3600 [A7], the angle of inclination of compressive strut θ_v is the angle between the axis of the concrete compressive strut and the longitudinal axis of the member. It is assumed to vary linearly between $30°$ when the minimum amount of shear reinforcement is used and $45°$ when the limiting amount of shear reinforcement corresponding to web crushing is used. For most practical beams with relatively small amount of shear reinforcement, the angle θ_v is close to $30°$ as the limiting amount of shear reinforcement corresponding to web crushing is much greater than $A_{st.\min}$.

2.5.2 Other researches on shear design

Ramirez and Breen

In the research of Ramirez and Breen [R1], a modified truss model design approach with variable angle of inclination struts and a concrete contribution for reinforced concrete beams with shear reinforcement was proposed as a viable and economic design tool. The shear resistance of a reinforcement concrete beam was treated as a combination of truss model capacity and concrete contribution. Followed from the traditional approach, the truss model capacity (essentially shear reinforcement contribution) was obtained by the equilibrium of summation of vertical forces:

$$V_{truss} = A_v f_y \frac{z}{s} \cot \alpha \qquad (2\text{-}39)$$

where A_v = area of the shear reinforcement,

f_y = yield strength of the shear reinforcement,

z = truss effective depth,

s = spacing of shear reinforcement,

α = angle of inclination of struts.

Ramirez and Breen [R1] pointed out that designing of shear reinforcement based entirely on the equilibrium condition of truss model described in Equation (2-39), unduly penalized the majority of beams which were subjected to low level of shear

stress or that had no or low amounts of shear reinforcement. Other components of the shear carrying mechanism which supplement the contribution of the truss model must be considered. They also indicated that the contribution of these components of the failure mechanism might be reflected by means of an additional concrete contribution. Thus, Ramirez and Breen [R1] proposed a concrete contribution for reinforced concrete beam in shear. This concrete contribution has been illustrated in graphical manner as following by them:

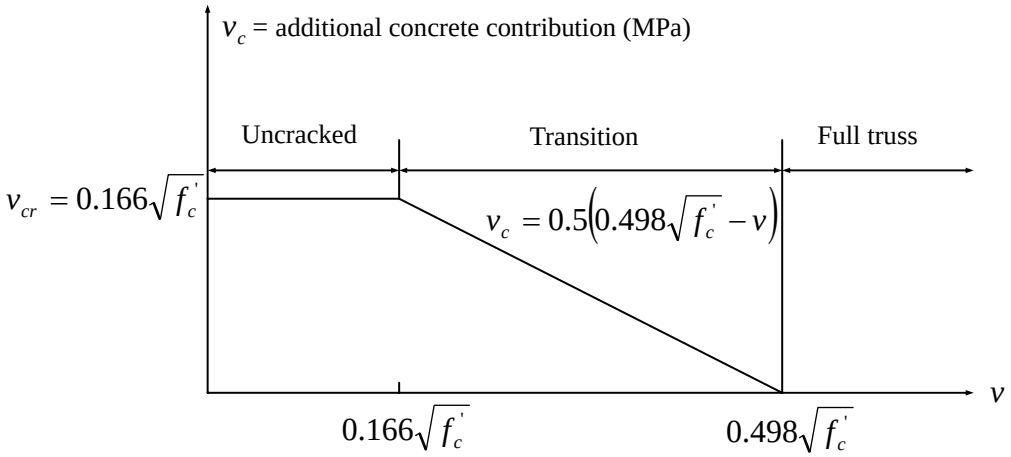

Figure 2.5: Diminishing concrete contribution for reinforced concrete beams [R1]

The horizontal axis represented the shear stress level v, produced by the applied loading $\frac{V_u}{b_w z}$, where V_u was the factored shear force at the section. As seen from the graph, the concrete contribution was a diminishing term with the increase of the shear stress level. This was compared with current ACI design code [A1] which specifies a constant concrete contribution term regardless of the concrete deterioration. Therefore, the total shear resistance in the modified truss model was:

$$V_{MTM} = V_{truss} + v_c b_w z \tag{2-40}$$

Another important condition was the proposed modified truss model design approach had limitations imposed on the angle of inclination of the truss struts. **Figure 2.6** showed that of the angle of inclination α of the truss struts was $45°$, the mean crack strain ε_r defined as the ratio of crack width to the distance between cracks is at the

minimum value for yielding of both the longitudinal and transverse reinforcement. Large deviations from $45°$ of the angle of inclination would demand excessive strains in the reinforcement together with extremely wide crack opening at failure. So in the proposed design procedure, the inclination of these struts must be within the limits of $30° \le \alpha \le 65°$ for reinforced concrete beams.

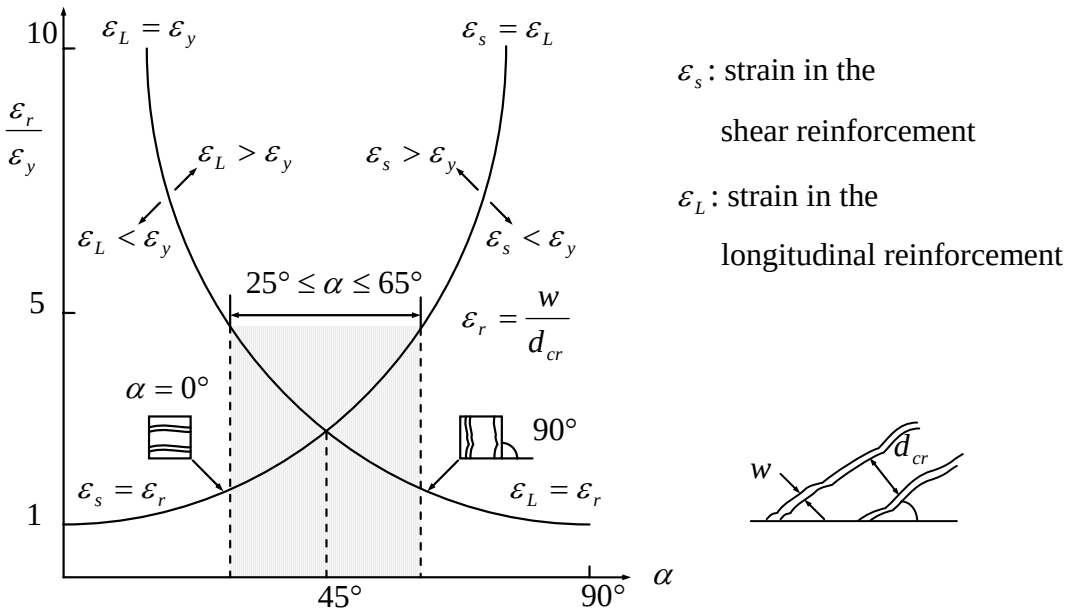

Figure 2.6: Relationship of strut angle with crack and strains in the reinforcement [T1]

Ramirez and Breen [R1] used this modified truss model to predict shear capacity of 59 reinforced concrete beams failed in shear. The shear capacity of the modified truss model included a concrete contribution as shown in **Figure 2.5** and an assumed variable angle truss model of $30°$ corresponding to the proposed lower limit which gave the maximum design estimation for a beam. Results showed that the modified truss model generally provided conservative shear capacity ($\frac{V_{TEST}}{V_{MTM}} \ge 0.97$) as compared with experimental measurements.

Hong and Ha

According to the research of Hong and Ha [H2], a new shear-friction truss model was presented for slender reinforced concrete beams to derive a simple design equation for ultimate shear strength. In their model, a portion of shear strength was provided by shear reinforcement and the remainder by the shear-friction mechanism. The shear-friction mechanism could be taken as a representation of shear carried by concrete. Thus, for the shear-friction truss model, the ultimate shear strength was:

$$V = V_t + V_f \tag{2-41}$$

where V_t = shear component carried by truss action,

V_f = shear component carried by friction mechanism.

First of all, Hong and Ha [H2] adopted shear reinforcement contribution as in the traditional truss model, which gave

$$V_t = \frac{A_v f_{sy} d}{s \tan\theta} \tag{2-42}$$

where A_v = cross-sectional area of shear reinforcement'

f_{sy} = yield strength of shear reinforcement,

d = effective depth of section,

s = spacing of shear reinforcement,

θ = crack angle.

Hong and Ha [H2] then recognized the fact that additional components other than shear reinforcement began to resist shear after inclined shear cracks formed, namely aggregate interlocking, the dowel action, and the shear in the uncracked zone. They explained these three different mechanisms commonly by the shear transfer across rough surface by the friction mechanism. The relative displacement along the rough crack mobilized the friction mechanism as shown in **Figure 2.7**.

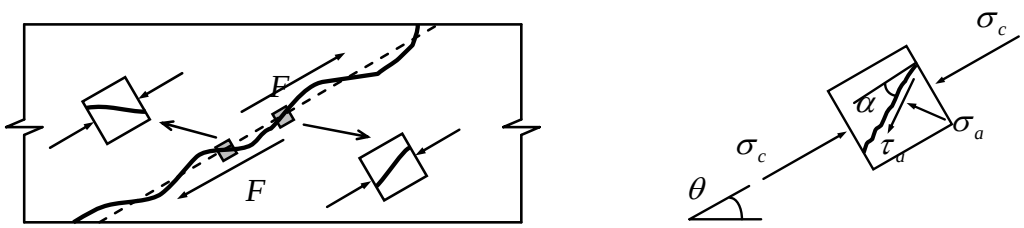

(a) Friction forces on the crack (b) Infinitesimal element on the crack

Figure 2.7: Shear-friction mechanism [H2]

From **Figure 2.7 (b)**, the infinitesimal element involved in the crack surface was under uniaxial compression and the equilibrium of stresses gave:

$$\sigma_a = \sigma_c \sin^2 \alpha \tag{2-43}$$

$$\tau_a = \sigma_c \sin \alpha \cos \alpha \tag{2-44}$$

where σ_c = uniaxial stress along the average crack orientation,

σ_a = the friction stress normal to the crack surface,

τ_a = the friction stress tangential to the crack surface.

For the angle of inclined strut in the traditional truss model, Hong and Ha [H2] modified the truss model to satisfy a state of balanced failure, when both shear reinforcement and longitudinal reinforcement yielded simultaneously. For the free body diagram of **Figure 2.8**, equilibrium for the left and right body yielded:

$$T' = 0.5V_t \cot \theta + F \cos \theta \tag{2-45}$$

$$A_s f_y \times d - T' \times d + F \cos \theta \times \frac{d}{2} - (V_t + F \sin \theta)\left(a - \frac{d}{2}\cot \theta\right) = 0 \tag{2-46}$$

where F = the shear-friction capacity,

A_s = cross-sectional area of longitudinal reinforcement,

f_y = yield strength of longitudinal reinforcement.

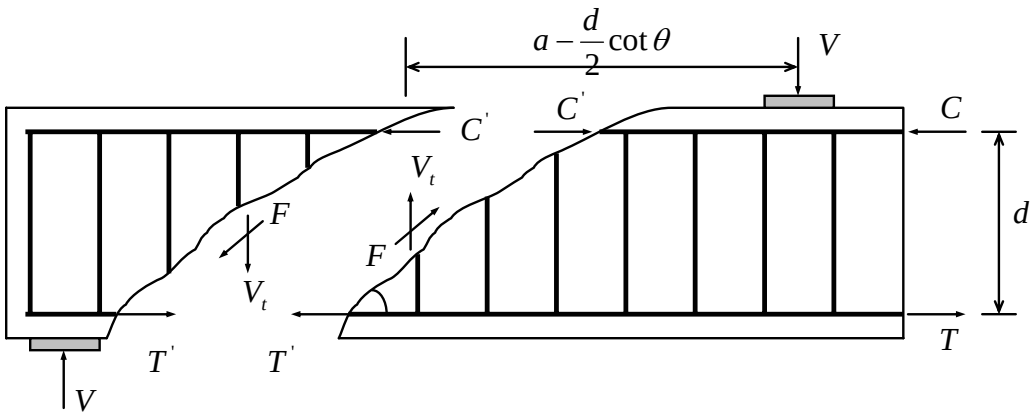

Figure 2.8: Free body diagram of cracked reinforced concrete beam [H2]

Hong and Ha [H2] took the shear-friction resistance as the sum of τ_a in the direction of average crack path and its magnitude depended on the $\cos\alpha$ of the deviation angle of the individual contact surface. They also found that only those crack surfaces, which deviated in the counter-clockwise according to **Figure 2.7**, contributed to the shear-friction mechanism. So only half of the crack surface could be used to evaluate friction force. Then the shear-friction τ_f in the direction of average crack path was obtained by calculating the mean value of the counter-clockwise deviation angle. Various probability functions, called contact density function $\rho(\theta)$, have been proposed to describe the distribution of local deviation angle. Hong and Ha [H2] used Li and Maekawa's [L4] suggestion of taking $\rho(\theta)=0.5\cos\theta$. This function was thesised to produce excellent correlation with specimen having $f_c^{'} \le 50$ MPa. Hence,

$$\alpha_{avg}=\frac{\int_0^{\frac{\pi}{2}}\alpha\cos\alpha d\alpha}{\int_0^{\frac{\pi}{2}}\cos\alpha d\alpha}=32.7^\circ \qquad (2\text{-}47)$$

$$\tau_f=\sigma_c\sin^2 32.7^\circ\cos^2 32.7^\circ=0.206\sigma_c \qquad (2\text{-}48)$$

According to Equation (2-48), shear-friction capacity of a rough surface was only about 20% of the uniaxial compressive stress present in the direction of average crack angle. Combining Equation (2-48) with the concept of effective contact area A_e, the

magnitude if friction could be calculated as:

$$F = \tau_f A_e = 0.206\sigma_c \frac{b_w(0.5d)}{\sin\theta} = 0.102 v_f f_c^{'} \frac{b_w d}{\sin\theta} \qquad (2\text{-}49)$$

where b_w = web width,

d = effective depth of section,

v_f = effective coefficient of concrete strength,

$f_c^{'}$ = compressive strength of concrete.

In Equation (2-49), σ_c has been replaced by $v_f f_c^{'}$, which was the effective strength of concrete in resisting shear on an inclined crack surface. Then, Hong and Ha [H2] gave the ultimate shear strength as:

$$V = \frac{A_v f_{sy} jd}{s \tan\theta} + 0.103 v_f f_c^{'} b_w d \qquad (2\text{-}50)$$

From Equation (2-50), inclined crack angle θ and effective coefficient v_f were obtained by the following procedure proposed by Hong and Ha [H2]:

1. Assume a linear relationship of $f_c^{'}$ and v_f: $v_f = A \times f_c^{'} + B$
2. Calculate θ and V using Equation (2-46) and Equation (2-50)
3. Find new coefficients A and B using linear regression of $f_c^{'}$ and v_f
4. Repeat Step 2 and Step 3 until satisfactory convergence is reached

Hong and Ha also gave a relationship for the effective coefficient of concrete strength based on experimental observations.

$$v_f = -0.003 f_c^{'} + 0.431 \qquad (2\text{-}51)$$

2.6 Concrete Plasticity and Modified Compression Field Theory

2.6.1 Concrete Plasticity

The Concrete Plasticity was developed by Nielsen [N1] in 1984. Based on the limit state design approach, which is more interested in designing a safe structure than in tracing its complete behavior throughout loading history, the Concrete Plasticity [N1] offers a useful tool to determine carrying capacity of structural members. Application of the Concrete Plasticity [N1] is of the following two theorems: the Lower Bound Theorem and the Upper Bound Theorem.

Lower Bound Theorem

According to the Lower Bound Theorem of the Concrete Plasticity [N1], a safe carrying capacity of a structural member can be found when equilibrium and boundary conditions are satisfied and the material does not exceed the yield condition anywhere. In **Figure 2.9**, a reinforced concrete beam is loaded with two concentrated loads applied at distance a from the supports. So the portions of the beams between the supports and load points are subjected to a shear force of P. The capacity of the beam is reached when one or more of the following conditions are attained:

- the longitudinal reinforcement yields,
- the transverse shear reinforcement yields, or
- the concrete crushes.

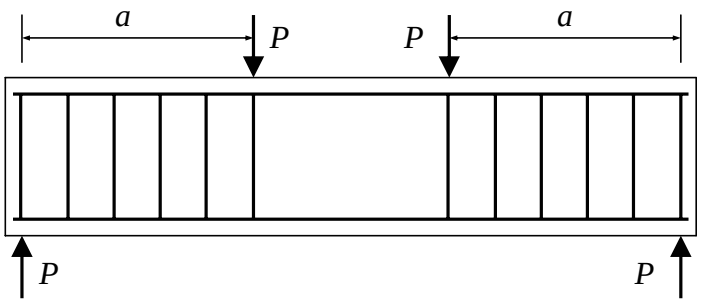

Figure 2.9: Beam loaded in shear by concentrated forces [N1]

In **Figure 2.10**, the left portion between support and load point of the beam is taken for analysis. It is assumed a diagonal compression stress σ_c of an angle θ is developed in the concrete web of the beam by the shear force P. So the shear reinforcement and the lower stringer are in tension and the upper stringer is in compression. Consider an infinitesimal element inclined at θ to the x-axis. The element is subjected to the uniaxial compression stress σ_c. By transforming σ_c into the $x-y$ directions, it gives:

$$\sigma_x = -\sigma_c \cos^2\theta \tag{2-52}$$

$$\sigma_y = -\sigma_c \sin^2\theta + r\sigma_s \tag{2-53}$$

$$\tau = \sigma_c \sin\theta\cos\theta \tag{2-54}$$

where r = shear reinforcement ratio,

σ_s = stress in the shear reinforcement,

τ = shear stress in the $x-y$ directions.

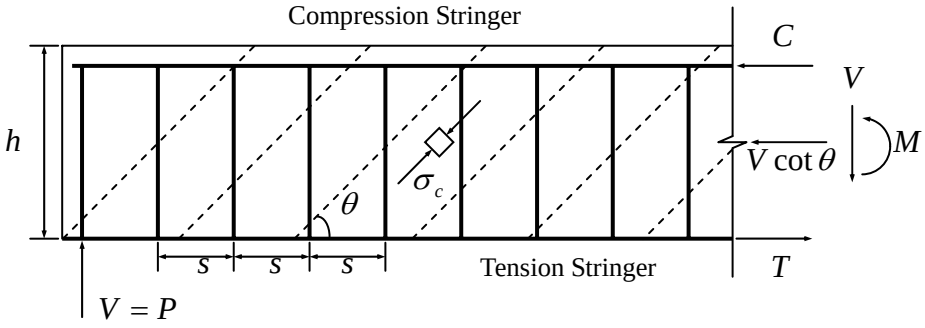

Figure 2.10: Diagonal compression field in the web [N1]

Equation (2-54) can be rewritten as:

$$\sigma_c = \frac{\tau}{\sin\theta\cos\theta} = \tau\left(\tan\theta + \cot\theta\right) \tag{2-55}$$

Vertical stress equilibrium requires $\sigma_y = 0$, therefore,

$$r\sigma_s = \sigma_c \sin^2\theta = \tau\tan\theta \tag{2-56}$$

Then, from Equation (2-55) and Equation (2-56),

$$\tan\theta = \frac{r\sigma_s}{\tau} = \frac{r\sigma_s}{\sigma_c}\frac{\sigma_c}{\tau} = \xi\left(\tan\theta + \cot\theta\right) \tag{2-57}$$

where $\xi = \dfrac{r\sigma_s}{\sigma_c}$ (degree of shear reinforcement)

From Equation (2-57), the strut angle θ for the lower bound solution is obtained as:

$$\tan\theta = \sqrt{\frac{\xi}{1-\xi}} \tag{2-58}$$

Hence, from Equation (2-55) and Equation (2-58),

$$\frac{\tau}{\sigma_c} = \sqrt{\xi(1-\xi)} \tag{2-59}$$

$$\left(\frac{\tau}{\sigma_c}\right)^2 + \left(\xi - \frac{1}{2}\right)^2 = \frac{1}{4} \tag{2-60}$$

Equation (2-60) represents a circle in the $(\dfrac{\tau}{\sigma_c}, \xi)$ coordinate system. In the range of $0 \le \xi \le \dfrac{1}{2}$, the right hand side of Equation (2-60) is a positive and monotonically increasing function of ξ. Therefore, τ is maximum for $(\sigma_c)_{\max} = f_c$ and for

$$\xi_{\max} = \frac{r(\sigma_s)_{\max}}{f_c} = \frac{rf_y}{f_c} = \psi \tag{2-61}$$

This solution is obtained when the concrete web crushes and shear reinforcement yields simultaneously. However, the longitudinal reinforcement remains elastic. Equation (2-60) gives the best lower bound solution as $\tau_{\max} = \dfrac{1}{2} f_c$. Equation (2-58) and Equation (2-59) show that when $0 \le \psi \le 0.5$, the compressive stress direction is $0° \le \theta \le 45°$. Thus, the Lower Bound Theorem produces a diagonal compression field at an angle that varies depending on the shear reinforcement ratio and does not exceed $45°$ to the longitudinal axis. It is noticed that the lower bound solution neither discusses displacement compatibility nor the special condition at the concentrated loads.

Upper Bound Theorem

The Upper Bound Theorem is to find the strength of the structure when failure mechanism is compatible with the geometrical constraints of the structure. Whereas lower bound solutions exist only in certain simple cases and are difficult to deal with for more complicated loadings, it is easier to develop upper bound solutions for even most complicated cases. Consider again a reinforced concrete beam with two concentrated loads. The beam has a constant shear reinforcement degree ψ. An upper bound solution is sought whereby the central portion of the beam slides along straight yield lines at angle β to the horizontal and displaces by a vertical distance u. The work equation by equating external and internal work is:

$$Pu = rf_y bh\cot\beta \times u + \frac{1}{2} f_c b(1-\cos\beta)\frac{h}{\sin\beta} \times u \qquad (2\text{-}62)$$

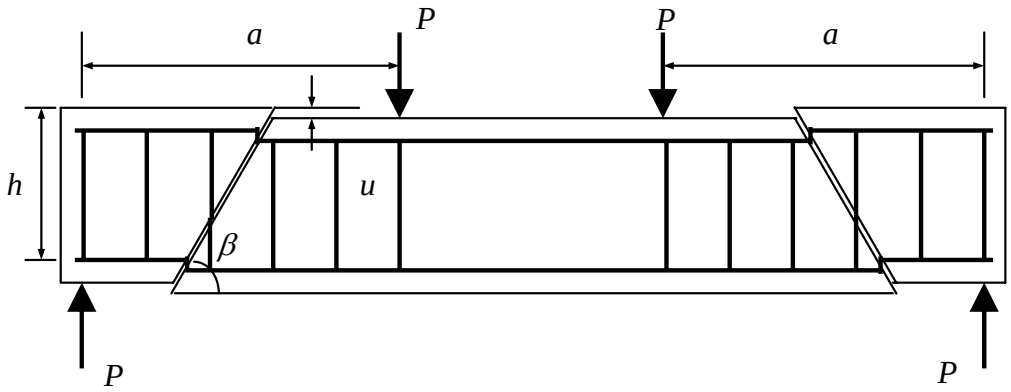

(a) Shear failure mechanism for a beam subjected to concentrated loads [N1]

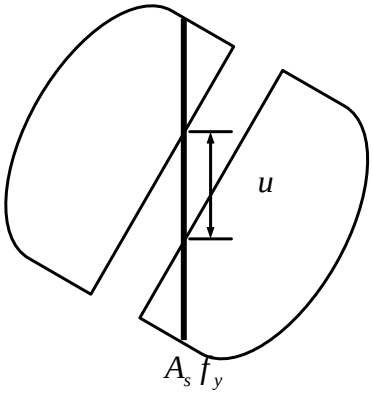

(b) Strain energy of shear reinforcement

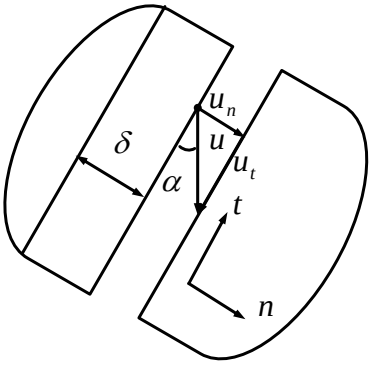

(c) Yield line (crack) in concrete web

Figure 2.11: Upper bound solution for a beam subjected by concentrated loads

The first term on the right-hand side is the dissipation in the shear reinforcement

crossing the yield line; the second term is the dissipation in the concrete determined form plane stress of the Modified Coulomb material. The upper and lower stringers do not contribute at all according to the assumption. From Equation (2-62), we can find the upper bound solution as:

$$\frac{\tau}{f_c} = \frac{P}{bhf_c} = \psi \cot\beta + \frac{1}{2}(1-\cos\beta)\frac{1}{\sin\beta} \tag{2-63}$$

If $\frac{\tau}{f_c}$ is minimized with respect to β, the solution is:

$$\frac{\tau}{f_c} = \sqrt{\psi(1-\psi)} \tag{2-64}$$

which is identical to the lower bound solution. The angle β is found to be:

$$\tan\beta = \frac{2\sqrt{\psi(1-\psi)}}{1-2\psi} \tag{2-65}$$

which may be shown to correspond to

$$\beta = 2\theta \tag{2-66}$$

where θ = angle from lower bound solution

For geometrical reasons, it is required that

$$\frac{h}{a} \le \tan\beta \le \infty \tag{2-67}$$

for the solution of Equation (2-64) to be valid. Then, inserting the value of β determined by $\tan\beta = \frac{h}{a}$ into equation (2-63),

$$\frac{\tau}{f_c} - \frac{1}{2}\left(\sqrt{1+\left(\frac{a}{h}\right)^2} - \frac{a}{h}\right) + \psi\frac{a}{h} \tag{2-68}$$

which is the shear capacity when $\tan\beta$ determined from Equation (2-65) does not

satisfy the first condition Equation (2-67). The straight line of Equation (2-68) is tangent to the circle of Equation (2-64), and since the inclination is known to be $\frac{a}{h}$, it is easily constructed. The value $\beta = \frac{\pi}{2}$ ($\tan\beta = \infty$) corresponds to a vertical yield line and is obtained for $\psi = 0.5$, where $\frac{\tau}{f_c} = 0.5$. An increase in the amount of shear reinforcement beyond this value evidently does not increase the load-carrying capacity. Therefore, for $\psi > 0.5$, the solution has $\frac{\tau}{f_c} = 0.5$. The final solution obtained is shown in **Figure 2.12**.

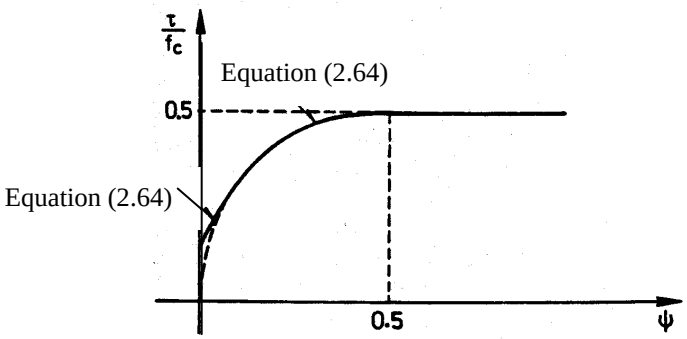

Figure 2.12: Upper bound solution for the maximum shear capacity

2.6.2 Modified Compression Field Theory

The Modified Compression Field Theory [V2], developed by Vecchio and Collins, provides a unified approach to the analysis of reinforced concrete elements under general in-plane stress conditions. In contrast to the limit state design approach of the Theory of Plasticity [N1], Modified Compression Field Theory [V2] describes the behavior of reinforced concrete elements through the entire cracked range up to failure. It idealizes cracked concrete as a material with coinciding principal stress and strain axes which are free to adapt their directions as required by the applied loads. The Modified Compression Field Theory [V2] utilizes tensile stresses in the cracked concrete to contribute to strengths of the elements. The key simplifying assumption of the Modified Compression Field Theory [V2] is that the principal strain directions

coincide with the principal stress directions. This assumption is justified by experimental measurements which show that the principal directions of stress and strain are parallel within $\pm 10°$. Also, concrete struts are at shallower angles than the cracks, and the compressive stress field must be transferred across the cracks, thus reducing strength from its uncracked state and inducing shear stress across the crack faces. The review here is on the extension of the theory to the analysis of reinforced concrete beams loaded in combined shear and moment.

Strain Compatibility

The strain compatibility relationships in the crack concrete web are established using the geometrical transformations represented by Mohr's circle of strain as shown in **Figure 2.13**. Useful equations derived include:

$$\gamma_{xy} = \frac{2(\varepsilon_x - \varepsilon_2)}{\tan\theta} \tag{2-69}$$

$$\varepsilon_x + \varepsilon_y = \varepsilon_1 + \varepsilon_2 \tag{2-70}$$

$$\tan^2\theta = \frac{\varepsilon_x - \varepsilon_2}{\varepsilon_y - \varepsilon_2} = \frac{\varepsilon_1 - \varepsilon_y}{\varepsilon_1 - \varepsilon_x} = \frac{\varepsilon_1 - \varepsilon_y}{\varepsilon_y - \varepsilon_2} = \frac{\varepsilon_x - \varepsilon_2}{\varepsilon_1 - \varepsilon_x} \tag{2-71}$$

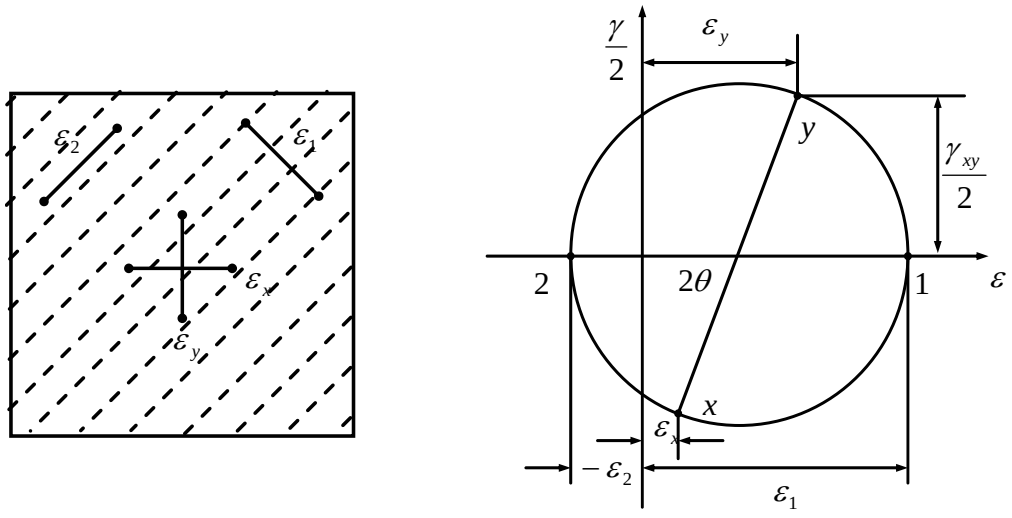

(a) Average strain in web element (b) Mohr's circle of strain

Figure 2.13: Strain compatibility of crack concrete web [V2]

Note that, for cracked concrete, these compatibility relationships are expressed in terms of "average" strains, i.e., strains measured over base lengths long enough to include

several cracks.

Stress-strain Relationship of Cracked Concrete

From **Figure 2.14**, an infinitesimal element in the web of a beam is subjected to biaxial stresses of compression and transverse tensile at the same time. Vecchio and Collins [V2] tested reinforced panels under biaxial stresses and found that the principal compressive stress f_2 is a function not only of the principal compressive strain ε_2, but also of the coexisting principal tensile strain ε_1. They suggested the following parabolic stress-strain relationship:

$$f_2 = f_{2\max}\left(2\left(\frac{\varepsilon_2}{\varepsilon_c'}\right)-\left(\frac{\varepsilon_2}{\varepsilon_c'}\right)^2\right) \qquad (2\text{-}72)$$

where $\dfrac{f_{2\max}}{f_c'} = \dfrac{1}{0.8-0.34\dfrac{\varepsilon_1}{\varepsilon_c'}} \le 1.0$,

$\varepsilon_c' = -0.002$.

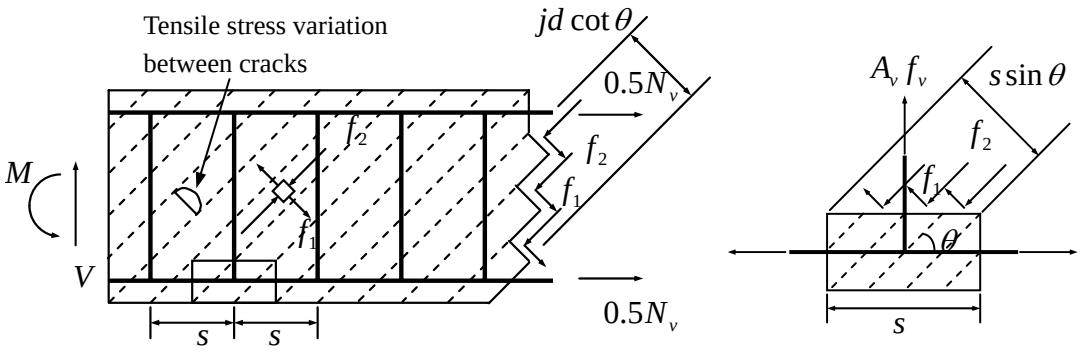

(a) Principal stresses in concrete

(b) Tension in web reinforcement

Figure 2.14: Equilibrium conditions for Modified Compression Field Theory

The relationship between the average principal tensile stress in the concrete and the average principle tensile strain is nearly linear prior to cracking and then shows

decreasing values of f_{c1} with increasing values of ε_1 (see **Figure 2.13**). The relationship suggested prior to cracking is:

$$f_{c1} = E_c \times \varepsilon_1 \tag{2-73}$$

where $E_c = 2\dfrac{f_c^{'}}{\varepsilon_c^{'}}$ (modulus of elasticity of concrete).

The relationship suggested after cracking is:

$$f_{c1} = \frac{f_{cr}}{1+\sqrt{200\varepsilon_1}} \tag{2-74}$$

where f_{cr} = stress in concrete at cracking.

In addition, the reinforcing steel behaves elastically:

$$f_{sx} = E_s \times \varepsilon_x \le f_{yx} \tag{2-75}$$

$$f_{sy} = E_s \times \varepsilon_y \le f_{yy} \tag{2-76}$$

where f_{sx} = average stress in the x-reinforcement,

f_{yx} = yield strength of x-reinforcement,

f_{sy} = average stress in the y-reinforcement,

f_{yy} = yield strength of y-reinforcement.

Equilibrium between Cracks

Again, **Figure 2.14** is used to establish the equations of equilibrium. Shear in the section is resisted by the diagonal compressive stress f_2 together with the diagonal tensile stress f_1. The tensile stress varied from 0 at the cracks to the maximum between cracks. The average value is used in the equilibrium formulation. Refer to the Mohr circle of stresses in **Figure 2.15**,

$$f_1 + f_2 = v(\tan\theta + \cot\theta) \tag{2-77}$$

where $v = \dfrac{V}{b_w jd}$.

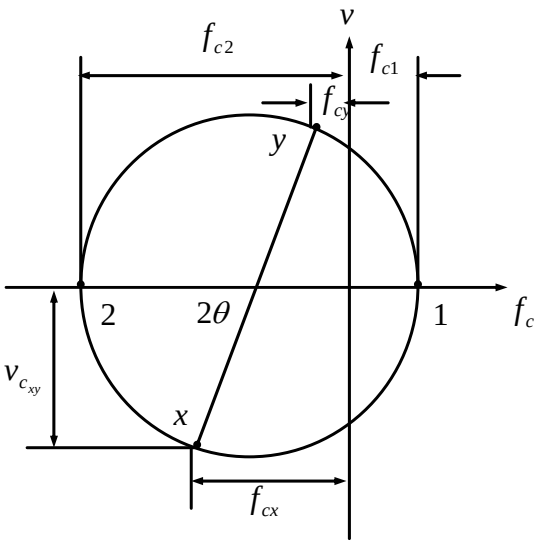

Figure 2.15: Average stress condition in a reinforced concrete element [V2]

In the concrete web, the diagonal compressive stress pushes apart the flanges of the beam while the diagonal tensile stress pulls them together. The vertical imbalance is carried by the tension in the shear reinforcement. So:

$$A_v f_v = (f_2 \sin^2\theta - f_1 \cos^2\theta) b_w s \tag{2-78}$$

From Equation (2-77) and Equation (2-78),

$$v = \frac{f_1}{\tan\theta + \cot\theta} + \frac{1}{\tan\theta + \cot\theta}\left(\frac{A_v f_v}{b_w s} + f_1 \cos^2\theta\right)\frac{1}{\sin^2\theta} \tag{2-79}$$

$$V = v b_w jd = \frac{A_v f_v b_w jd}{b_w s}\frac{\cos^2\theta + \sin^2\theta}{(\tan\theta + \cot\theta)\sin^2\theta} + \frac{f_1 b_w jd}{\tan\theta + \cot\theta} \tag{2-80}$$

$$V = \frac{A_v f_v}{s} jd \cot\theta + f_1 b_w jd \cot\theta \tag{2-81}$$

$$V = V_s + V_c = \text{Steel Contribution + Concrete contribution} \tag{2-82}$$

So the steel contribution is based on the variable angle truss model, whereas the concrete contribution is the shear resisted by the tensile stress of cracked concrete.

Equilibrium across the Cracks

In checking the condition at a crack, the actual complicated crack pattern is idealized as a series of parallel cracks, all occurring at an angle θ to the longitudinal axis. In the cracked surface, transmitting shear stress requires a local shear stress v_{ci}. The equilibrium between cracks and equilibrium across cracks must be statically equivalent. Equivalence of vertical forces at the two locations requires:

$$A_v f_v \left(\frac{jd}{s \tan\theta} \right) + f_1 \frac{b_w jd}{\sin\theta} \cos\theta = A_v f_{vy} \left(\frac{jd}{s \tan\theta} \right) + v_{ci} b_w jd \qquad (2\text{-}83)$$

To maintain this equality, the average tensile stress f_1 must be

$$f_1 = v_{ci} \tan\theta + \frac{A_v}{b_w s} \left(f_{vy} - f_v \right) \qquad (2\text{-}84)$$

For the vast majority of concrete, cracking will occur along the interface between the cement paste and the aggregate particles. The resulting rough cracks can transfer by aggregate interlock. The relationships between the shear across the crack v_{ci}, the crack width w, and the required compressive stress on the crack f_{ci} have been experimental studied by a number of investigations. Vecchio and Collins [V2] adopted Walraven's [W1] work and derived the following relationship:

$$v_{ci} = 0.18 v_{ci\max} + 1.64 f_{ci} - 0.82 \frac{f_{ci}}{v_{ci\max}} \qquad (2\text{-}85)$$

where $v_{ci\max} = \dfrac{\sqrt{f_c'}}{0.31 + 24 \dfrac{w}{a+16}}$,

a = maximum aggregate size in millimeters.

The crack width w to be used in Equation (2-85) should be the average crack width over the crack surface. It can be taken as the product of the principal tensile strain and the crack spacing s_θ. That is:

$$w = \varepsilon_1 \times s_\theta \tag{2-86}$$

where $s_\theta = \dfrac{1}{\dfrac{\sin\theta}{s_{mx}} + \dfrac{\cos\theta}{s_{my}}}$,

s_{mx} = indicator of the crack control characteristics of the x-reinforcement,

s_{my} = indicator of the crack control characteristics of the y-reinforcement.

Solution Algorithm

Vecchio and Collins [V2] have given the solution of the Modified Compression Field Theory. Given the strains in a reinforced concrete beam, it is reasonably direct procedure to calculate the stresses which cause these strains. The only iteration that may be required is in determining f_{ci} if the reinforcement is not capable of transmitting the tension in the concrete across the cracks. To find the beam strains, given the stresses, is a more difficult problem that requires a trial-and-error solution.

2.7 Summary

A review of present day truss model and strut-and-tie model literatures has been presented. Researchers, from time to time, contributed to this approach and turned the very rudimentary truss analogy into quite sophisticated strut-and-tie model. The review conducted in this chapter shows that truss model is the prevailing concept used in the shear design. Based on limited state design approach, truss model provides the contribution from shear reinforcement. On top of that, shear carried by concrete supplements the shear strength. However, the concrete contribution is not an analytical method but empirical or semi-empirical equations. Modified Compression Field Theory [V2] provides a good approach to analyze both the shear strength and deformation on the basis of truss model representation. Strut-and-tie model is mainly for design of the regions with complicated stress flows. The differentiation in the structures or structural elements between B-regions and D-regions enabled the appropriate treatment according to the stress state of structural concrete elements. The Concrete Plasticity [N1] also came into the picture and assisted in promoting complicated non-linear inelastic analysis.

The truss model and the strut-and-tie model can reflect realistically the internal stress flows and have been proven to be rational approaches in structural concrete design. Work has been done towards unifying the design and detailing concepts based on the truss and the strut-and-tie models. Some study attempts have been made in the performance behavior such as in the area of strength, ductility, and deformation capacity. However, there is still a lack of theoretically based approach to design of reinforced concrete member, especially in shear. As reviewed, the truss and strut-and-tie methodology, which has been developed for more than a century, still provides great potential in the study of the behavior of structural concrete. Hence, this thesis works towards a more appropriate and consistent analytical method with the truss model and strut-and-tie model for various structural elements.

CHAPTER 3

PREDICTING THE OVERALL RESPONSE OF REINFORCED CONCRETE BEAMS SUBJECTED TO SHEAR USING MODIFIED TRUSS MODEL

3.1 Introduction

The truss model analogy has greatly influenced the shear design procedure for strength throughout the years. Moreover, current ACI 318-02 [A1] design code also comments that requirement for serviceability besides the strength limit state should be complied when using the truss model analogy for design. Thus, there is a need to investigate deformation of reinforced concrete members when modeled by truss analogy. For this purpose, this chapter presents a modified truss model to predict overall response of reinforced concrete beams under monotonic loading. The modified model focuses on optimum strength and deformation of the beams. Some of those which are relevant to the research in this chapter are reviewed here.

In 1967, Bresler & MacGregor [B1] reviewed the mechanism and analyses of concrete beams failing in shear. For shear failure analyses, they commented that truss model analogy is generally a more useful model for the design of reinforced concrete beams with transverse reinforcement. Bresler & MacGregor [B1] gave graphic illustrations on a classical truss model which was actually a constant angle truss model and a modified truss model which in turn was essentially the early concept of the variable angle truss model. Although a further analytical work on these models has not been provided, they gave a very good conceptual basis for further research on truss model analogy. For more complicated statically indeterminate truss models, Bresler & MacGregor [B1] pointed out that these models were partly to account for the shear capacity of the concrete and partly to account for the complex stress field in the real reinforced

concrete beams. Finally, they concluded that a general design method appeared to be possible and further development of shear analysis should lead to the formulation of suitable practical design criteria.

When estimating stiffness of coupling beams after cracking, Paulay [P3] recognized shear deformation owing to truss action. He indicated that a considerable portion of shear force was transferred from one support to the other by the stirrups which together with the diagonal concrete struts formed a truss. Paulay [P3] showed an analogous truss model with tapered struts and studied principal dimensions, vertical forces, and deformation of a typical shear transfer linkage. Then from compatibility condition, he derived shear rotation of the analogous truss model. Paulay's analogous truss model with tapered struts was actually a variable angle truss model and his work laid the foundation for further detailed analysis with the truss model analogy.

In 2000, To *et al* [T3] thesised a study on an initial attempt to develop strut-and-tie model formation procedure, which allowed the cyclic hysteretic response of reinforced concrete structures to be examined. For this purpose, they proposed an idealized uniaxial fiber model to simulate the axial force-displacement characteristic of a combined concrete and steel reinforcing element. This model was subsequently employed as the top and bottom chord members in the strut-and-tie model. Then they briefly discussed about dimensioning of chords, struts and ties and allowable strength of these members. The strut-and-tie model from this procedure gave satisfactory analytical results to the experimental observations. However, the suggested procedure was simple and thus resulted in several deficiencies in the prediction.

As reviewed, truss model analogy has demonstrated its convenience and potential in analyzing stiffness, and hence deformation of reinforced concrete members. However, there is no mature method to calculate displacement in a truss model by hand until now. Therefore, the modified truss model is developed for computer analysis. The model is comprehensive which is rendered as a more realistic representation of internal stress flow of beams subjected to shear.

3.2 Proposed Modified Truss Model

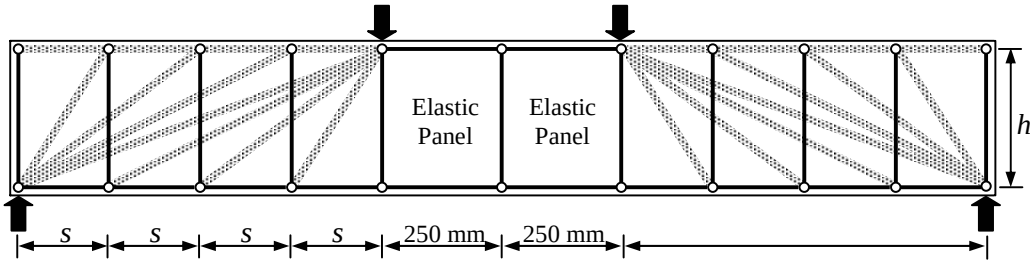

Figure 3.1: Proposed modified truss model

A graphical presentation of the overall setup of the modified truss model is given in **Figure 3.1**. Compressive members are shown in dash lines while tensile members are shown in full lines. Particularly, the shear span of the reinforced concrete beam is modeled by a variable angle truss model which is statically indeterminate. In the middle region between the two loading points, where the moment is constant and the shear force is zero, two two-dimensional elastic panels are used in the model without losing any generality. Every type of members in the modified truss model will be illustrated in detail here. The top chord members, which representing top reinforcing bars and concrete are subjected to compression, are modeled by idealized uniaxial fiber model according to To *et al* [T3] to simulate the axial force-displacement characteristics of a combined action of concrete and steel reinforcement. On the other hand, for the bottom chord members, which are in tension, there are only the bottom longitudinal reinforcing bars in this position. The height of the modified truss model is standardized and defined to be the distance between the centroid of the top and that of the bottom reinforcing bars. Thus, the top chord members are located at the centroid of the top reinforcement and the bottom chord members remain at the centroid of the bottom reinforcement. The top and bottom chord members are further connected by compressive struts and transverse tensile ties between them.

The compressive struts and tensile ties in the transverse direction are the principle mechanisms for shear transfer and resistance. The choice of the strut configurations needs reasonable justification. Considering equilibrium in the shear span of a beam, the

moment resistance of the beam is expressed by:

$$M = Tjd \tag{3-1}$$

This equation ignores the contribution of the dowel force towards flexural resistance. Combining Equation (3-1) with the well-known relation between shear and the rate change of bending moment along a beam, the following modes of internal shear resistance result:

$$V = \frac{dM}{dx} = \frac{d}{dx}(Tjd) = jd\frac{dT}{dx} + T\frac{d(jd)}{dx} \tag{3-2}$$

The first term of Equation (3-2) expresses the behavior of a true flexural member in which the internal tensile force T acting on a constant lever arm jd changes from points to points along the beam. It is the equation for perfect "beam action". The second term of Equation (3-2) is the extreme case that the bond between steel and concrete is destroyed over the entire length of the shear span. Under such circumstances the external shear can be resisted only by inclined internal compression. This extreme case may be termed "arch action". In a normal reinforced concrete beam in which the full bond force required for beam action cannot be developed, these two mechanisms offer a combined resistance against shear forces.

Test parameters showed that all modeled beam has normal shear span to effective depth ratio (which is in the range of 2.41-3.01). Experiments also showed long and wide crack formed by joining the loading point and support. Thus arch action was pronounced in these beams and therefore could be an important mode of shear resistance. Hence, both the beam and the arch actions should be considered when modeling. The proposed modified truss model caters for this arch mechanism by introducing compressive struts directly connecting the loading points and the supports. In the mean while, beam action is represented by diagonal struts with a variable angle of inclination. This variable angle of inclination is achieved by dividing the shear span into four equal parts and each part has a strut connected to the loading point in the lower portion or to the support in the upper portion. This simple and direct method to

construct the variable angle truss model is found to be sufficient as the results later show. Concrete contribution in the beam action is also included in these variable angle struts and to be discussed in detail in a later section.

3.3 Properties of the Modified Truss Model

As the main part of the modified truss model is statically indeterminate, it is the best to be solved with the aid of computer program. Therefore, members in the modified truss model must have their respective material and geometrical properties defined before it can be analyzed for overall response of reinforced concrete beams. In the first place the concrete and steel in the model should have their constitutive relations to follow during the computational analysis. In the proposed model, the stress-strain relationship for concrete follows the proposal by Kent and Park [K1] as shown in **Figure 3.2**. The equations governing the behavior are:

For region AC :

$$f_c = f_c^{'}\left[\frac{2\varepsilon_c}{0.002} - \left(\frac{\varepsilon_c}{0.002}\right)^2\right] \tag{3-3}$$

For region CD :

$$f_c = f_c^{'}\left[1 - Z\left(\varepsilon_c - 0.002\right)\right] \tag{3-4}$$

$$Z = \frac{0.5}{\varepsilon_{50u} + \varepsilon_{50h} - 0.002} \tag{3-5}$$

$$\varepsilon_{50u} = \frac{3 + 0.002 f_c^{'}}{f_c^{'} - 1000} \tag{3-6}$$

$$\varepsilon_{50h} = \frac{3}{4}\rho_{sv}\sqrt{\frac{b^{"}}{s}} \tag{3-7}$$

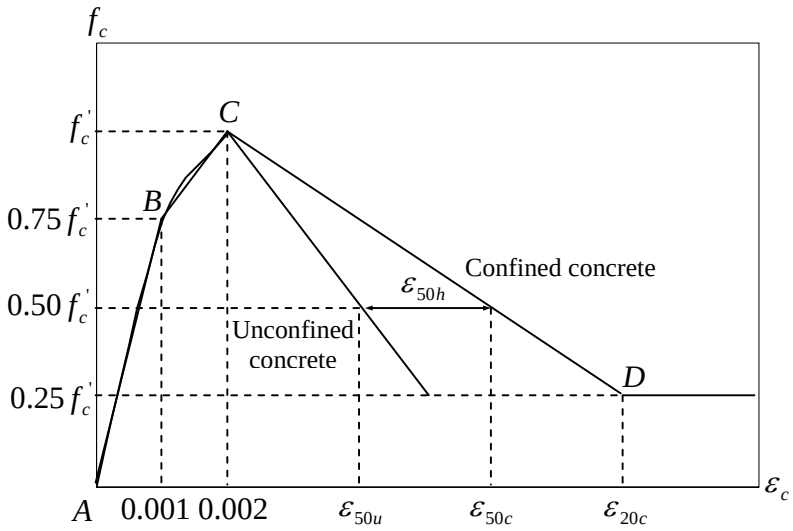

Figure 3.2: Stress-strain relationship for concrete [P2]

In this analysis here, the ascending parabola is simplified by bilinear sections *ABC* while the descending branch remains the same. The stress-strain relationship for reinforcing steel in **Figure 3.3** is bilinear and has a general strength-hardening ratio of 0.005. The yielding stress and strain are specified from the experimental works accordingly.

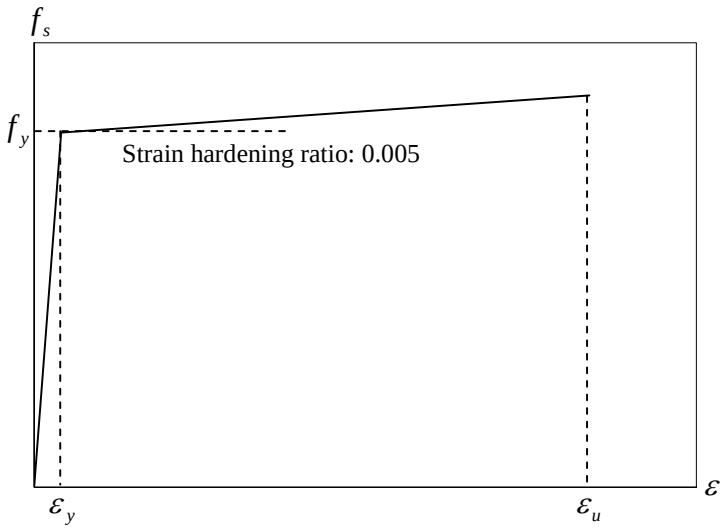

Figure 3.3: Stress-strain relationship for steel

Various researches have found that the truss model analogy overestimates the shear strength and stiffness when the failure stress of the concrete struts is assumed to be the

uniaxial compressive strength of standard concrete cylinders, f_c'. Thus the stress that each type of concrete member can achieve should be carefully considered. In normal flexural moment theory, in which the uniaxial compression of concrete is assumed to prevail, concrete strength is taken as 0.85 time the characteristic cylinder strength f_c'. The factor 0.85 considers for the effect of the difference between the strength of the concrete in cylinders and in the actual structures. Moreover, the compressive strength of concrete is affected by the presence of transverse stresses. A concrete member in a reinforced concrete structure under shear is actually subjected to biaxial stress with tensile stress in the direction perpendicular to the principle compressive stress. Therefore, the strength in the principal compressive direction is reduced by the principal tension in the perpendicular direction. This softened compressive stress is referred as the "effective compressive stress of concrete" and it is a function of certain factors. Considerable research has been conducted in an effort to determine the limiting concrete compressive stress.

The research in this chapter follows the suggestion by Schlaich *et al* [S1, S2] for the effective stress of concrete. Therefore, $0.8 f_c'$ is taken for the chord concrete member as parallel cracking with normal crack width. A compressive strength of $0.4 f_c'$ is chosen for the diagonal compressive struts to cater for skew cracks with extraordinary crack width. These reductions together with 0.85 make up the stress levels that are applied to the compressive strength for regulating the concrete members in the modified truss model.

Top chord members, consisting of top steel bars and concrete compressive stress block, are modeled by the uniaxial fiber element. In the model, the area of steel can be recognized as the top reinforcement. The concrete area is defined as the area of concrete compressive stress block obtained from the flexural theory. This portion of concrete, however is centered at the centroid of the concrete compressive stress block, is away from the centroid of the top steel bars. Since the height of the modified truss

model is defined as the distance between the centroid of the top and bottom reinforcing bars, the area of concrete should be transformed into an equivalent area centered at the centroid of top reinforcement by maintaining internal moment equilibrium. To accomplish this transformation computationally, it is assumed that the extreme fiber in the compressive concrete passes the strain at the maximum stress when the ultimate strength is reached and concrete compressive stress block can be simplified as an equivalent rectangular distribution. This assumption is nearly true as the strain at the maximum stress for concrete is quite small and can be achieved shortly after loading. Then **Figure 3.4** illustrates this transformation and the equivalent concrete area in the uniaxial fiber element is derived as:

$$A_{cm} = \frac{\dfrac{A_s f_s}{0.85 f_c^{'}}\left(d - \dfrac{A_s f_s}{1.7 f_c^{'} b_w}\right)}{h} \tag{3-8}$$

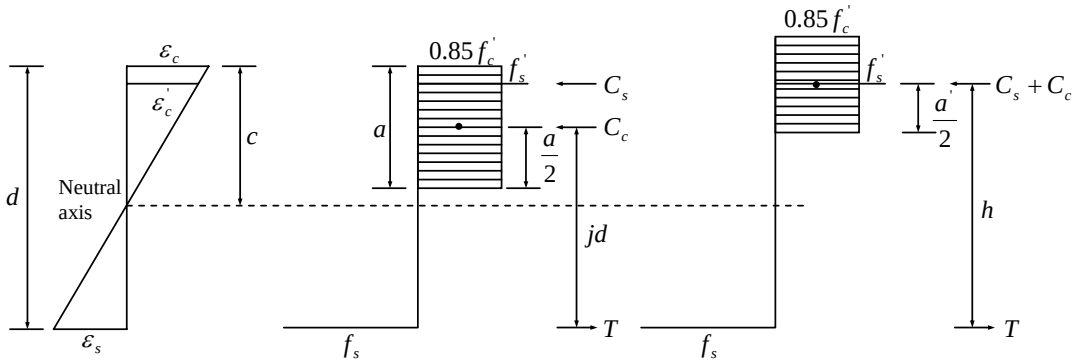

Figure 3.4: Transformation of compressive stress block

Ideally, Equation (3-8) gives the concrete area of each top chord member as long as the stress f_s of the corresponding bottom longitudinal reinforcement below it is known. However, this is not very much operational as f_s, which is obtainable from experimental strain gauge reading and steel stiffness, may not be available at every desired section. To overcome this disadvantage in the transformation, another equation is proposed from the view of moment capacity that a top chord member can sustain. The top chord member must be able to withstand the ultimate moment at a reasonable

stress state. Then from this consideration, the area of the concrete in the top chord can be written as;

$$A_{cm} = \frac{M}{f_c' h} \tag{3-9}$$

In deriving Equation (3-8) and Equation (3-9), the influence of the top reinforcement is not included in the transformation as the area of top reinforcement is small and also it is only subjected to low strain in most beam problems. Furthermore, under the simplification made, both Equation (3-8) and Equation (3-9) give the maximum available concrete area for top chord members. For the bottom chord elements, the properties are readily defined as the bottom reinforcement in the position.

Next, the diagonal compressive struts are discrete representation of the stress field inside the beams. One strut covers the stress flow in its nearby region. As the stress flow is continuous in the beams, the areas of the compressive struts are determined from the geometrical consideration of the beams. An effective section l_b is defined on this basis for each strut. The sketch in **Figure 3.5** illustrates this concept. It can be seen that the area defined is actually the maximum allowable for each strut and is given as:

$$A_{sm} = l_b \times b_w \tag{3-10}$$

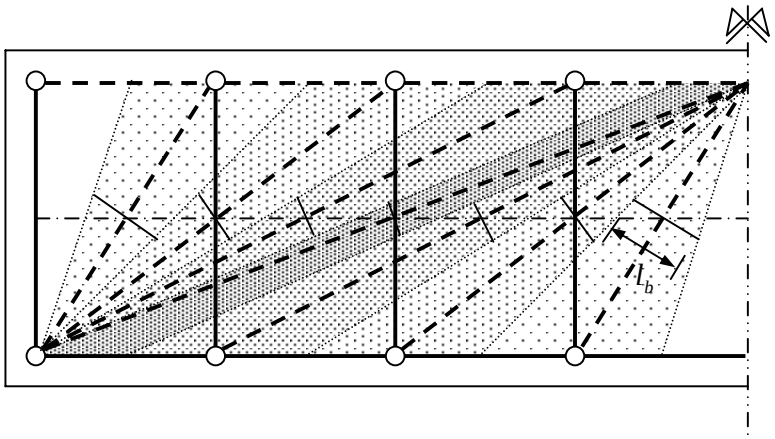

Figure 3.5: Geometry of the variable inclination struts

The geometrical property of the arch member is calculated in the same way as described above together with the struts for beam action. The analytical results show that the arch action contribution for shear is highly related to this area determined here. From above, it should be noticed that maximum available area adopted for both concrete in top chord members and struts. Therefore, the behavior of these concrete members is reflected through the stress variations of them. These stresses are average stresses within the members and will be shown later.

3.4 Discussion on Concrete Contribution in Shear Strength in the Modified Truss Model

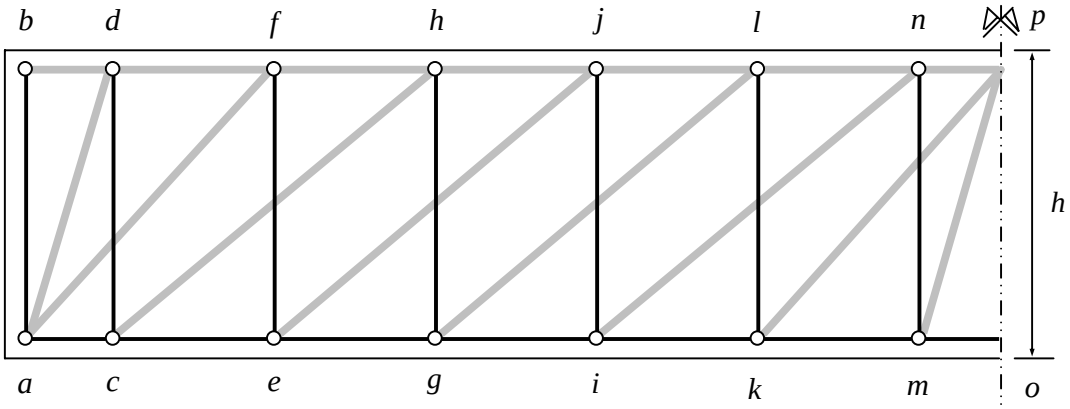

Figure 3.6: A standard truss model

In a standard truss model shown in **Figure 3.6**, one typical tensile tie member ij in the transverse direction is formed by lumping all the stirrups cut across by the compressive strut that connects to it. The ideal distribution of stirrups would correspond to all stirrups reaching yield by the time the failure load is reached if all struts inclined at a same angle. Therefore, it is appropriate to assume that all the stirrups have yielded and each develops a force of $A_{st} f_y$. Based on these assumptions,

the truss shown becomes statically determinate. From the equilibrium condition, the truss model capacity in shear V_s is obtained, where;

$$V_s = A_{st} f_y \frac{h}{s} \cot\theta \tag{3-11}$$

From this point, it can be seen that the shear resistance mechanism in the standard truss model mainly comes from the transverse ties or the stirrups. Hence, the truss model ignores the shear components from the concrete contribution such as shear in the compression zone, aggregate interlock across crack, and the dowel action [M7]. The modified truss model proposed here works the same way as the standard truss model in principle when concrete contribution in shear is null. This again is verified from an analysis of the proposed modified truss model for Beam S2-3 and S2-4 from Kong and Rangan [K4] with no concrete contribution. Result in **Figure 3.7** indicates that at the point of tensile tie yielding, the shear strength developed is only 58% of the experimental ultimate strength. Also, the overall shear stiffness of the model is smaller than the test beam. A larger displacement is obtained for the modified truss model at the same level of shear force as compared with the experiment. Further more, due to the lower shear strength, the ultimate displacement in the experiment cannot be achieved satisfactorily for the model without concrete contribution in shear.

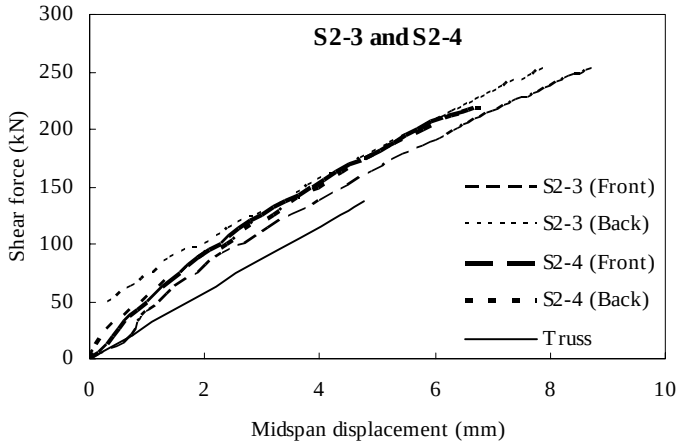

Figure 3.7: Analytical result of a truss model without concrete contribution in shear

Thus, it is concluded that a truss model without considering the concrete contribution in shear results in excessive conservation in both shear strength, stiffness, and deformation. The additional strength and stiffness required to capture the realistic behavior of the reinforced concrete beam with a truss model could only come from the shear resistance mechanism of the concrete contribution correctly incorporated. The importance of the inclusion of some of the components of the concrete shear failure mechanism to shear strength design has already been noticed under the current ACI design philosophy. ACI 318-02 [A1] specifies a term of concrete contribution as:

$$V_c = \left(0.16\sqrt{f_c'} + 17.2\rho_w \frac{Vd}{M}\right) b_w d \le 0.3\sqrt{f_c'}\, bd \qquad (3\text{-}12)$$

This additional term is a supplementary to the truss model that ACI adopts.

A conceptual distribution between concrete contribution V_c and truss contribution V_s can be visualized in **Figure 3.8** [P6]. The concrete contribution here remains constant throughout the monotonic loading process. This is justified for high strength concrete as the crack surface for high strength concrete is distinctly smoother [E2, P6], indicating that the subsequent effect of wearing off of the aggregate interlocking mechanism due to future loading is minimum. The dowel action always present unless the longitudinal reinforcement is broken apart. Therefore, the concrete contribution in shear can be reasonably recognized as a non-diminishing term in this analysis as Kong and Rangan [K4] used high strength concrete in their experiment.

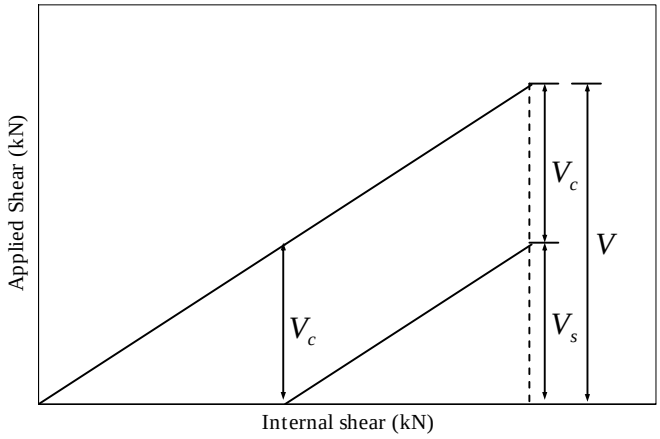

Figure 3.8: Distribution of shear strength in reinforced concrete beams with web reinforcement [P6]

A truss model that works as a shear analytical tool relies on compressive struts to transfer the shear stress to the tensile ties and the tensile ties actually act against this stress. So it has inherent difficulty in incorporating the concrete shear mechanism such as aggregate interlocking which is a shear resistance between struts and dowel action along the longitudinal reinforcement. Any other additional created member for concrete contribution into the truss model is not feasible. In this chapter, an equivalent shear reinforcement ratio concept is proposed to deal with this problem in the modified truss model. A conversion can be done to the concrete contribution term V_c with equivalent transverse shear reinforcement and its known yielding strength f_y.

$$A_{sc} = \frac{V_c}{f_y} \tag{3-12}$$

The concrete contribution V_c in this chapter follows the existing one in ACI 318-02 [A1] (Equation (3-12)). The yielding strength should be corresponding to that of the stirrups in the experiment. This equivalent steel area is then uniformly distributed among the ties that have been crossed by the struts for beam action. Finally, a tensile tie should take into account both the distributed equivalent steel area and lump summed area from the shear reinforcement.

3.5 Behavior of the Modified Truss Model for Beams in Shear

The experimental data used for basic verification of the modified truss model are the data thesised by Kong and Rangan [K4]. The overall behavior, especially strength and stiffness, of the fourteen reinforced concrete beams can be modeled with the plastic truss approach. These fourteen beams were of various properties and all failed in shear. Beams S2-1, S2-2, S2-3, S2-4, and S4-5 varied in their shear reinforcement degree, while Beams S3-1, S3-2, S3-3, S3-4, S3-5, and S3-6 were different in their longitudinal reinforcement content. Lastly, Beams S5-1, S5-2, and S5-3 were of different shear span to effective depth ratio. The variation of these parameters significantly influenced experimental beam shear response in respective ways. These parameters also take effects in the modified truss model and will be illustrated in this section later.

With the complete methodology introduced in previous sections, a modified truss model can be established for each beam according to its dimension. These modified truss models with established member properties are analyzed with the program DRAIN-2DX [P7, P8]. Analytical results in terms of shear force versus mid-span displacement response (shown until the shear strength is reached) are plotted and compared with experiment data. The full results are illustrated in **Figures 3.9** to **3.11**. The modified truss models demonstrate good reliability in these analyses.

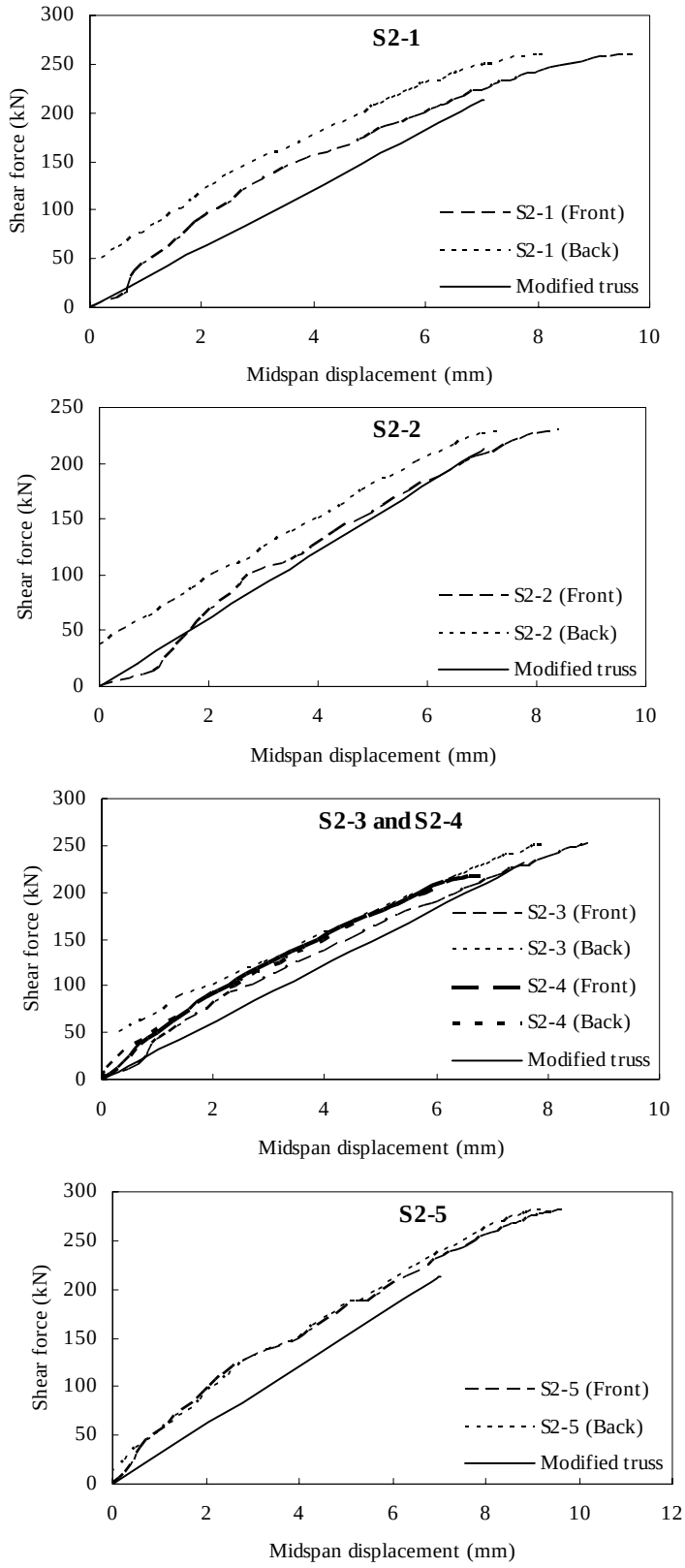

Figure 3.9: Comparison of predicted and measured load-displacement responses of the Series 2 beams

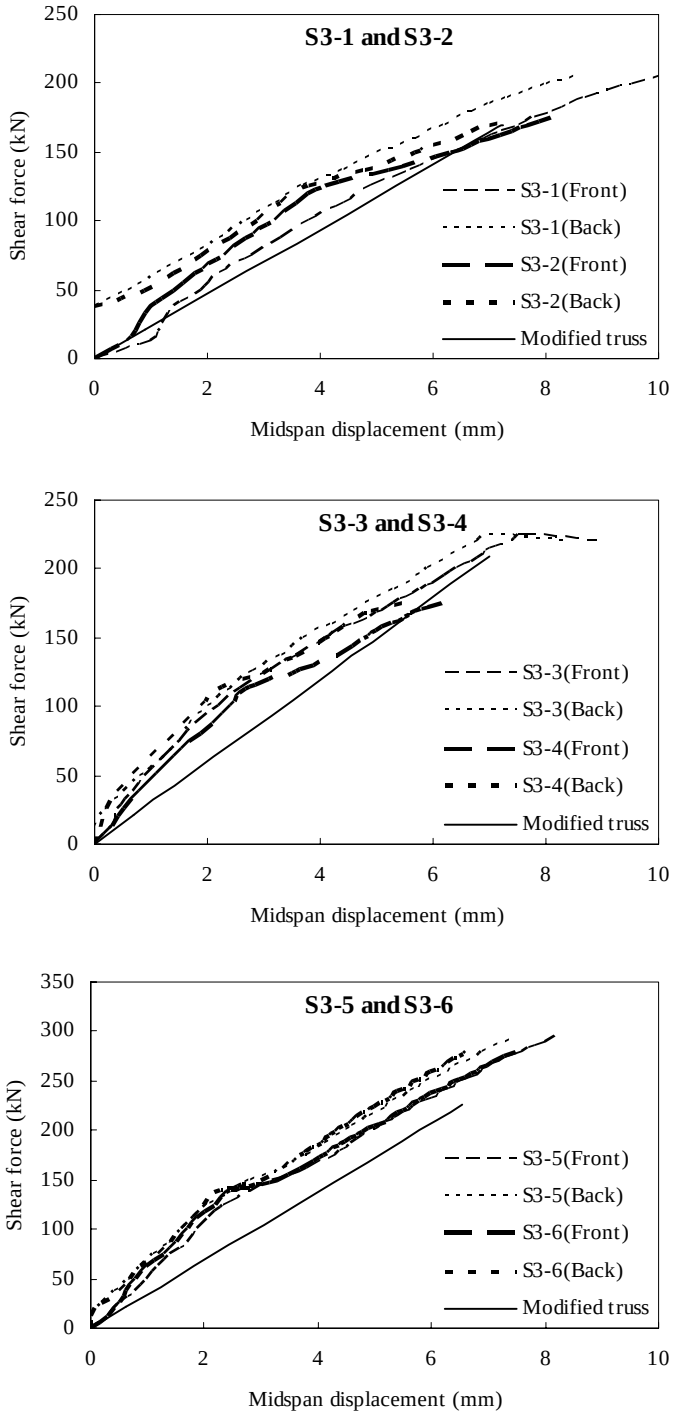

Figure 3.10: Comparison of predicted and measured load-displacement responses of the Series 3 beams

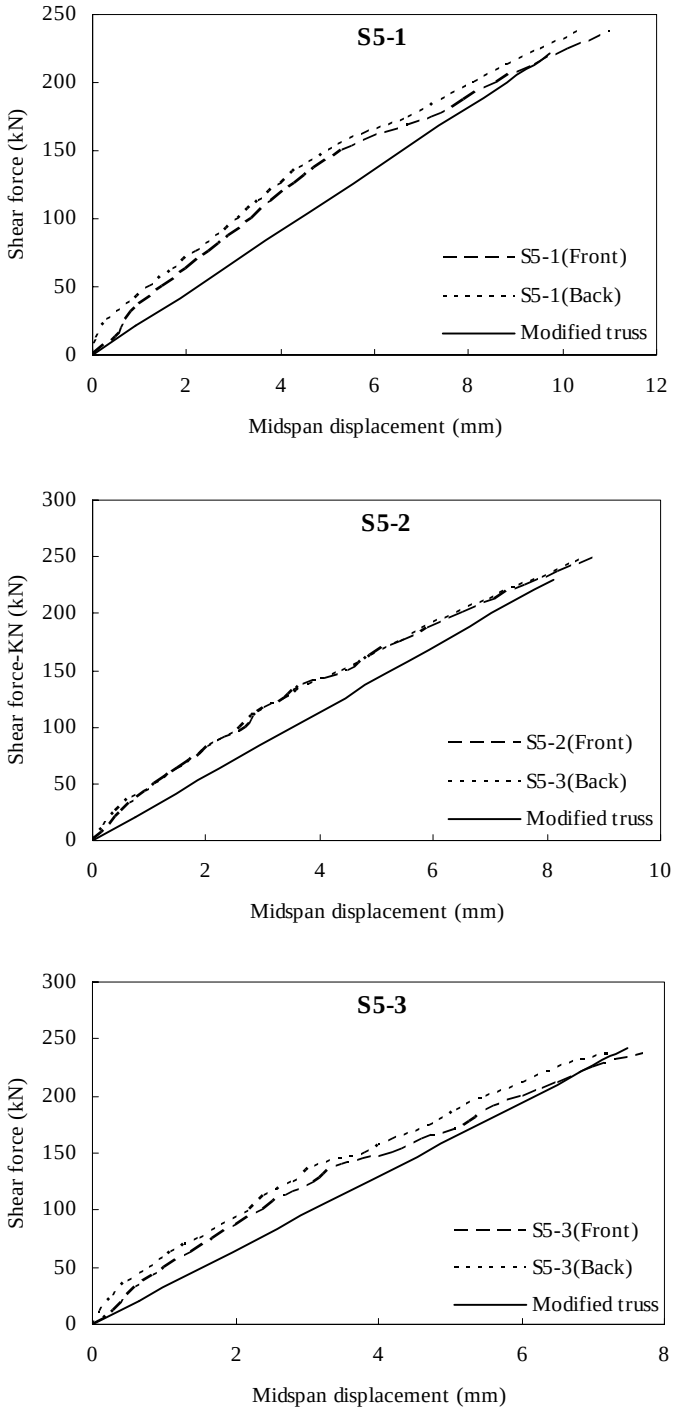

Figure 3.11: Comparison of predicted and measured load-displacement responses of the Series 5 beams

Reasonable matching of test and analysis curves is observed. The deficiency of the modified truss model is that the predicted shear force versus mid-span displacement response is nearly linear and the stiffness can only be seen as the average overall stiffness from the experiment. The stiffness in the initial loading stage is also small as compared to experiment. This deficiency could be owing to two reasons. Firstly, the concrete contribution is assumed to be constant throughout the loading and this would produce the linear shear force versus mid-span displacement response. Secondly, the truss model analogy is strictly not applicable to the uncracked reinforced concrete beams. If the truss model analogy is used for that range of loading, smaller stiffness predicted is foreseeable.

Shear strength of each modeled beam is the key factor that has been examined in the modified truss model for each beam. Traditionally, the shear strength of the truss model is attained when any tensile ties in the model yields. In the modified truss model here, yielding of the tensile ties indicates that concrete contribution and lumped shear reinforcement in that position have fully participated in the shear resistance. Thus, the shear strength is reached too. The DRAIN-2DX [P7, P8] output shows that under the current configuration of the modified truss model, yielding is first observed at the second tensile tie from the middle of each beam modeled. This result corresponds well with Paulay's assumption for the stirrup force intensity variation along the span of the coupling beam under analogous truss[P3]. Summary of the shear strength is given in **Table 3.1**. Mean value of 0.914 for the experimental ultimate strength shows that the modified truss models predict the shear strength well without any over conservation compared to ACI [A1] predictions. For the coefficient of variance of the two predictions to the experimental ultimate strength, the modified truss model is also better with less variant results.

Table 3.1: Shear strength of modified truss models

Beam Mark	$V_{experiment}$ (kN)	V_{truss} (kN)	V_p (ACI) (kN)	$\frac{V}{V_u}$	$\frac{V_p}{V_u}$
S2-1	260.3	199.4	166.4	0.766	0.639
S2-2	232.5	212.9	175.1	0.916	0.753
S2-3	253.3	231.0	188.2	0.911	0.743
S2-4	219.4	231.0	188.2	1.053	0.858
S2-5	282.1	257.6	209.9	0.913	0.744
S3-1	209.2	170.1	158.9	0.813	0.760
S3-2	178.0	170.1	158.9	0.956	0.893
S3-3	228.6	210.0	166.4	0.917	0.728
S3-4	174.9	210.0	166.4	1.201	0.951
S3-5	296.6	225.6	179.3	0.761	0.606
S3-6	282.9	225.6	179.3	0.797	0.634
S5-1	241.7	221.8	193.2	0.918	0.799
S5-2	259.9	230.0	195.7	0.885	0.753
S5-3	243.8	242.4	199.1	0.994	0.817
			Average	0.914	0.763
			COV	0.147	0.265

With good overall behavior of the modified truss model, further effort is made in this through an examination of the internal stress distribution of the models. Member forces of the modified truss models when the shear strength is reached are taken from the DRAIN-2DX [P7, P8]. And then these forces are converted to stresses of respective members. This allows a better visualization of how the load is being carried by the members resulting in a better understanding the shear problem. For concrete members, the stresses are expressed in terms of f_c', while the stresses for steel members are expressed with f_y. **Figures 3.12** to **3.14** show results of the analysis. In these figures, crack patterns are shown in dotted line for comparison.

In general, each member in the modified truss models acts according to the properties specified and no over stress of any member is found. As the test beams were all failed in shear, the modified truss models for the beams also demonstrated distinct shear

governing behavior with shear reinforcement reaches yielding first. Flexural longitudinal reinforcement for all models is below yielding point at every position along the shear span. Stress for the top chord concrete member is of a bit fluctuating manner however. This is because that the member area determined from Equation (3-9) depends on the ultimate moment from the experiment. However, the experimental data were not consistent in some cases. For tensile ties, as discussed above, the yielding first starts at the second tie from the center. The other two ties are of moderate stress level from 60% to 70% of f_y, respectively. Reduction factors for concrete compressive strength work well for concrete member as these members are regulated into desirable stress states. For concrete in the top chord members, the reduction is approximately $0.72 f_c^{'}$ and the maximum average stress reached of all modified truss models is around $0.40 f_c^{'}$. For struts, the applied reduction factor is 0.34 to $f_c^{'}$. While for analysis results of the modified truss models, the maximum average stress for these members is around $0.25 f_c^{'}$. This value is lower than that specified and thus the web crushing failure is prevented. This correlates well with the current design practice which requires that failure due to concrete crushing prior to yielding of the reinforcement is avoided with the use of the truss model approach within the general ductile framework.

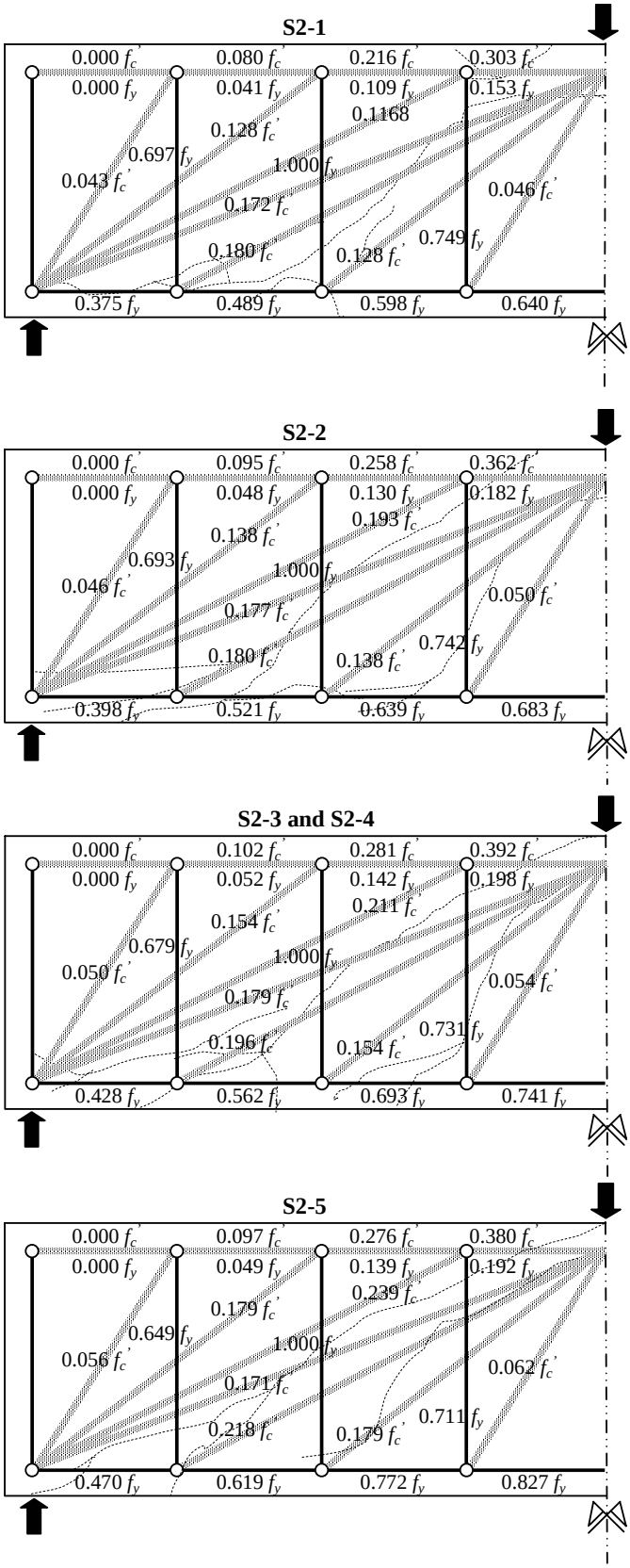

Figure 3.12: North shear span of the Series 2 beams with modified truss models

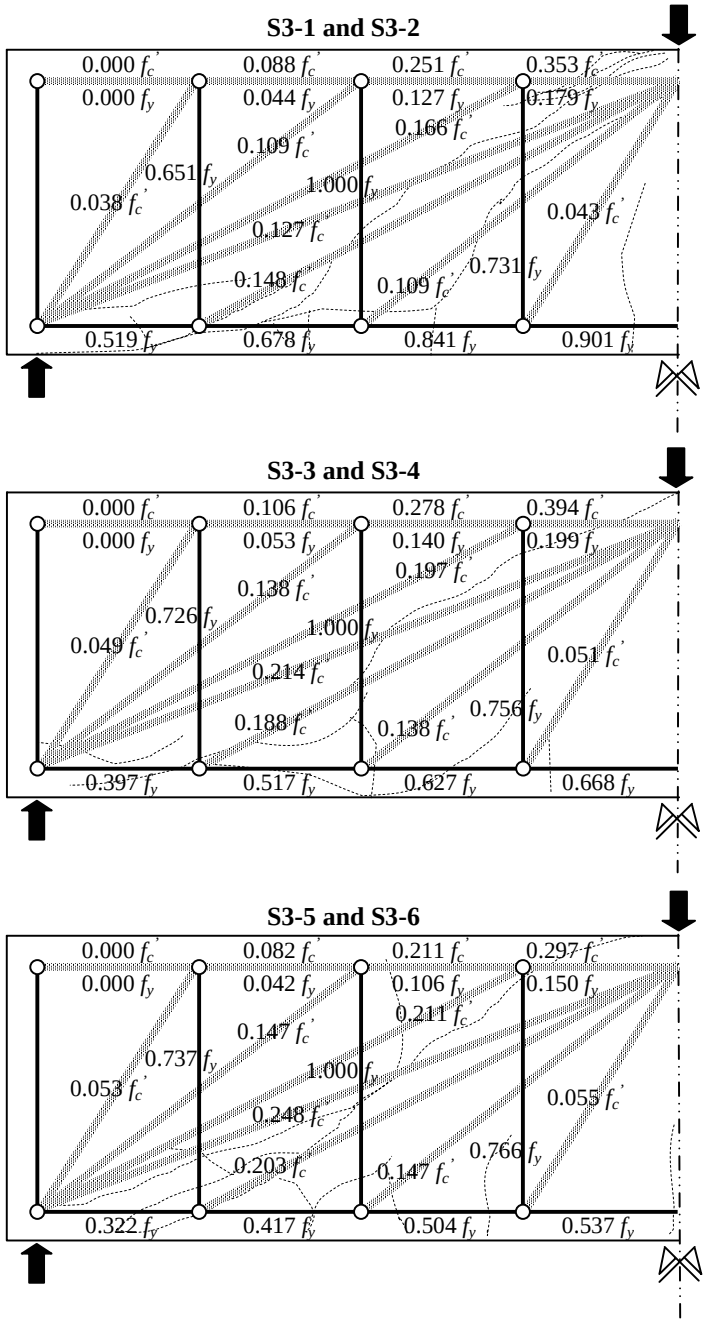

Figure 3.13: North shear span of the Series 3 beams with modified truss models

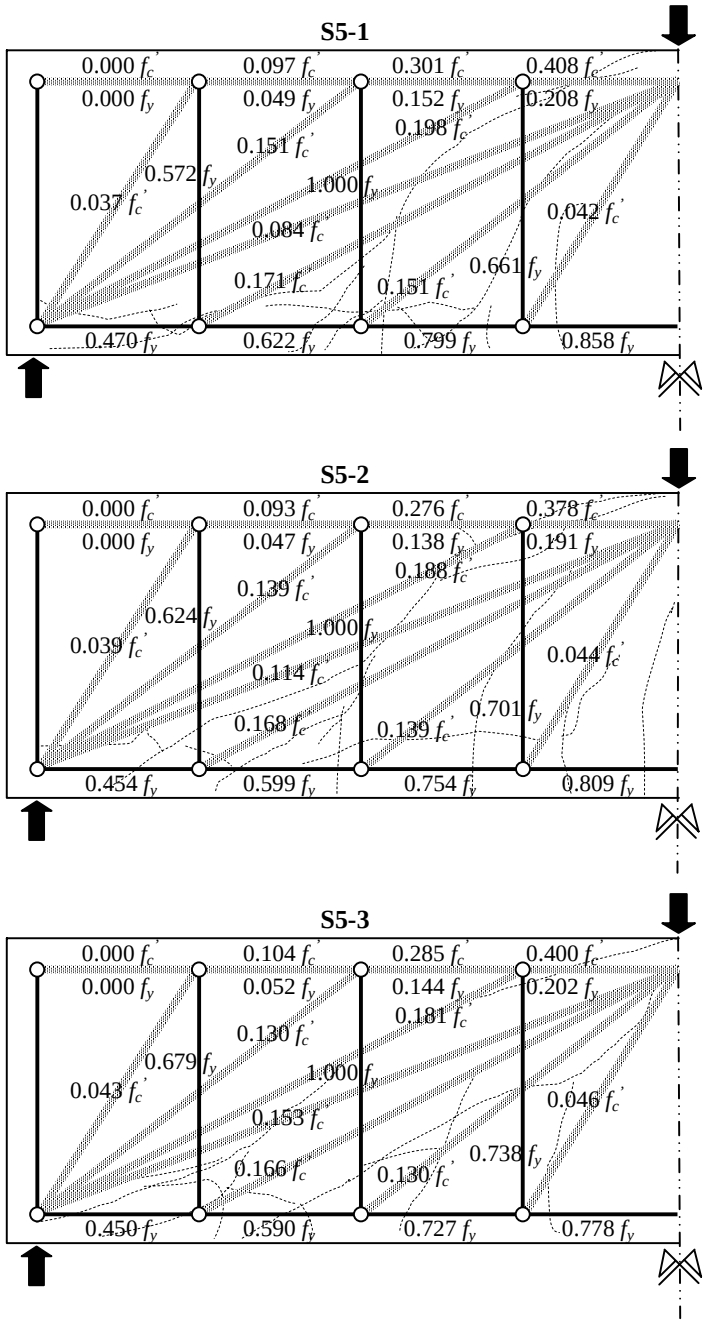

Figure 3.14: North shear span of the Series 5 beams with modified truss models

The effects of the test parameters such as the shear reinforcement degree, longitudinal reinforcement content, and shear span to effective depth ratio can be reflected from the stress analysis of the modified truss models. For Beams S2-1, S2-2, S2-3, S2-4, and S2-5, shear reinforcement degree varied decreasingly in spacing of the stirrups. With the increase of the shear reinforcement degree, the shear strength of the beams increased as expected in the modified truss models. **Figure 3.15** shows this trend and compared it with experimental strength. Stress of the longitudinal reinforcement also increases as more shear reinforcement enhances shear capacity and shift the behavior of the beams towards a flexural domain. More shear reinforcement provides a confinement effect on the concrete core and enhances the performance of the struts.

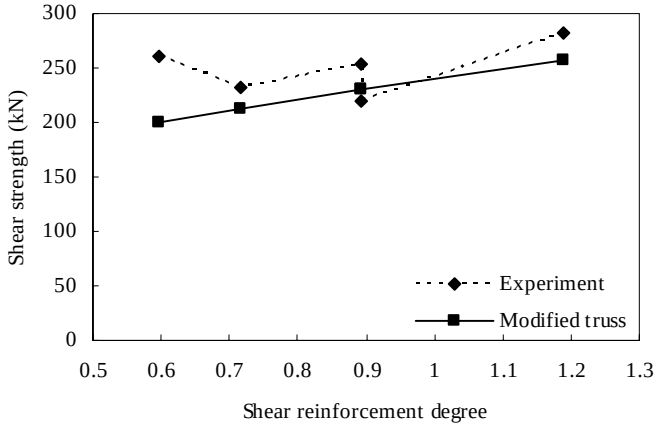

Figure 3.15: Shear strength versus shear reinforcement ratio for the Series 2 beams

Thus, struts develop higher stresses with the increase of shear reinforcement degree. It is interesting to note that the shear strength contribution from the arch members remain relatively constant with the increase of the shear reinforcement degree.

The longitudinal reinforcement ratio was the test parameter for the Beams S3-1, S3-2, S3-3, S3-4, S3-5, and S3-6. The shear strength of this beam series increases as with more longitudinal reinforcement is used in the tests. **Figure 3.16** gives the illustration of the analysis. The shear strength from experiments grew faster with the increase of the longitudinal reinforcement content, which is much slower in the modified truss

models. However, the stresses for the bottom chord members demonstrate a decreasing trend as the ratio goes higher. On the other hand, stresses in the struts also build up. Especially for the arch members, the stresses go up at a faster rate and eventually become the critical member among all the compressive struts.

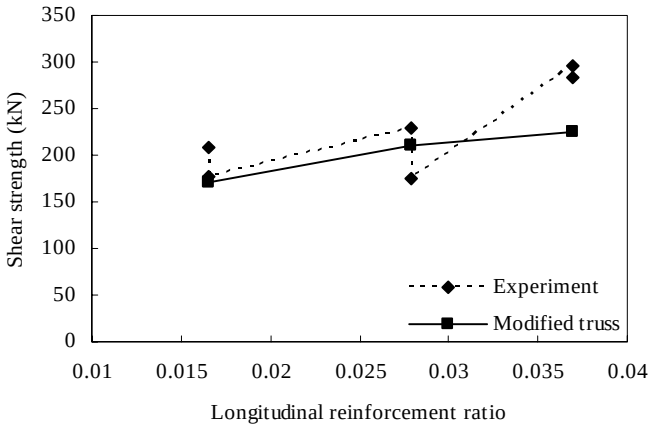

Figure 3.16: Shear strength versus longitudinal reinforcement ratio for the Series 3 beams

Beams S5-1, S5-2, and S5-3 had a constant effective depth while their respective shear-span decreased which gave a decrease in the shear span to effective depth ratio, $\frac{a}{d}$. The behavior of shear domain is more pronounced with the decrease of shear span to an effective depth ratio. This is proven from the decreasing trend of the flexural longitudinal reinforcement stresses. Also, the shear strength goes up for this series of beams, but the rate is rather gentle as shown in **Figure 3.17**. It is also found that the stresses of the struts catering for the beam action reduce with a lower shear span to an effective depth ratio. However, the arch members build up significantly as the ratio goes down.

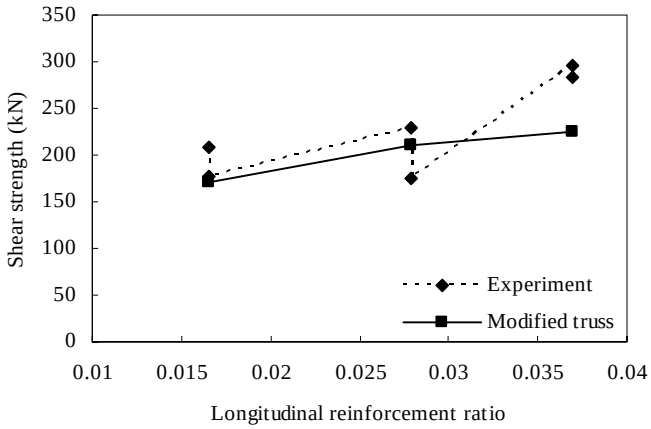

Figure 3.17: Shear strength versus shear span to effective depth ratio for the Series 5 beams

3.6 Summary

The concept of the variable angle truss model has been proposed for a long time. Yet few satisfactory analyses have been accomplished with it for reinforced concrete elements. This chapter herein modifies the variable angle truss model into a modified truss model with concrete contribution in shear incorporated and evaluates the complete response of reinforced concrete beams loaded in shear with the aid of this modified truss model. In the study, it is found that even the variable angle truss model, which only utilizes shear reinforcement as the shear resistance mechanism, is not sufficient in the analysis of beam shear problem, particularly for strength. On this basis, the proposed modified truss model offers a procedure of equivalent shear reinforcement to deal with the concrete contribution in shear. With these considerations, the analytical results with the proposed modified truss model show reasonable agreement with experimental data

Traditionally, the truss model analogy is restricted to strength design in shear. This chapter manages to show that with a proper construction of the truss model and determination of the member properties, the truss model analogy can be extended to more complicated analytical problems, such as stiffness and deformation. Truss model analogy, or particularly the modified truss model here, demonstrates clearly the stress

flow in beam which can result in a better understanding of the reinforced concrete elements subjected to external loading.

Also, according to the findings of this chapter, using truss model analogy to analyze complete response of reinforced concrete beams can be improved in two ways. Firstly, the treatment of the concrete contribution as a non-diminishing term in the analysis is an insufficient simplification as this will lead to near linear behavior in terms of shear versus displacement response. Concrete contribution can be possibly taken as a variable during the whole loading process. Secondly, the inclination of the struts is very much predefined when configuring the modified truss model. A more rigorous procedure can be developed to determine the exact solution. These two aspects will be handled in the next chapter. And due to its indeterminate nature, it can only have limited usage in design. An approach with variable angle truss model yet enables hand calculation for strength and stiffness is much more needed.

To conclude, the truss model analogy actually can solve strength, stiffness, and deformation of reinforced concrete elements as proven from the modified truss model for reinforced concrete beams here.

CHAPTER 4

A THEORETICAL APPROACH TO DETERMINE STRUT ANGLES OF A VARIABLE ANGLE TRUSS MODEL FOR REINFORCED CONCRETE BEAMS

4.1 Introduction

Truss model analogy has been widely used as the basis of most of current shear design procedures for reinforced concrete beams where at the failure stage the inclined concrete struts formed as shown in **Figure 4.1** represent the concrete blocks between adjacent cracks. These struts transfer external loads to ties connected to them, which are the shear reinforcement in the transverse direction and are represented as lumped areas of reinforcement crossed by the struts and which act as the component for shear resistance under this truss model analogy. Top and bottom chords consisting of concrete compressive stress blocks and longitudinal reinforcement respectively are the members that generally do not contribute in the shear resistance for strength.

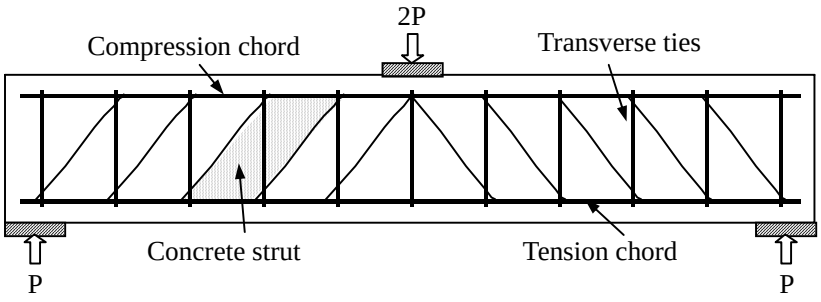

Figure 4.1: Truss model analogy for reinforced concrete beams under shear [V2]

According to the truss model analogy, it is well understood that the shear reinforcement ratio and strut angle are two key quantities related to the shear strength of the reinforced concrete beams. Generally, the shear strength from shear reinforcement is:

$$V_s = A_{st} f_y \frac{d}{s} \cot\theta \qquad (4\text{-}1)$$

However, this equation may be found insufficient when estimating shear strength from experimental evidences as it ignores the shear carried by the concrete. Thus, the ACI 318 [A1] code introduced an empirical term called "concrete contribution" to supplement the above Equation (4-1) which was derived from regression analysis of tested beam data.

The current shear design philosophy has two critical problems, namely, the strut angle and the concrete contribution. For simplicity in dealing with strut angles, Ritter [R4] and Morsch [M8] assumed the concrete struts to be inclined at $45°$ corresponding to the first shear cracking angle and so the ACI 318 [A1]code adopted this assumption. However, such an assumption as the $45°$ inclination angle may lead to a low contribution from the shear reinforcement especially in the case of the shear strength for lightly reinforced concrete beams. Consequently, other researchers for example by Ramirez & Breen [R1] and Priestley *et al* [P9] have instead suggested taking $30°$ as the struts inclination. The common observation found however in these proposals was the assumption of one constant strut angle over the entire shear span of beams. This assumption may be erroneous as past experiments always showed cracks orientated towards different direction at different regions along the shear span of a beam, indicating the varying directions of diagonal compression. Hence, a variable angle of inclination appears to be more desirable in fact. On this basis, variable angle truss models have been conceptually developed in some research [R3]; however the exact variable strut angles have not been given in these conceptual models as mathematical solutions nor by mechanical approaches. Also, there has been little said about how these variable angle truss model are related to strength design.

On the other hand, the $45°$ strut angle is first assumed and then the contribution from shear reinforcement is determined as shown in the ACI 318 [A1] code. With the concrete contribution representing the difference between the shear reinforcement contribution and the ultimate shear strength, most of the concrete contribution terms in various codes are merely achieved through regression analysis of the beam test data. In short, the concrete contribution such as that in the ACI 318 [A1] code is indeed a term

regardless of the level of shear stress and only applicable in the case of a $45°$ strut angle. Hence, a proper mechanical model combining a few influential factors is needed to better understand the shear carried by concrete as far as shear strength design is concerned.

To solve the two problems in shear design as mentioned earlier, this chapter therefore focuses on a theoretical method to determine strut angles. According to this method, a variable angle truss model along the shear span of a beam can be generated. Then, to verify the developed method, the load-displacement response based on the variable angle truss model needs to be predicted. However before that, the concrete contribution in shear is incorporated into the variable angle truss model by strain compatibility analysis to achieve a satisfactory ultimate strength.

4.2 Evaluating Strut Angle of a Variable Angle Truss Model

Figure 4.2 shows the shear transfer mechanism for a typical region along a beam member. This transfer mechanism can be reasonably represented by the truss model analogy as shown in **Figure 4.3**. Under this analogical assumption, a few truss units can be formed along the shear span of a cracked “long” beam member. By deconstructing the beam shear span in this manner, it is found that the rigidity and stiffness are more easily accessed for each truss units. The rigidity and stiffness of the truss unit is the summations of all the members in the unit from which the deformation of each truss unit can be computed. Further, external work done to each truss unit can be determined. This allows the strut angle to be examined by minimizing the external work done. It is noteworthy that the principle of virtual work is the basic analytical tool in this part of the chapter.

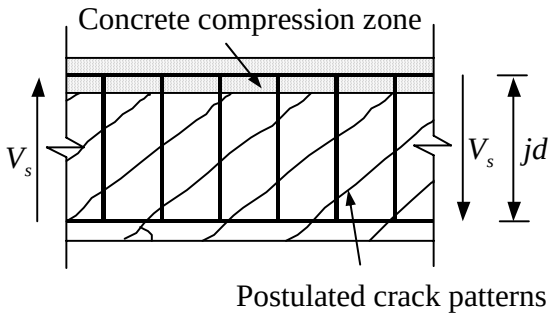

Figure 4.2: Shear transfer mechanism for a typical region along a beam

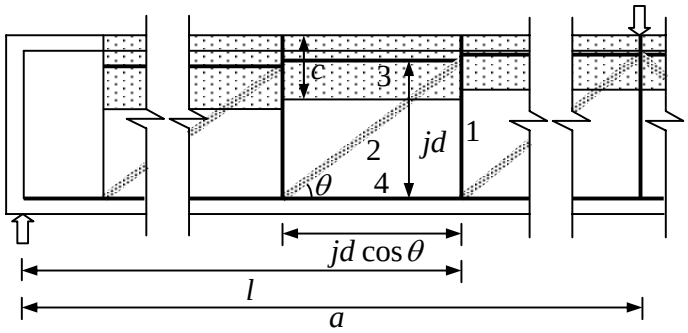

Figure 4.3: Analysis by the principle of virtual work of the typical truss unit

When applying the principle of virtual work to each truss unit, the axial rigidity of each member forming the truss unit is the most important part and must be studied with care. Consider again the typical truss unit subjected to a shear force V_s as shown in **Figure 4.3**. Firstly, it is assumed that the transverse shear reinforcement is uniformly distributed over the length of the member. Under this smeared shear reinforcement assumption, the axial rigidity of the tie is:

$$(EA)_t = \cot\theta \rho_{st} n E_c A_v \tag{4-2}$$

For the inclined strut, the area is determined from geometrical consideration. Conventionally, it is taken as:

$$A_{sm} = b_w jd\cos\theta \tag{4-3}$$

Then the axial rigidity of the strut is:

$$(EA)_s = b_w jd\cos\theta E_c = \cos\theta E_c A_v \tag{4-4}$$

For the flexural members, it is assumed that the bottom tensile member is placed at the centroid of the bottom longitudinal reinforcement, while the top compressive member is at the centroid of the concrete compressive stress block. Hence, the height of the truss is the internal level arm jd . A distinction in axial rigidity should also be made between the bottom tensile member and the top compressive member. For the tensile member, the concrete around its position would normally crack and does not contribute significantly to the axial rigidity compared to the reinforcement there. On the other hand, in addition to the concrete compressive stress block, there is a rigidity contribution from the top longitudinal reinforcement for the top compressive member. Generally, the centroid of the top longitudinal reinforcement differs from that of the concrete compressive stress block. In this chapter, the top longitudinal reinforcement is simplified to be at the same position of the centroid of the concrete compressive stress block. This simplification might cause a slightly greater deformation of the top longitudinal reinforcement when the centroid of the concrete compressive stress block is deeper than that of the position of the longitudinal reinforcement. Thus, the axial rigidity of the bottom tensile member is:

$$(EA)_T = E_s A_s = \rho_s n E_c A_g \tag{4-5}$$

For the top compressive member, the axial rigidity should be:

$$(EA)_C = \left(\frac{c}{d} + \rho_s^{'} (n-1) \right) E_c A_g \tag{4-6}$$

These two equations describe the dimensioning of the top and bottom chord members.

Member forces of the truss unit can easily be found by static equilibrium. Then the deformation of the truss unit due to applied shear force can be calculated using the principle of virtual work. A summary of the analysis is presented in **Table 4.1**.

Table 4.1: Analysis by the principle of virtual work

Member	Member force F	Unit load f	Length L	Axial Rigidity (EA)
1	V_s	1	jd	$\cot\theta\rho_{st}nE_cA_v$
2	$-\frac{V_s}{\sin\theta}$	$-\frac{1}{\sin\theta}$	$\frac{jd}{\sin\theta}$	$\cos\theta E_cA_v$
3	$\left(\frac{l}{jd}-\cot\theta\right)V_s$	$\frac{l}{jd}-\cot\theta$	$jd\cot\theta$	$\left(\frac{c}{d}+\rho'_s(n-1)\right)E_cA_g$
4	$\frac{l}{jd}V_s$	$\frac{l}{jd}$	$jd\cot\theta$	$\rho_s nE_cA_g$

The deformation of the truss unit is the sum of the member deformations, thus,

$$\Delta=\sum_1^4\frac{Ffl}{EA}=\frac{1+\rho_{st}n\cos ec^4\theta}{\rho_{st}n\cot\theta E_cA_v}jdV_s+\left(\frac{\left(\frac{l}{jd}-\cot\theta\right)^2\cot\theta}{\left(\frac{c}{d}+\rho'_s(n-1)\right)E_cA_g}jdV_s+\frac{\left(\frac{l}{jd}\right)^2\cot\theta}{\rho_s nE_cA_g}jdV_s\right) \tag{4-7}$$

The deformation of the truss unit is formatted in such a way that the first term in Equation (4-7) is the deformation contributed from shear members (strut and tie) and the second term is from the flexural members. The drift angle is determined by dividing the deformation by the length of the truss unit, thus,

$$\alpha=\frac{\Delta}{jd\cot\theta}=\frac{1+\rho_{st}n\cos ec^4\theta}{\rho_{st}n\cot^2\theta E_cA_v}V_s+\left(\frac{\left(\frac{l}{jd}-\cot\theta\right)^2}{\left(\frac{c}{d}+\rho'_s(n-1)\right)E_cA_g}V_s+\frac{\left(\frac{l}{jd}\right)^2}{\rho_s nE_cA_g}V_s\right) \tag{4-8}$$

Therefore, the stiffness of one typical truss unit about drift angle is:

$$K = \frac{V_s}{\alpha} = \frac{\rho_{st} n \cot^2 \theta E_c A_v}{1 + \rho_{st} n \cos ec^4 \theta} + \frac{1}{\frac{\left(\frac{l}{jd} - \cot\theta\right)^2}{\left(\frac{c}{d} + \rho_s^{'}(n-1)\right) E_c A_g} + \frac{\left(\frac{l}{jd}\right)^2}{\rho_s n E_c A_g}} \qquad (4\text{-}9)$$

Clearly, the first term of Equation (4-9) indicates the shear stiffness of the typical truss unit while the second term is the flexural stiffness. The first term of Equation (4-9) is the same as that of the shear stiffness presented by Dilger [D1] for 90° transverse shear reinforcement for a general truss model. Later, when they performed calculations on a differential truss model, the same expression was also derived. By deriving this shear stiffness term on a typical truss unit in the way shown in Equation (4-9), it should not only be taken as shear stiffness for a constant angle truss model but also as a general description of shear stiffness. Together with the flexural stiffness derived in the expression, the variable angle truss model can actually be developed.

As noted previously, the strut angle θ is very important since it affects the strength as well the as the stiffness (Equation (4-9)) of a reinforced concrete beam. In this chapter, an attempt to give the theoretical determination of the strut angle θ is made. From the above analysis, the external work done due to an applied unit shear force to the typical truss unit is the total deformation obtained. Thus,

$$EWD = \Delta \times 1 = \frac{1 + \rho_{st} n \cos ec^4 \theta}{\rho_{st} n \cot \theta E_c A_v} jd + \left(\frac{\left(\frac{l}{jd} - \cot\theta\right)^2 \cot\theta}{\left(\frac{c}{d} + \rho_s^{'}(n-1)\right) E_c A_g} jd + \frac{\left(\frac{l}{jd}\right)^2 \cot\theta}{\rho_s n E_c A_g} jd \right) \qquad (4\text{-}10)$$

In this study, it is assumed that the diagonal compression will develop in the orientation that requires a minimum amount of external energy. Hence, the angle θ that can minimize Equation (4-10) is the strut angle. Thus by differentiating the equation with

respect to θ and minimizing the external work done, the outcome leads to the strut angle causing the minimum energy:

$$\frac{d(EWD)}{d\theta} = 0 \tag{4-11}$$

Carrying out the differentiation of Equation (4-11) leads to the following solution for the crack angle θ:

$$\left(\frac{1}{\rho_{st} n E_c A_v} + \frac{1}{E_c A_v}\right)\tan^4\theta - \left(\frac{2}{E_c A_v} + \frac{\left(\frac{l}{jd}\right)^2}{\left(\frac{c}{d} + \rho_s'(n-1)\right)E_c A_g} + \frac{\left(\frac{l}{jd}\right)^2}{\rho_s n E_c A_g}\right)\tan^2\theta$$
$$+ \frac{4\left(\frac{l}{jd}\right)}{\left(\frac{c}{d} + \rho_s'(n-1)\right)E_c A_g}\tan\theta - \left(\frac{3}{\left(\frac{c}{d} + \rho_s'(n-1)\right)E_c A_g} + \frac{3}{E_c A_v}\right) = 0 \tag{4-12}$$

This is a quatic equation with only one variable θ. An analytical solution can be found for this equation; however, a trial and error procedure to get a solution for the strut angle θ is good enough.

The solutions for the strut angles vary along the shear span of the beam as the variable l, which represents the available span length and is different for each truss unit. For a particular shear level, the solution procedure starts from the loading point and moves towards the support in a shear span. According to Equation (4-12), strut angle θ for the first truss unit can be found by substituting the total shear span length a to the variable l. With this θ value, a check of $jd\cot\theta$ which represents the length of this unit truss can be done. If the result shows that $jd\cot\theta$ is smaller than a, the solution procedure should continue for the next truss unit by updating the variable l with a new value $(a - jd\cot\theta)$. Then the strut angle θ for the next truss unit can be obtained with Equation (4-12) again. The process will be terminated when the check shows that variable l used to calculate strut angle θ for a new truss unit is smaller

than the length ($jd\cot\theta$) of this newly formed truss unit (the available span length is not enough for a new truss unit). Therefore the solutions for the strut angles for truss units along the shear span of a beam differ in a decreasing manner when moving towards the support as the variable l gets smaller. Moreover, when the shear increases, a few variables such as c in Equation (4-12) are also affected, and hence the solutions of the strut angles are different. Thus, a continuous profile of struts orientation development can be found in this analysis. **Figure 4.4** shows the results of this analysis at the ultimate stage of a reinforced concrete beam. The beam and the crack pattern were extracted from Bresler & Scordelis [B2].

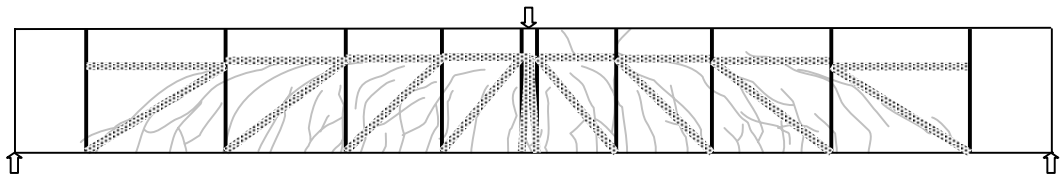

Figure 4.4: Calculated strut angles compared to crack pattern of the Beam A-2

To summarize, this theoretical method has two distinct characteristics for the evaluation of the strut angle θ. Firstly, the strut angles calculated from this method are different along the shear span from the load point to the support (different strut angle for different truss unit). This effectively develops a variable angle truss model for reinforced concrete beams. Secondly, the strut angles can vary with the increase of the shear force level. Thus the change of direction in the development of the diagonal compression can be seen and which intends to correspond with the crack patterns observed in most of the reinforced concrete beam tests.

4.3 Strain Compatibility Analysis in a Typical Truss Unit for Shear Carried by Concrete

In the previous section of this chapter, the evaluation of the strut angles theoretically develops a variable angle truss model for reinforced concrete beams subjected to shear. This variable angle truss model is applicable not only to the ultimate stage, but also to

the whole loading process. However, due to the differing strut angles for different truss units, the amount of reinforcement for each tie is different too. So at the present stage, the shear resistant capacity for every truss unit might be different. This situation may not be true as only a unique overall strength for any particular beam and the static equilibrium must be observed at any time. Therefore the shear carried by concrete must be incorporated in the variable angle truss model to achieve this balance.

Shear carried by concrete has been termed as "concrete contribution" in many occasions and it has been recognized as an important portion of the ultimate shear strength of a reinforced concrete beam. Many design codes have utilized it to supplement strength from shear reinforcement. This concrete contribution consists of three basic resisting mechanisms: dowel action, aggregate interlocking, and shear carried by the compression zone. Some research has attempted to measure these three quantities through experimentation, however no reliable data has been collected up until now and only qualitative analysis has been available [P2]. On the other hand, some research has tried to use other parameters to represent this concrete contribution., but among all these parameters, transverse tensile stress and strain have prevailed [V2, K2, and A4]. In the truss model analogy, the concrete contribution can be reasonably understood and represented as the angle of the principal compression (strut) is at an angle to the crack and thereby creating a shear stress on the crack surface. Thus the use of the transverse tensile stress and strain in relation to the concrete contribution can be carefully incorporated in the variable angle truss model here because the compatibility conditions which allows the transverse tensile stress and strain to be assessed exist in each truss unit.

Referring to **Figure 4.5**, the local stress conditions at a crack are shown. The strut inclined at θ transfers the diagonal compression which can be regarded as the principal compressive stress in its direction. In the direction perpendicular to the strut, principal tensile strain presents and then induces principal tensile stress on the strut. Consider an infinitesimal element of concrete in the strut of a typical truss unit as shown in **Figure 4.5** where strain compatibility conditions are presented. In the

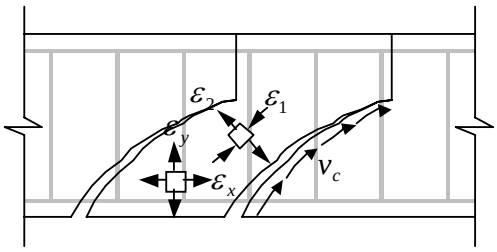

Figure 4.5: Local stresses and strains at a crack

longitudinal direction, when considering the cross-section of a beam, the basic Bernoulli's Principle in which the plane sections remain plane after bending is adopted. Thus the longitudinal strain in the concrete and the steel at various points across the section is proportional to the distance from the neutral axis. Then the longitudinal strain ε_x for the infinitesimal element is equivalent to the average value of the longitudinal strain in the cross-section. However, this average value has been found to be difficult to access. In the transverse direction, it is noticed that tensile strain prevails. The tensile strain in this direction can be considered as the strain in the shear reinforcement according to Vecchio and Collins [V2]. As this strain is uniform in general, the transverse strain for the infinitesimal element is determined to be ε_y if the shear reinforcement does not yield, where

$$\varepsilon_y = \frac{V_s s}{A_{st} E_s jd \cot\theta} \tag{4-13}$$

For the infinitesimal element, the principal stress directions are the direction of the inclined strut, which forms θ from the longitudinal direction and the direction perpendicular to it. At this stage the element has a compressive stress along the strut direction and a tensile stress perpendicular to it. However, the directions of the principal strains deviate somewhat from the direction of the principal stresses. Vecchio and Collins [V2] have summarized a number of experimental data and found that principal strains only differed from the principal stresses by $\pm 10°$. Therefore it is reasonable to assume that the principal strain directions and the principal stress directions for an infinitesimal element of concrete coincide with each other and that the principal strain in the compressive direction is readily determined by the stress and

geometrical condition of the strut, thus,

$$\varepsilon_1 = -\frac{V_s}{jdb_w E_c \sin\theta\cos\theta} \tag{4-14}$$

With the known value θ, ε_y, and ε_1, a Mohr's Circle can then be constructed to calculate the tensile strain ε_2. **Figure 4.6** gives the Mohr's Circle and ε_2 is:

$$\varepsilon_2 = \frac{2(\varepsilon_y - \varepsilon_1)}{|\cos 2\theta| + 1} - \varepsilon_1 \tag{4-15}$$

This equation takes consideration that θ may be more than $45°$.

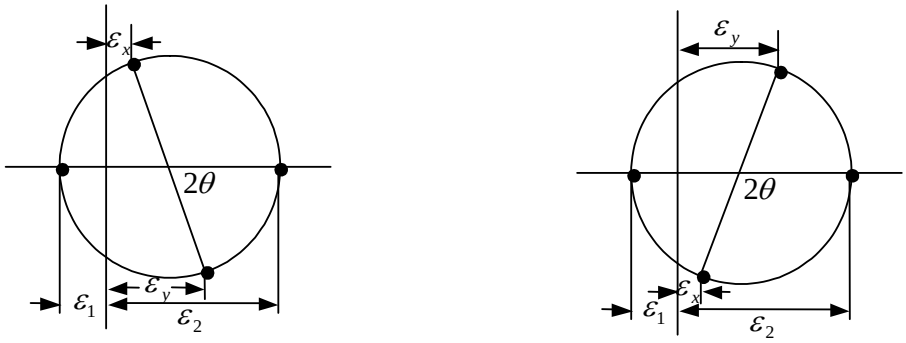

(a) $\theta \le 45°$ (b) $\theta > 45°$

Figure 4.6: Compatible stain conditions in a reinforced concrete element

Many research includeing Walraven [W1] has concentrated on the experimental relationships between the shear carried by concrete v_c and the tensile strain ε_2. Based on Walraven's work, the following limiting value of shear stress transferred across the crack was derived by Vecchio and Collins [V2]:

$$v_c = \frac{0.18\sqrt{f_c'}}{0.31 + 0.24\dfrac{w}{a+16}} + 1.64 f_{ci} - 0.82 \frac{\dfrac{f_{ci}^2}{\sqrt{f_c'}}}{0.31 + 0.24\dfrac{w}{a+16}} \tag{4-16}$$

where a is the maximum aggregate size in millimeters and w is the crack width. The crack width w to be used in an equation should be the average crack width over the cracked surface. It can be taken as:

$$w = \varepsilon_2 s_\theta \tag{4-17}$$

Where

$$s_\theta = \frac{1}{\frac{\sin\theta}{s_{mx}} + \frac{\cos\theta}{s_{my}}} \tag{4-18}$$

and where s_{mx} and s_{my} are the indicator of the crack control characteristics of the longitudinal and transverse reinforcement respectively. According to the provision of the CEB-FIP Code [C2]:

$$s_{mx} = 2\left(c_x + \frac{s_x}{10}\right) + 0.25k_1\frac{d_{bx}}{\rho_s} \tag{4-19}$$

$$s_{my} = 2\left(c_y + \frac{s}{10}\right) + 0.25k_1\frac{d_{by}}{\rho_{st}} \tag{4-20}$$

where k_1 is equal to 0.4 for deformed reinforcing bars or 0.8 for plain reinforcing bars.

The calculated v_c from Equation (4-16) is the shear stress transferred at the cracks surface. In the truss model proposed in this chapter, crack surface can be approximated along the strut direction and hence the shear strength contributed from concrete is:

$$V_c = \frac{jdb_w}{\sin\theta} v_c \sin\theta = jdb_w v_c \tag{4-21}$$

4.4 Solution Algorithm for Load-Displacement Response

In the previous sections of this chapter, theoretical strut angles and concrete contribution have been addressed for the variable angle truss model theoretically. The method to develop the variable angle truss model and treatment of the concrete contribution can be verified by predicting the load-displacement response of reinforced concrete beams subjected to shear. To do that, firstly, the strength of the variable angle truss model is made up of two portions: V_s and V_c. V_s is the contribution from the shear reinforcement and will cause a deformation in each truss unit which in turn mobilizes V_c (the shear carried by concrete) in the truss unit. At a low shear level, V_c calculated from Equation (4-21) may be larger than the applied shear force which probably explains the reason why the concrete has not been cracked and only part of the V_c mechanism has been utilized. At this point, shear reinforcement or the ties are assumed to have no participation in the shear resistance. At a higher shear level, V_c is fully utilized first and then followed by the shear reinforcement subjected to the shear stress generated. With an increase in the load level, the shear reinforcement may eventually yield. Post yielding behavior of shear reinforcement could also be taken into consideration in this model. Secondly, the deformation resulting from V_s is calculated for each truss unit as in Equation (4-7). The displacement of the variable angle truss model is the sum of all the deformations from every truss unit. Therefore, a procedure to predict the load-displacement response as well as the ultimate strength of the variable angle truss model is developed. The step-by-step solution process is summarized in the flowchart shown in **Figure 4.7**. The solution process is repeated for different load levels until a complete load-displacement response is obtained.

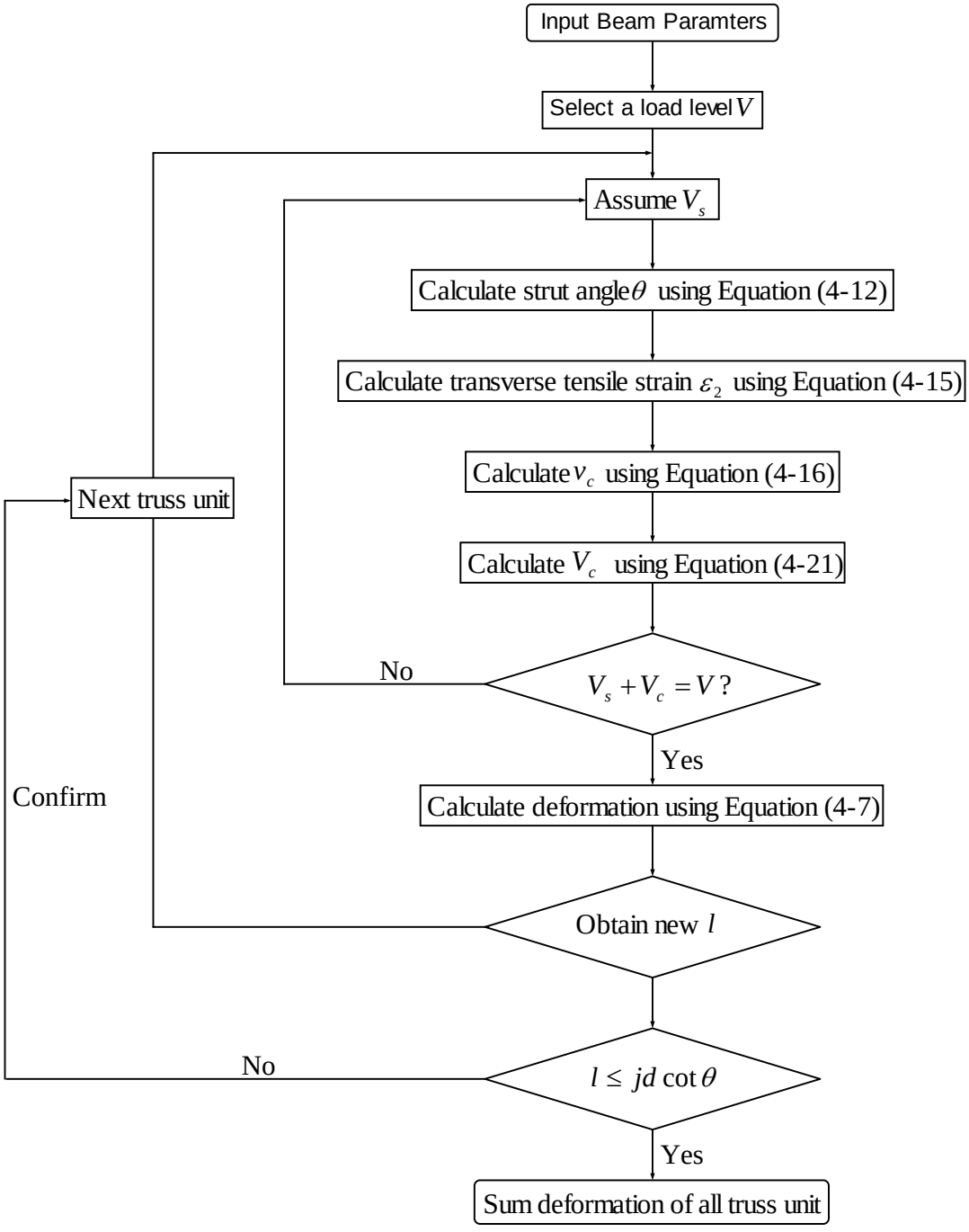

Figure 4.7: Flowchart showing the solution algorithm

4.5 Comparisons with Previous Experiments

To validate the proposed model, two case studies were undertaken. The first case study was on the reinforced concrete beams tested by Bresler and Scordelis [B2], the second on reinforced concrete beams by Anderson [A6]. Bresler and Scordelis [B2] conducted a set of accurate experiments for reinforced concrete beams which failed in shear. Beams A-2, B-2, and C-2 of the test were taken to be modeled in this analysis. The analysis results in terms of load-displacement response are shown in **Figures 4.8** to **4.10**. A reasonable match with the experimental data is observed. Importantly, this analysis method is always on the safe side throughout the whole loading process.

To further investigate the calculated strut angles of a variable angle truss model in predicting the behavior of reinforced concrete beams subjected to shear, another set of experiments conducted by Anderson [A6] was also modeled in this research. For the four beams selected from Anderson's tests, the global behaviors of the load-displacement responses (see **Figures 4.11** to **4.14**) predicted are found to have very close agreements with the experimental data. Calculated strut angles are compared with the experimentally recorded crack patterns. In these graphs of **Figures 4.15** to **4.18**, the strut inclinations are observed to have similar orientations to the cracks developed. The performance of the variable angle truss model is proved by plotting the strain developments of shear reinforcement during the loading process. **Figures 4.19** to **4.22** demonstrate the results when compared with experimental data. For example, in Beam N3, considering the different location of the stirrups in the experimental beam and ties in the analytical truss model, Member 3-4 (tie) should be compared with Stirrups No. 3 and No. 4, whereas Member 5-6 (tie) should be compared with Stirrups No. 5. Thus, a similar trend of strain development can be seen. The pairing does not fully match due to the fact that any tie in the truss model represents lumped shear reinforcement in one truss unit and its strain and stress should be the average of a few stirrups covered in that truss unit. The larger strains obtained in the variable angle truss model are because of the stress-strain relationship with the strain hardening ratio specified. Lastly, three additional short span reinforced concrete

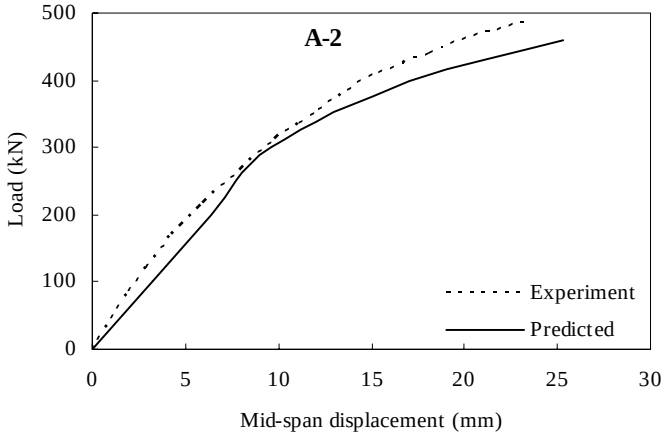

Figure 4.8: Comparison of predicted and measured load-displacement responses of the Beam A-2

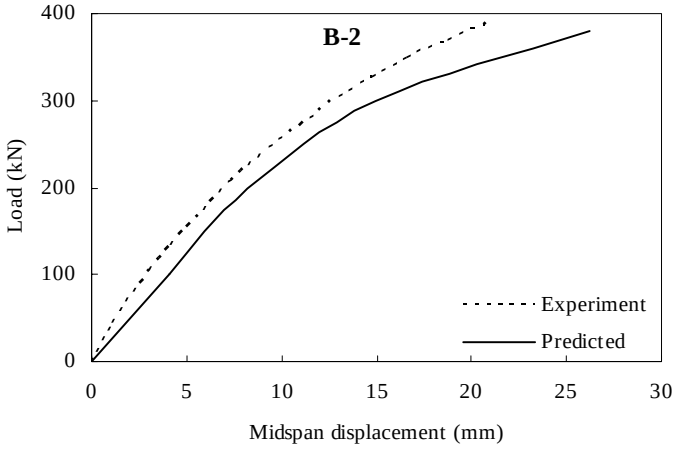

Figure 4.9: Comparison of predicted and measured load-displacement responses of the Beam B-2

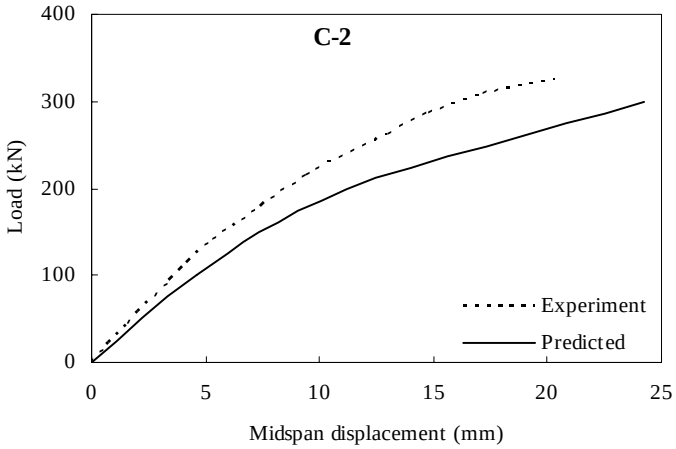

Figure 4.10: Comparison of predicted and measured load-displacement responses of the Beam C-2

beams tested by Al-Nahlawi [A5] were also modeled. Results are shown in a similar manner in **Figures 4.23** to **4.28**. Generally, the variable angle truss models give realistic results in all the aspects.

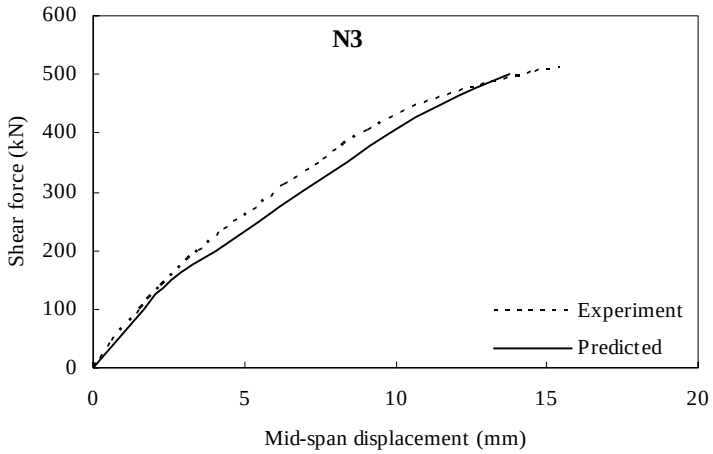

Figure 4.11: Comparison of predicted and measured load-displacement responses of the Beam N3

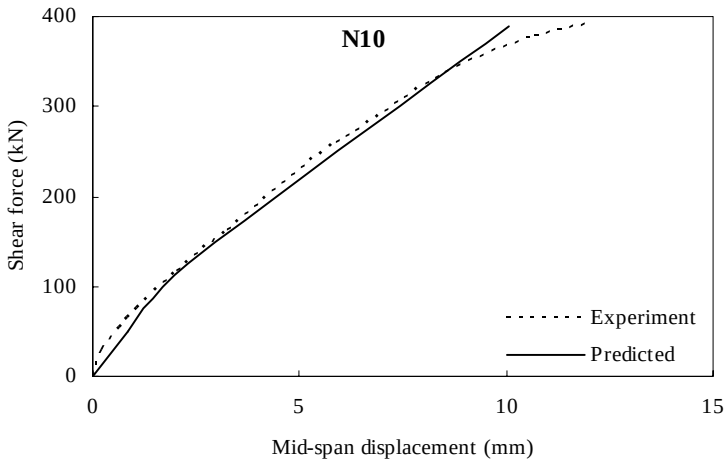

Figure 4.12: Comparison of predicted and measured load-displacement responses of the Beam N10

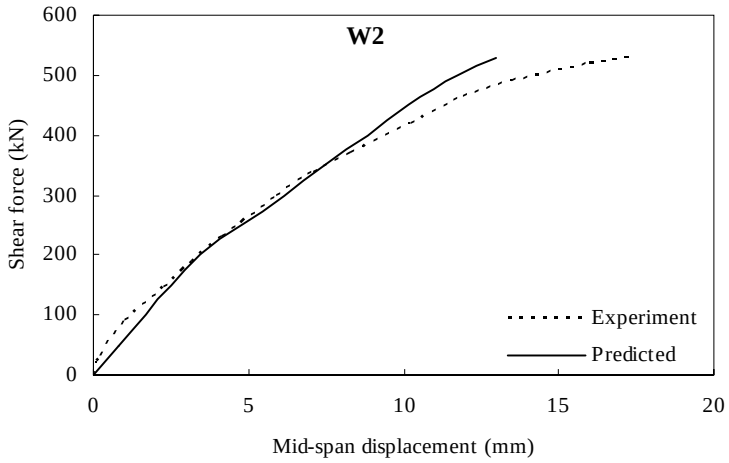

Figure 4.13: Comparison of predicted and measured load-displacement responses of the Beam W2

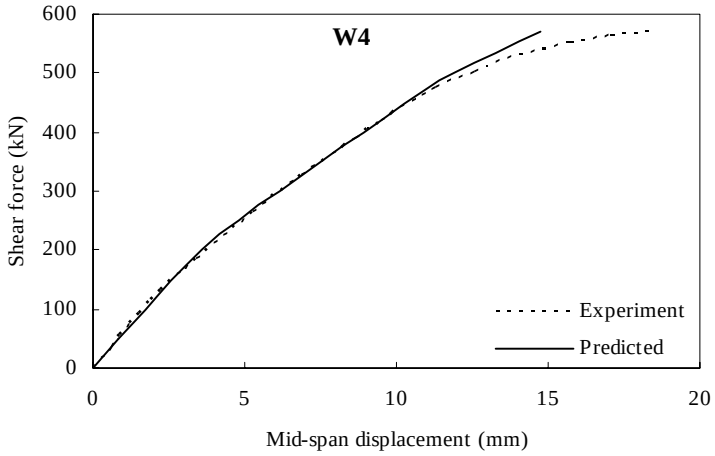

Figure 4.14: Comparison of predicted and measured load-displacement responses of the Beam W4

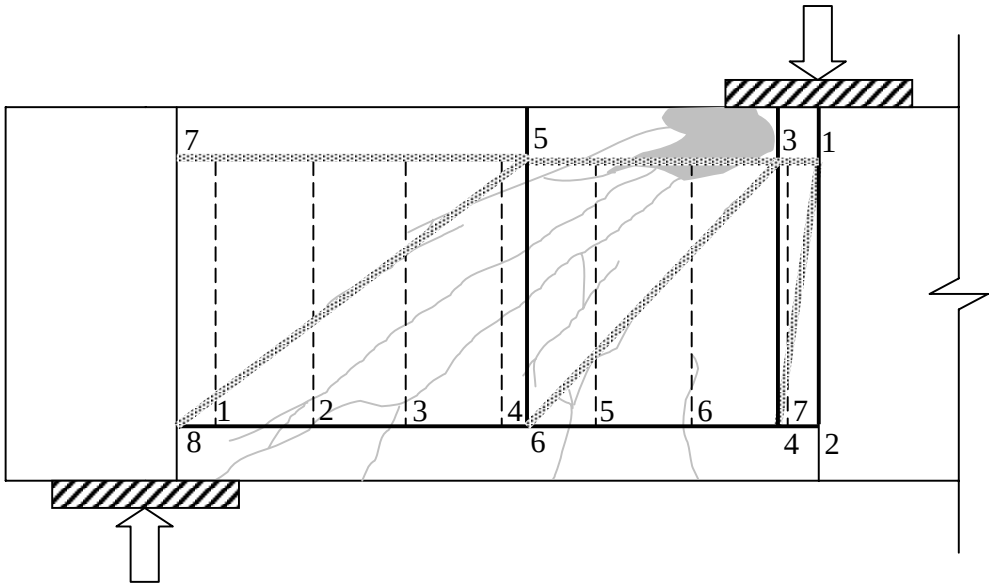

Figure 4.15: Calculated strut angles compared to the crack pattern of the Beam N3

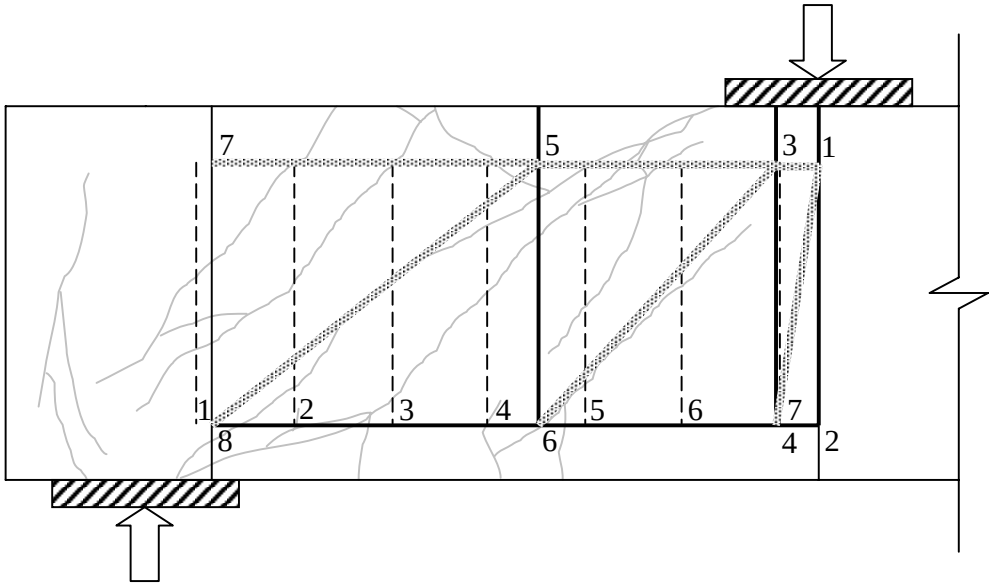

Figure 4.16: Calculated strut angles compared to the crack pattern of the Beam N10

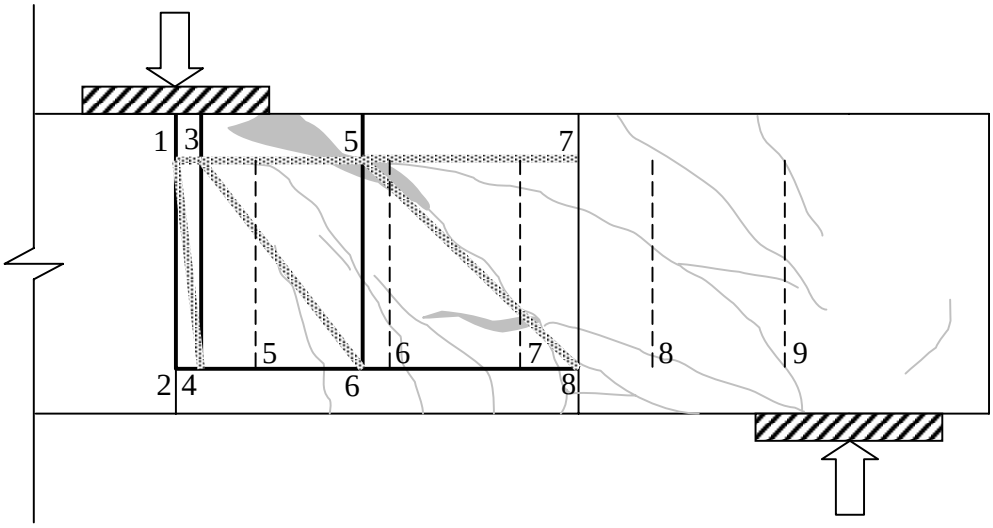

Figure 4.17: Calculated strut angles compared to the crack pattern of the Beam W2

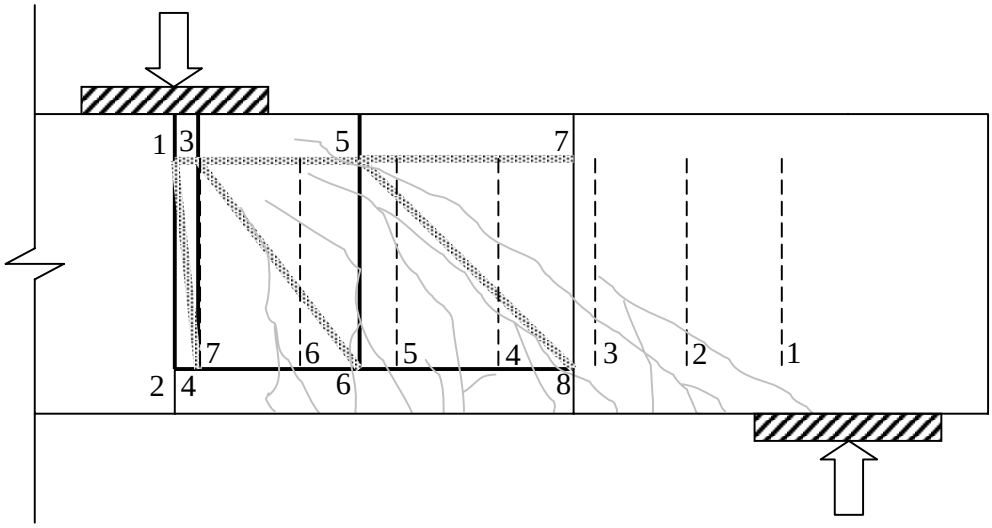

Figure 4.18: Calculated strut angles compared to the crack pattern of the Beam W4

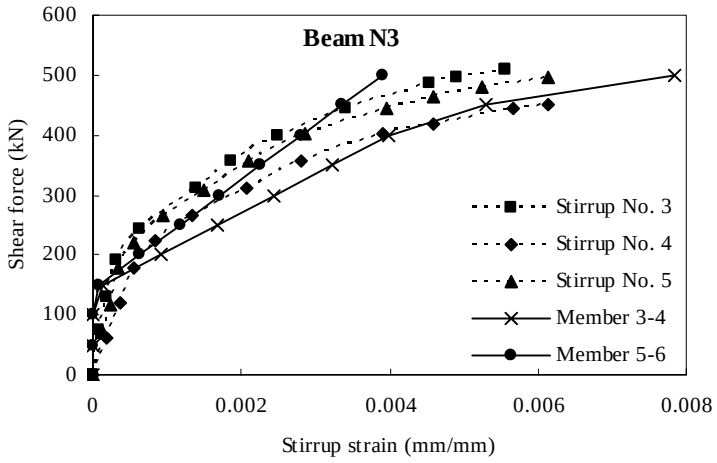

Figure 4.19: Comparison of predicted and measured shear reinforcement behaviors of the Beam N3

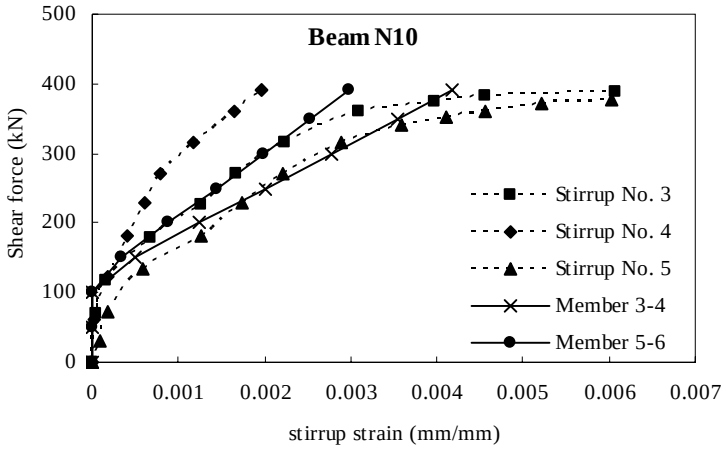

Figure 4.20: Comparison of predicted and measured shear reinforcement behaviors of the Beam N10

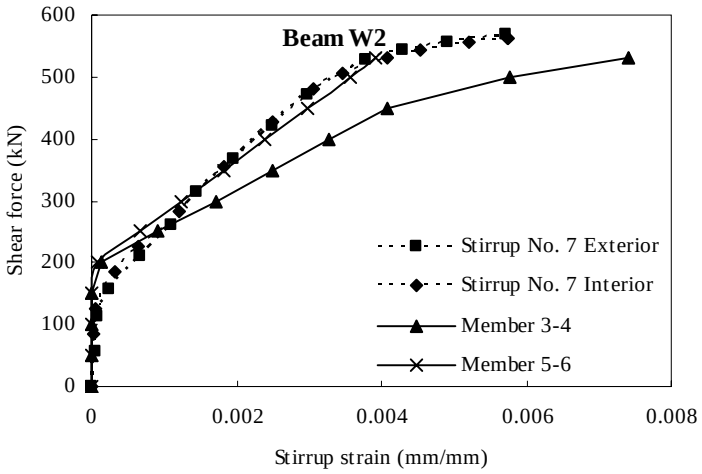

Figure 4.21: Comparison of predicted and measured shear reinforcement behaviors of the Beam W2

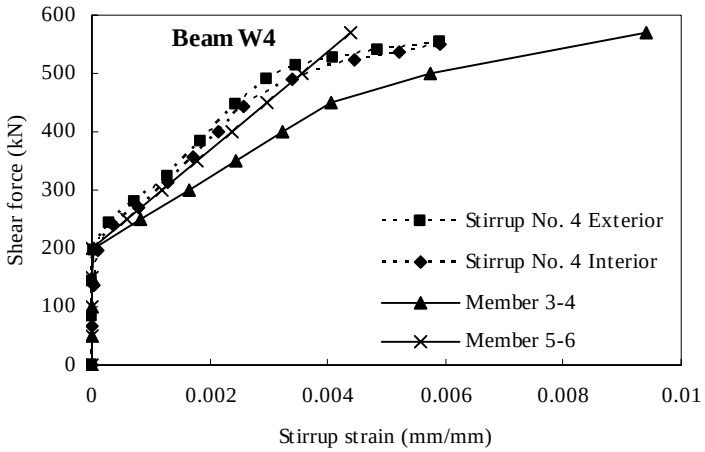

Figure 4.22: Comparison of predicted and measured shear reinforcement behaviors of the Beam W4

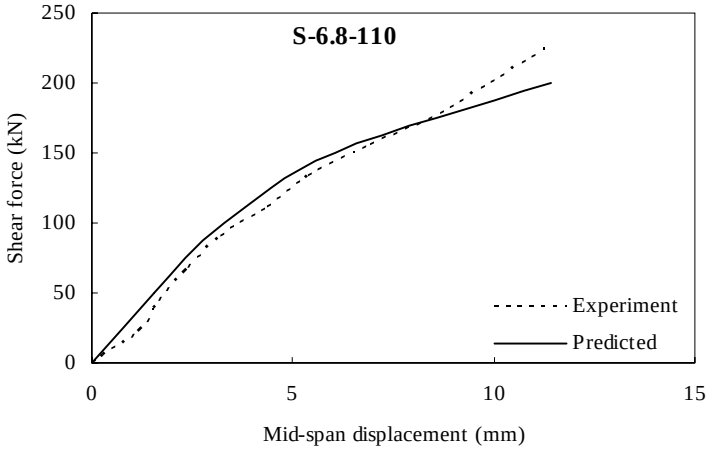

Figure 4.23: Comparison of predicted and measured load-displacement responses of the Beam S-6.8-110

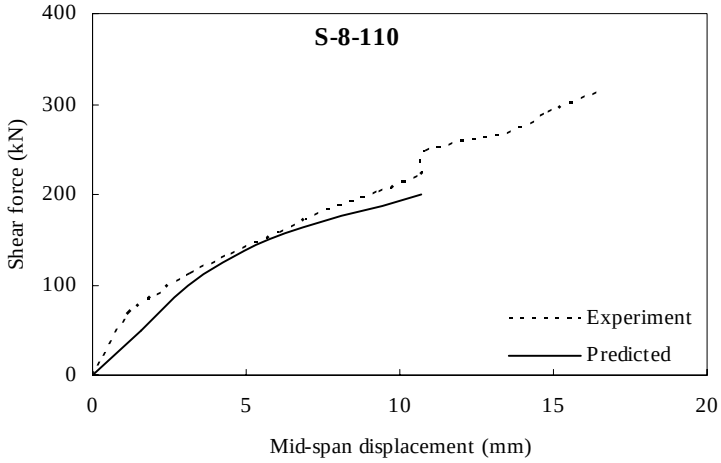

Figure 4.24: Comparison of predicted and measured load-displacement responses of the Beam S-8-110

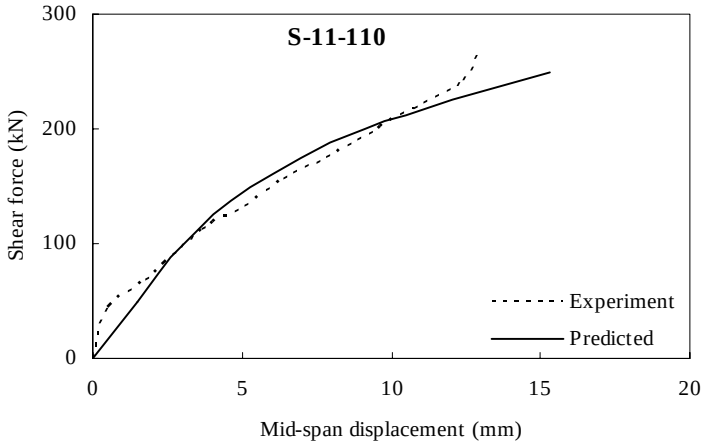

Figure 4.25: Comparison of predicted and measured load-displacement responses of the Beam S-11-110

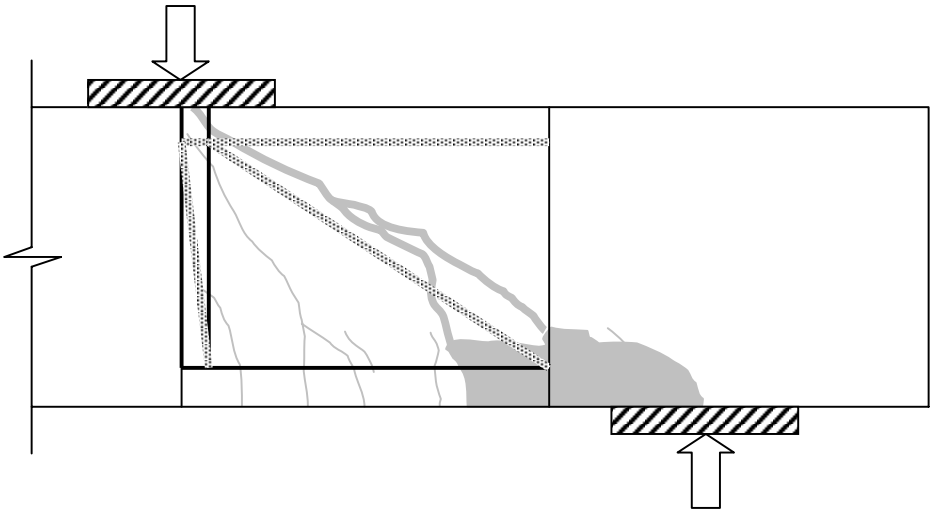

Figure 4.26: Calculated strut angles compared to the crack pattern of the Beam S-6.8-110

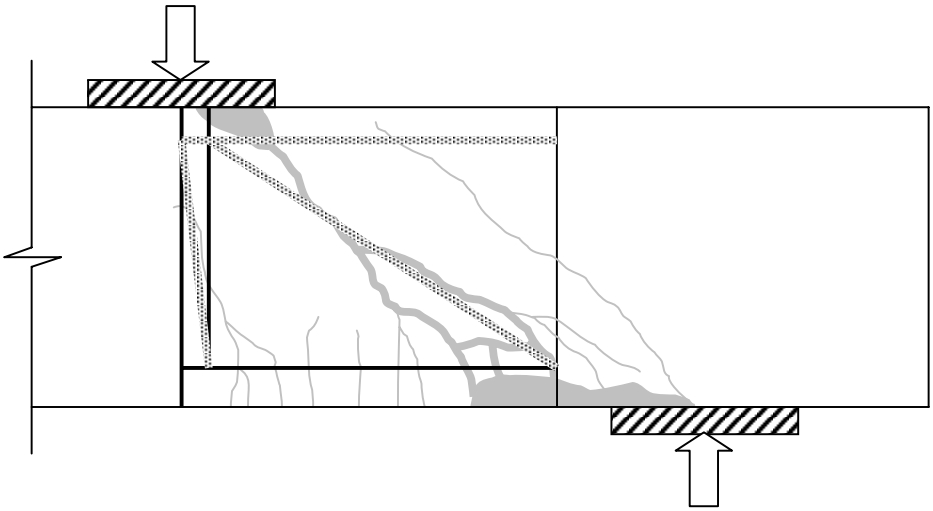

Figure 4. 27: Calculated strut angles compared to the crack pattern of the Beam S-8-110

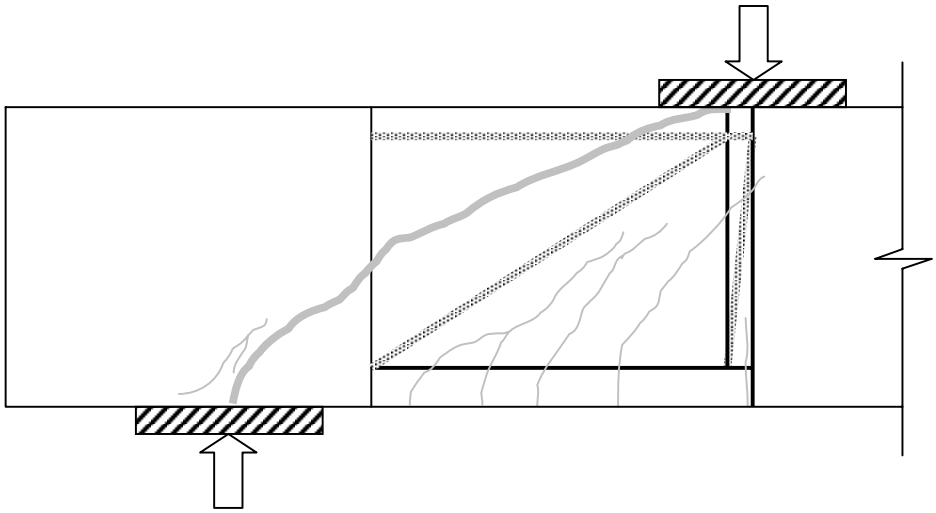

Figure 4.28: Calculated strut angles compared to the crack pattern of the Beam S-11-110

A few points need to be considered when the analysis procedure in **Figure 4.7** is applied. First, the depth c for the concrete compressive stress block must be determined for the axial rigidity of the top compressive member as in Equation (4-6). The strain profile for the concrete compressive stress block can be then calculated from the linear strain distribution over the cross-section by knowing the strain in the longitudinal reinforcement. Then a proper stress-strain relationship can be employed for the stress and c is obtained from either the internal force or the moment equilibrium. Next, when deriving Equation (4-12) for a strut angle solution, it is noted that the two flexural members are only subjected to part of the strength V_s. However, in determining the axial rigidity for the top compressive member in Equation (4-6) which will be used in Equation (4-12), it is suggested that c is calculated based on full load. Also, when considering the deformation of the flexural members, it is more reasonable to take both V_s and V_c into account. Lastly, based on the analysis method thus developed, a few truss units are formed along the shear span of the beam. The calculation of the crack angle stopped when variable l used to calculate strut angle θ for a new truss unit is found to be smaller than the length ($jd\cot\theta$) of this newly formed truss unit. So there could be a little beam length leftover of certain beam length

near the support. This portion of beam does not contribute to displacement as it is assumed that the deformation is concentrated only on the formed truss units.

4.6 Current Experimental Verification

The theoretical approach proposed here has been compared with a number of existing data and satisfactory performance of it has been seen. For supplementation, a small experimental program that consisted of testing of two reinforced concrete beams subjected to two concentrated static loading was done. The experiement helped to establish a greater understanding of the behavior of reinforced concrete beam under shear. The results obtained were used for further verification of the proposed strut angle calculation for a varible angle truss model.

The two tested reinforced concrete had a dimension of $250 \times 450 \times 4500$ mm. The shear reinforcement provided for them consisted of R8 bars at a spacing of 200 mm. The details of the two specimen are shown in **Figure 4.29**. On the drawing, the positions of the strain gauges attached to the reinforcing bars were marked out and these gauges were numbered to facilitate further data analysis.

Ready-mix concrete was used for casting. The nominal concrete compressive strength was 40 MPa. The maximum aggregate size was 20 mm and the measured slump value was 11 mm. At the date of beam testing, two standard concrete cylinder were tested and the compressive strength $f_c^{'}$ obtained was 36.96 MPa. Two types of steel bar, including high yield steel bar (hot rolled) with nominal yield strength of 460 MPa and hot rolled mild steel bar with nominal yield strength of 250 MPa were used in the two specimens. **Table 4.2** presents the tested strength of the reinforcing bars.

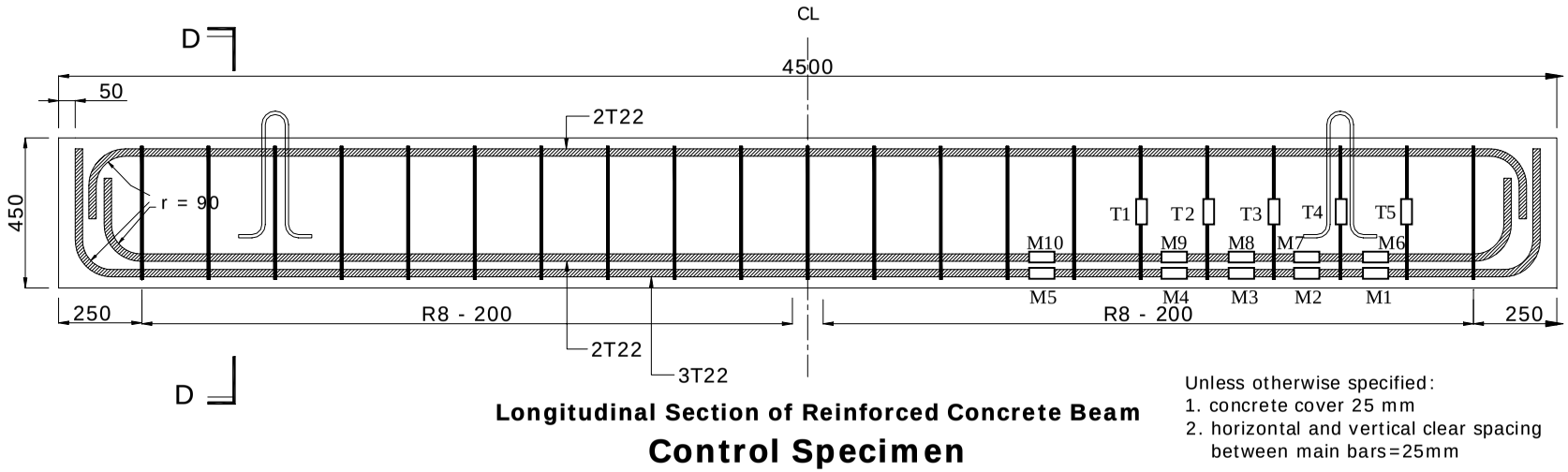

Figure 4.29: Details of two reinforced concrete beams

Table 4.2: Measured steel bar properties

Types	Modulus of Elasticity E_s (MPa)	Yield strength f_y (MPa)	Ultimate strength f_y (MPa)
R8	178910	469	568
T22	204375	366	434

The specimens were loaded in a two point loads, each spaced 1000 mm away from the center to create constant shear force at the 1000 mm length end sections of the beam. The detailed loading arrangement and setup of the reinforced concrete beams are shown in **Figure 4.30**. Three Linear Variable Differential Transformers (LVDTs) were installed to measure deformations below the mid-span and two point load of the reinforced concrete beams.

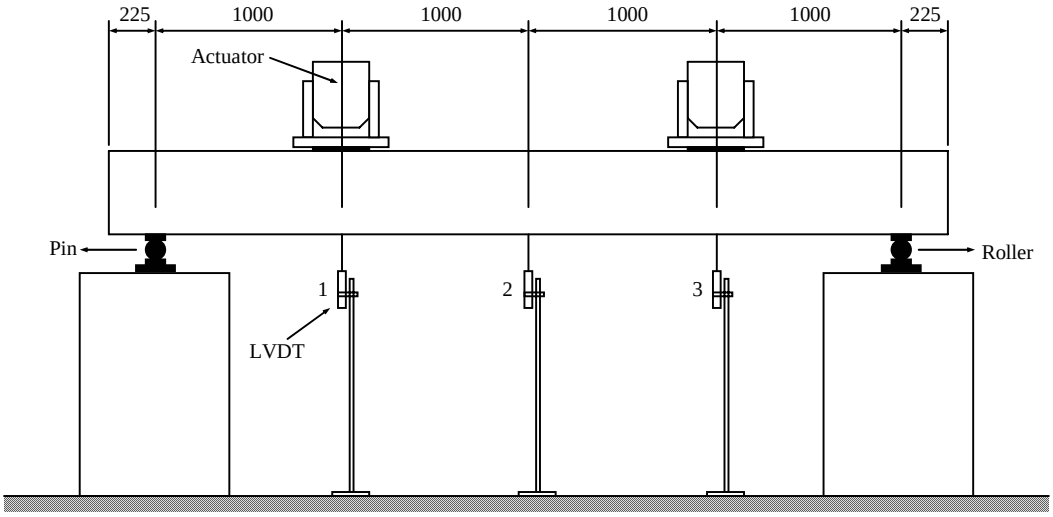

Figure 4.30: Experimental setup and loading arrangement

During the testing, the two specimens were experienced static type of loading. For Beam 1, the load was applied at a increamental of 25 kN and stopped at 225 kN. The load to Beam 2 was initially applied at a increamental of 25 kN to 125 kN. Then the increamental was reduced to 10 kN and evetually stopped at 205 kN. The two specimens were not loaded to failure as they would be used for sebsquent research on retrofitting and so the cracking condition of the beams were closely monitored

during the loading process. Once the diagonal crack width exceeded 3.0 mm, the loading stopped. The experimental results are presented in **Figure 4.31** in terms of shear force versus mid-span displacement response. Other results such as the strain gauge readings of the shear reinforcement and displacements belwo the loading points will be presented together with the analytical results.

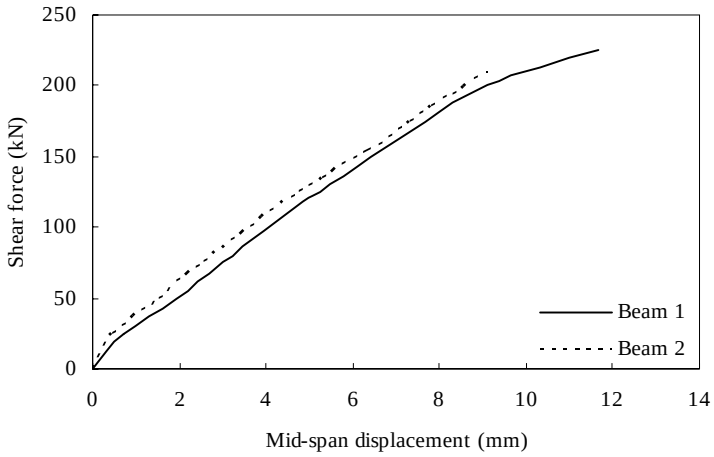

Figure 4.31: Shear force versus mid-span displacement responses of the two tested reinforced concrete beams

Figure 4.32 dipicts the crack patterns for the two reinforced concrete beams after the loading was terminated. Diagonal cracking was observed for both specimens. It could be expected that if the loading continued, the beams would fail in shear.

(a) Crack pattern of Beam 1 on the left shear span

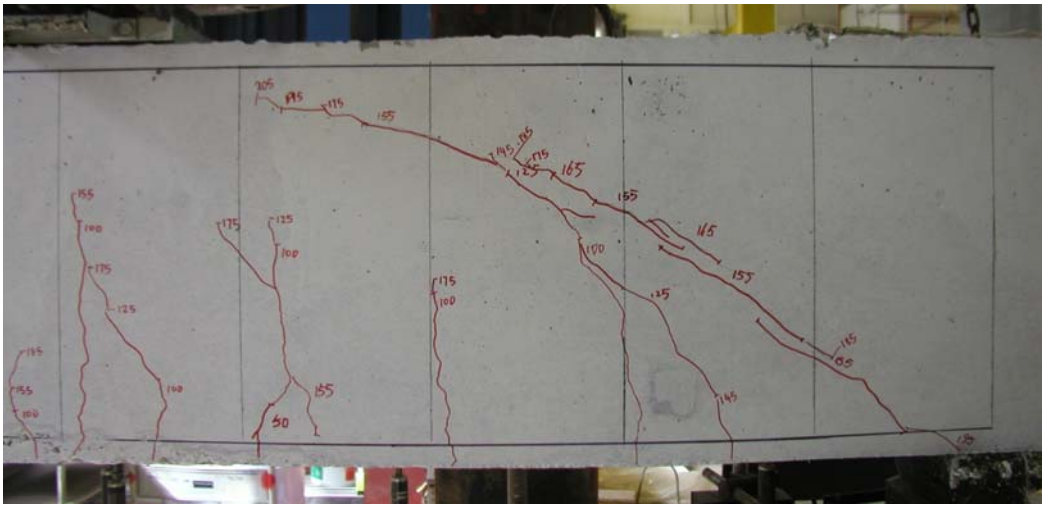

(b) Crack pattern of Beam 2 on the right shear span

Figure 4.32: Crack patterns of the two reinforced concrete beams

The cracks occurred in the experiments indicated the inclinations of the struts in the truss model analogy. So the crack patterns can be directly compared with the calculated strut angles in the variable angle truss model. The strut angles of the variable angle truss model are determined according to the methodology developed in the previous sections. **Figure 4.33** gives the comparison at the final stage of the loading. It can be found that the predicted struts in the variable angle truss model inclined at very similar angles to the cracks and specially, long diagonal cracks developed on the shear spans are very well modeled in the third truss unit.

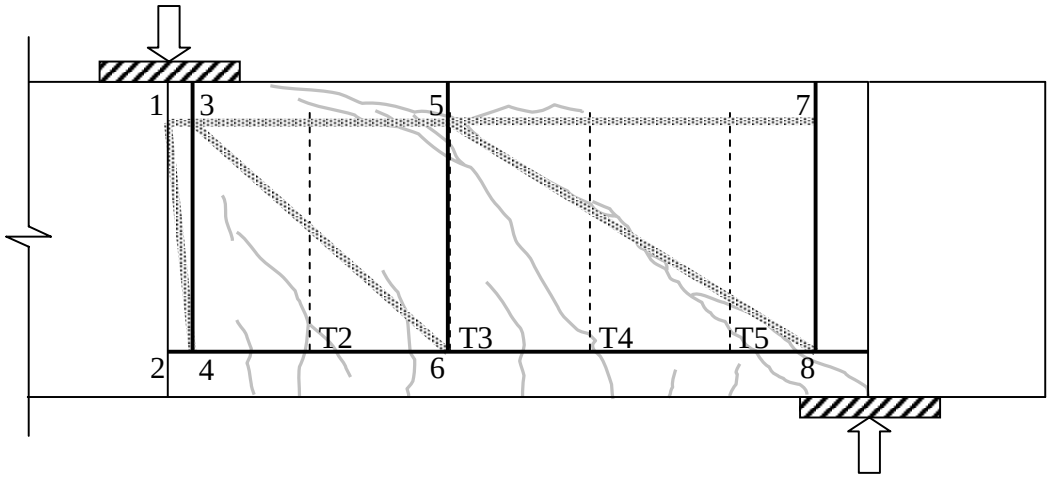

(a) Calculated strut angles compared to the crack pattern of Beam 1

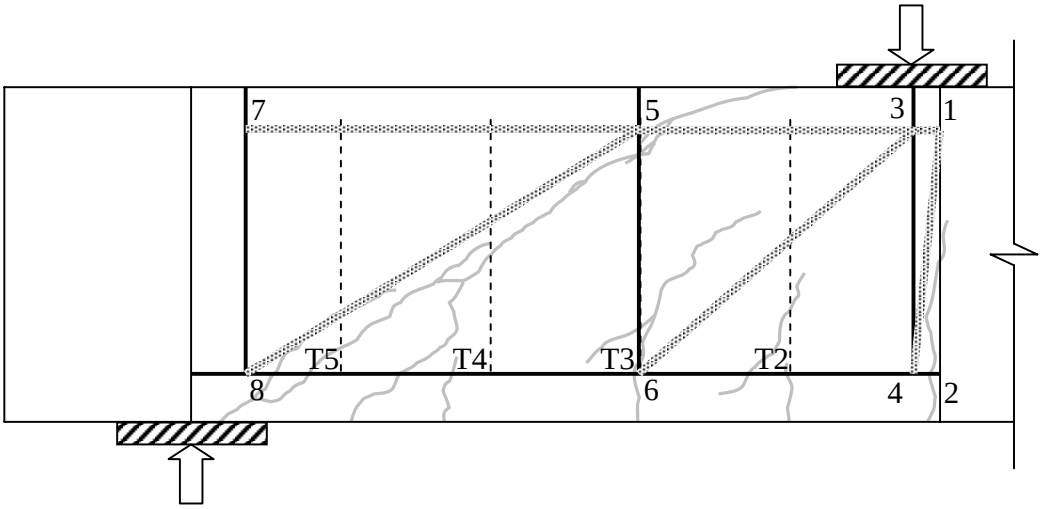

(b) Calculated strut angles compared to the crack pattern of Beam 2

Figure 4.33: Comparison between calculated strut angles and the crack patterns

Then displacement can be predicted from the proposed strut angle calculation of the variable angle truss model. Again, the displacement prediction follows the proposal in the previous sections. As the variable angle truss model is developed for the shear span of the reinforced concrete beams, it is more reasonable to compare to the displacements measure below the loading points in the experiment. The comparisons are shown in **Figure 4.34** and a close match between the analytical and experimental results is observed.

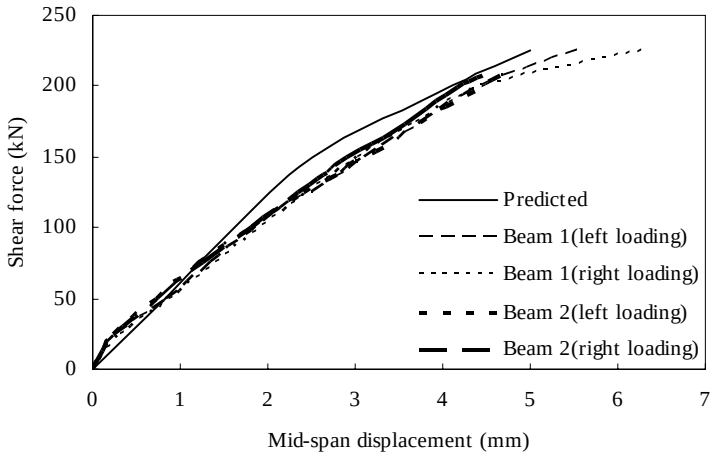

Figure 4.34: Comparison of predicted and measure load-displacement responses below the loading points of the tested reinforced concrete beams

The strain gauge readings on the shear reinforcement are important data that can be used to validate the proposed strut angel calculations. Five strain gauges were installed on the shear reinforcement at the right shear span of each reinforced concrete beam. The strains of the ties in the variable angle truss model can be compared to the readings recored in the gauges to verfiy that the behavior of the ties is reasonable. The comparisons are shown in **Figure 4.35**. According the calculated positions of the ties, the strain of Member 5-6 should be comapred with readings from strain gauge T3 and T4 and that of Member 7-8 should be comapred with T1, T2, and T3. Clearly, the trend in the strain development for the ties in the variable angle truss model and shear reinforcement in the reinforced concrete beams is very similar to that has been shown in the comparison with Anderson's beams [A6] previously. However, there are some numerical differences in the comparison and the reasons for this could be from the adopted method for concrete contribution calculation and the localized strain in the bars with the average strain in the ties.

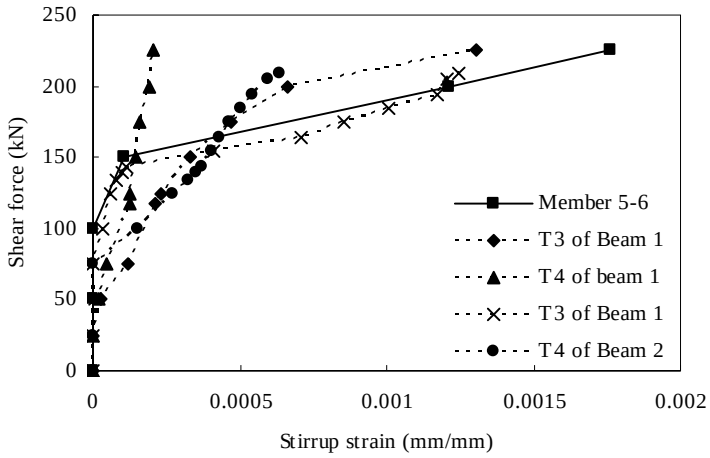

(a) For Member 5-6

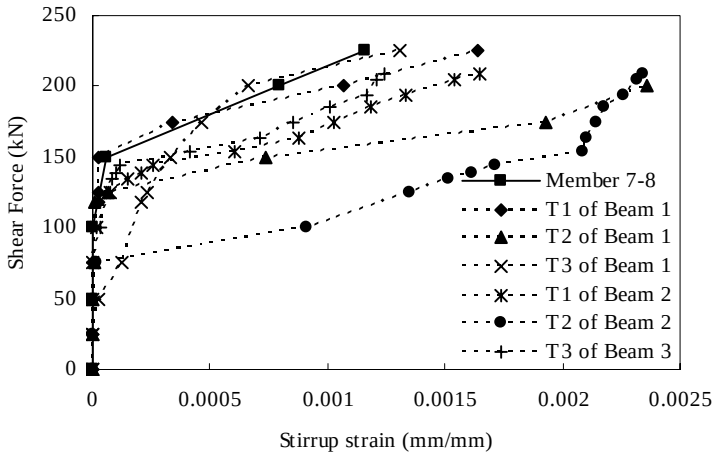

(b) For Member 7-8

Figure 4.35: Comparison of predicted and measured shear reinforcement behaviors of the tested reinforced concrete beams

Through the experimental program on reinforced concrete subjected to shear, it is again proven that the proposed method on calculation of strut angles of a variable angle truss model is reasonable.

4.7 Summary

For a reinforced concrete beam analyzed by truss model analogy, the proposed method here is capable of calculating the strut angles mathematically. Improvements on truss model analogy have been made through this method. Firstly, the strut angles are determined theoretically according to the detail of reinforced concrete beams with the principle of virtual work. Secondly, the strut angle evaluated in each truss unit varies due to the changes in available span length. Finally, the strut angle also changes with the applied shear level. Hence this method successfully develops a variable angle truss model for reinforced concrete beams subjected to shear. Stiffness and deformation are both readily defined in the variable angle truss model.

In essence, the truss model analogy only represents shear contribution from the shear reinforcement, even in the variable angle truss model. Therefore, the concrete contribution is incorporated in the variable angle truss model thus developed. A rational method from the strain compatibility condition of each truss unit is used to relate transverse tensile strain to the concrete contribution. With all the above relationships addressed, the load versus displacement response of reinforced concrete beams subjected to shear is predicted to verify the proposed method.

The predicted developments of strut angles along the shear span of a beam agrees well with experiments and the load versus displacement curves obtained are of realistic correlation to the test data.. This method provides a comprehensive tool which is user-friendly for manual calculation and it can be used to analyze reinforced concrete beams from the view point of truss model analogy. It also can be further enhanced into shear design methodology to overcome the arbitrary empirical formulations. In conclusion, the method presented in this chapter serves as a rational way to address the shear problem.

CHAPTER 5

EXPERIMENTAL PROGRAM OF REINFORCED CONCRETE WALLS WITH OPENINGS

5.1 Introduction

Another application of the strut-and-tie approach is to develop a model according to possible load path and to analyze the force transfer mechanism of reinforced concrete elements with static or geometrical discontinuities. The reinforced concrete wall with openings represents a typical two-dimensional element with sophisticated stress flow and the purpose of the following research is to explain the force transfer mechanism of reinforced concrete walls with openings and to make some recommendations for future design in relation to the strut-and-tie approach. Marti [M2] once postulated a reinforced concrete wall with openings, in which the stress flow was clearly visible under the given loads. He then proposed a possible strut mechanism to represent the stress flow pattern. Extended from Marti's [M2] research, this chapter includes an experimental program of reinforced concrete walls with openings, which were modified from Marti's [M2] wall model. The primary aim of this experimental program was to obtain reliable experimental results regarding possible stress flow patterns demonstrated by the specimens under a reversed cyclic loading.

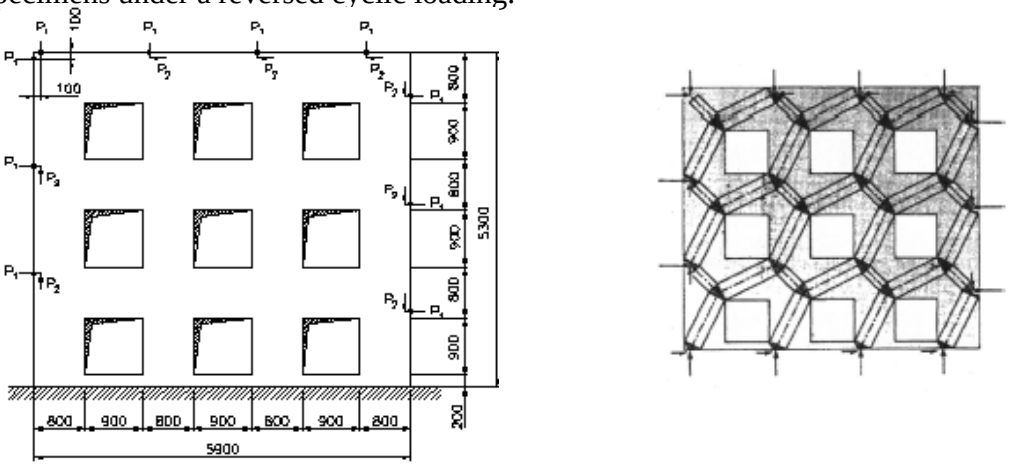

Figure 5.1: Low rise reinforced concrete shear wall and its strut-and-tie model by Marti [M2]

5.2 Design of the Reinforced Concrete Wall Specimens

Figures 5.2 to **5.4** show the details of three specimens designed. Each specimen consisted of three subassemblies: the top beam, the web, and the foundation beam. The web of each specimen was scaled down to 44% of Marti's [M2] shear wall model to fit into the existing loading frame. The Specimen W1, which was a solid wall, was designed first as the control specimen. The placement of horizontal and vertical reinforcement was carefully considered to facilitate further design of the other wall specimens with openings. The resulting vertical reinforcement ratio was 0.60% and that of the horizontal was 0.51% . The testing of the Specimen W1 later showed that the solid wall designed in this manner had only limited ductility. For the other two specimens with openings, the same amount of vertical and horizontal main reinforcing bars were applied at webs and concentrated along the possible load paths. Mild steel bars were added in the other regions, such as the panel zones, as nominal bars to limit the cracking of the concrete where necessary. The openings in the web of Specimen W3 followed the same pattern as that of Marti's shear wall model while the openings in Specimen W2 was modified.

The openings on Specimens W2 and W3 covered large areas on the web of the walls and as they were regularly placed, the webs of Specimens W2 and W3 were naturally zoned by them. For Specimen W2, four panel zones formed, while for Specimen W3, a few column and beam zones formed between the openings. Panel zones and beam and column zones were critical regions in the load paths and will be examined later in Chapter 6. So the panel zones in Specimen W2 and the beam and column zones in Specimen W3 have been numbered respectively to facilitate further analysis. The numbering systems for the two specimens were as follows In **Figures 5.5** and **5.6**.

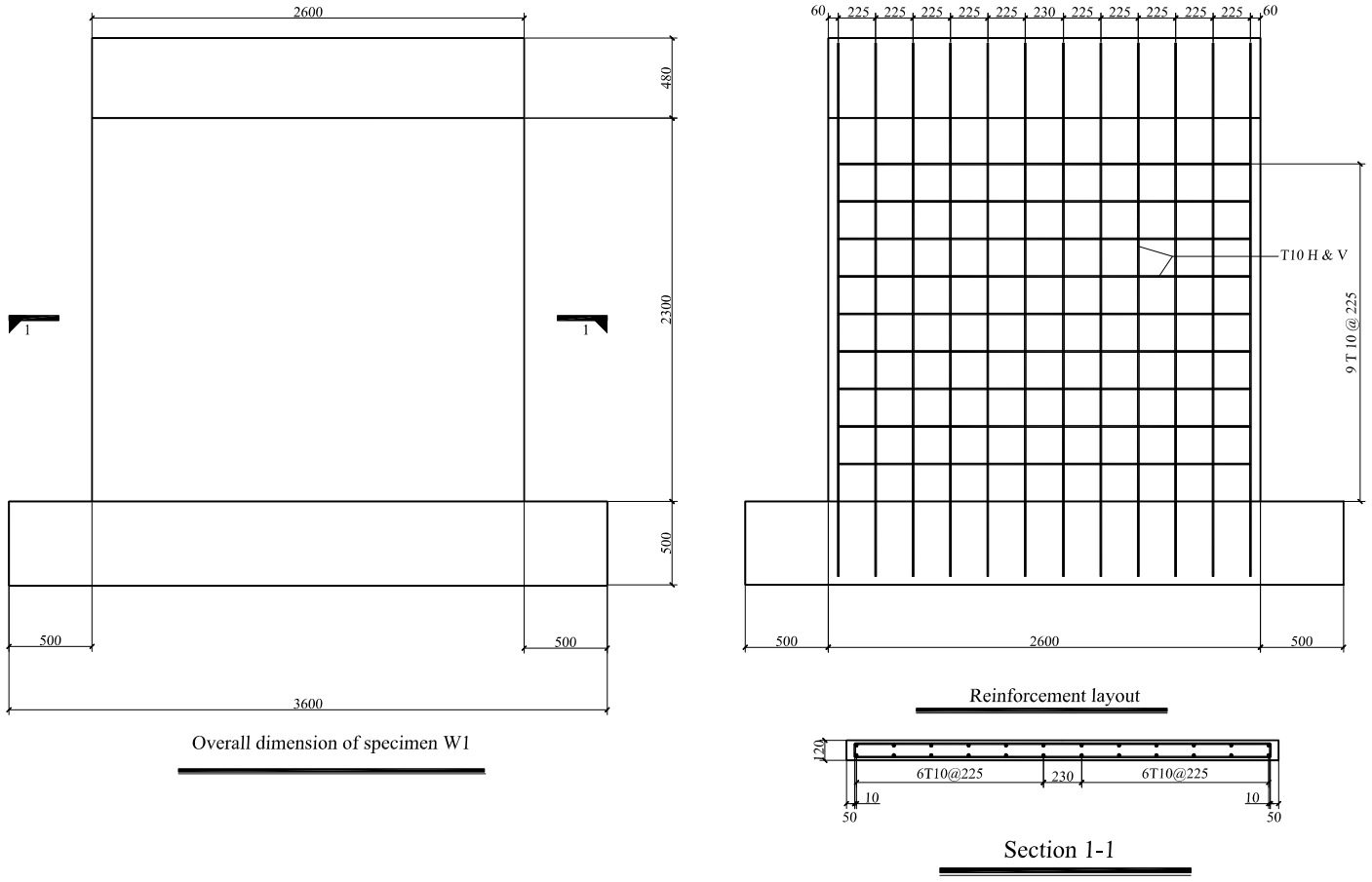

Figure 5.2: Details of Specimen W1

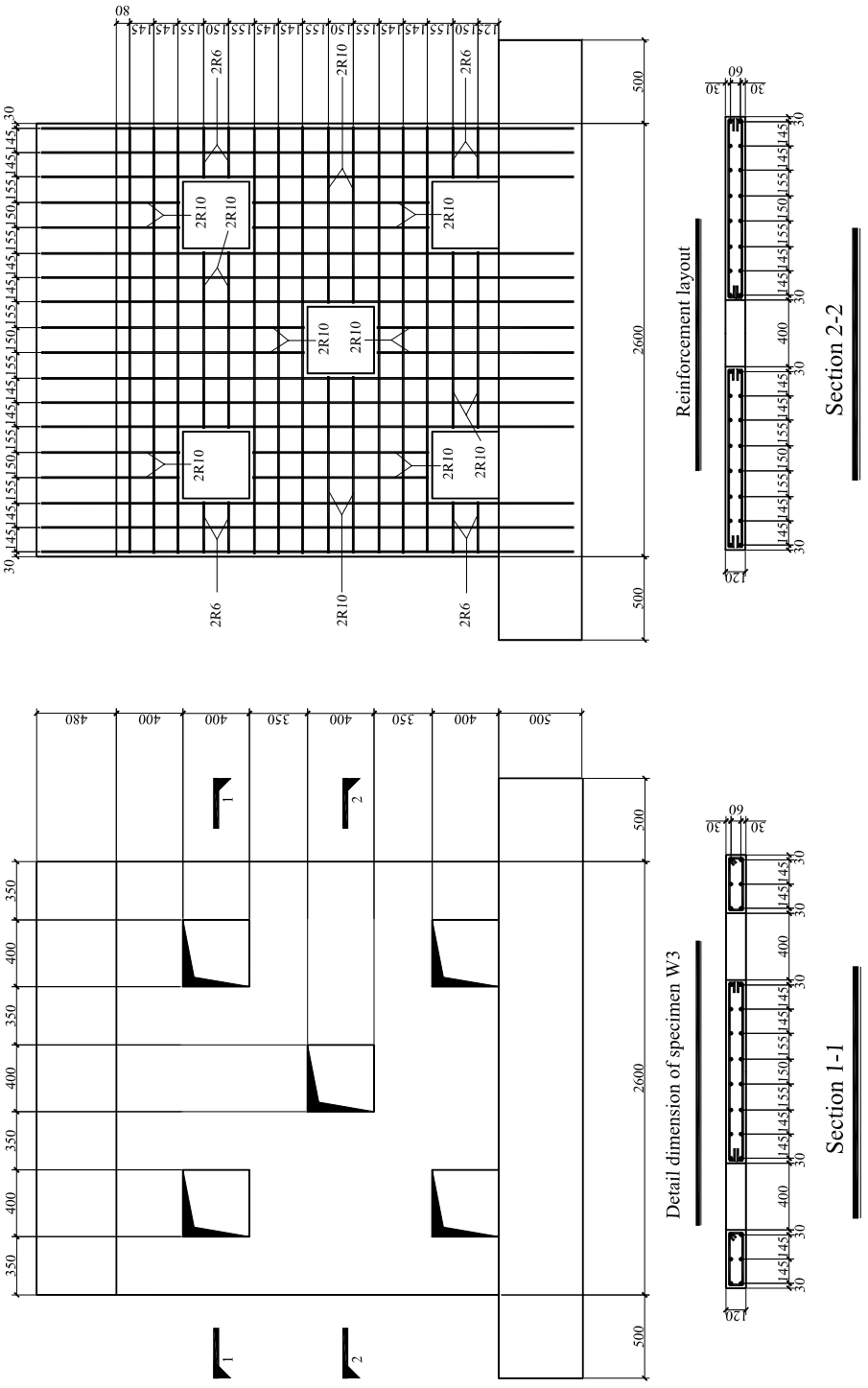

Figure 5.3: Details of Specimen W2

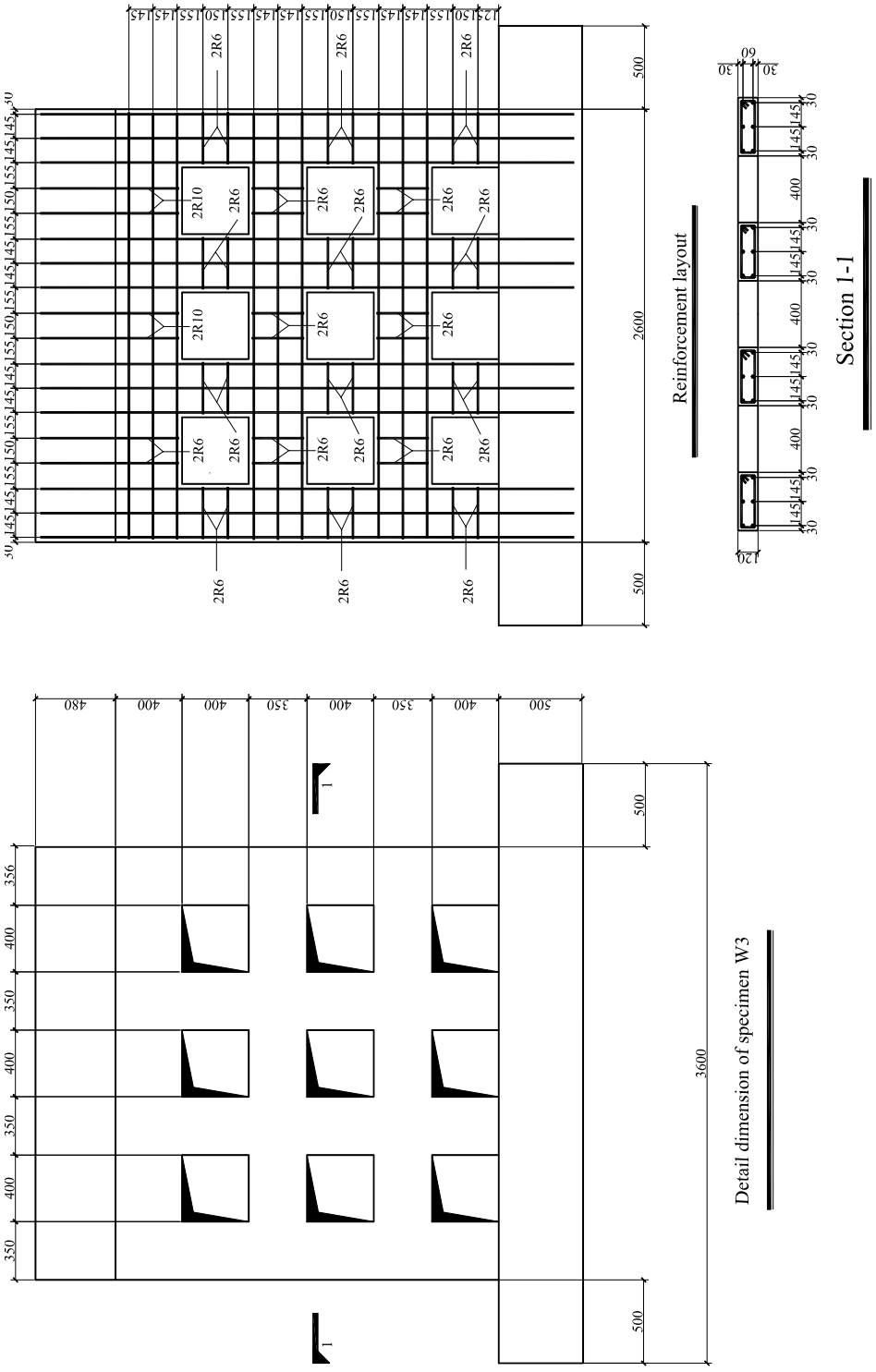

Figure 5.4: Details of Specimen W3

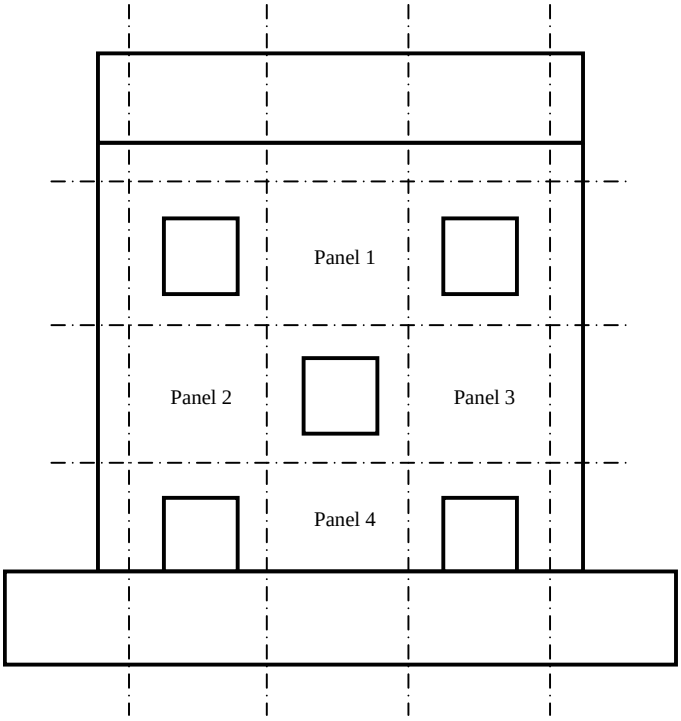

Figure 5.5: Panel zones on the web of Specimen W2

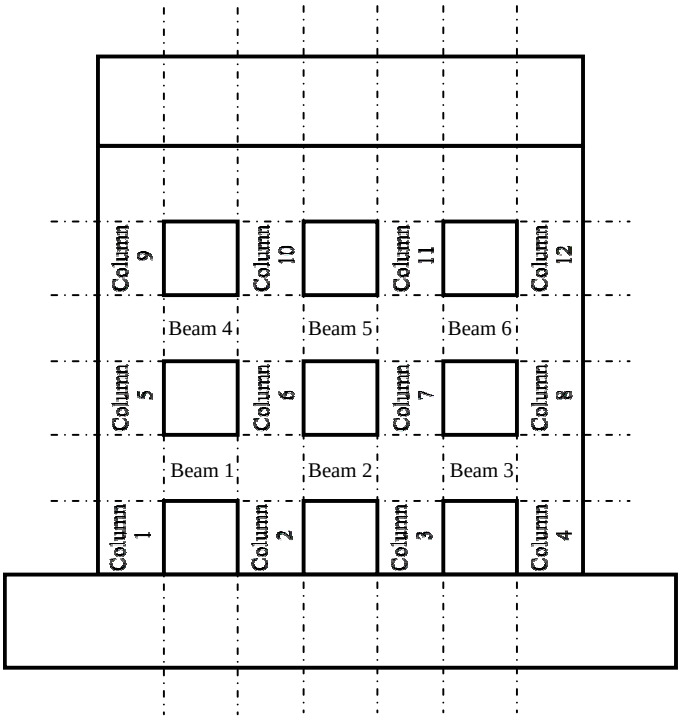

Figure 5.6: Beam and column zones on the web of Specimen W3

5.3 Material Properties

5.3.1 Concrete

Ready-mix concrete, which had a characteristic strength of 30 MPa, 13 mm maximum size aggregate, and a slump100 mm, was used to cast the specimens. Totally twelve $150\times150\times150$ mm cubes and twelve 150×300 mm cylinders were cast and cured following to the standard procedures and stored under the same condition with the specimens. The cylinder compressive strengths f_c' and cube compressive strengths f_{cu}' were tested on the day of testing each individual specimen. The results are shown in **Table 5.1**.

Table 5.1: Measured compressive strength of concrete

Specimens	Age at testing day (day)	Average f_{cu}' (MPa)	Average f_c' (MPa)
W1	77	47.99	38.13
W2	76	48.73	38.25
W3	79	46.87	39.13

5.3.2 Reinforcement

Two types of steel bars, including high yield steel bar (hot rolled) with a nominal yield strength of 460 MPa and hot rolled mild steel bar with a nominal yield strength of 250 MPa were used for all specimens. **Table 5.2** presents the tested strength of the reinforcing bars. T10, R10 and R6 bars were used in the web of the walls while T13 and T20 bars were applied in the loading beams and foundation beams. The yield strength of high yield steel bar was those values at point of $f_{y0.2\%}$. The yield strain of this bar was equal to the elastic limit strain plus 0.002. **Figure 5.7** shows the typical stress-strain relationships of the bars.

Table 5.2: Measured steel bar properties

Types	Modulus of Elasticity E_s (MPa)	Yield strength f_y (MPa)	Ultimate strength f_u (MPa)
R6	179734.7	308.4	428.3
R10	183283.3	385.1	502.0
T10	176547.7	480.0	545.1
T13	177862.0	492.5	580.9
T20	201178.8	512.0	606.6

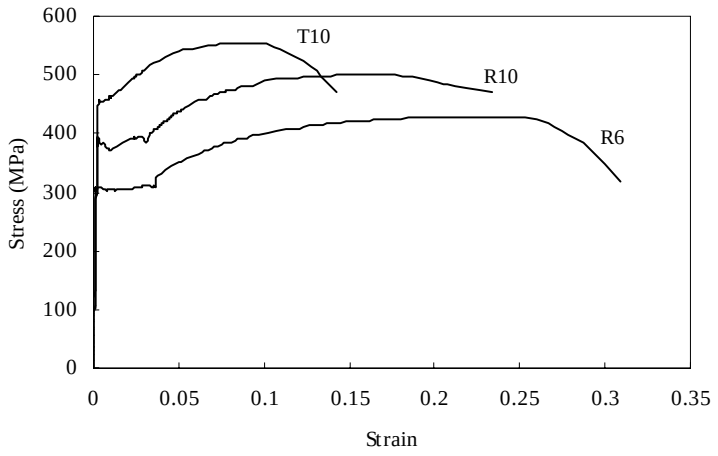

Figure 5.7: Typical stress-strain relationships for steel bars

5.4 Construction of Wall Specimens

The three specimens were all fabricated at the contractor's workshop. The reinforcing bars were cut and bent according to their design length within a tolerance of ± 2 mm. The reinforcement cages were tied in two steps, using soft steel tying wire. Firstly, the reinforcement nets in the web of each wall were constructed separately in two pieces. After the strain gauges were pasted in the bars and the wires of gages were properly arranged, the two pieces of reinforcement nets were then set up together to form a steel cage. The cage was later put into the formwork and its position was adjusted to satisfy the required tolerance.

The wall specimens were cast horizontally. **Figure 5.8** shows the photographs of the formworks and steel cages for the two specimens with openings. The formworks, made from thickened steel sheets, were designed by the contractor and inspected for satisfactory quality. The horizontal levels of all surfaces in the wall specimens were specially checked to ensure that no eccentricities occurred. The surfaces of the frameworks were oiled before the concrete casting. Special clampers were applied to ensure the positions of the preset plastic components and the holes.

The three specimens were cast in sequence at an interval of nine days. The nine-day interval was to ensure that every specimen was cured to enough strength so that it could be taken out from the formwork without any damage. During the casting, concrete of all specimens was compacted using internal vibrators and special attention was paid to the joint regions, such as the joint between the foundation beam and the wall web, to ensure the concrete quality there. The exposed web surface of every specimen was made smooth for drawing crack patterns during testing. After casting, the specimens were cured according to the standard procedure.

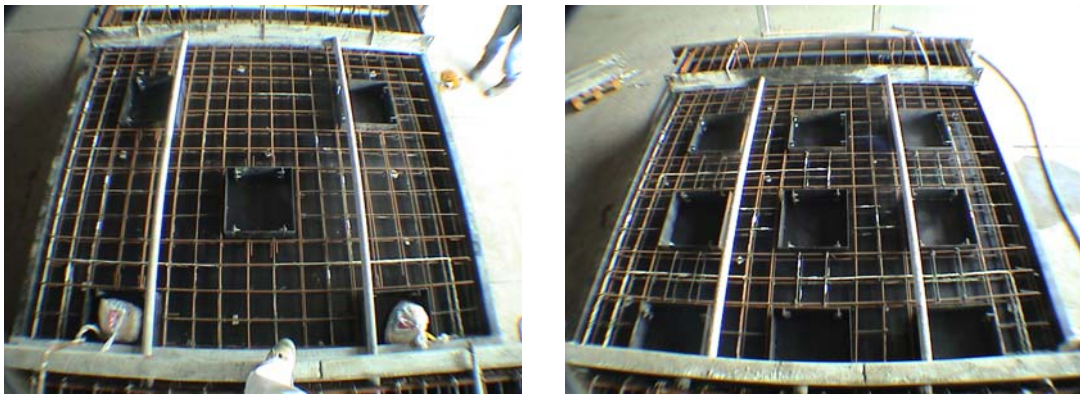

Figure 5.8: Steel cages and formwork of the specimens

5.5 Loading Frame and Loading Sequence

5.5.1 Loading frame

The testing rig, shown in **Figure 5.9**, consisted of two systems: an in-plane loading

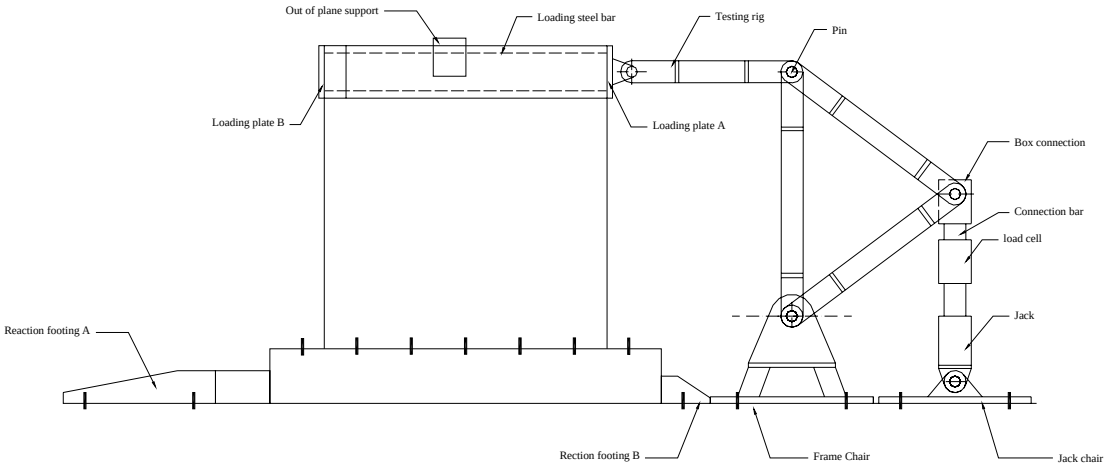

(a) Drawing of the loading frame

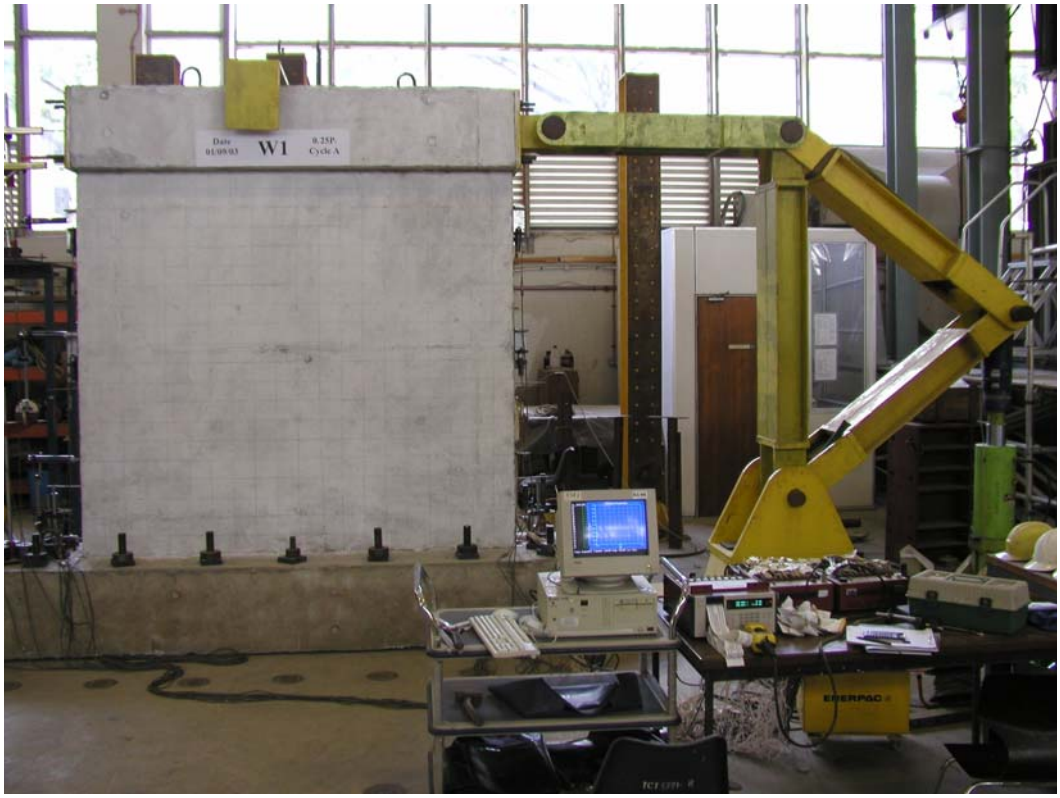

(b) Photography of the loading frame

Figure 5.9: Details of the loading frame

system and an in-plane base beam reaction system. The in-plane loading system included a double action hydraulic jack and four steel beams. The system was arranged in such a configuration so that the two directional lateral loads could be applied to the walls. Four high strength steel rods were pre-set in the top beam of the wall specimens so that the reversed cyclic lateral loading could be introduced as compression on the two end faces of the top beam. The base beam reaction system was designed to resist the rotation and sliding of the wall specimen when the load was applied. In the system, reaction footings provided balance reaction during the lateral loading. The foundation beam of each wall and the chair of the testing rig were attached to the strong floor by high strength rods, to which a prestress scheme was applied to resist sliding.

5.5.2 Loading sequence

A reversed cyclic lateral loading was applied to the top beam of each wall according to the loading sequence recommended by Park [P1]. The loading sequence began with three load-controlled cycles, which assumed that the structure was still within the elastic range, followed by the displacement controlled cycles, in which the displacement was increased according to the ductility factor. In the load-controlled cycles, the horizontal loadings increase from $\pm 0.25P_i$ to $\pm 0.75P_i$ by $\pm 0.25P_i$, where P_i is the horizontal load at the middle of the top beam associated with the nominal flexure strength M_i being reached at the critical sections of the walls. Then according to the top drift $\Delta_{0.75}$ obtained from $\pm 0.75P_i$ cycles, the yield displacement of the structure can be calculated by the equation

$$\Delta_y = \frac{\Delta_{0.75}}{0.75} \tag{5-1}$$

The displacement controlled loading process began with one cycle in ductility factor $\mu = \pm 1$, followed by the two cycles in each successive ductility factor, which was $\mu = \pm 2$, ± 3, ± 4 ... where μ was calculated by

$$\mu = \frac{\Delta}{\Delta_y} \tag{5-2}$$

5.6 Instrumentation

The objectives of the instrumentation on the wall specimens were to observe the following parameters:

1) lateral force imposed by the hydraulic jack,
2) lateral displacement at the top of the walls,
3) flexural deformation in the walls,
4) shear deformation in the walls,
5) horizontal sliding of the walls,
6) deformation of some important regions in the walls, and
7) strains in selected reinforcing bars.

5.6.1 Hydraulic jack and load cell

Load to the wall specimens were applied through a hydraulic jack which has a capacity of 2000 kN in compression and 1200 kN in tension. The stroke of jack is 405 mm. In order to measure the applied load, a two way action (compression and tension) load cell with capacity 2000 kN were connected to the hydraulic jack using high steel rod with threads as shown in **Figure 5.9**. According to the loading frame used in the experiment, the lateral loading applied to the top of the wall was 0.67 time of the measured load from the load cell.

5.6.2 Linear Variable Differential Transducer (LVDT)

Three types of Linear Variable Differential Transducers (LVDT), with 300 mm travel, 100 mm travel, and 50 mm travel, were applied to measure top drift, flexural deformations, and shear deformations. LVDTS with 300 mm-travel were set up to the middle of end of top beam to measure top drift. **Figures 5.10** to **5.12** show the distribution of transducers in every specimen. Similarly, the transducers were numbered to facilitate data recording and analysis.

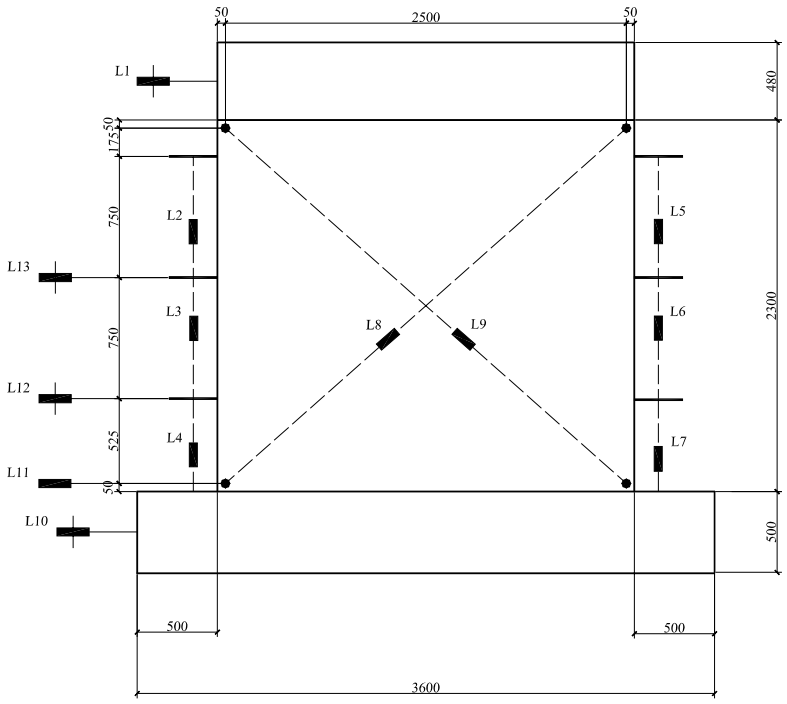

Figure 5.10: LVDT positions of Specimen W1

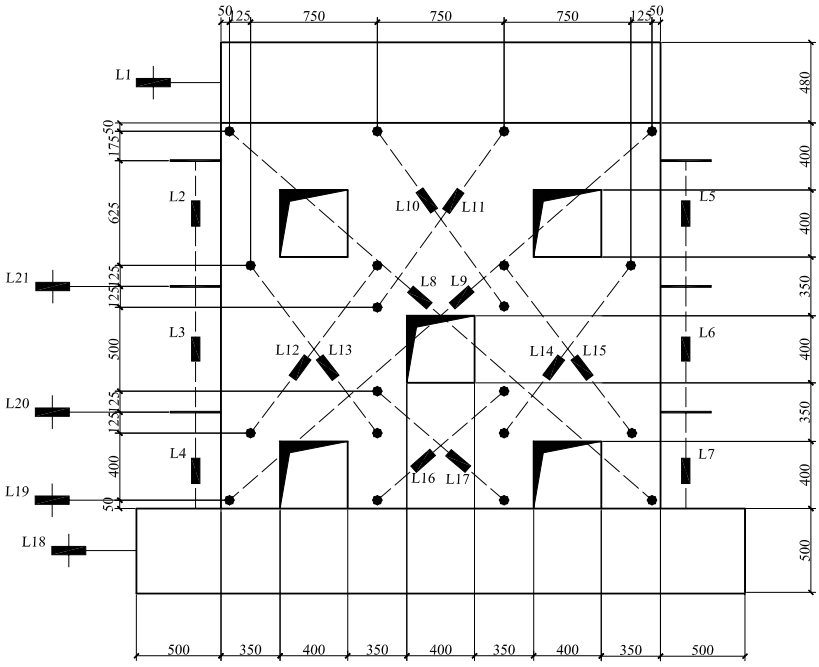

Figure 5.11: LVDT positions of Specimen W2

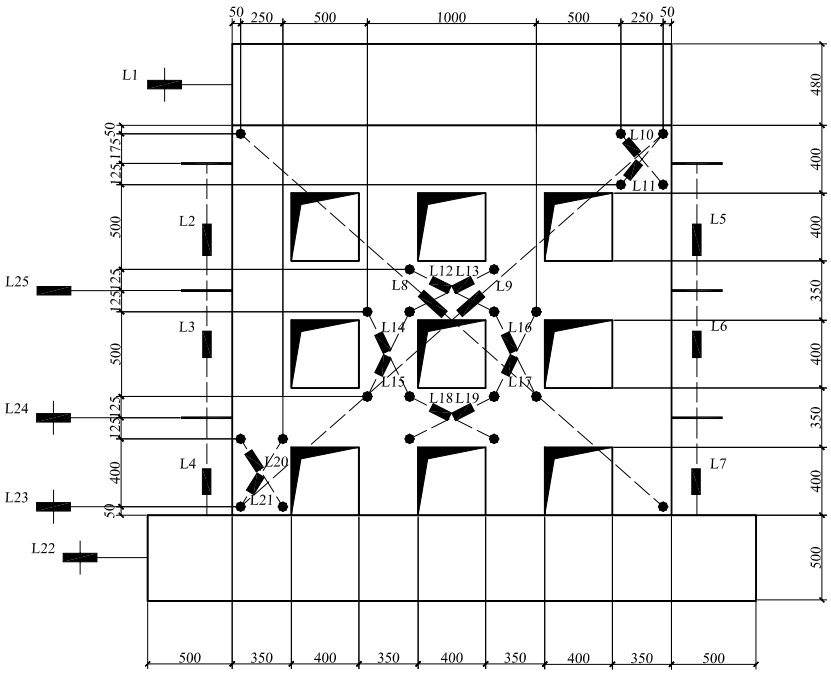

Figure 5.12: LVDT positions of Specimen W3

5.6.3 Strain gauges

The FLA type 5 mm-gauge length strain gauges, which has 10 m vinyl-insulated lead wires, were used to measure the local strains in the steel reinforcing bars. To obtain satisfactory experimental results with limited number of strain gauges, a few principles of strain gauge placement were observed. Firstly, for any particular position, one strain gauge was placed on one piece of the reinforcement net. Only for those critical regions, such as near the joint between the web and the foundation beam, two strain gauges were pasted at the same position on both reinforcement nets. Secondly, a few horizontal and vertical reinforcing bars, which were uniformly selected from the reinforcement nets, were applied with strain gauges at distributed locations to ensure that a continuous profile of strain development can be seen. Thirdly, for regions with concentrated stress flow, more strain gauges were used for better data recording.

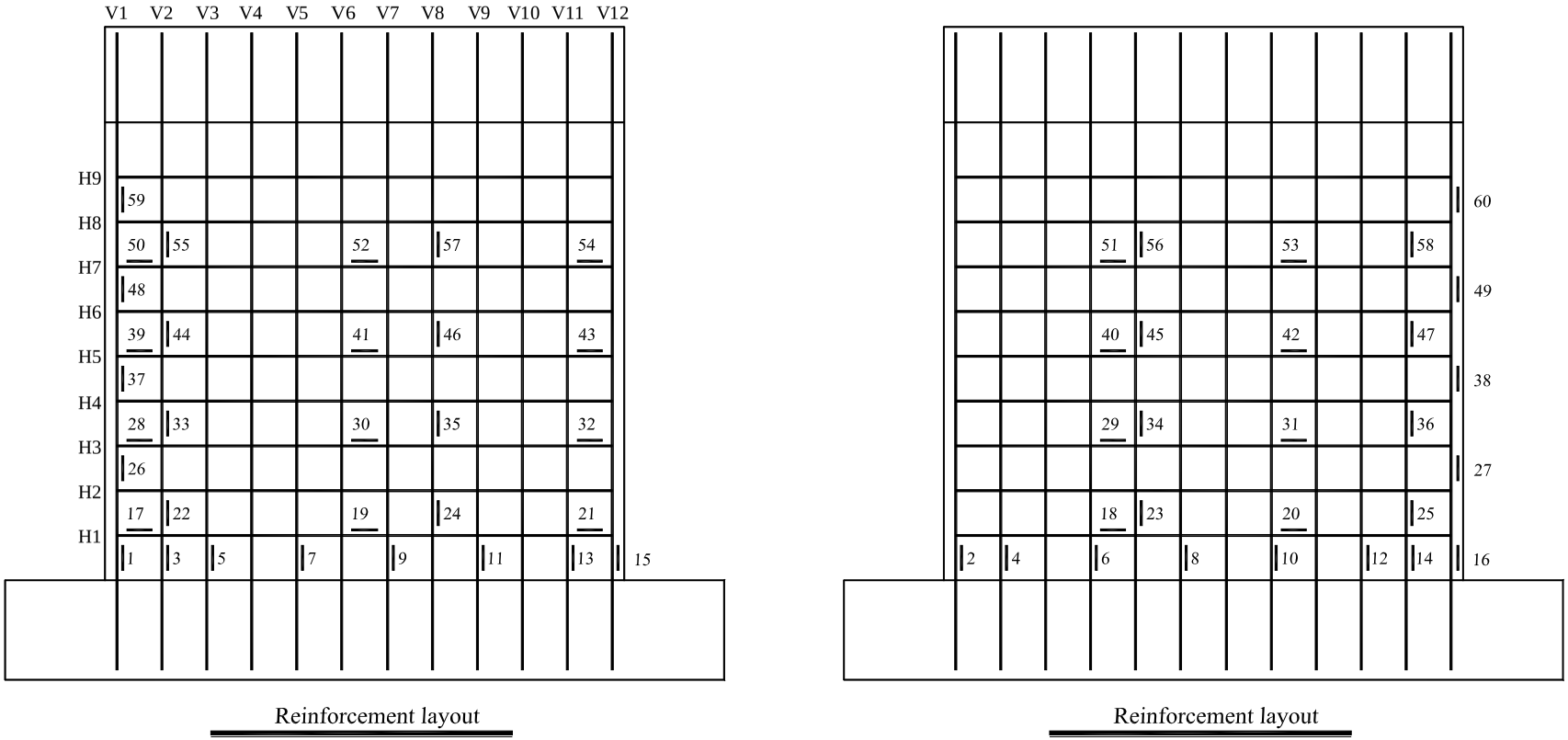

Figure 5.13: Strain gauge position of Specimen W1

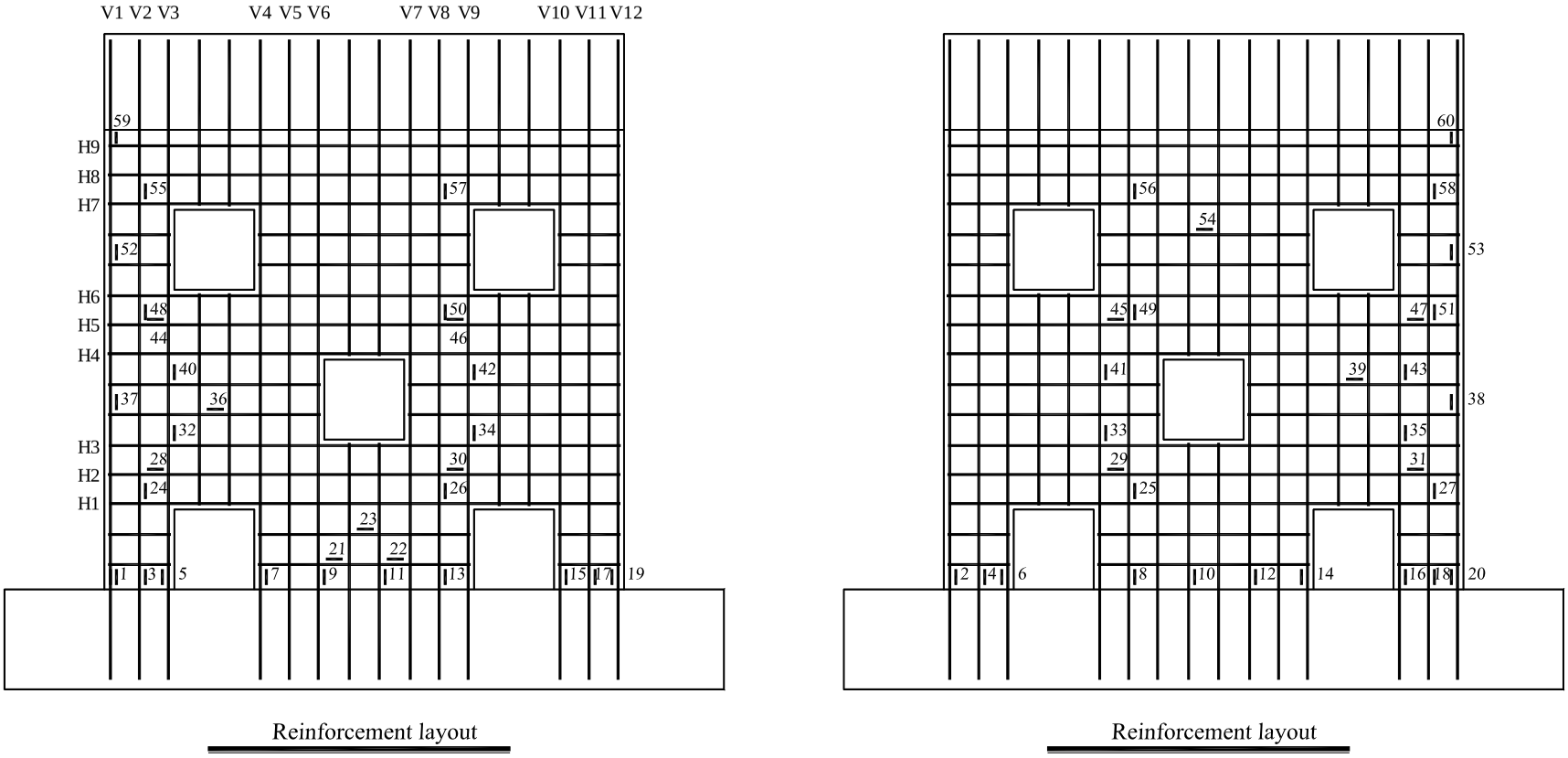

Figure 5.14: Strain gauge position of Specimen W2

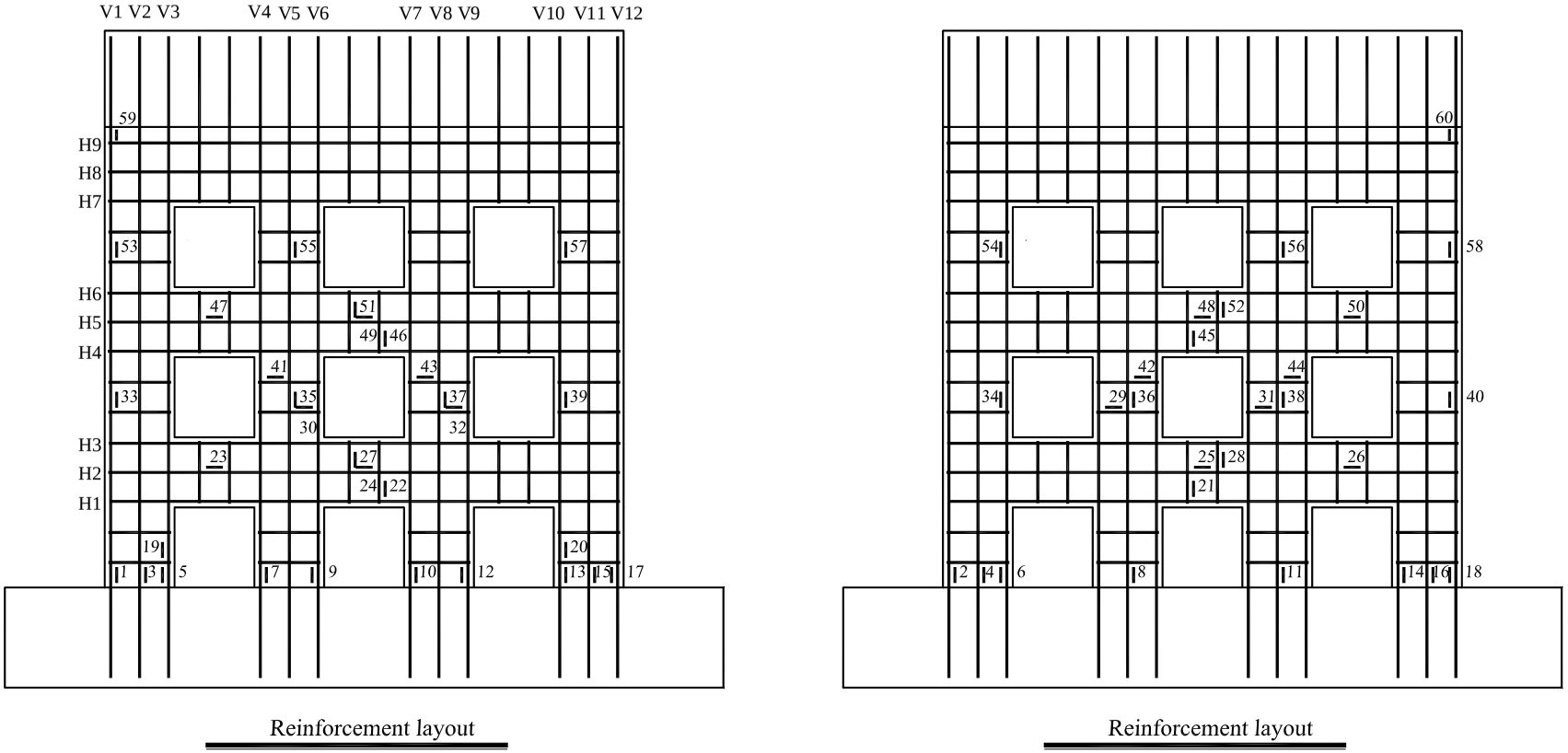

Figure 5.15: Strain gauge position of Specimen W3

With all these guilds, each wall specimen had with sixty strain gauges placed at desired locations. For strain gauges in each specimen, a numbering system was applied. The numbering started from bottom left of each specimen and moved to the top. **Figures 5.13** to **5.15** show strain gauges in each wall specimen with marked numbers. Each pair of horizontal and vertical main reinforcing bars is numbered for the ease of future data presentation.

5.7 Test Result of Specimen W1

Specimen W1 was a solid reinforced concrete wall and served as the control specimen in this experiment. Observations from the other two specimens, which had openings, could be compared to it frequently.

5.7.1 Loading history

Figure 5.16 shows the loading history experienced by Specimen W1. Every dot indicated the top displacement introduced to the specimen. The first three cycles were load-controlled cycles where maximum load of $\pm 0.25P_i$, $\pm 0.5P_i$ and $\pm 0.75P_i$ were applied. P_i was determined to be 398 kN according to the nominal flexural strength of the solid wall, assuming a linear distribution of the strain in any section. Then the yield displacement Δ_y could be estimated by the displacements obtained in the $\pm 0.75P_i$ cycle, which was 5.7 mm. Displacements for subsequent ductility levels were determined on this basis. The loading ended after first cycle of $DF = \pm 6$ when the capacity of the specimen was dropped significantly and the failure was clearly observed.

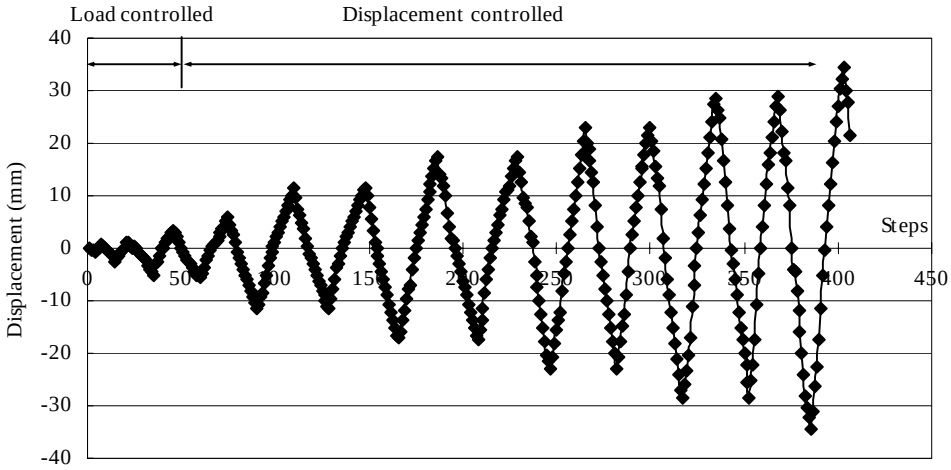

Figure 5.16: Loading history of Specimen W1

5.7.2 The overall response of Specimen W1

Figure 5.17 shows the lateral load versus top lateral displacement hysteretic response of Specimen W1 recorded during the experiment. In general, a very smooth and well-behaved hysteretic loop was observed. A definite pinching, which was induced by shear, was also observed. The resistance capacity of the specimen reached its maximum

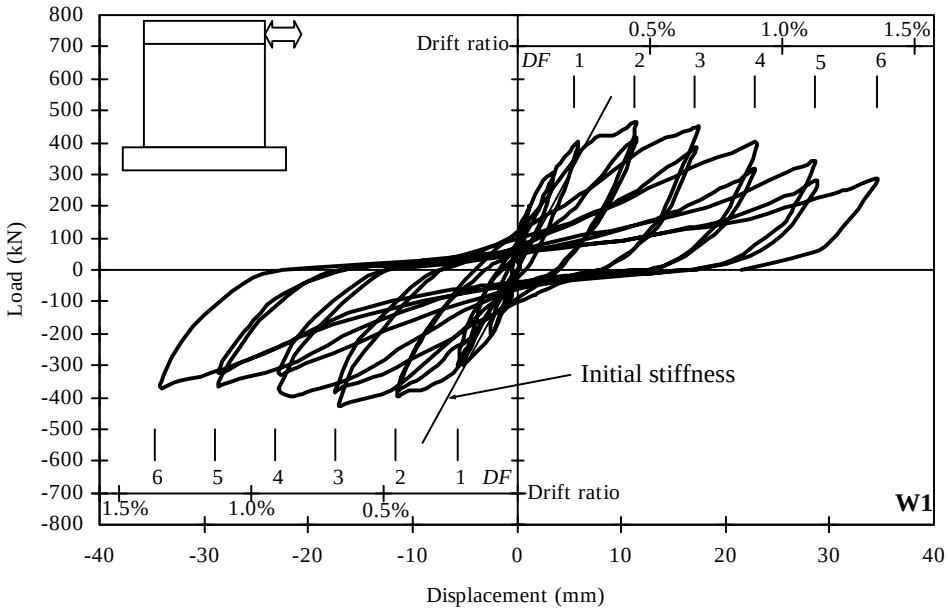

Figure 5.17: Lateral load-displacement response of Specimen W1

at $DF = \pm 3$ and started to decrease after that. Strength was reduced for the second cycle in each ductility factor. It also could be seen that the hysteretic loop was flattened as the ductility level increased, which meant that the stiffness of the wall degraded with the increase of cycles. Failure of this specimen occurred at $DF = \pm 6$. In the first cycle at this ductility level, the maximum strength developed was 40% smaller than the peak strength recorded, which indicated a clear failure.

The initial stiffness of Specimen W1 obtained from the test was 60.6 kN/mm. The trend of stiffness degradation was also measured and shown in **Figure 5.18**. The stiffness shown on the graph was the average secant stiffness of the negative and positive loading cycles. The secant stiffness of Specimen W1 decreased exponentially. At failure, the stiffness dropped to 15% of the initial amount.

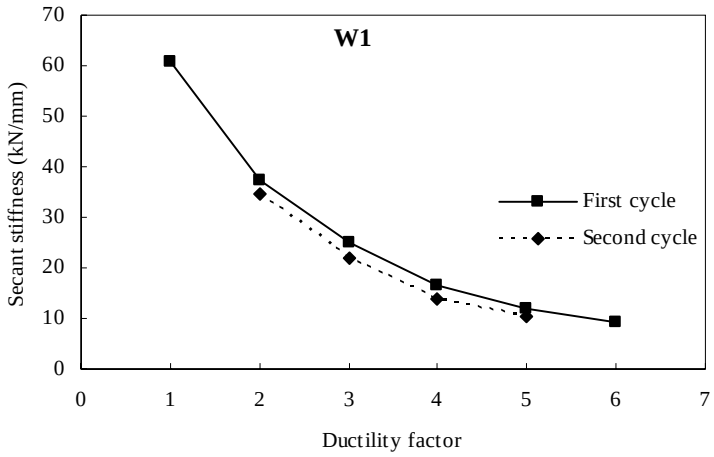

Figure 5.18: The stiffness degradation trace in Specimen W1

5.7.3 Behavior of Specimen W1

The following table presents the detailed behaviors of Specimen W1 at different loading stages.

Table 5.3: Observed behavior of Specimen W1

Loading history	Behaviour of W1
$0.25P_i$	The specimen was in the elastic range. No cracks were observed.
$0.50P_i$	The specimen was in the elastic range. No cracks were observed.
$0.75P_i$	Flexural cracks appeared on the bottom half of the web. These cracks normally extended from edges to 1/3 width of the web. It was noted that these cracks were spaced uniformly in the web. The end of these cracks started to develop into inclined diagonal cracks.
$DF = \pm 1$	No new major cracks formed at this stage, but existing cracks kept on extending into diagonal cracks. The crack width measured was 0.48 mm for the negative loading cycle and 0.5 mm for the positive loading cycle.
$DF = \pm 2$	Loud cracking sound was heard when new major cracks formed at the upper half of the web. These cracks had a shorter horizontal length and developed into diagonal cracks quickly. Existing cracks extended in both length and width. The crack width measure was 2.0 mm for the negative loading cycles and 2.5 mm for the positive loading cycles. Many minor cracks formed at the bottom of the web near the joint to the foundation beam.
$DF = \pm 3$	Compression cracks formed in the concrete at the right bottom edge. This was the stage for further crack development in width. The crack width measured was 5.0 mm for the negative loading cycles and 6.0 mm for the positive loading cycles. Crushing and spalling of concrete cover were observed. As a result, a vertical reinforcing bar at the right bottom edge of the web was buckled at the second cycle (**Figure 5.19 (a)**). A bottom slipping face, which was around 100 mm above the joint with the foundation beam, clearly formed (**Figure 5.19 (c)**).
$DF = \pm 4$	At this stage, all major cracks all formed. Deformation was concentrated along the sliding face at the bottom. The vertical reinforcing bar at the left bottom edge of the web was also buckled (**Figure 5.19 (b)**) and more bars were buckled at the right bottom edge. Large piece of concrete started to spall.
$DF = \pm 5$	A large piece of concrete separated at the right bottom edge of the web and the reinforcing bars there became free-standing (**Figure 5.19 (d)**). A total number of three pairs of reinforcing bars were buckled there. Minor cracking above the joint to the foundation cause severe spalling of the concrete cover there.
$DF = \pm 6$	After one cycle at this ductility level, the outermost pair of reinforcing bars was fractured at the right bottom edge of the web (**Figure 5.19 (e)**). Due to this, the strength of the specimen dropped to 60% of the maximum resistance capacity recorded. Thus the Specimen W1 was considered to be failed.

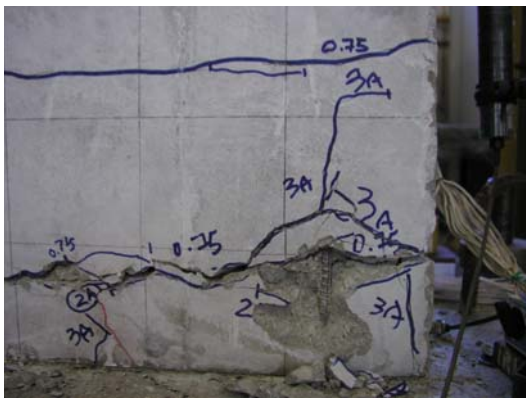

(a) Buckling of reinforcing bars at $DF = \pm 3$

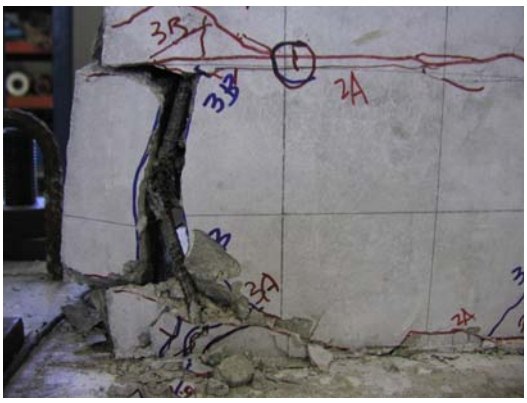

(b) Bucking of reinforcing bars at $DF = \pm 4$

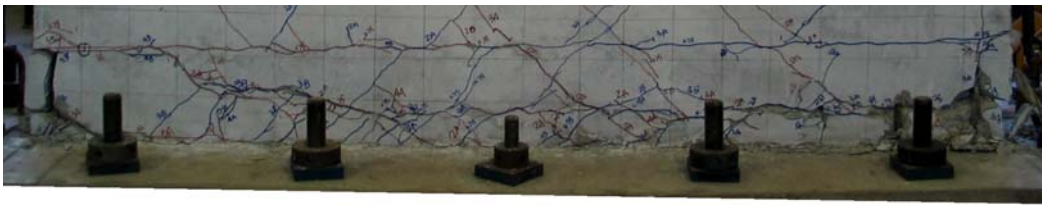

(c) Bottom sliding face formed at $DF = \pm 3$

ns o

ism

pec l

lines represented the cracks formed during the negative loading cycles, while the dash lines represented the cracks formed during the positive loading cycles. A full picture of crack development can be gathered under this series of drawings. All the major cracks

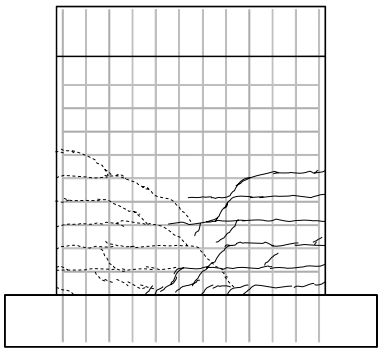

(a) at $0.75P_i$

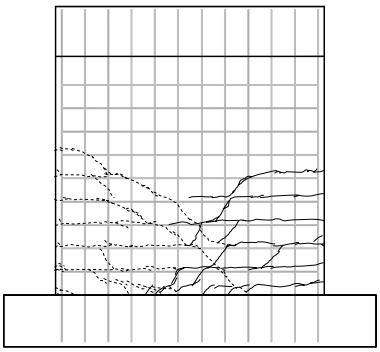

(b) at $DF = \pm 1$

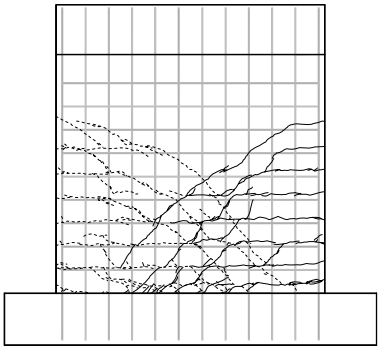

(c) at $DF = \pm 2$

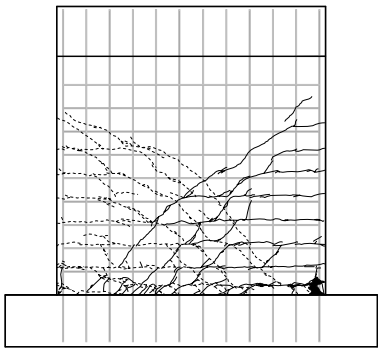

(d) at $DF = \pm 3$

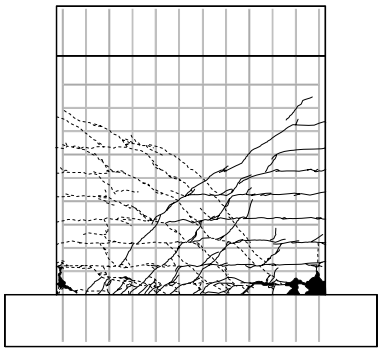

(e) at $DF = \pm 4$

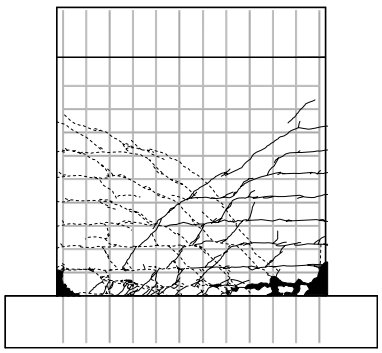

(f) at $DF = \pm 5$

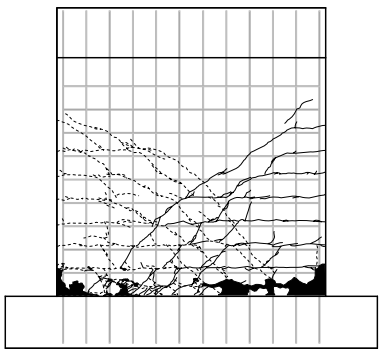

(g) at $DF = \pm 6$

Figure 5.20: Crack patterns of Specimen W1

all appeared first as horizontal flexural cracks and developed into inclined diagonal cracks. These cracks extended through the entire web of the wall and a clear diagonal strut mechanism can be seen. That meant that the imposed lateral loading was transferred to the foundation beam through the diagonal struts. Because of the boundary condition influence of the top beam, no cracks were observed in the upper $1/3$ of the web.

Cracks formed at the negative and positive loading cycles became connected under the action of reversal cyclic loading. Then the cracks kept on opening and caused crushing and spalling of the concrete especially at the bottom of the web. As a result, the vertical reinforcing bars were eventually buckled. A sliding face, which greatly affected the stiffness and strength of the wall, was observed as shown in the **Figure 5.19 (c)**. Finally at $DF = \pm 6$, the reinforcing bars fractured and the specimen failed.

5.7.5 Deformations measured by LVDTs

All together 13 LVDTs were installed in Specimen W1 to measure deformations at desired regions during the experiment. The location of each LVDT was shown as in **Figure 5.10**. The purpose of these LVDTs can be divided into four categories: for lateral drift, for flexural deformation, for shear deformation, and for sliding displacement along the joint between the web and the foundation beam of the wall.

The flexure deformation was measured by three groups of the LVDTs, including L2 & L5, L3 & L6, and L4 & L7. Most part of the flexure deformation was concentrated at the bottom, which was taken by L4 and L7. Three graphs in **Figure 5.21** show the variation of the flexural deformations at different sections along the web measured at the both sides of the wall. It was common to observe significantly differences in the deformations between negative and positive loading cycles for every LVDT. This was understandable as flexural deformation was much more pronounced at the tensile zone than that in the compressive zone.

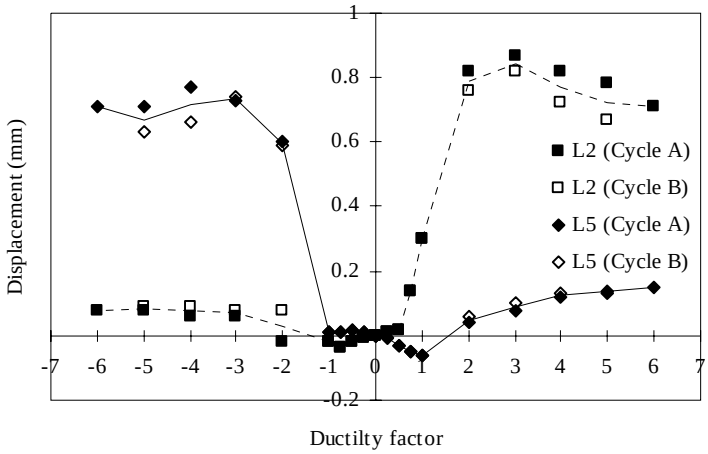

(a) By L2 and L5

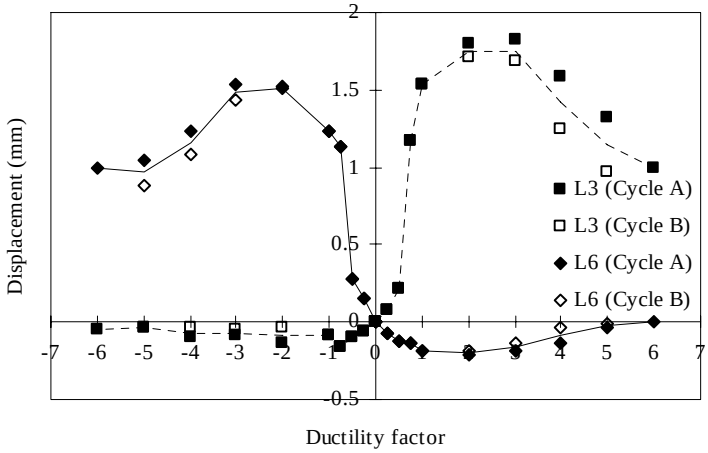

(b) By L3 and L6

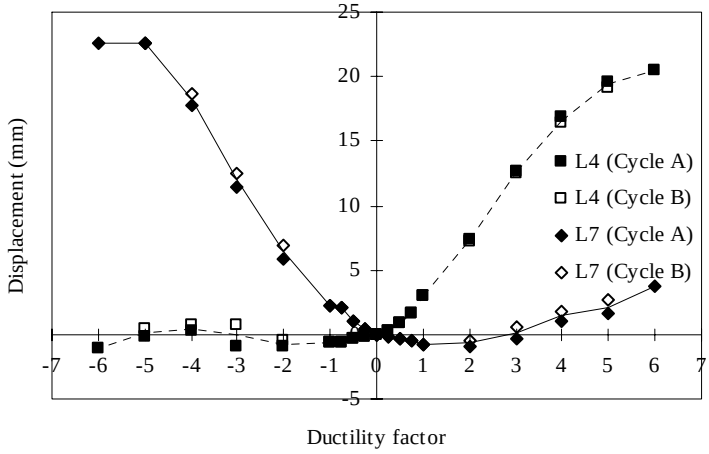

(c) By L4 and L7

Figure 5.21: Flexural deformations of Specimen W1 measured by LVDTs

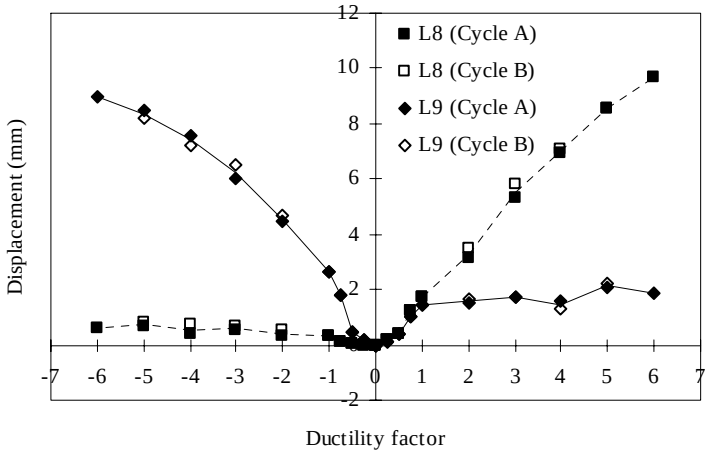

Figure 5.22: Shear deformation of Specimen W1 measured by L8 and L9

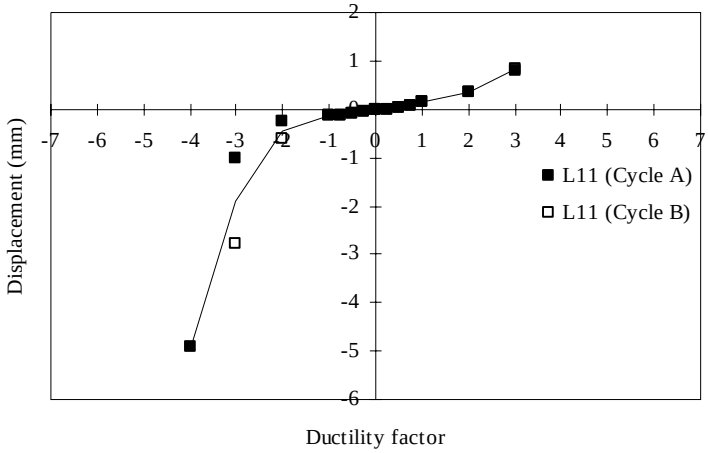

Figure 5.23: Sliding shear displacement of Specimen W1 measured by L11

Shear deformation of the web panel was measure by the L8 and L9. **Figure 5.22** shows the deformation variation with each ductility level. It can be seen that the panel shear deformation was low for the solid wall. This may be due to the large shear stiffness of the solid wall without any opening and the sliding occurred along the bottom crack. The deformations were also different between two loading directions.

Figure 5.23 shows the sliding displacement along the joint between the foundation beam and the web. The LVDT installed for this measurement became ineffective after the first cycle of $DF = \pm 4$ as the concrete at its nearby region was crushed and spalled away. However, the data recorded at $DF = \pm 4$ was already quite significant as it shared about

20% of the total lateral drift introduced at the top.

As can be seen in the above figures, the imposed top lateral drift caused flexural and shear deformations on the specimen. The percentage of flexural and shear deformation in the total lateral drift respectively can be determined from the readings of the installed LVDT on the specimen. The detailed method of obtaining flexural component and shear component in the total drift is given in Appendix B. **Figure 5.24** shows the calculated displacement decomposition results for every loading cycle in both the negative and positive directions. For the negative loading cycles, the lateral drift caused by flexure decreased from 70% initially to 40% at the failure. The shear component was at a constant level of 20% out of the total drift. For the positive loading cycles, the flexure component had a small variation around 60% of the total for all the cycles. The shear component was similar as that in the negative loading cycles and around 20% throughout. For both of the two loading directions, the sum of the flexural and shear component was smaller than the total lateral drift for almost all the cycles. The un-accounted for portion in each loading cycle should be from the sliding shear deformation that has been observed and measured for Specimen W1. For example at $DF = -4$, the measure deformation along the bottom sliding face was 20% of the total imposed lateral drift. This reading was well related to the displacement decomposition result which shows that the unanswered portion at $DF = -4$ is 17%.

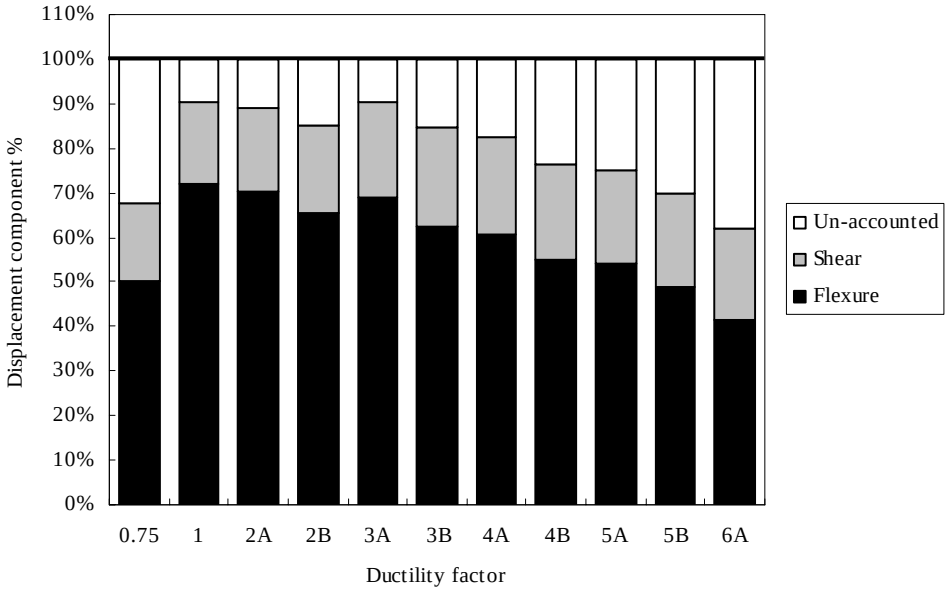

(a) For the negative loading cycles

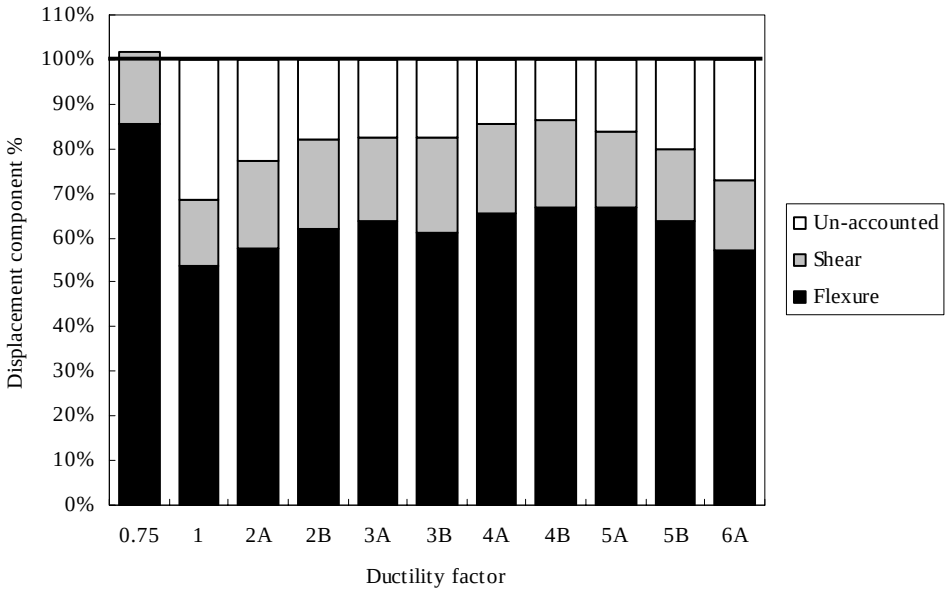

(b) For the positive loading cycles

Figure 5.24: Displacement decomposition results for Specimen W1

5.7.6 Strains of the reinforcing bars

Figure 5.25 shows six vertical reinforcing bars at selected locations along the horizontal section of the web. Each bar had five strain gauges attached from the bottom to the top. The general observations of the bar strains are summarized as follows. To begin with, every bar experienced greater strain at the bottom and gradually lessened when moving up at the same ductility level. Secondly, bars at the edges of the web were more strained compared with the bars at the middle along the same vertical position. Lastly, compressive strains were recorded when the bars under compression. However these compressive strains were smaller than the tensile strains. The behavior of each individual reinforcing bar will be illustrated below.

The Bar V1 had five strain gauges (#1, #26, #37, #48, #59) distributed on it from the bottom to the top in the web. This bar was under compression for the negative loading cycle and under tension for the positive loading cycle. As shown in **Figure 5.25 (a)**, the bottom of this bar (#1) yielded in compression at $DF = -2$ while yielded in tension at $DF = +1$. When moving up, the compressive strain was reduced and even became tensile (#48, #59). The tensile strain in the positive loading cycles was also reduced, and yielding was not observed for #59.

For Bar V2 with Gauges #3, #22, #33, #44, and #55, compressive strains were also recorded (#3 and #22) for the negative loading cycles but yielded at a later stage ($DF = -3$). From the bottom up, the compressive strains decreased and turned to be tensile at the top (#55). In the positive loading cycles, all the strain gauges, except #55, started yielding from $DF = +1$.

Bars V5 and V8 were located at the central region of the web. And tensile strains were mostly recorded during the testing of the specimen. Both of them reached yielding only after $DF = \pm 2$.

Bar V11 with Gauges #14, #25, #36, #47, and #58 recorded compressive strains in the positive loading cycles and tensile strains in the negative loading cycles. The bottom of V11 (#14) yielded in compression at $DF = -3$. Immediately after yielding, the bar strain

drastically changed to a very large tensile strain, which indicated the bar had been buckled at the bottom. For tension in the negative loading cycles, yielding of the bar occurred after $DF = +1$.

Bar V12 had Gauges #16, #27, #38, #49, and #60. This bar was under compression for the positive loading cycles and under tension for the negative loading cycles. Yielding in compression was earlier at $DF = -2$ as compared to V11. After $DF = -3$, the bar strain also jumped to tensile and was buckled. Tensile yielding for the negative loading cycles was again at $DF = +1$.

The two graphs in **Figure 5.26** shows the vertical strain profiles of Bars V1 and V12 at $DF = \pm 2$. They clearly presented the strain variation in the vertical direction of the two critical reinforcing bars at the edges of the web. **Figure 5.27** is the strain profile along the bottom section of the web at $DF = \pm 3$. From this drawing, we can roughly see the neutral axis position in the web of the wall at the bottom section.

Figure 5.28 give the strains of four horizontal reinforcing bars (H1, H3, H5, and H7) distributed along the vertical section of the web. Again, each bars had five strain gauges attached to it from the left to the right. Generally, these bars only developed tensile strains to provide a confinement effect on the web. The tensile strains were all well below the yielding. It was found that the strains of H3 and H5 were larger than H1 and H7. This could be the reason why the top beam and foundation beam had some confinement effect on the vertical reinforcing bars nearby. Further plots on the horizontal strain profiles of the four selected bars are shown in **Figure 5.29**. These profiles were horizontal bar strain conditions at $DF = \pm 2$. It can be seen that Bar H1 and H3 were less strained at the two ends and more strained at the middle for both of the loading cycles. For Bar H5, the strains recorded by the five strain gauges on it were relatively constant besides one unusual reading. Bar H7 was more strained at the two ends and had almost no strain in the middle portion.

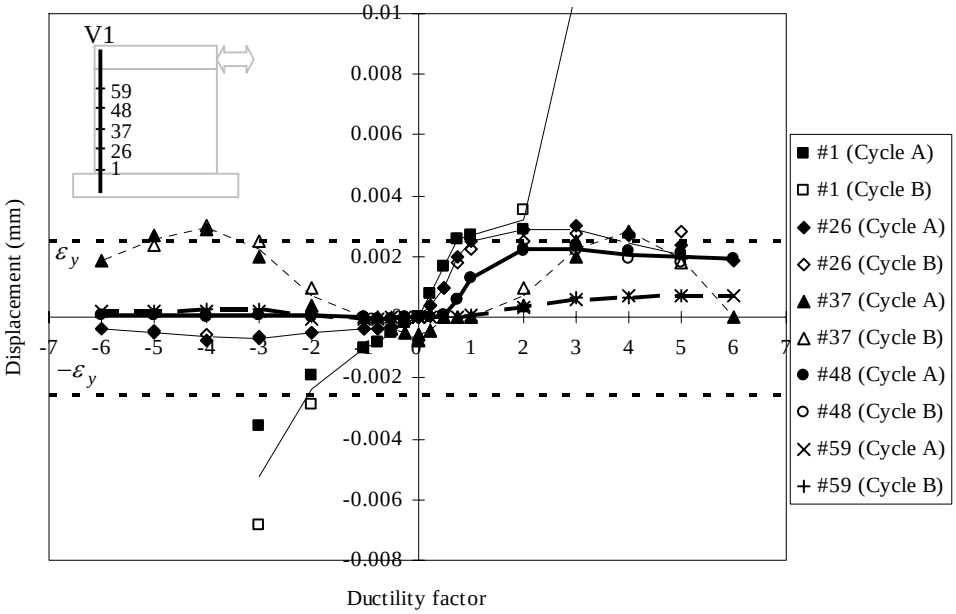

Figure 5.25 (a) Strain distribution of vertical Bar V1

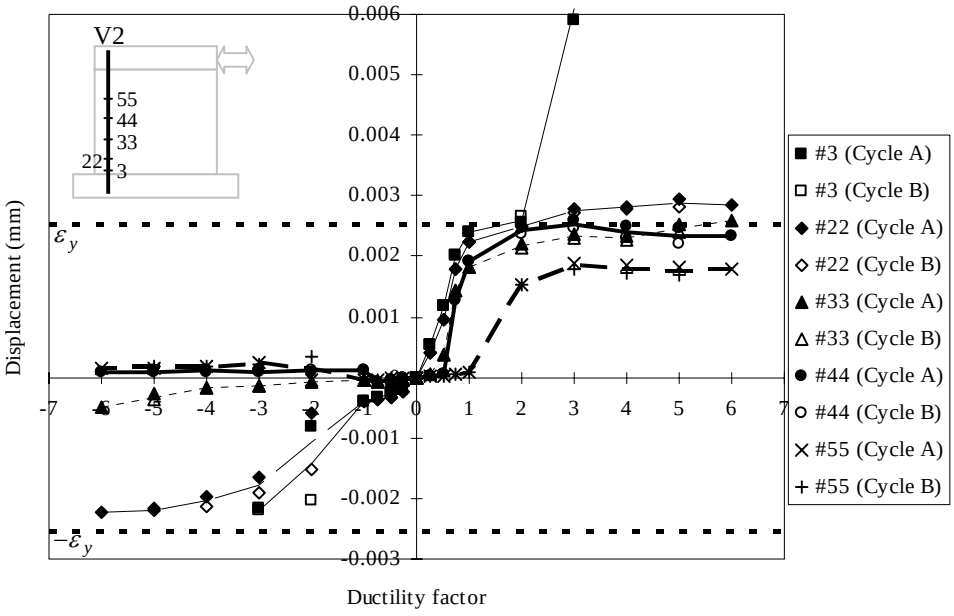

Figure 5.25 (b) Strain distribution of vertical Bar V2

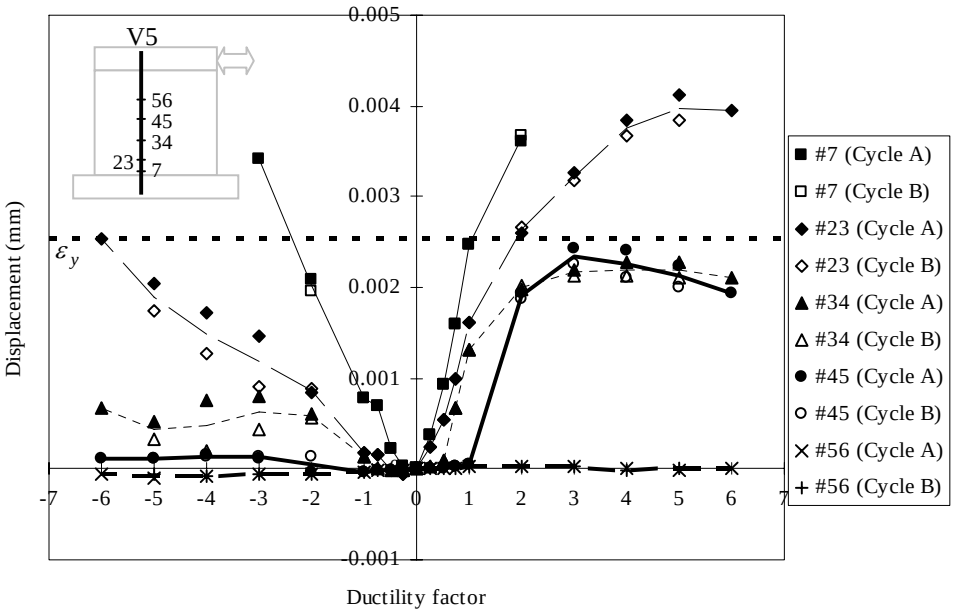

Figure 5.25 (c) Strain distribution of vertical Bar V5

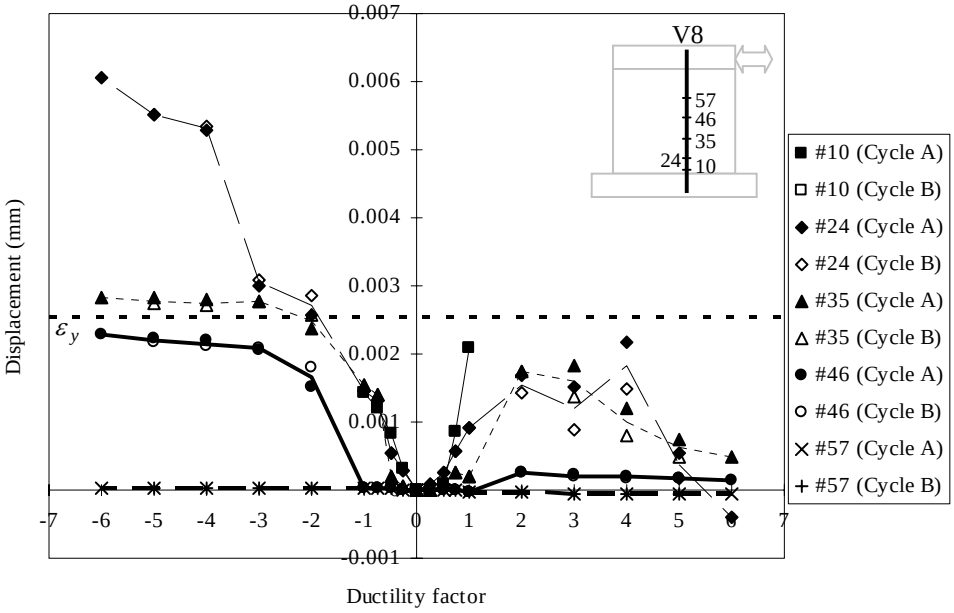

Figure 5.25 (d) Strain distribution of vertical Bar V8

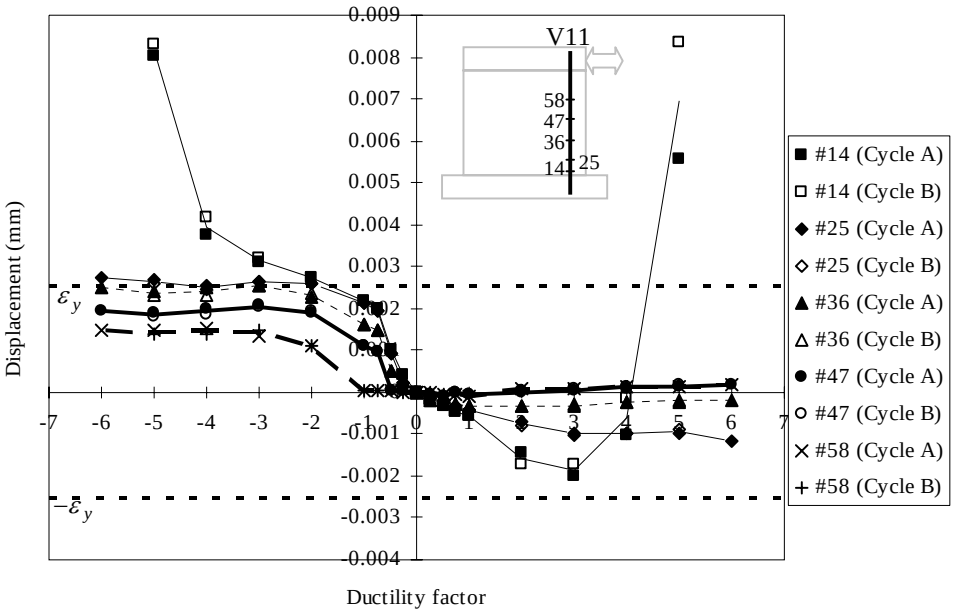

Figure 5.25 (e) Strain distribution of vertical Bar V11

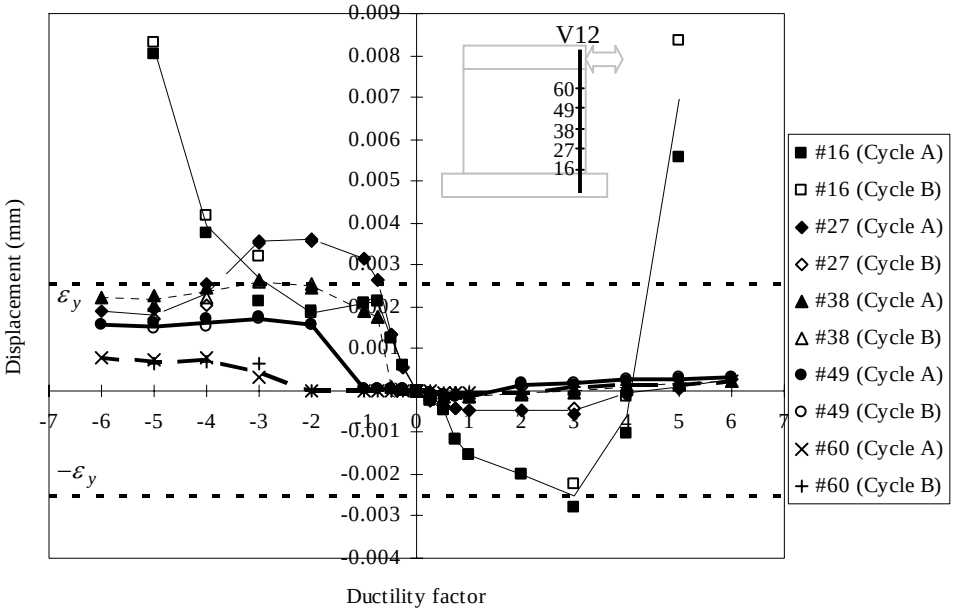

Figure 5.25 (f) Strain distribution of vertical Bar V12

Figure 5.25: Strain distributions of some vertical reinforcing bars

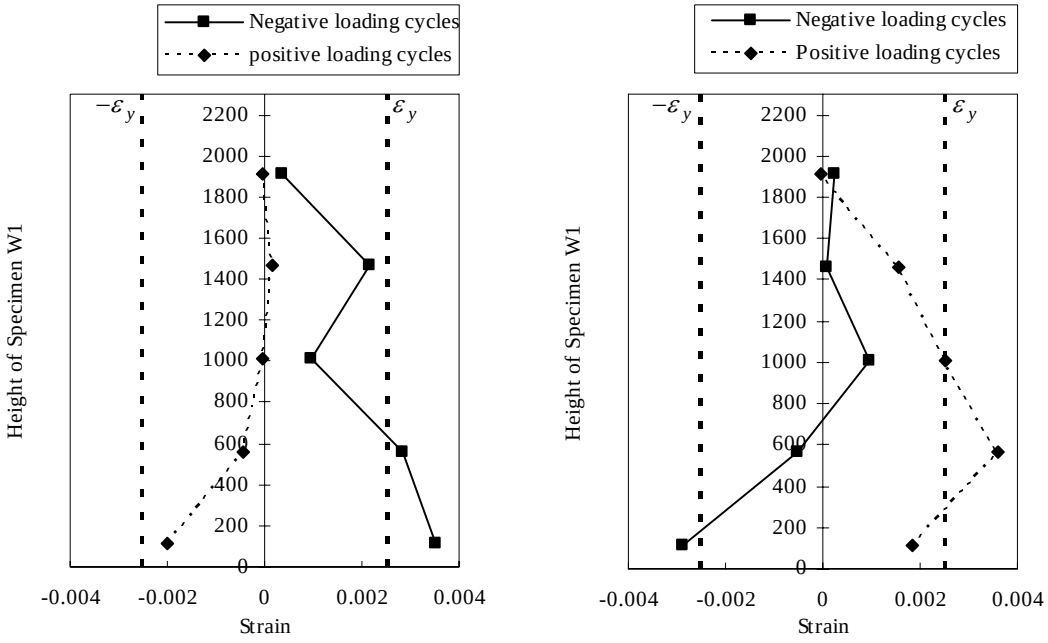

(a) Bar V1 at $DF = \pm 2$ (b) Bar V12 at $DF = \pm 2$

Figure 5.26: Strain profiles of Bar V1 and V12 at $DF = \pm 2$

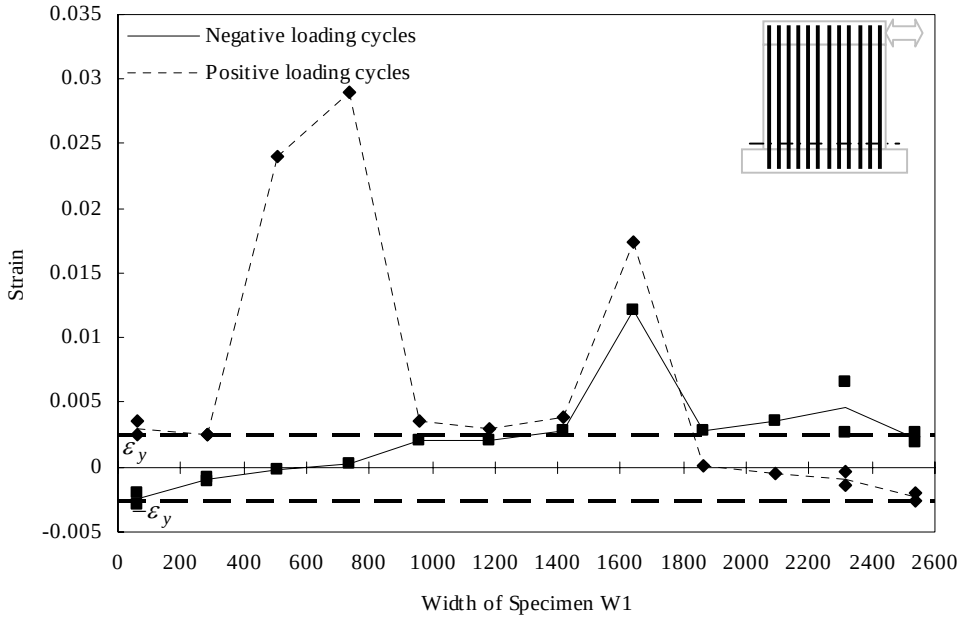

Figure 5.27: Strain profile of reinforcing bars along the bottom of the web

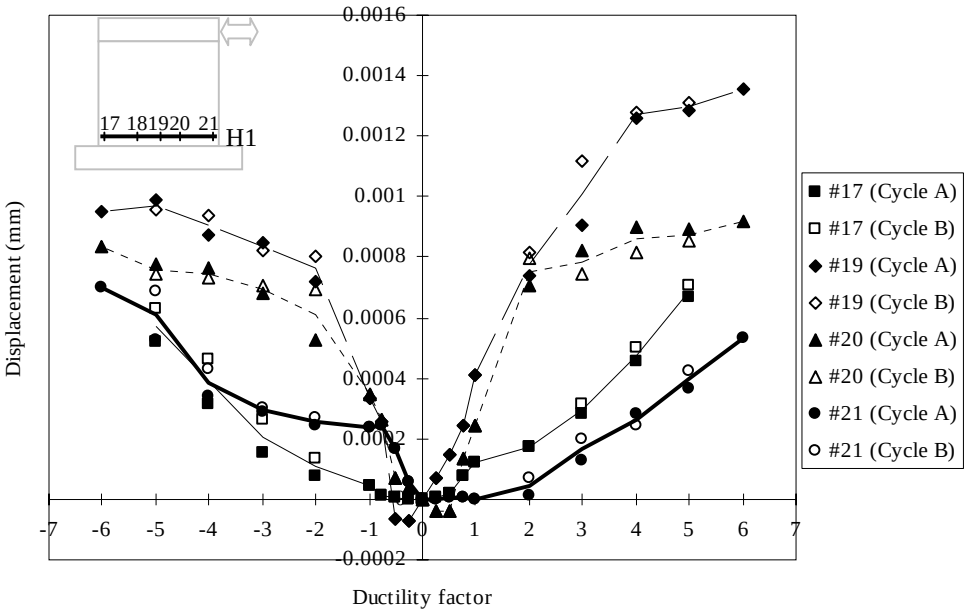

Figure 5.28 (a) Strain distribution of horizontal Bar H1

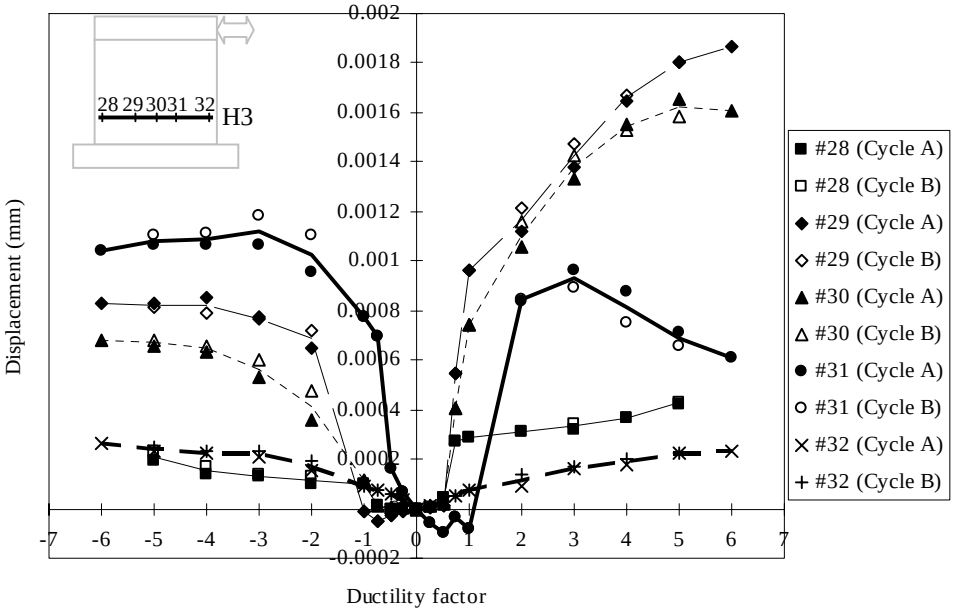

Figure 5.28 (b) Strain distribution of horizontal Bar H3

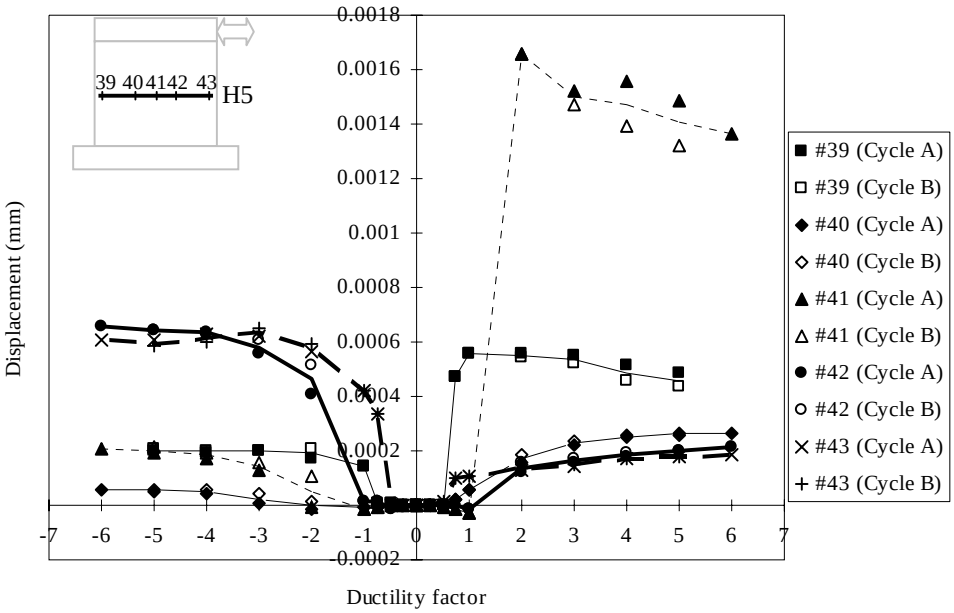

Figure 5.28 (c) Strain distribution of horizontal Bar H5

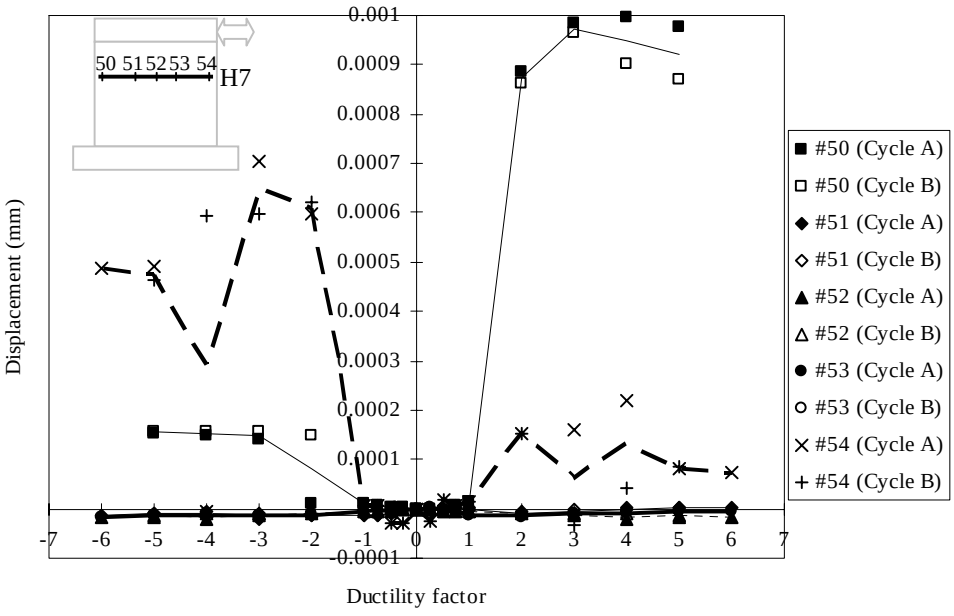

Figure 5.28 (d) Strain distribution of horizontal Bar H7

Figure 5.28: Strain distributions of some horizontal reinforcing bars

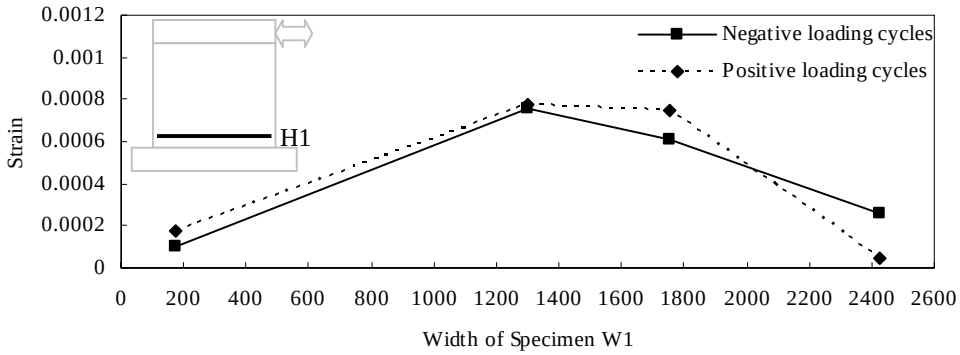

(a) Bar H1

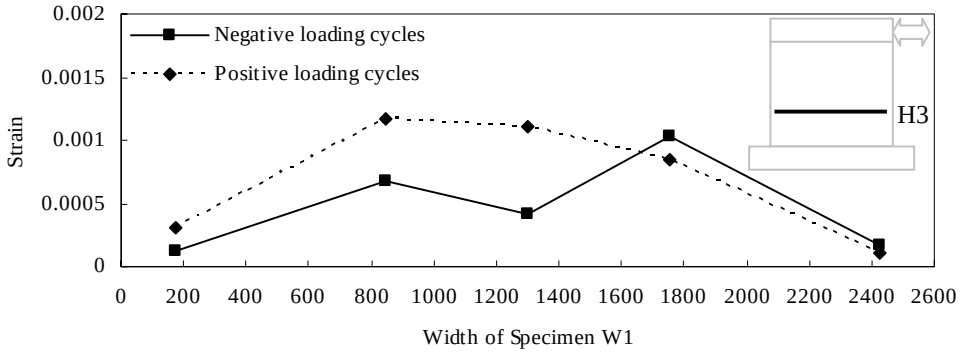

(b) Bar H3

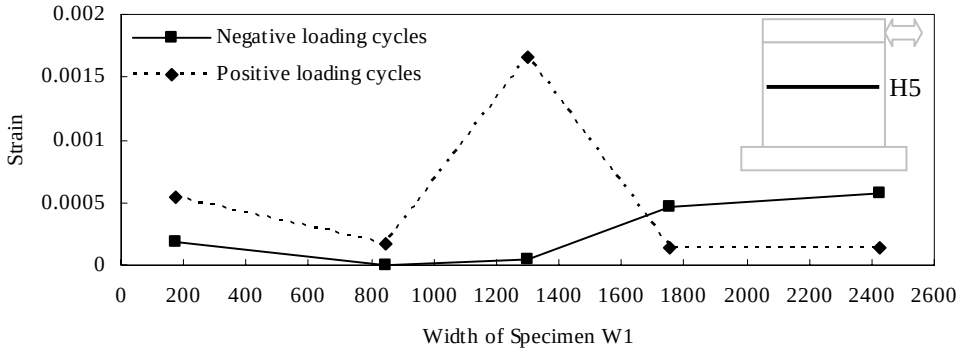

(c) Bar H5

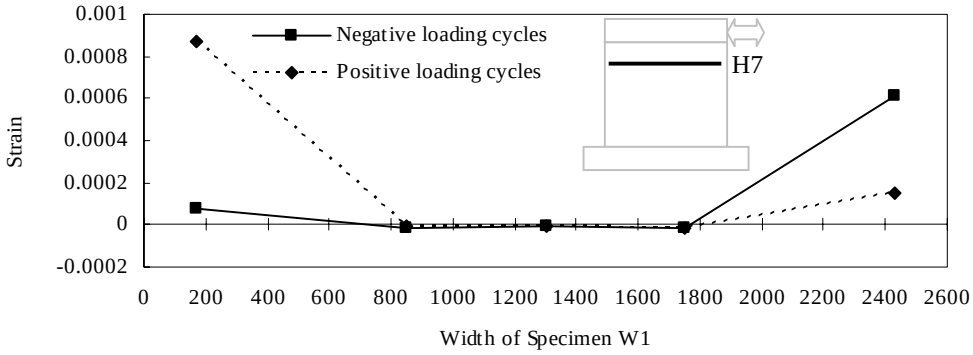

(d) Bar H7

Figure 5.29: Strain profiles along some horizontal reinforcing bars

5.8 Test Result of Specimen W2

Specimen W2 was a wall with five regularly placed openings as shown in **Figure 5.3**. This wall specimen was a modified design from the shear wall model proposed by Marti [M2]. Instead of direct strut mechanism, panel action was seen in this wall.

5.8.1 Loading history

Figure 5.30 shows the loading history experienced by the Specimen W2. P_i for Specimen W2 was determined at 377 kN according to a preliminary finite element analysis using the program UC-WIN/MESH & UC-WIN/WCOMD with the nominal material strength to establish the three initial load-controlled cycles. In order to have a direct comparison, the yield displacement Δ_y followed the control Specimen W1, which was 5.7 mm. The subsequent ductility levels for displacement–controlled cycles were defined on this basis. The loading ended at $DF = \pm 5$ when the capacity of the specimen was dropped significantly and the failure was clearly observed.

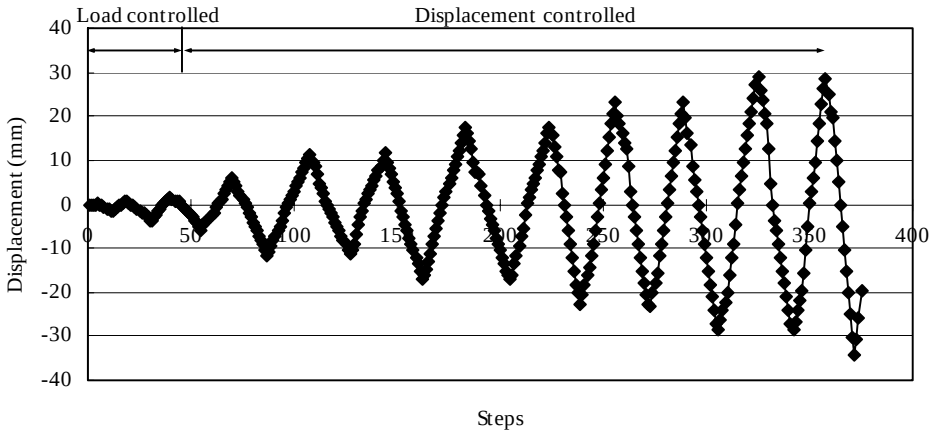

Figure 5.30: Loading history of Specimen W2

5.8.2 The overall response of Specimen W2

Figure 5.31 shows the lateral load versus top lateral displacement hysteretic response of Specimen W2 recorded during the experiment. In general, a very smooth and well-behaved hysteretic loop was again recorded. The definite pinching, which was induced by shear, was also observed in this specimen. The resistance capacity of the specimen reached its maximum at $DF = \pm 2$ and started to decrease after that. It was noticed that the strength difference between the negative and positive loading cycles was quite obvious at $DF = \pm 2$. This situation improved for subsequent ductility factors. Other common behaviors similar to Specimen W1 in the hysteretic loop were also observed. Strength was lowered for the second cycle in each ductility factor. It also could be seen that the hysteretic loop was flattened as the ductility level increased, which meant that the stiffness degraded with the increase of cycles. Although the testing of the specimen stopped after one cycle for the negative loading direction at $DF = -6$, the Specimen W2 had already failed at $DF = \pm 5$, when the maximum strength developed was 40% smaller than the peak strength recorded, which indicated a clear failure.

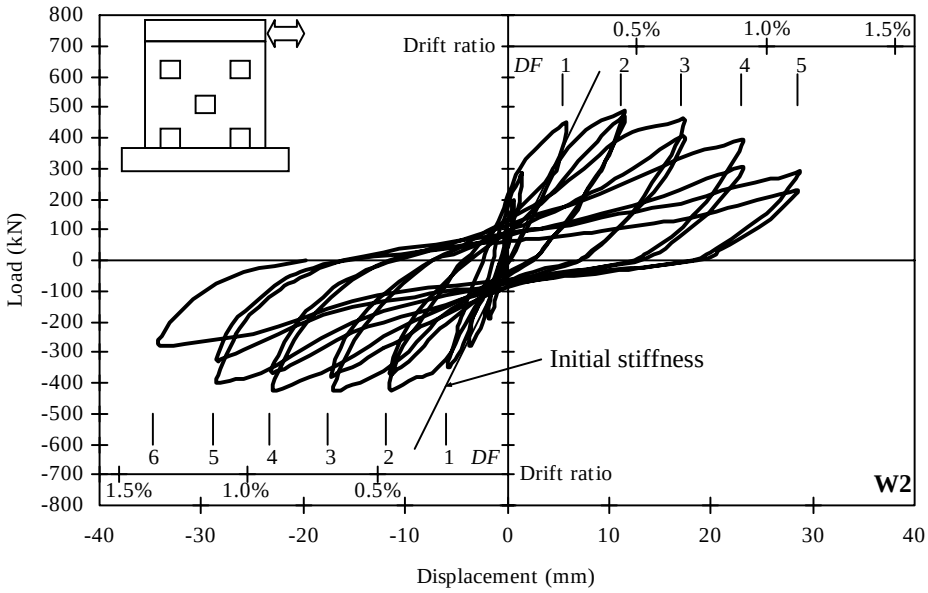

Figure 5.31: Lateral load-displacement response of Specimen W2

The initial stiffness of Specimen W2 obtained from the test was 68.3 kN/mm, which was slightly larger than that of Specimen W1. It could be concluded that five openings configured on the web as Specimen W2 would not have any effect on the initial stiffness. The trend of secant stiffness degradation was also traced and shown in **Figure 5.32**. The secant stiffness of Specimen W2 also decreased exponentially and the rate of the degradation was similar when compared to that of Specimen W1. At failure, the stiffness dropped to 13.9% of the initial one.

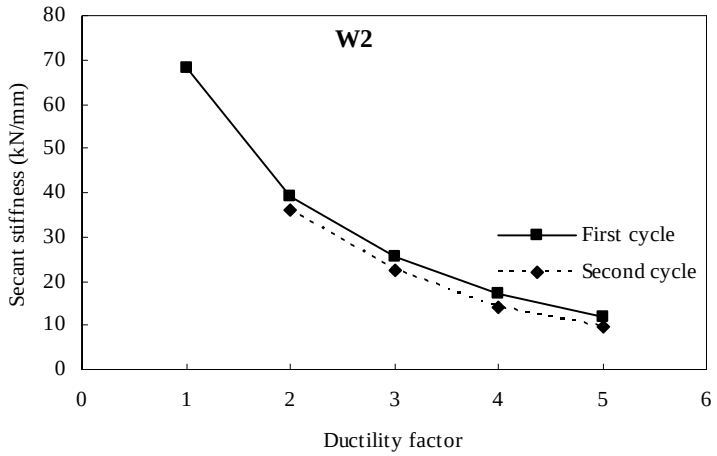

Figure 5.32: The stiffness degradation trace in Specimen W2

5.8.3 Behavior of Specimen W2

The following table presents the detailed behaviors of Specimen W2 at different loading stages.

Table 5.4: Observed behavior of Specimen W2

Loading history	Behaviour of W2
$0.25P_i$	The Specimen was in the elastic range. No cracks were observed.
$0.50P_i$	The Specimen was in the elastic range. No cracks were observed.
$0.75P_i$	Only a few cracks were noted in the two short columns at the bottom edges of the web. These cracks were all horizontal cracks and induced by flexure of the lateral loading.
$DF = \pm 1$	Cracking increased suddenly, especially during the positive loading cycle. Flexural cracks appeared at a closer spacing with a shorter developed length as compared to Specimen W1. They then extended to be inclined diagonal cracks. Diagonal cracks passed through the openings without changing their angle of inclination. The crack width measured was 0.4 mm for the negative loading cycle and 0.5 mm for the positive loading cycle.
$DF = \pm 2$	Cracking displayed a balanced display under both negative and positive loading cycles. Major diagonal cracks were fully developed. The crack width measured was 1.5 mm for the negative loading cycles and 3.0 mm for the positive loading cycles. An obvious kink on the hysteretic loop signed yielding of major reinforcement during the first negative loading cycle.
$DF = \pm 3$	Compression cracks formed in the two short columns at the bottom. This was the stage for crack widening. Cracking in the bottom panel zone between three openings was extensive with many minor cracks appeared (**Figure 5.33 (a)**). The crack width measured was 6.5 mm for the negative loading cycles and 8.0 mm for the positive loading cycles. Crushing and spalling of concrete cover were observed. As a result, a vertical reinforcing bar in the column at the right bottom edge showed signs of buckling during the second cycle (**Figure 5.33 (b)**).
$DF = \pm 4$	Deformation was concentrated on the two short columns at the bottom edges of the web. Crashing and spalling of the concrete was very severe there. For the right column, three pairs of vertical reinforcing bars were all exposed with obvious buckling (**Figure 5.33 (d)**). For the left column, the outermost pair of vertical reinforcing bars and one stirrup were exposed (**Figure 5.33 (c)**).
$DF = \pm 5$	The two short columns at the bottom edges of the web were totally damaged with bars being buckled and even fractured (**Figure 5.33 (e)**). The buckling of the reinforcing bars extended to the middle panel zone at the bottom (**Figure 5.33 (f)**). Two pairs of the bars were buckled at the edges of the panel. The peak strength of these cycles dropped to 60% of the maximum strength recorded and Specimen W2 was considered to be failed.

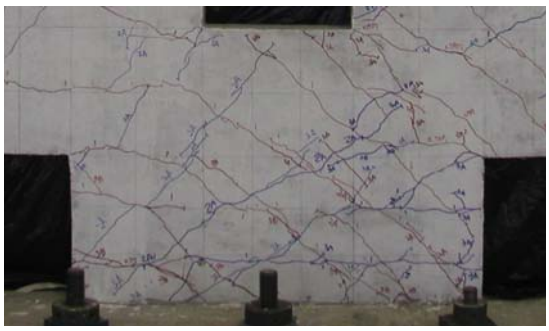

(a) Cracking of the bottom panel zone at $DF = \pm 3$

(b) Cracking of bottom right column at $DF = \pm 3$

(c) Buckling of reinforcing bars at left bottom column of at $DF = \pm 4$

(d) Buckling of reinforcing bars at right bottom column at $DF = \pm 4$

(e) Damage of bottom right column at $DF = \pm 5$

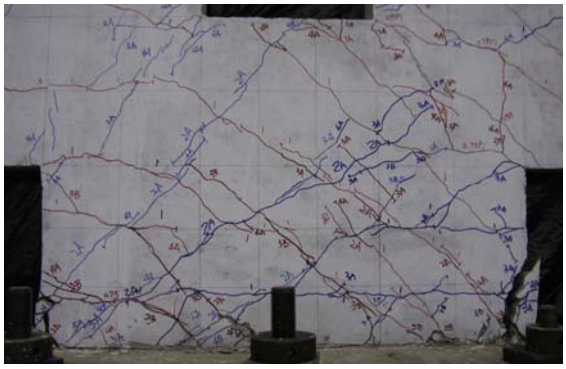

(f) Buckling of reinforcing bars at the bottom panel zone at $DF = \pm 5$

Figure 5.33: Detailed illustrations of Specimen W2 by photography

5.8.4 Crack pattern and failure mechanism

Figure 5.34 shows the crack pattern of Specimen W2 at every ductility level. The full lines represented the cracks formed during the negative loading cycles, while the dash lines represented the cracks formed during the positive loading cycles. A full picture of crack development is illustrated through this series of drawings. All the major cracks all appeared first as horizontal flexural cracks and developed into inclined diagonal cracks. However, compared with Specimen W1, the flexural cracks in this specimen had a shorter length. This could be the effect of the openings. The existence of openings also required mobilizing more concrete sections and so cracks were observed over the entire height of the wall web. But the opening did not affect the angle of inclination of the diagonal cracks. The lateral loading was still transferred to the fixed base through the diagonal strut mechanism in the panel.

At higher ductility levels, cracking growth was concentrated on the two short columns at the bottom edges of the web, which caused severe crushing and spalling of the concrete as shown in **Figure 5.33 (e)**. As a result, the vertical reinforcing bars there were buckled. Finally at $DF = \pm 5$, reinforcing bars were fractured and the specimen failed.

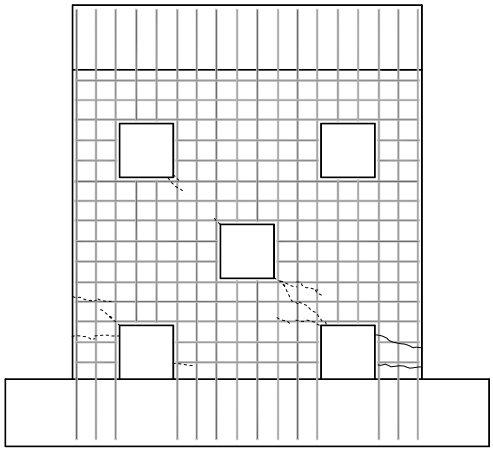

(a) at $0.75P_i$

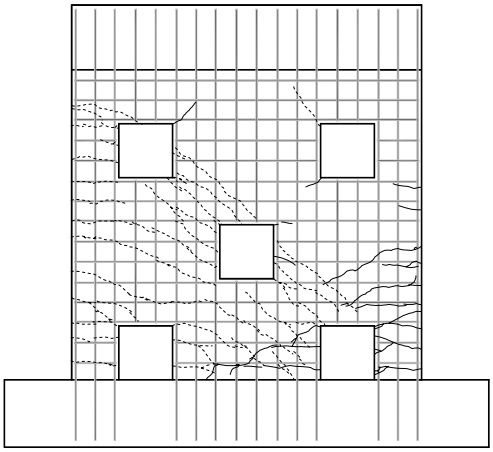

(b) at $DF = \pm 1$

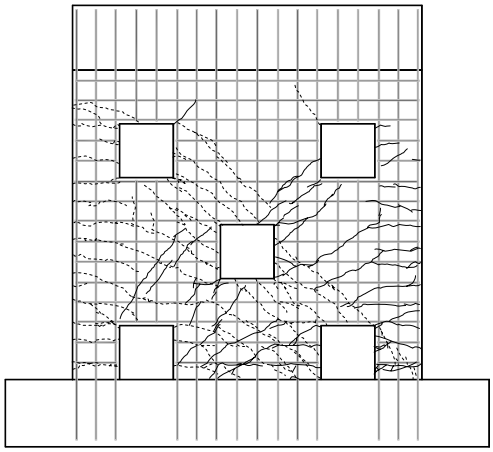

(c) at $DF = \pm 2$

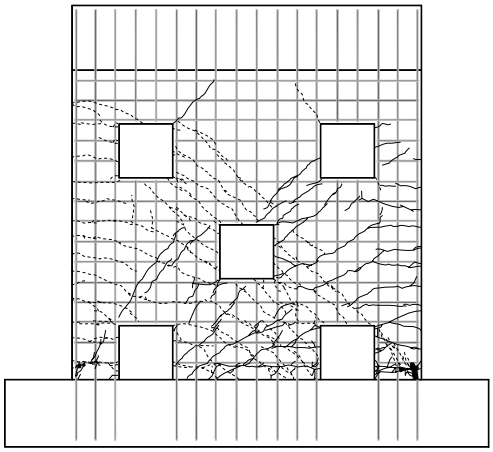

(d) at $DF = \pm 3$

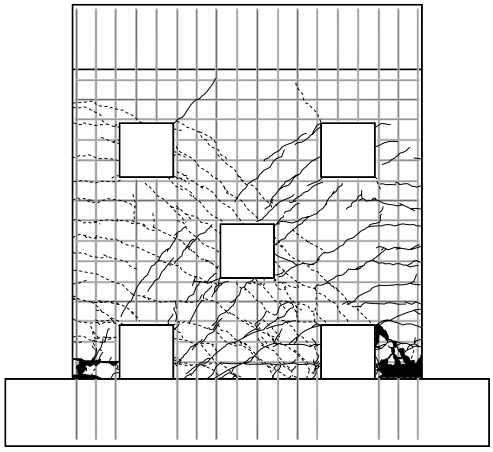

(e) at $DF = \pm 4$

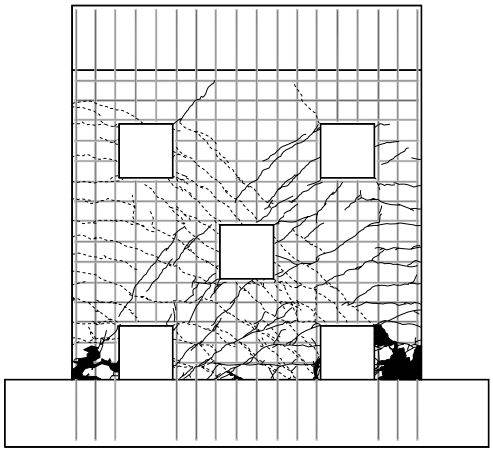

(f) at $DF = \pm 5$

Figure 5.34: Crack patterns of Specimen W2

5.8.5 Deformations measured by LVDTs

All together 21 LVDTs were installed in Specimen W2 to measure the deformations at desired regions during the experiment. The location of each LVDT has been shown as in **Figure 5.11**. The purpose of these LVDTs can be divided into five categories: for lateral drift, for flexural deformation, for shear deformation, for panel shear deformation, and for possible sliding displacement along the joint between the web and the foundation beam of the wall.

Flexure deformation was measured by three groups of the LVDTs, including L2 & L5, L3 & L6, and L4 & L7. Most part of the flexure deformation was concentrated at the bottom, which was taken by L4 and L7. Three graphs in **Figure 5.35** show the variation of the flexural deformations at different section along the web measured at the both sides of the wall. It was common to observe significantly differences in the deformations between negative and positive loading cycles for every LVDT. This was understandable as flexural deformation was much more pronounced in the tensile zone than that in the compressive zone. Large negative readings (**Figure 5.35 (c)**) were recorded when the particular LVDT was in the compressive zone which the nearby concrete was crushed and spalled away.

Shear deformation of the web panel was measure by the L8 and L9. **Figure 5.36** shows the deformation variation in relation to the ductility factor. It can be seen that the deformations recorded by the two LVDTs were not even after $DF = \pm 3$, indicating that the subsequent damage caused by the cyclic loading was different for the two directions. Specimen W2 experienced similar shear deformations as Specimen W1 until $DF = \pm 3$. The influence of the openings was not yet seen. However, Specimen W2 increased faster after that for the negative loading cycles, indicating that a localised failure, particularly at the right bottom column, had occurred. Openings could be responsible for this localised failure.

Four groups of LVDTs were installed to measure the shear deformation of the panels. Due to the configuration of the openings, four panels formed at the wall web. These

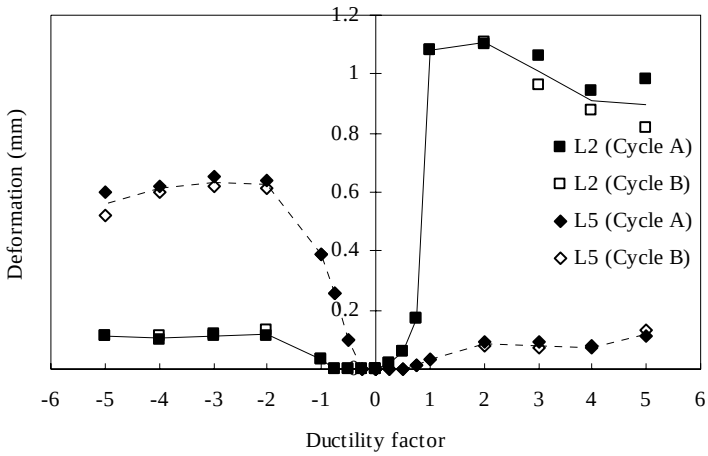

(a) By L2 and L5

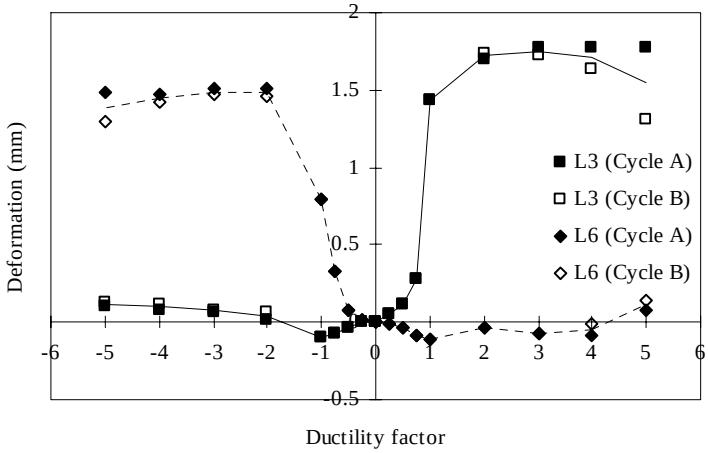

(b) By L3 and L6

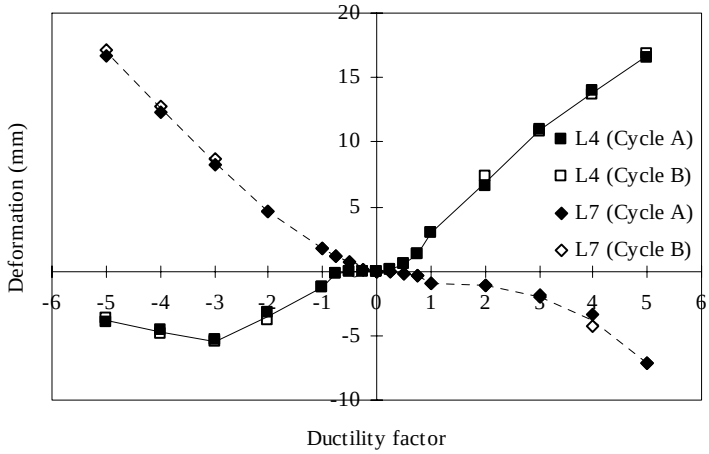

(c) By L4 and L7

Figure 5.35 Flexural deformations of Specimen W2 measured by LVDTs

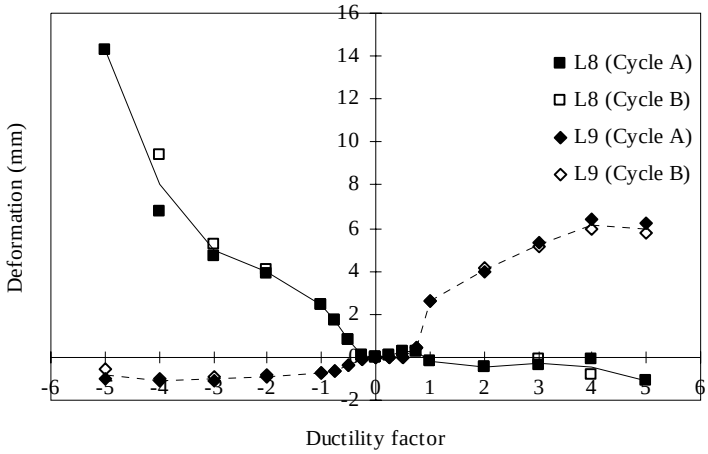

Figure 5.36: Shear deformation of Specimen W2 measured by L8 and L9

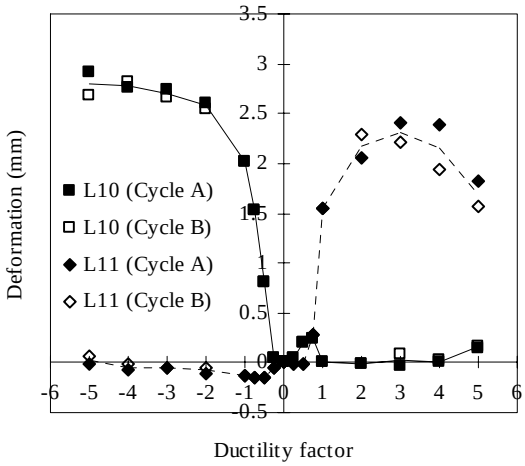

(a) Panel 1

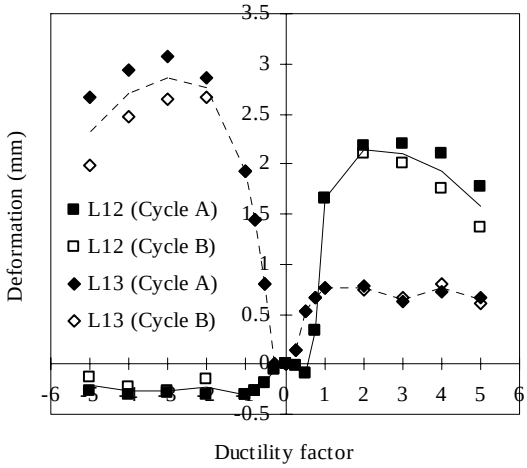

(b) Panel 2

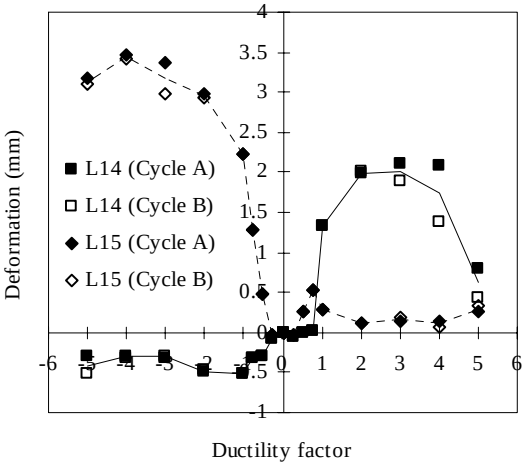

(c) Panel 3

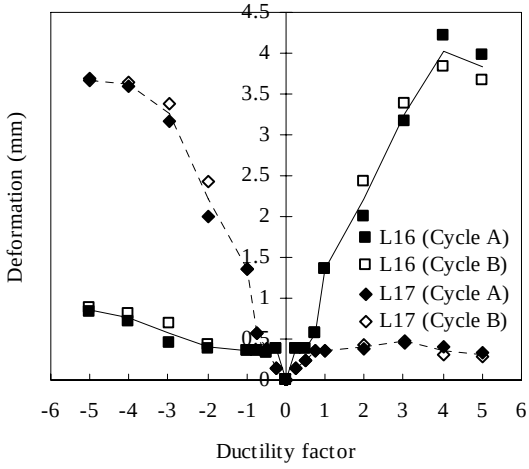

(d) Panel 4

Figure 5.37: Panel shear deformations of Specimen W2 measured by LVDTs

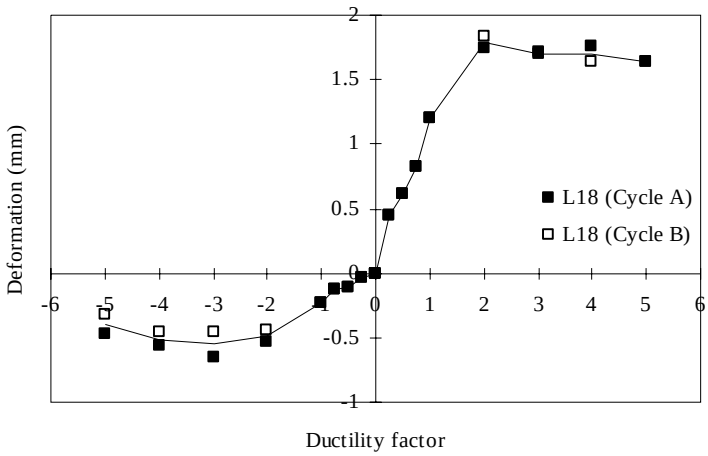

Figure 5.38: Sliding shear displacement of Specimen W2 measured by L18

panels, although were extensively cracked, were not loaded up to damage level. So the shear deformations recorded during the experiment were small and ranged from 3 to 4 mm. The data for the two loading directions were also quite uniform. These data will be helpful later when analyzing the mechanism of the panels.

Figure 5.38 shows the sliding displacement along the joint between the web and the foundation beam of the wall. To avoid the previous undesirable early non-effectiveness of this LVDT, L18 was installed at a slightly higher position than L10 of Specimen W1. Full range of data was collected. However, the deformation caused by sliding shear was not so significant for Specimen W2 as it only took 3.2% of the total lateral drift applied at maximum.

The decomposition of the imposed lateral drift into flexural and shear contributions was also conducted for Specimen W2. **Figure 5.39** shows the calculated displacement decomposition results for every loading cycle in both the negative and positive directions. For the negative loading cycles, the lateral drift caused by flexure was around the 60% level besides the first two cycles which have smaller flexural contribution. The shear component ranged from 25% to 30% for ductility factor 2 to 4 after which the shear contribution increased to 40% for the last three cycles. The shear contribution for the negative loading cycles in this specimen was more than that in Specimen W1 for the

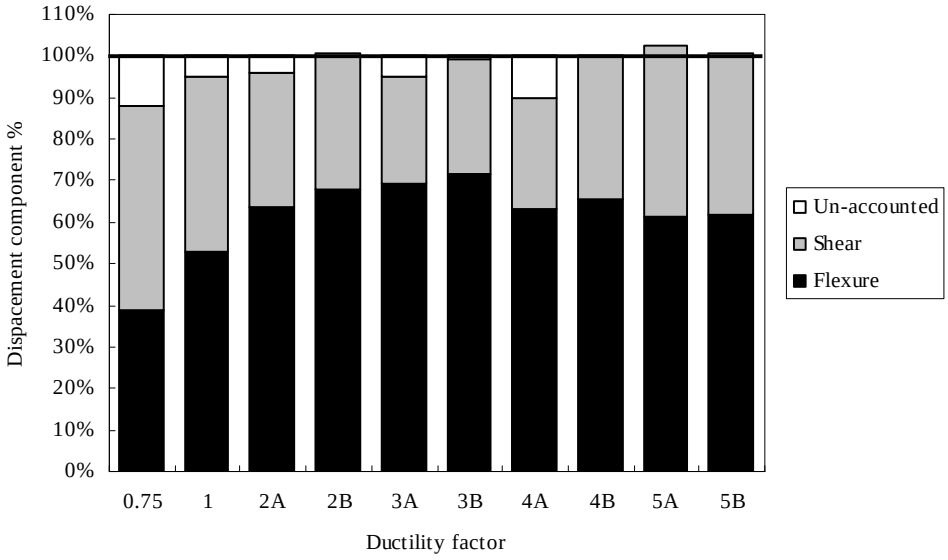

(a) For negative loading cycles

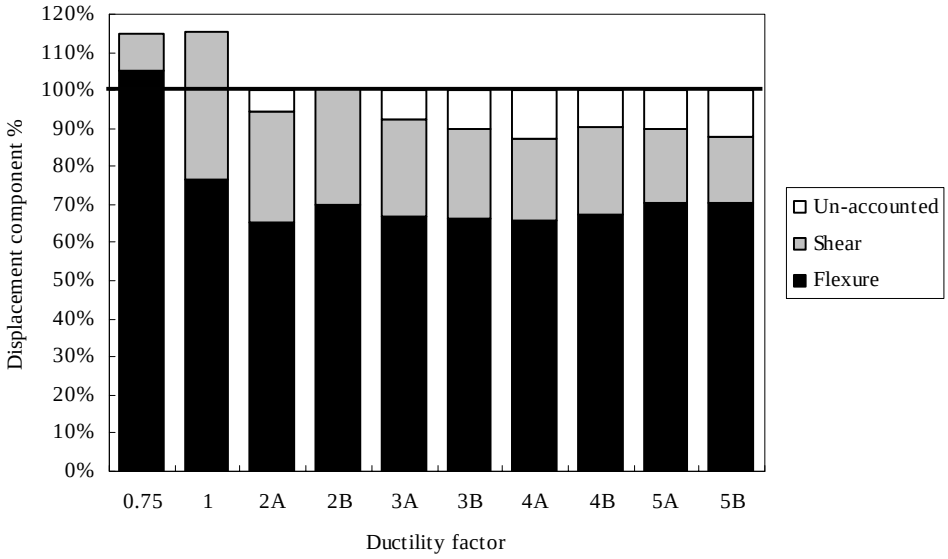

(b) For positive loading cycles

Figure 5.39: Displacement decomposition results for Specimen W2

openings reduced the shear stiffness in the negative loading direction. The sum of the flexural and shear component was almost equal to the imposed drift for all the loading cycles in this direction. This finding was well related to the observation that no sliding shear deformation occurred in this loading direction in the experiment. For the positive

loading cycles, the flexure component was around 70% besides the first two cycles and it was 10% more than that in the negative loading cycles. The shear component was smaller than that in the negative loading cycles and was around 20% throughout. In this loading direction, the sum of the flexural and shear component was 10% smaller than the total lateral drift from $DF = +2$ onwards. The un-accounted portion in these loading cycles should be from the sliding shear deformation that has been measured for this loading direction. The recorded sliding displacement was around 2 mm starting from $DF = +2$ and the percentage taken deceased from 15% to 5% of the total drift.

5.8.6 Strains of the reinforcing bars

Figure 5.40 shows six vertical reinforcing bars at selected locations along the horizontal section of the web. Each bar had four strain gauges attached from the bottom to the top. The general observations of the bar strains are summarized here. Firstly, every bar had a larger strain at the bottom and gradually reduced on moving up under the same ductility level. Secondly, bars at the edges of the web were more strained compared with those at the middle along the same vertical position. Thirdly, compressive strains were recorded when the bars were under compression. However, these compressive strains were smaller than tensile strains. The behavior of each individual reinforcing bar will be illustrated below.

The Bar V1 had four strain gauges (#1, #37, #52, #59) distributed along it from the bottom to the top in the web. This bar was under compression for the negative loading cycles and under tension for the positive loading cycles. As shown in **Figure 5.40 (a)**, the bottom of this bar (#1) yielded in compression at $DF = -2$ while yielded in tension at $DF = +1$. When moving up, the compressive strain decreased and even became tensile (#52, #59). The tensile strains in the positive loading cycles also decreased and yielding was not observed for #59.

For Bar V2 with Gauges #3, #24, #48, and #55, compressive strains were also recorded (#3 and #22) for the negative loading cycles but yielding was not so pronounced. And #24 demonstrated larger compressive strains than #3, which could be the influence of the

opening there. From the bottom up, the compressive strains decreased and turned to be tensile at the top (#55). In the positive loading cycles, Gauges #3 and #24 reached yielding at $DF = +1$.

Bars V5 and V8 were located at the regions between the openings of the web. Small compressive strains were recorded at the bottom two strain gauges of each bar. That was because the presence of the openings extended the compressive zone in the wall web at the bottom. Yielding in tension was only observed for the two bottom strain gauges (#8and #13) and the strains were not large.

Bar V11 with Gauges #18, #27, #51, and #58 recorded compressive strains in the positive loading cycles and tensile strains in the negative loading cycles. Small compressive strains existed for #18 and #27 until $DF = -1$. After that and even before the bar reached yielding there, this strain drastically changed to large tensile at $DF = -2$, which indicated that the bar was buckled at the bottom. For tension in the negative loading cycles, yielding of the bar was find after $DF = +1$.

Bar V12 had Gauges #20, #38, #53, and #60. This bar was under compression for the positive loading cycle and under tension for the negative loading cycle. For #1 strain gauge, the strain jumped from being compressive to tensile at $DF = -1$ and was buckled later. Tensile yielding for the negative loading cycles was at a earlier stage and before $DF = +1$.

The two graphs in **Figure 5.41** shows the vertical strain profiles of Bars V1 and V12 at $DF = \pm 1$. They clearly presented the strain variation in the vertical direction of the two critical reinforcing bars at the edges of the web for Specimen W2. Similar trend as Specimen W1 was observed. **Figure 5.42** is the strain profile along the bottom section of the web at $DF = \pm 1$. From this drawing, we can roughly see the neutral axis in the wall web at the bottom section.

Figure 5.43 gives the strains of two horizontal reinforcing bars (H2 and H5) distributed along the vertical section of the web between openings. Again, each bars had four strain

gauges attached from the left to the right. It was noticed that small compressive strains were found for some strain gauges in this group. Tensile strains were more significant but still well below the yielding. It could be seen that the horizontal reinforcing bar developed similar or even smaller strains as compared with Specimen W1 and thus it is then concluded that the wall specimen with openings needed no extra lateral confinement. Further plots on the horizontal strain profiles of the two selected bars are shown in **Figure 5.44**. These profiles were horizontal bar strain conditions at $DF = \pm 1$. On Bar H2, only three strains were effective and their profiles were less meaningful. From the strain profile of Bar H5 however, the effect of openings can be seen. At the negative loading cycles, only Gauge #46 had considerable tensile strains and the other gauges had almost zero readings. Similarly at the positive loading cycles, only Gauge #45 generated considerable readings and the rest gave nearly zero readings. Gauges #45 and #46 were at the middle between two openings.

Figures 5.45 to **5.47** present strains along the diagonals of three typical panels in the web. Due to the locations of the two middle panels, they were subjected to the combined actions of flexure and stress flow across. Apart from the flexure (by omitting the strains gauges that were more influenced by flexure such as #24 and #27), the stress flow in the panel developed quite uniform strains along the diagonal. This confirmed that the imposed lateral load was transferred by the panel zones with a concentrated stress flow. The strains observed were below the yielding and the panels were not damaged and still possibly within the elastic range. The bottom panel was influenced by the joint between the web and the foundation beam (#7 and #14). Although more extensive cracking was observed in the region, the strains along the diagonals of the panel were still quite uniform and below yielding. Together with the findings of panel deformations, it is concluded that panel zone is a strong mechanism in transferring the stress flow due to its large concrete section available. The reinforcement provided for it is can be nominal for crack control purpose without any adversary effect.

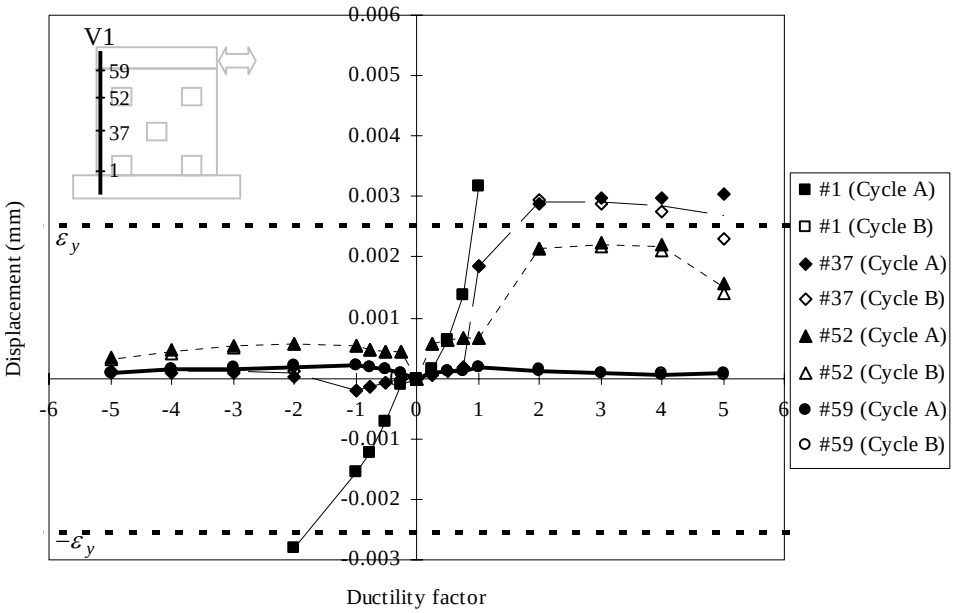

Figure 5.40 (a) Strain distribution of vertical Bar V1

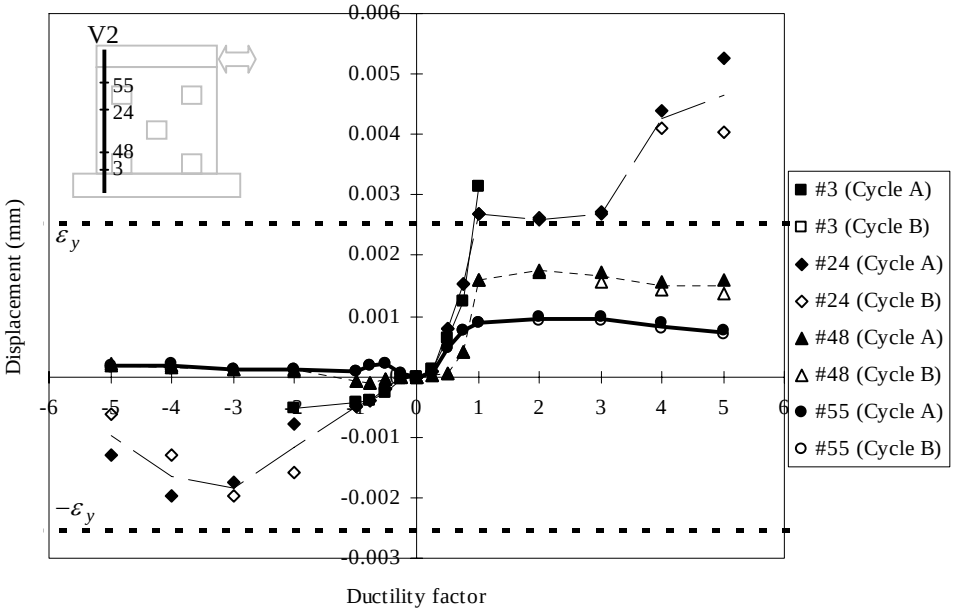

Figure 5.40 (b) Strain distribution of vertical Bar V2

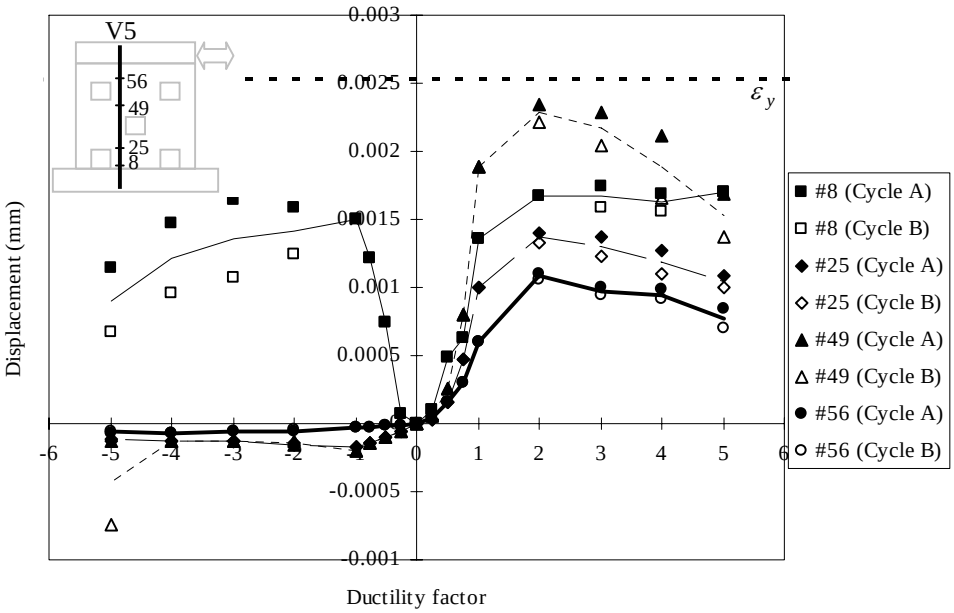

Figure 5.40 (c) Strain distribution of vertical Bar V5

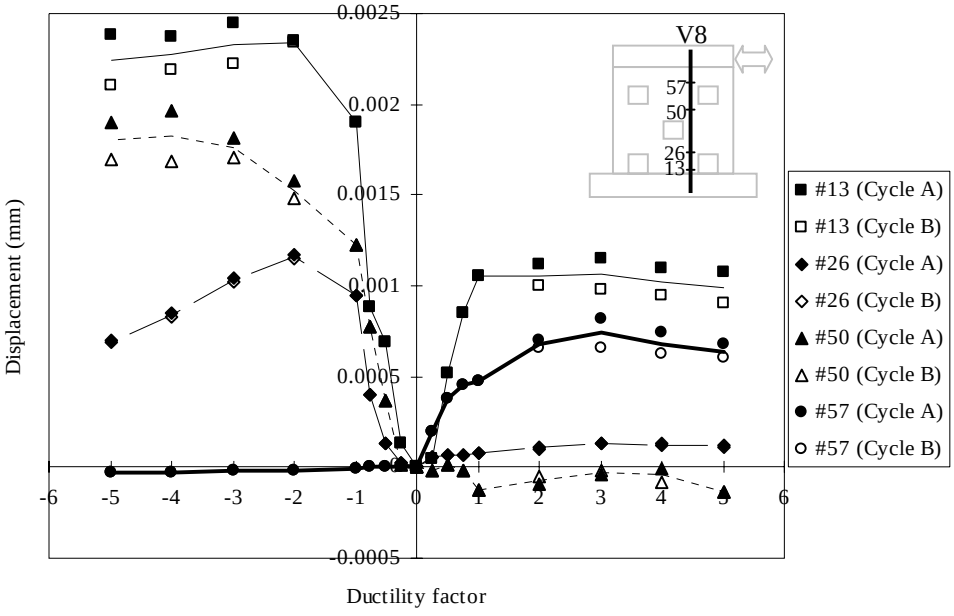

Figure 5.40 (d) Strain distribution of vertical Bar V8

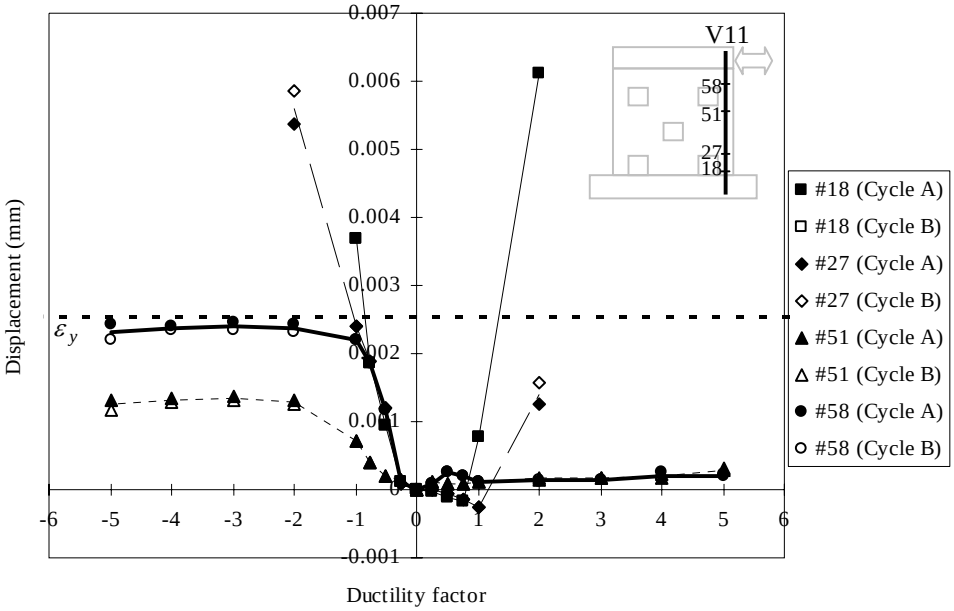

Figure 5.40 (e) Strain distribution of vertical Bar V11

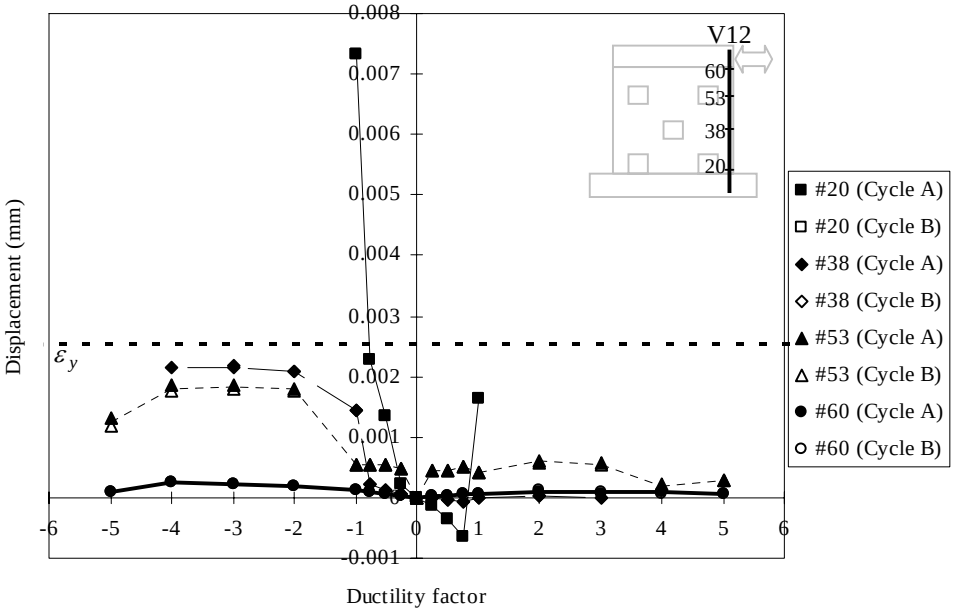

Figure 5.40 (f) Strain distribution of vertical Bar V12

Figure 5.40: Strain distributions of some vertical reinforcing bars

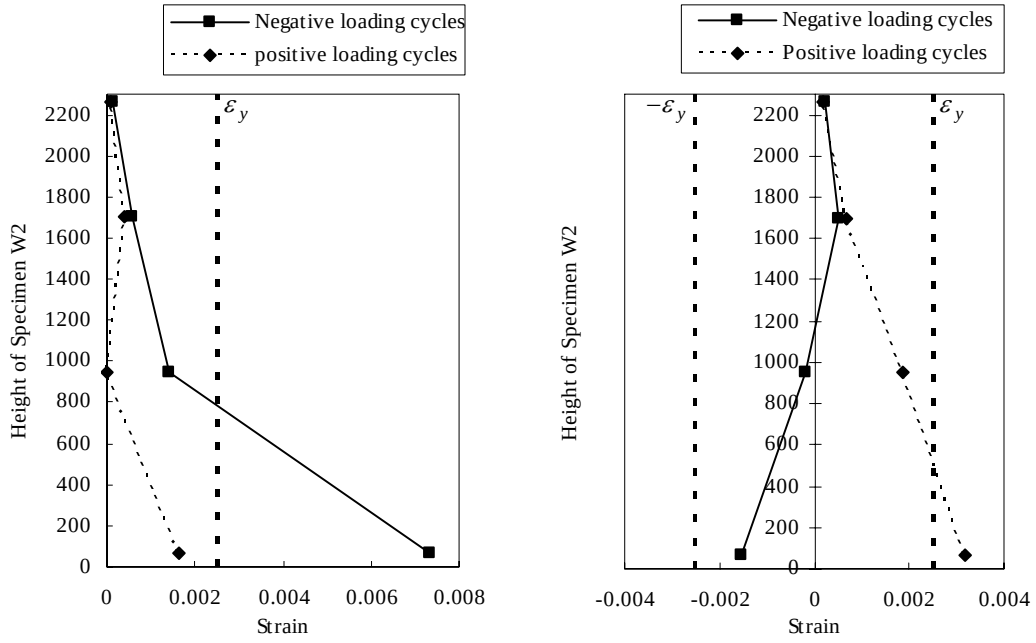

(a) Bar V1 at $DF = \pm 2$ (b) Bar V12 at $DF = \pm 2$

Figure 5.41: Strain profiles of Bars V1 and V12 at $DF = \pm 2$

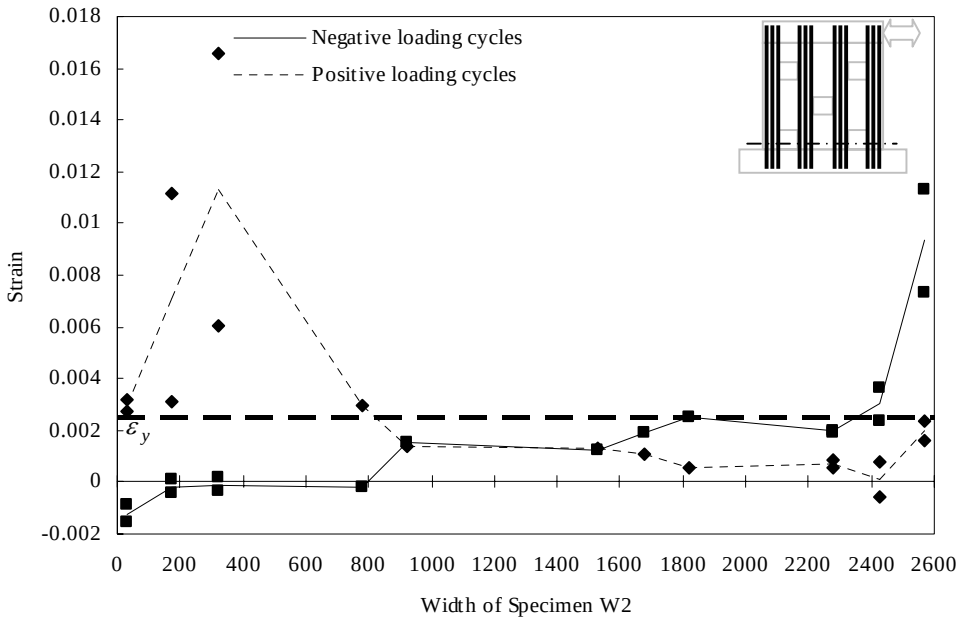

Figure 5.42: Strain profiles of reinforcing bars along the bottom of web

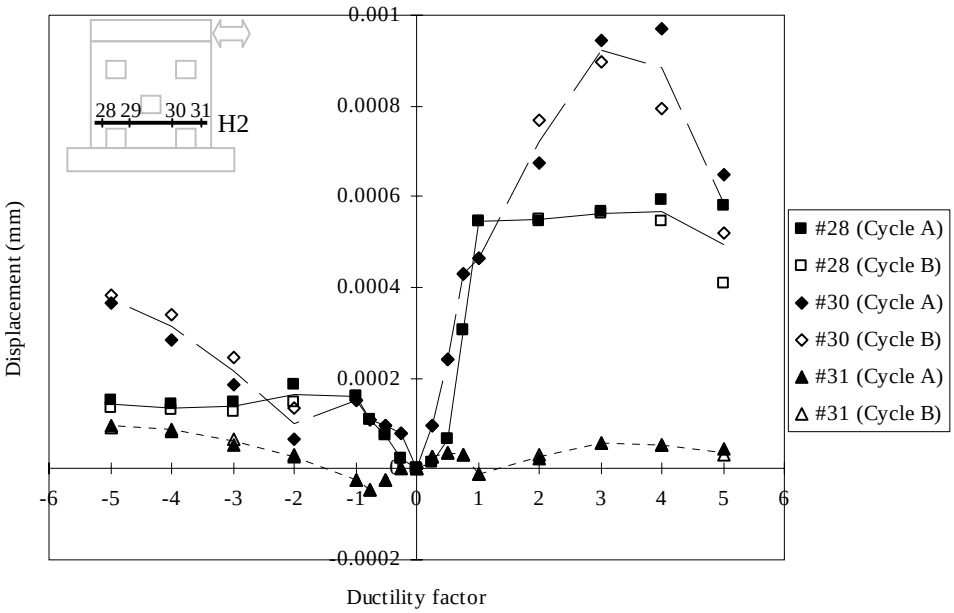

(a) Bar H2

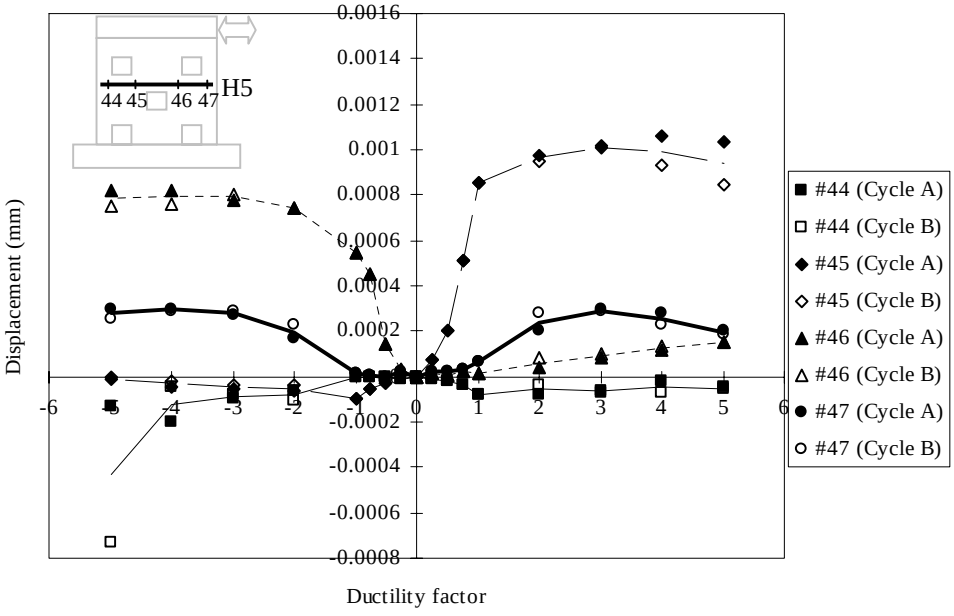

(b) Bar H5

Figure 5.43: Strain distributions of some horizontal reinforcing bars

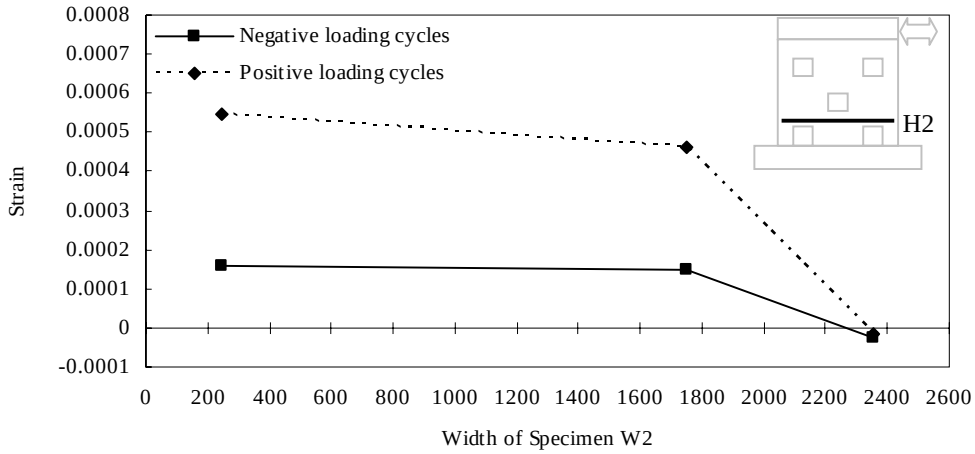

(a) Bar H2

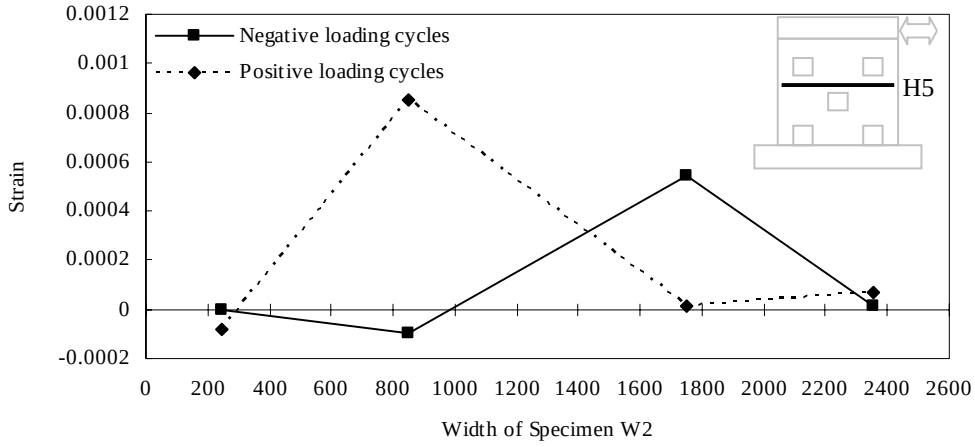

(b) Bar H5

Figure 5.44: Strain profiles along two horizontal reinforcing bars

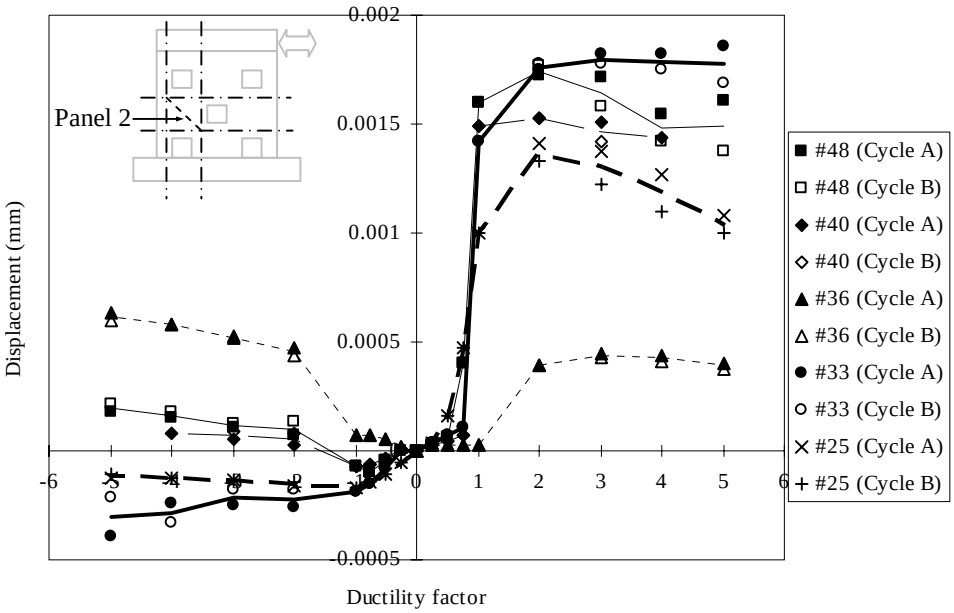

(a) Along the top right to the bottom left diagonal

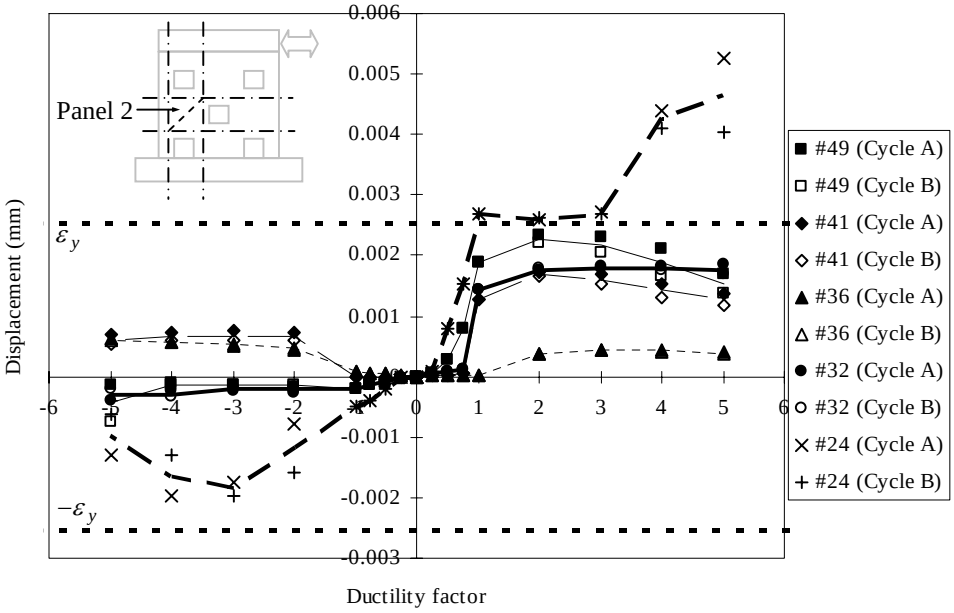

(b) Along the top left to the bottom right diagonal

Figure 5.45: Strains along diagonals of Panel 2

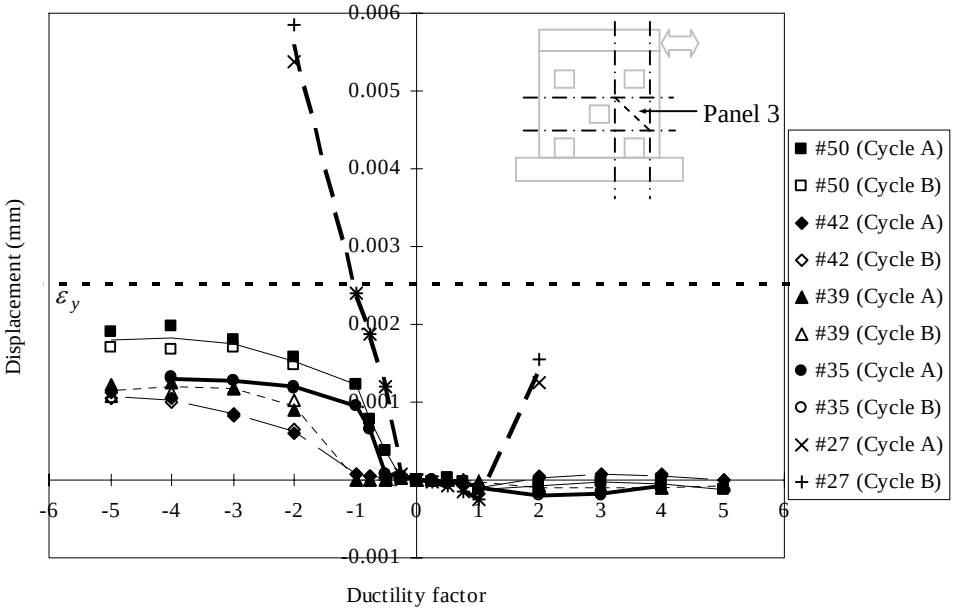

(a) Along the top right to the bottom left diagonal

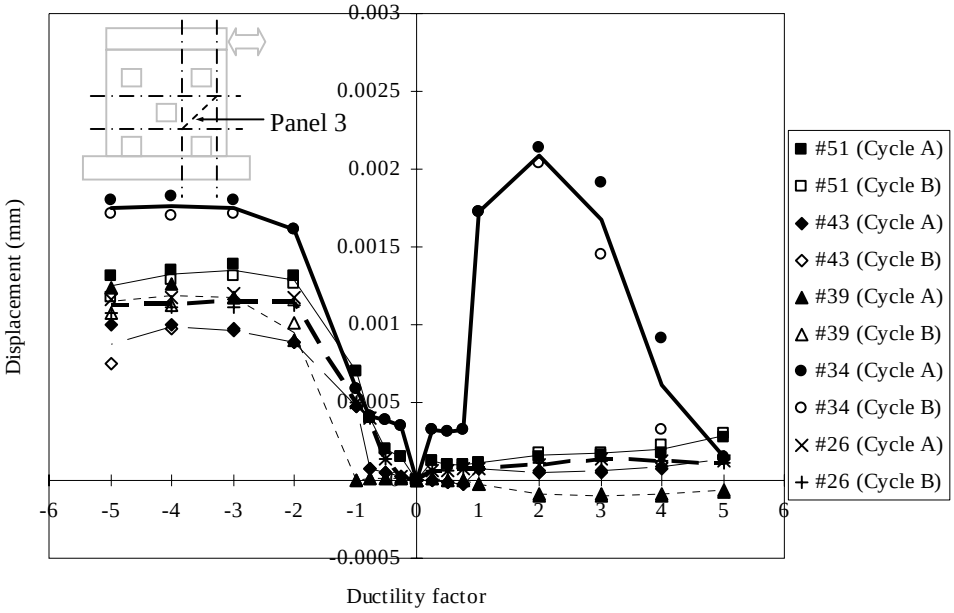

(b) Along top left to bottom right diagonal

Figure 5.46: Strains along diagonals of Panel 3

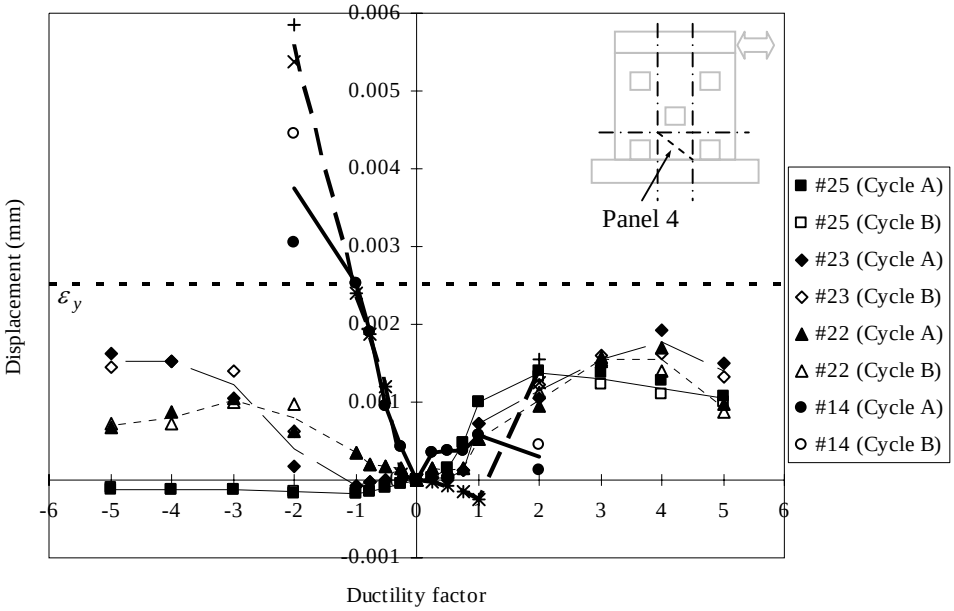

(a) Along the top right to the bottom left diagonal

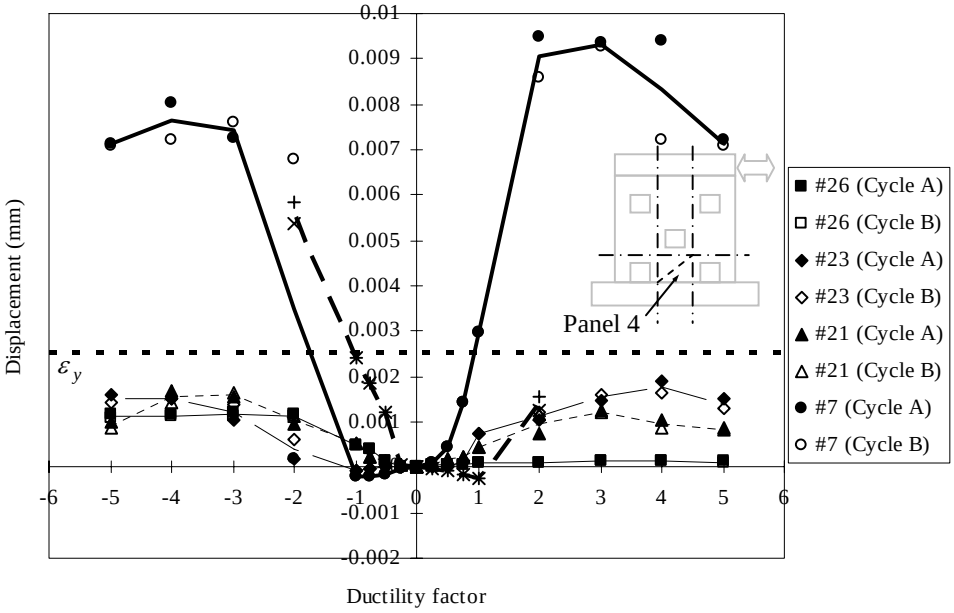

(b) Along the top left to the bottom right diagonal

Figure 5.47: Strains along diagonal of Panel 4

5.9 Test Result of Specimen W3

Specimen W3 was a wall with nine regularly placed openings as shown in **Figure 5.4**. The web of this wall specimen has been designed to have the same configuration as the postulated shear wall by Marti [M2].

5.9.1 Loading history

Figure 5.48 shows the loading history experienced by the Specimen W3. P_i of Specimen W3 was determined to be 342 kN by a preliminary finite element analysis using the program UC-WIN/MESH & UC-WIN/WCOMD with the nominal material strength for the load-controlled cycles. For this specimen, the yield displacement Δ_y still followed the control Specimen W1 and the displacements forr all the ductility factors were calculated accordingly. Due to the low stiffness of this specimen, displacements for $\pm 0.75P_i$ cycle were very close to that of the $DF = \pm 1$ cycle. So, $DF = \pm 1$ cycle was directly recorded after $0.5P_i$ cycle for this specimen. The loading ended after the first cycle of $DF = \pm 7$ when the capacity of the specimen was dropped significantly and the failure was clearly observed.

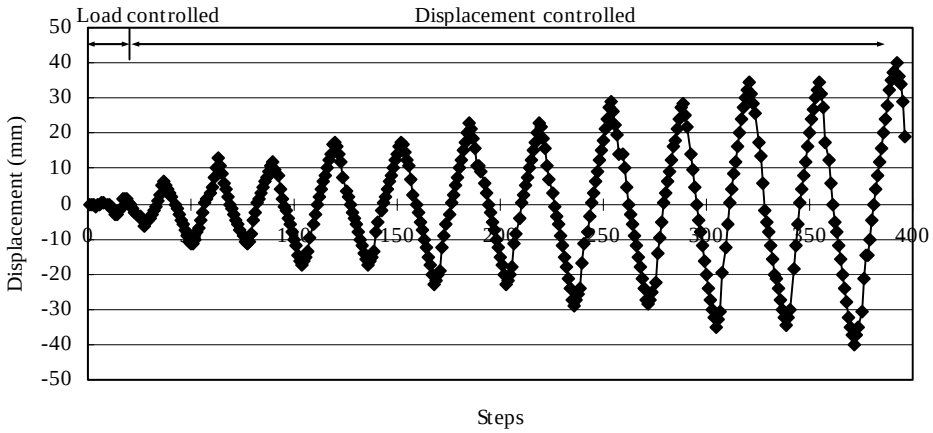

Figure 5.48: Loading history of Specimen W3

5.9.2 The overall response of Specimen W3

Figure 5.49 shows the lateral load versus top lateral displacement hysteretic response of Specimen W3 recorded during the experiment. In general, a smooth and well-behaved hysteretic loop was again recorded. The definite pinching, which was induced by shear, was also observed in this specimen. This phenomenon was true for all the three specimens tested. Compared with the other two specimens, the ultimate strength of Specimen W3 was more than 20% smaller. The effects of more openings reduced the overall stiffness of the element and improved the ductility. The resistance capacity of the specimen reached its maximum at $DF = \pm 2$ and started to decrease after that. Unlike Specimen W2, the strength developed for the two loading directions was almost equal for this specimen, which was the true for the symmetrically configured element. Some common behaviors as Specimens W1 and W2 in the hysteretic loop were also found. Strength was lowered for the second cycle in each ductility factor. It also could be seen that the hysteretic loop was flattened as the ductility level increased, which meant that the stiffness degraded with the increase of cycles. Failure of this specimen occurred at $DF = \pm 7$. After the first cycle of this ductility factor, the maximum strength developed

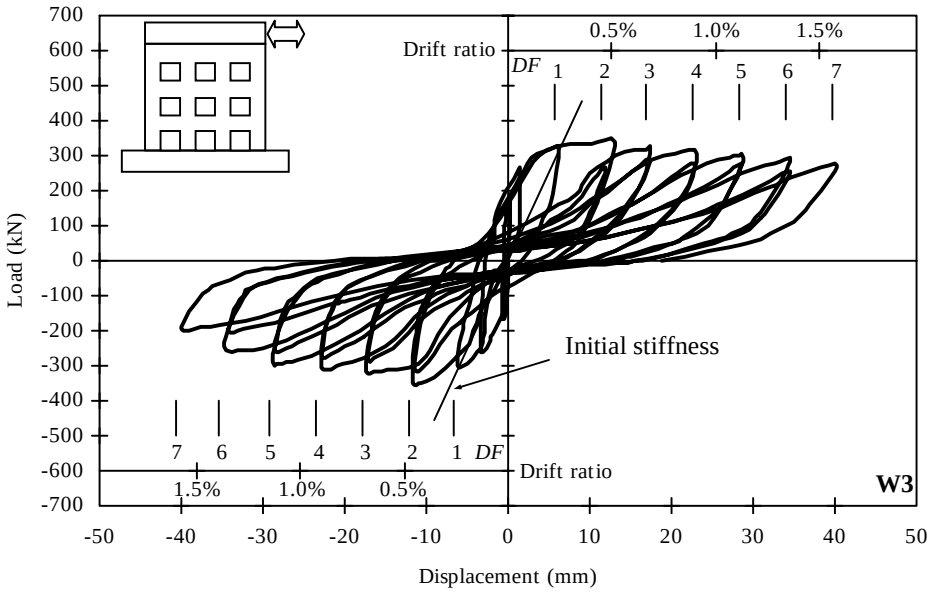

Figure 5.49: Lateral load-displacement response of Specimen W3

was 47% smaller than the peak strength recorded, which indicated a clear failure.

The initial stiffness of Specimen W2 obtained from the test was 50.8 kN/mm, which was 16% smaller than that of Specimen W1. The nine regularly placed openings on the web of the wall significantly reduced the initial stiffness. The trend of secant stiffness degradation was also traced and shown in **Figure 5.50**. The secant stiffness of Specimen W3 also decreased exponentially and the rate of the degradation was slower for this specimen when compared to that of Specimen W1. At failure, the stiffness dropped to 11.3% of the initial amount.

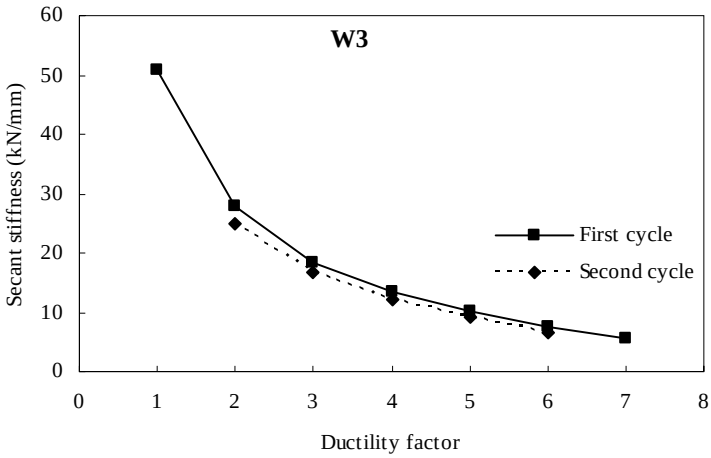

Figure 5.50: The stiffness degradation trace of Specimen W3

5.9.3 Behavior of Specimen W3

The following table presents the detailed behaviors of Specimen W3 at different loading stages.

Table 5.5: Observed behavior of Specimen W3

Loading history	Behaviour of W3
$0.25P_i$	The specimen was in the elastic range. No cracks were observed.
$0.50P_i$	Cracks were mainly flexural. A few diagonal cracks started to develop at the beam and column zones. The crack width measured was 0.2 mm for the negative loading cycle and 0.4 mm for the positive loading cycle.
$DF = \pm 1$	This is the stage for the formation of diagonal cracks. A loud sound was heard when concrete cracked during the positive loading cycle. Three major parallel diagonal cracks in the positive loading cycle had been formed. The crack width measure was 0.6 mm for the negative loading cycle and 1.5 mm for the positive loading cycle
$DF = \pm 2$	Diagonal cracks continued to grow (**Figure 5.51 (a)**). The load sound of concrete cracking was heard again, but for the negative loading cycles only. Three major parallel diagonal cracks in the negative loading cycles were formed too. The crack width measured was 1.5 mm for the negative loading cycles and 3.0 mm for the positive loading cycles.
$DF = \pm 3$	Major cracks fully formed at this stage (**Figure 5.51 (b)**). Diagonal cracks increased greatly in width. The crack width measured was 9.0 mm for the negative loading cycles and 10.0 mm for the positive loading cycles.
$DF = \pm 4$	A lot of minor cracks developed in the beam and column zone and the concrete started to be crushed as seen in **Figure 5.51 (c)**.
$DF = \pm 5$	Deformation was concentrated along the three sets of major diagonal cracks for both loading directions. Crushing and spalling of the concrete was severe (**Figure 5.51 (d)**). Cracks opened wide and you could see through the web.
$DF = \pm 6$	Crushing of the concrete became very severe for the two columns at the bottom edges (**Figure 5.51 (e)**). Large pieces of concrete separated from the web. Reinforcing bars were exposed and buckling was observed too.
$DF = \pm 7$	Obvious movement could be observed along the diagonal cracks (**Figure 5.51 (f)**). The four columns at the bottom were severely damaged (**Figure 5.51 (g)**). A large piece of concrete cover was spalled away and bars were buckled. One reinforcing bar in the right bottom column was even fractured. The maximum strength developed was 47% smaller than the peak strength recorded and the specimen failed.

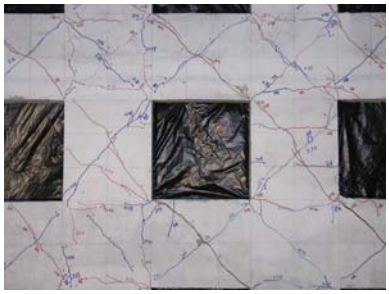

(a) Diagonal cracks at $DF = \pm 2$

(b) Diagonal cracks at $DF = \pm 3$

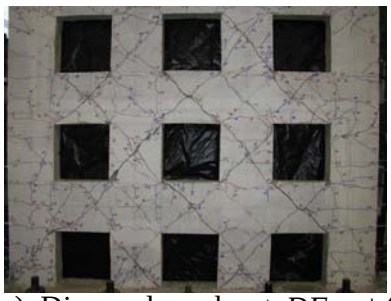

(c) Diagonal cracks at $DF = \pm 4$

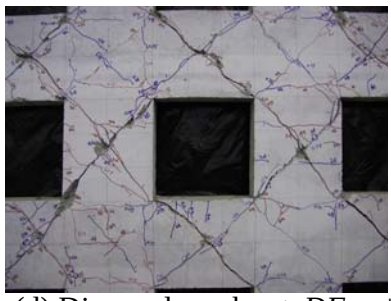

(d) Diagonal cracks at $DF = \pm 5$

(e) Crushing of the two columns at the bottom edges at $DF = \pm 6$

(f) Damage of the four bottom columns at $DF = \pm 7$

(g) Diagonal cracks at $DF = \pm 7$

Figure 5.51: Detailed illustrations of Specimen W3 by photography

5.9.4 Crack Pattern and Failure Mechanism

Figure 5.52 shows the crack pattern of Specimen W3 at every ductility level. The full lines represented the cracks formed during the negative loading cycles, while the dash lines represented the cracks formed during the positive loading cycles. A full picture of crack development is illustrated through this series of drawings. Different from Specimens W1 and W2, this specimen cracked earlier, at $\pm 0.5P_i$. Horizontal flexural cracks appeared first between the edges and nearby openings, however due to the existence of the more openings, these cracks were cut off and did not develop into diagonal cracks. Obvious diagonal cracks started to be visible after $DF = \pm 1$ at beam and columns zones between openings. For both loading cycles, there were three major sets of diagonal cracks developed, which were almost parallel to each other. The larger opening area in the web also mobilized more concrete sections and so cracks were observed over the entire height of the web.

At large ductility factors, crack growth was concentrated at the three long diagonal cracks, which caused severe crushing and spalling of the concrete and as a result the damage of the two bottom edge columns was not as severe as Specimen W2. Crushing of the concrete there was at as late as $DF = \pm 5$. In the end, the reinforcing bars were still buckled and fractured at these two column zones.

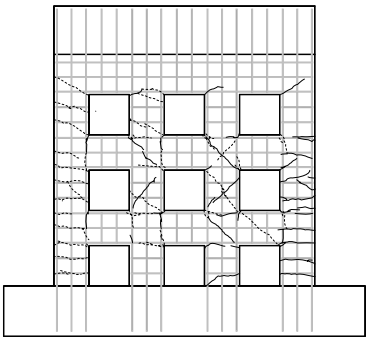

(a) at $0.5P_i$

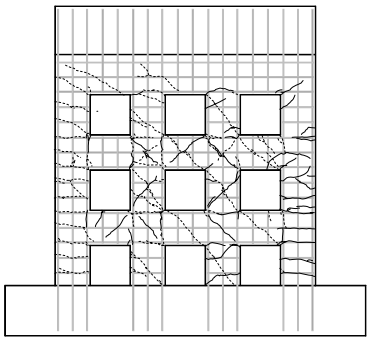

(b) at $DF = \pm 1$

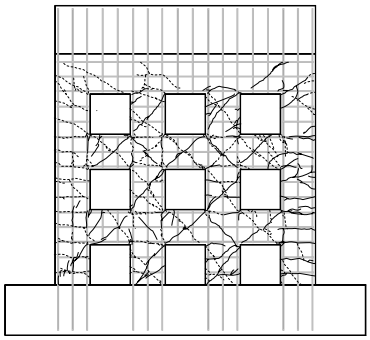

(c) at $DF = \pm 2$

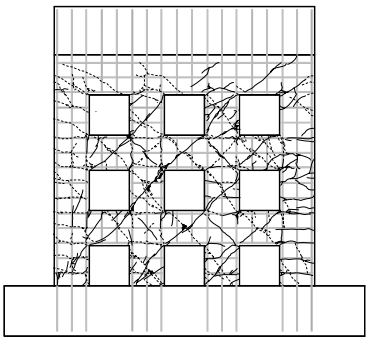

(d) at $DF = \pm 3$

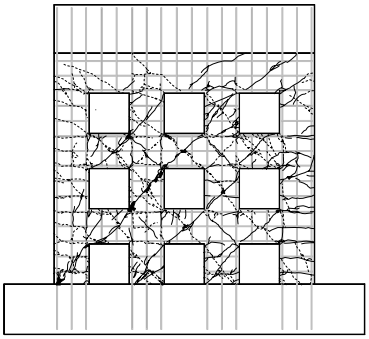

(e) at $DF = \pm 4$

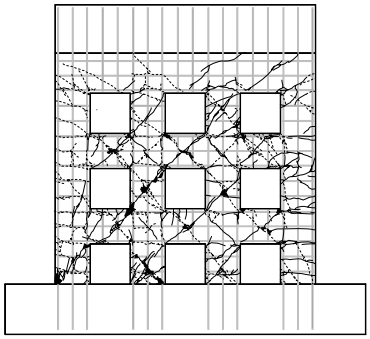

(f) at $DF = \pm 5$

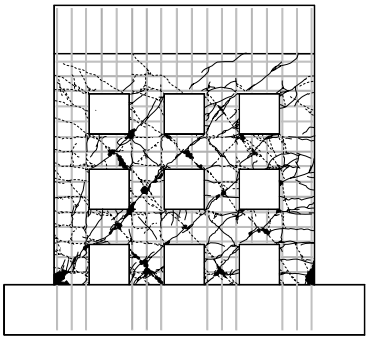

(g) at $DF = \pm 6$

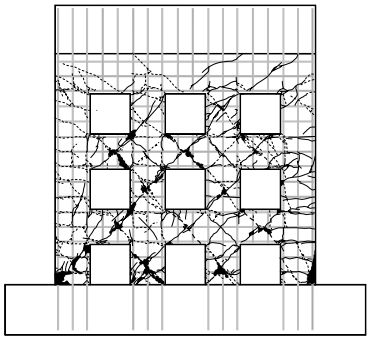

(h) at $DF = \pm 7$

Figure 5.52: Crack patterns of Specimen W3

5.9.5 Deformations measured by LVDTs

All together 25 LVDTs were installed in Specimen W3 to measure the deformations at desired regions during the experiment. The location of each LVDT has been shown as in **Figure 5.12**. The purpose of these LVDTs can be divided into five categories: for lateral drift, for flexural deformation, for shear deformation, for shear deformation at the beam and column zones, and for possible sliding displacement along the joint between the web and the foundation beam of the wall.

Flexure deformation was measured by three groups of the LVDTs, including L2 & L5, L3 & L6, and L4 & L7. Three graphs in **Figure 5.53** show the variation of the flexural deformations at different sections along the web measured at the both sides of the wall. It was noticed that flexural deformations measured at the top and middle of the web took greater share of the total flexural deformation, hence the flexural deformation at the bottom was reduced. This phenomenon was different from Specimens W1 and W2. Difference in deformations still existed for the negative and positive loading cycles. This was understandable as flexural deformation was much more pronounced in the tensile zone than that in the compressive zone. Negative readings were recorded at the bottom when L4 and L7 were in the compressive zone, indicating that concrete was compressed there. Possible crushing of concrete internally was the reason for this.

Shear deformation of the web was measure by the L8 and L9. **Figure 5.54** shows the deformations variation in relation to the ductility levels. Shear deformation was uniform for the two loading directions, but Specimen W3 had much larger shear deformation as compared to Specimens W1 and W2. The nine opening significantly reduced the shear stiffness of the specimen. Specimen W3 also recorded very large negative readings for shear deformations in both of the LVDTs. This showed that the entire web was significantly compressed diagonally under shear significantly. The nine regularly placed opening turned the web into a frame-like mechanism, and caused the compression under lateral loading.

Five groups of LVDTs were installed to measure the deformations along the diagonals of

selected beam and column zones in the web as shown in **Figures 5.55** and **5.55**. In the two beam zones measured, the diagonals could all be elongated and compressed to a similar extend under the cyclic lateral loading. Elongation and compression were both around 4 mm when the specimen failed. For the column at the left bottom edge, it was subjected to flexure and localized behavior presented. So the deformations along the diagonals were not regular. However, for the other two column zones, it was found that L15 and L17 recorded no negative readings for the negative loading cycles and the elongations were around 1 mm larger than those for the beam zones. As the very obvious stress flowed through the diagonals of the beam and column zones, the deformation along the diagonals could be later used to explain the strut mechanism (representing the stress flow) under the strut-and-tie model.

For Specimen W3, no sliding face at the bottom of the wall web was formed and so sliding shear was not a possible failure mechanism for this specimen. The data collected from L23 was very small and not plotted.

The decomposition of the imposed lateral drift into flexural and shear contributions was also conducted for Specimen W3. **Figure 5.57** shows the calculated displacement decomposition results for every loading cycle in both the negative and positive directions. The results for the two loading directions are similar. After $DF = \pm 1$, the flexural contribution was maintained at 40% of the total drift for each cycle and the flexural component was smaller than that in Specimens W1 and W2. On the other hand, the shear contribution of Specimen W3 was generally around 60% of the total drift and larger than that in Specimens W1 and W2. The nine regularly placed

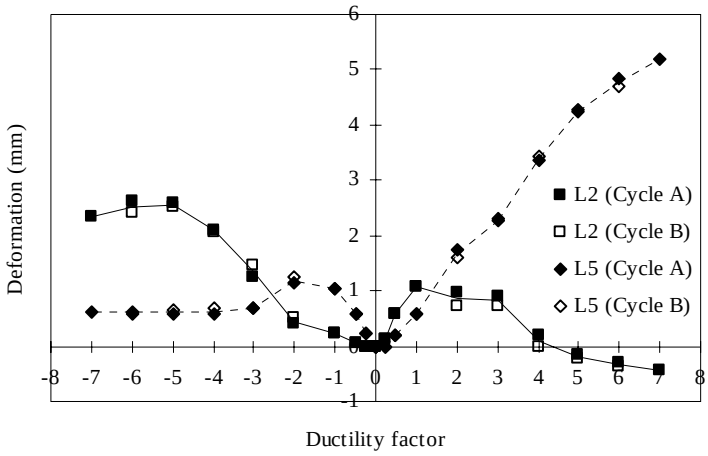

(a) By L2 and L5

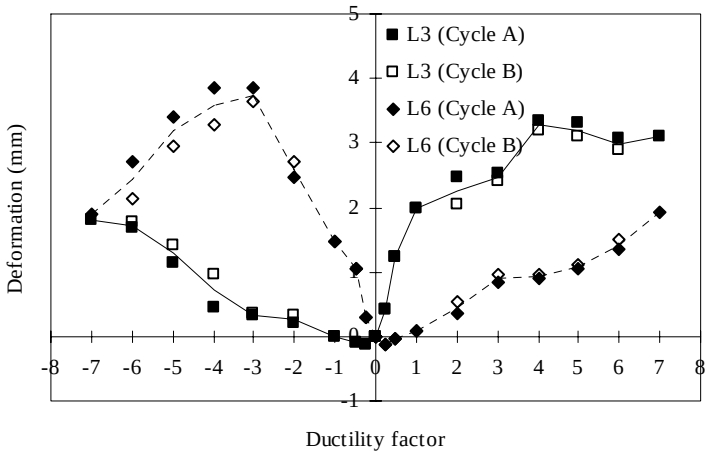

(b) By L3 and L6

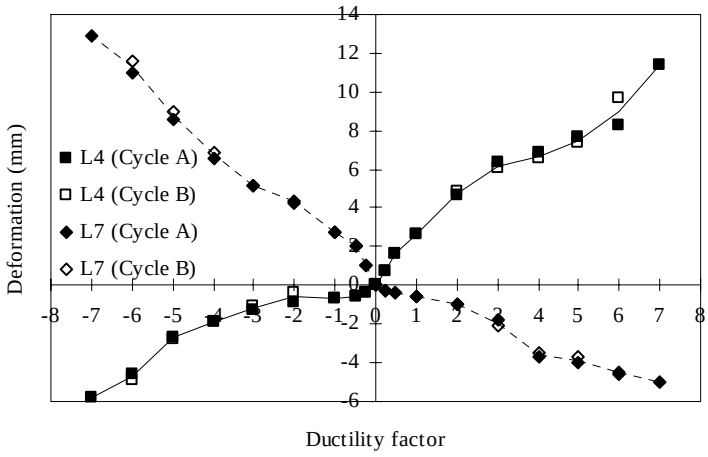

(c) By L4 and L7

Figure 5.53: Flexural deformations of Specimen W3 measured by LVDTs

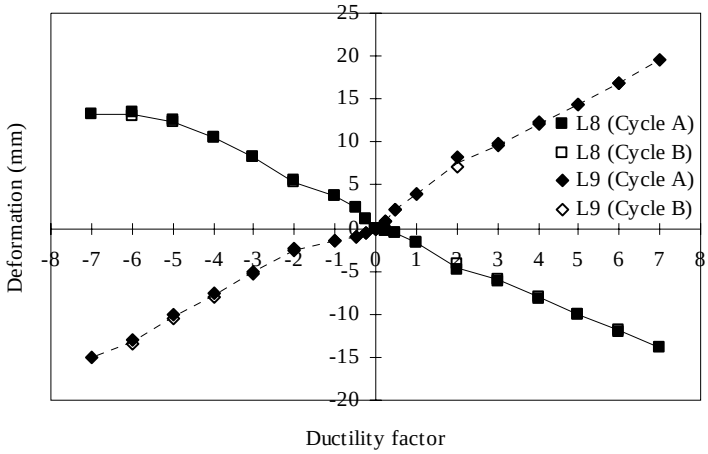

Figure 5.54: Shear deformation of Specimen W3 measured by L8 and L9

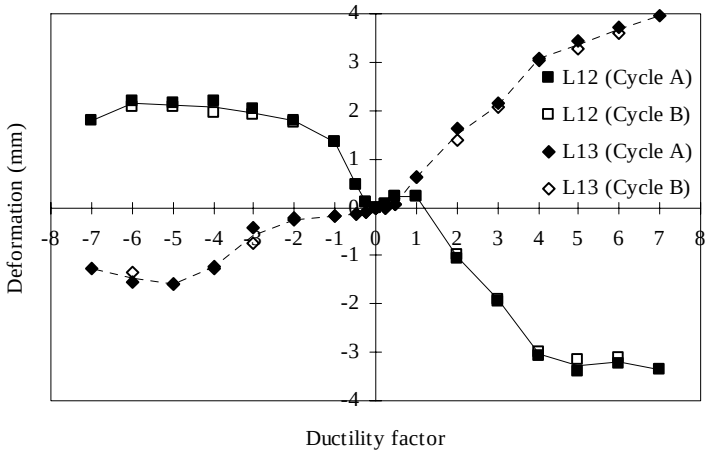

(a) Beam 5

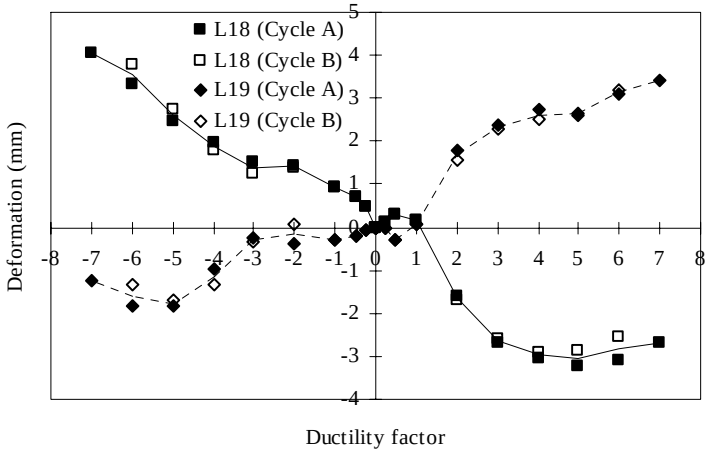

(b) Beam 2

Figure 5.55: Beam shear deformations of Specimen W3 measured by LVDTs

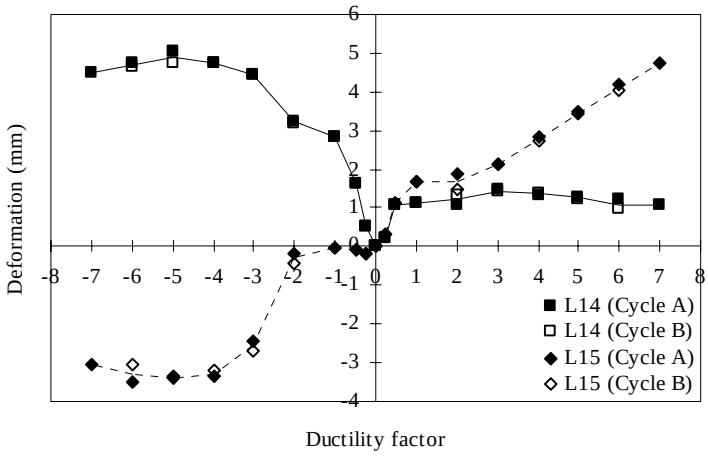

(a) Column 6

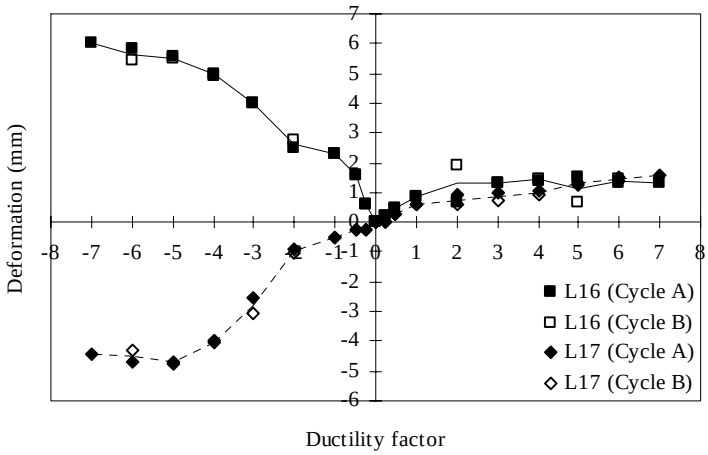

(b) Column 7

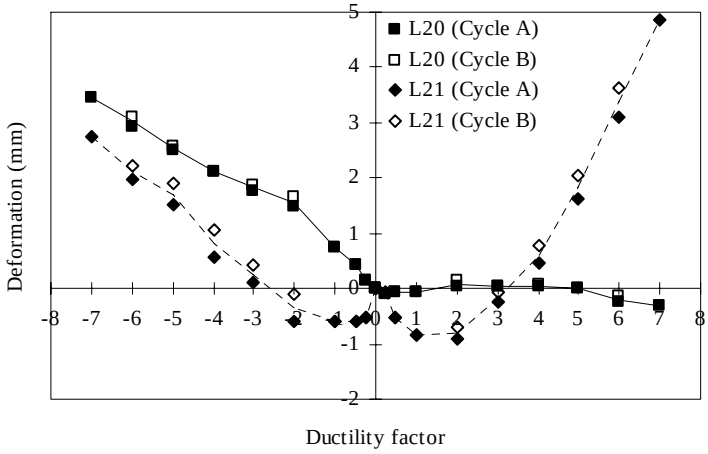

(c) Column 1

Figure 5.56: Column shear deformations of Specimen W3 measured by LVDTs

openings greatly reduced the shear stiffness of Specimen W3. The sum of the flexural and shear components for every cycle is equal or more than the total imposed drift. This finding here proves that Specimen W3 had no significant sliding displacement as observed during the experiment.

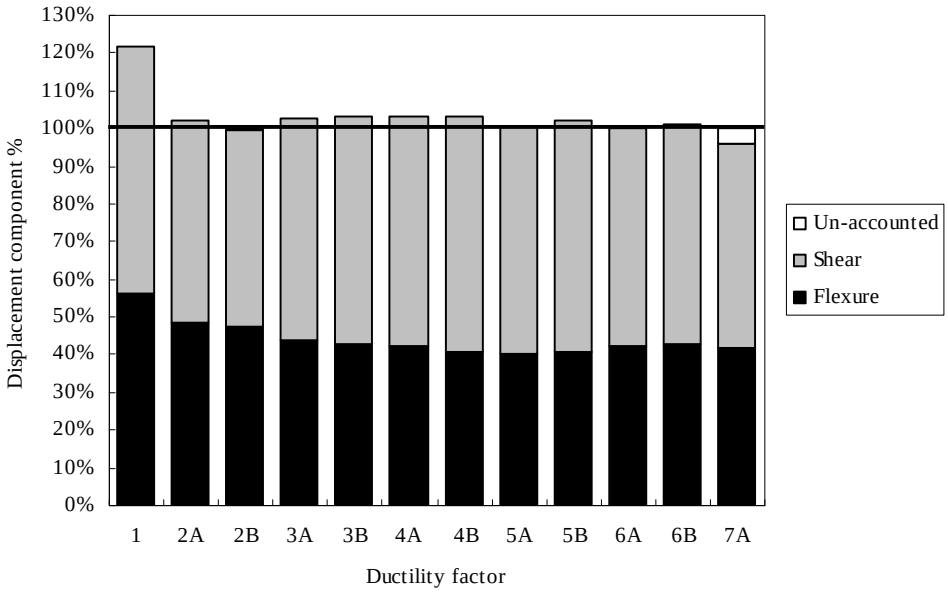

(a) For negative loading cycles

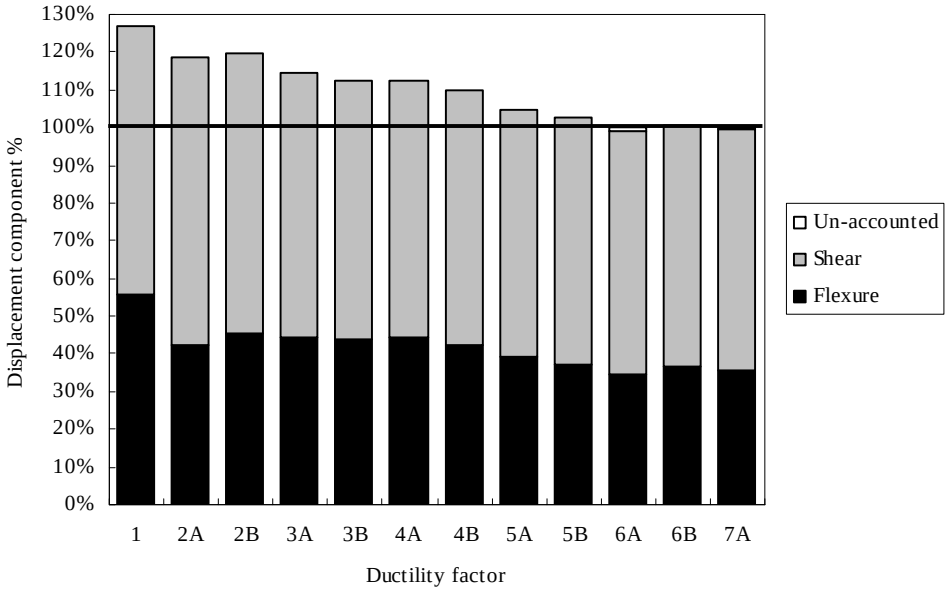

(b) For positive loading cycles

Figure 5.57: Displacement decomposition results for Specimen W3

5.9.6 Strains of the reinforcing bars

Due to the nine regularly placed openings, the web of Specimen W3 demonstrated a frame-like action. The beam and column zones were deformed locally, which could be different from deformation when the web was an integral panel as in the case of Specimen W1. Openings also restrained the stress flows to be concentrated along certain beam and column zones and so the strain gauge readings were greatly affected by these two actions. The results have been analyzed as the following.

Figure 5.58 shows six vertical reinforcing bars at selected locations along the horizontal section of the web. Each bar had four strain gauges attached from the bottom to the top. The behaviors of the bars could be categorized into three groups: V1 and V12, V3 and V10, V5 and V8.

The Bar V1 had four strain gauges (#1, #33, #53, #59) distributed along it from the bottom to the top. This bar located at the left edge of the web and should generally show the influence of flexure (under compression for the negative loading cycles and under tension for the positive loading cycles) mostly. However, as shown in **Figure 5.58 (a)**, only #1, which was at the bottom of this bar, demonstrated this behavior. Other gauges like #53 and #59 had very large tensile strains for the negative loading cycles and #59 even had compressive strains for the positive loading cycles. Although the upper portion of the vertical reinforcing bars of Specimens W1 and W2 recorded tensile strains when the section was in compression, the magnitudes were not as significant as this specimen. The #1 strain gauge yielded in compression at $DF = -1$ while yielded in tension at $DF = +1$.

Bar V12 had Gauges #18, #40, #58, and #60 and was located at the right edge of the web. This bar was under compression for the positive loading cycle and under tension for the negative loading cycle. It was also mostly influenced by flexure. Only #18 gave compressive strain values for the positive loading cycles. The other strain gauges were tensile although the values were not large for this loading direction. This bar had larger

strains as compared to V1. #18, #58, and #60 recorded strains beyond yielding at $DF = +1$. #18 also yielded in compression after $DF = -2$.

For Bar V3 had Gauges #5, #19, #34, and #54, #19 with #34, and #54 were positioned beside the openings from the bottom to the top. #5 and #19 were in Column 1 and had tensile strains for the both loading directions. They gave strains near yielding for the positive loading cycles and value below yielding for the negative loading cycles. Gauge #54 was in Column 9. It had tensile strains for the negative loading cycles, and mostly compressive strains for the positive loading cycles. This could be because of the local deformation of Column 9.

Bar V10 had Gauges #13, #20, #39, and #57, and among those #20, #39, and #57 were located besides the openings from the bottom to the top. #13 and #20 were in Column 4 and had tensile strains for the both loading cycles. These strains passed yielding after $DF = +2$ for both loading directions. #39 and #57 recorded tensile strains for the negative loading cycles and compressive strains for the positive loading cycles. These strains were below the yielding strain of the steel bar.

Bars V5 and V8 were both at the middle between two set of openings. Tensile strains prevailed throughout the loading history. The bottom of V5 yielded at $DF = \pm 3$.V8 had larger strains and yielded at $DF = \pm 1$. Strain gauges, such as #36, #37, and #38, were likely to be crossed by concentrated stress flows. As a result, their strains were large and near the yielding value.

The two graphs in **Figure 5.59** shows the vertical strain profiles of Bars V1 and V12 at $DF = \pm 1$. They clearly presented the strain variation in the vertical direction of the two critical reinforcing bars at the edges of the web. When compared to Specimen W1, localized deformation of the specimen can be identified. **Figure 5.60** is the strain profile along the bottom section of the web at $DF = \pm 1$. From this drawing, we can roughly see the neutral axis in the wall web at the bottom section. Two obvious abnormal readings for each loading direction both appeared at the edges of the two internal columns and were probably caused by localized deformations.

Figure 5.61 gives the strains of two horizontal reinforcing Bars (H2 and H5) distributed along the vertical section of the web between the openings. Again, each bars had four strain gauges attached from the left to the right. The majority of the strains recorded were tensile and when compared with the horizontal bars of Specimens W1 and W2, W3 developed larger strains up to the yielding values for some strain gauges. This was because the strain gauges in the horizontal bars were at the positions along concentrated stress flows and thus large strains were induced. Further plots on the horizontal strain profiles of the four selected bars are shown in **Figure 5.62**. These profiles were horizontal bar strain conditions at $DF = \pm 1$. Although four strain gauges were pasted on each bar, they were actually in three positions. Therefore, any trend in strain development or the effect of openings could be hardly observed from these two figures. However it can be seen that the bar strains varied a lot between the negative and positive loading cycles.

Figures 5.63 to **5.66** present strains along the diagonals of some beam and column zones at the central region of the web. The data collected showed that reinforcing bars in the beam and column zones selected were all under tensile stresses. This was a clear evidence that lateral load applied was transferred through those beam and column zones along the diagonal direction. The bars were normally yielded at $DF = \pm 1$ when the diagonal cracks at the beam and column zones started to form. Stirrups in the beam and column zones were significantly strained. They usually became non-effective after $DF = \pm 3$. So, to control cracks at the beam and column zones, more stirrups could be provided. Also, capacity of stress transfer could be improved.

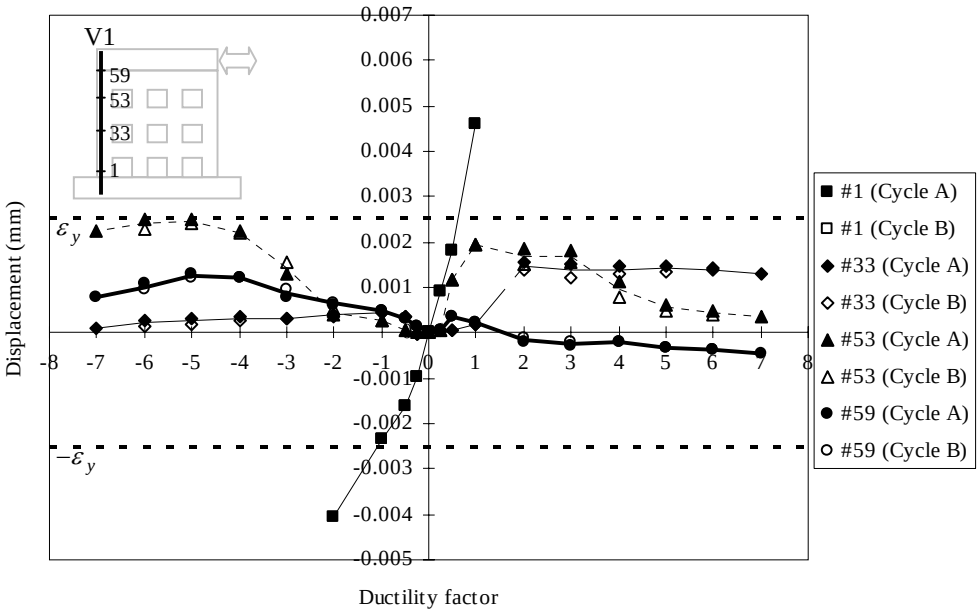

Figure 5.58 (a) Strain distribution of vertical Bar V1

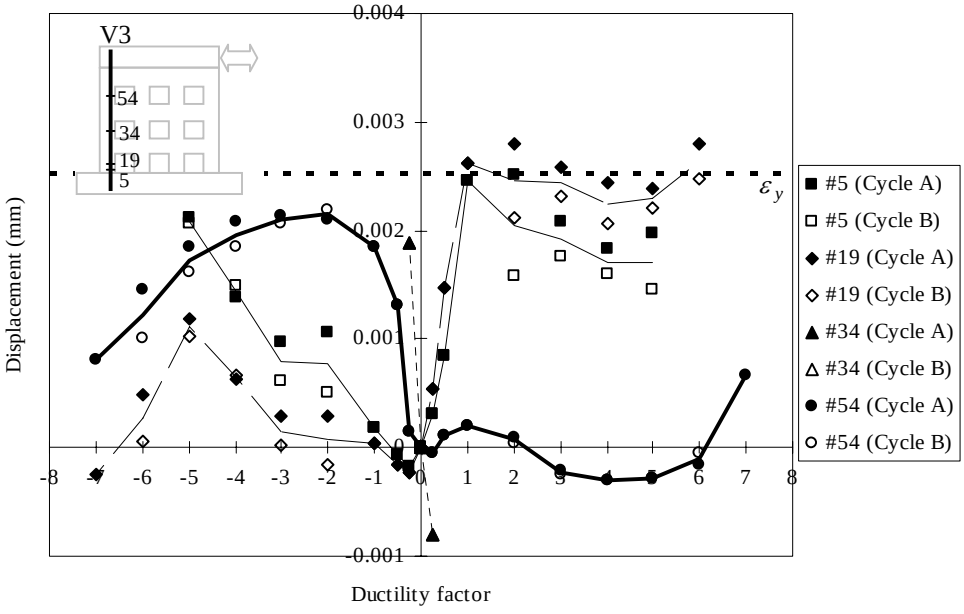

Figure 5.58 (b) Strain distribution of vertical Bar V3

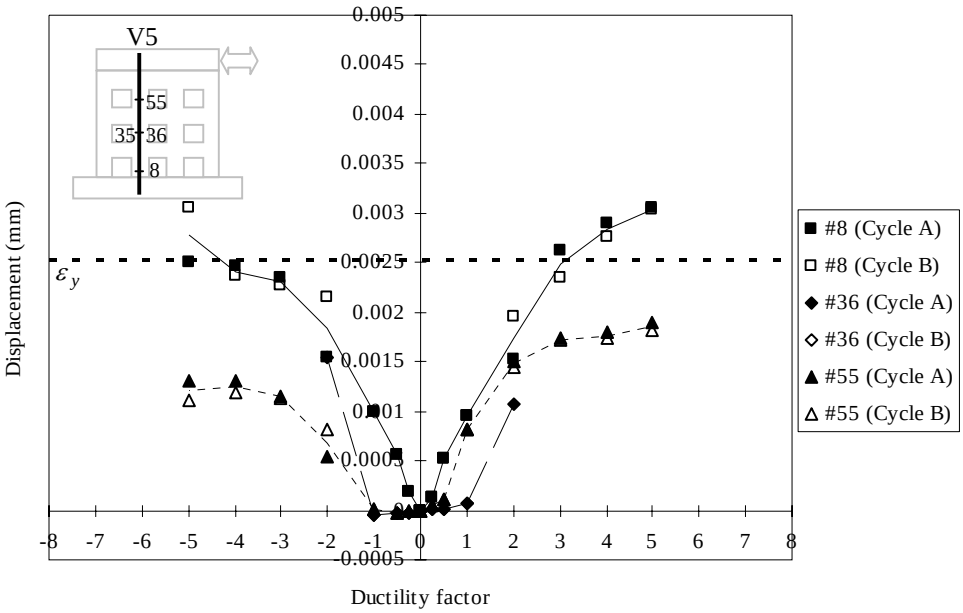

Figure 5.58 (c) Strain distribution of vertical Bar V5

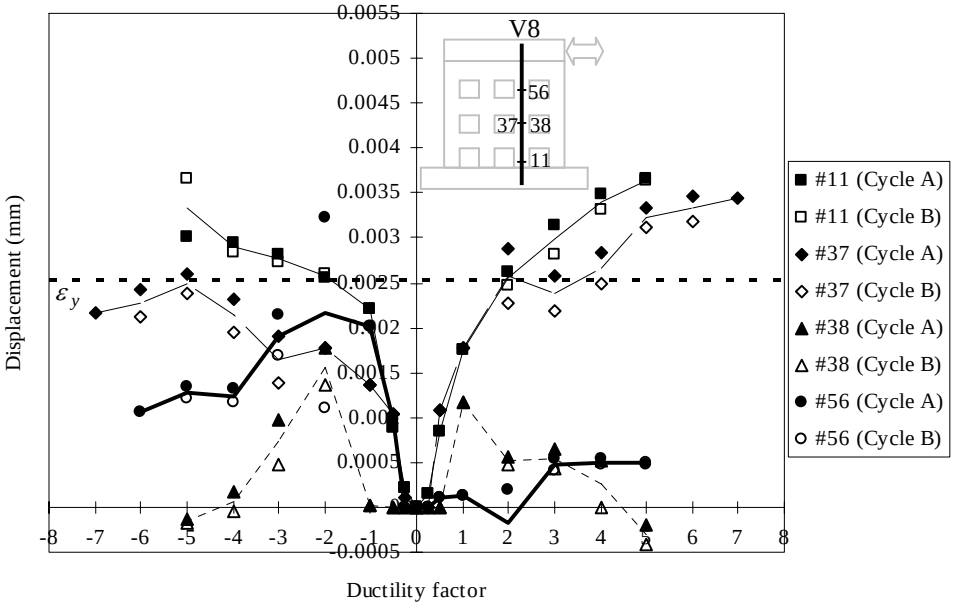

Figure 5.58 (d) Strain distribution of vertical Bar V8

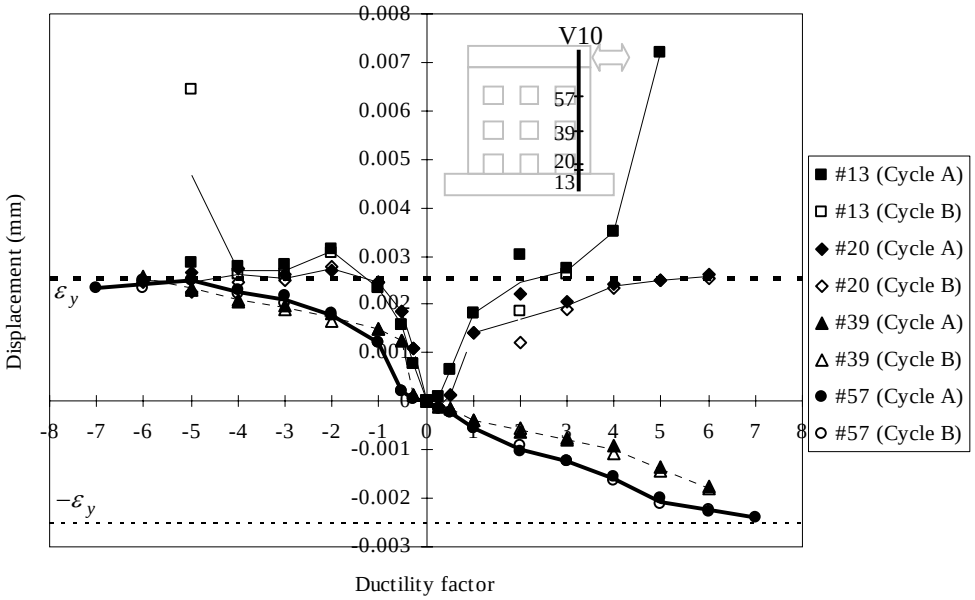

Figure 5.58 (e) Strain distribution of vertical Bar V10

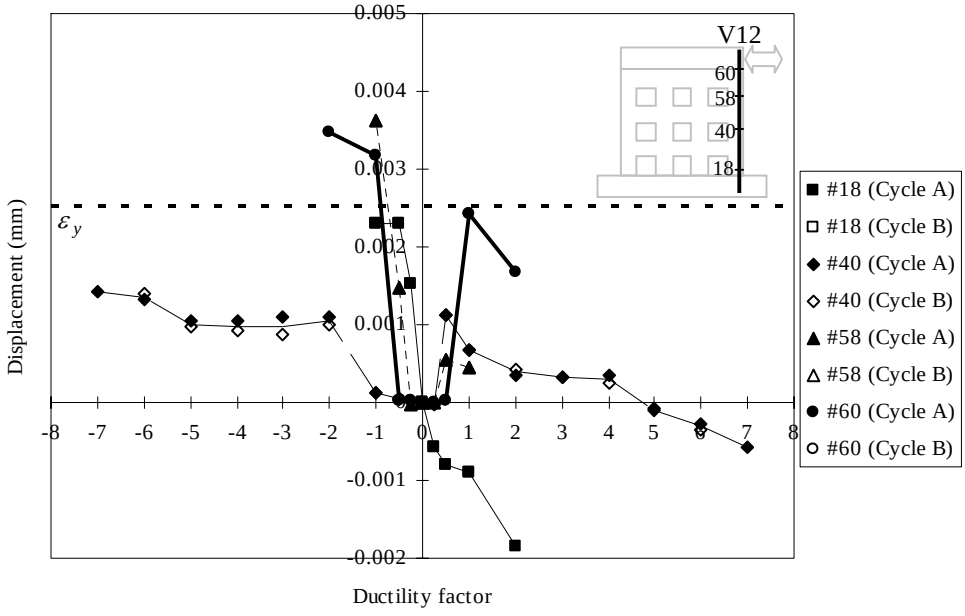

Figure 5.58 (f) Strain distribution of vertical Bar V12

Figure 5.58: Strain distributions of some vertical reinforcing bars

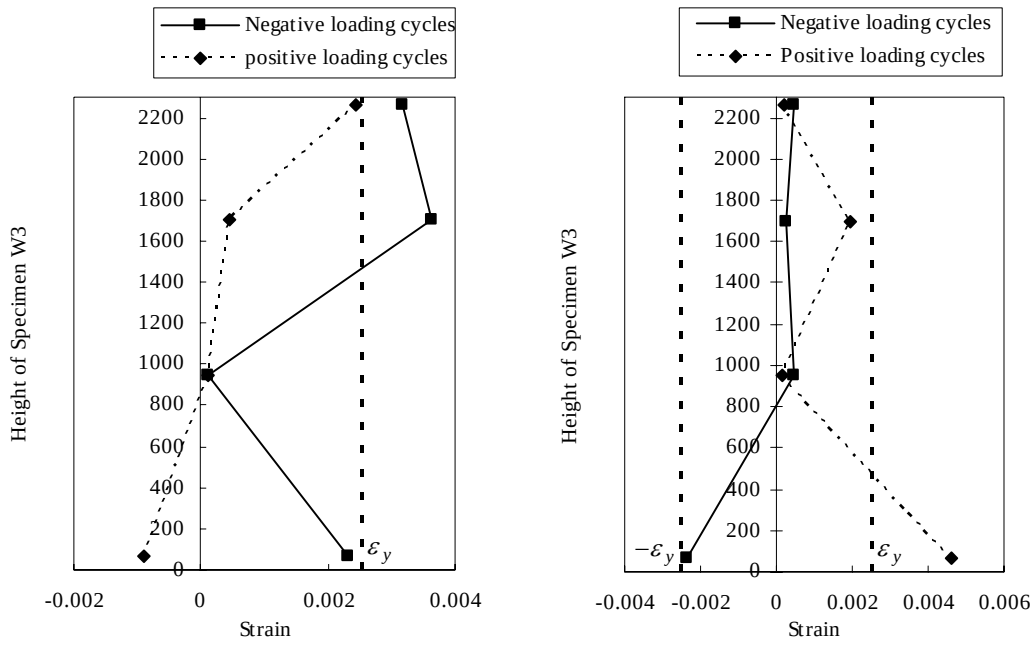

(a) Bar V1 at $DF = \pm 1$ (b) Bar V12 at $DF = \pm 1$

Figure 5.59: Strain profiles of Bars V1 and V12 at $DF = \pm 1$

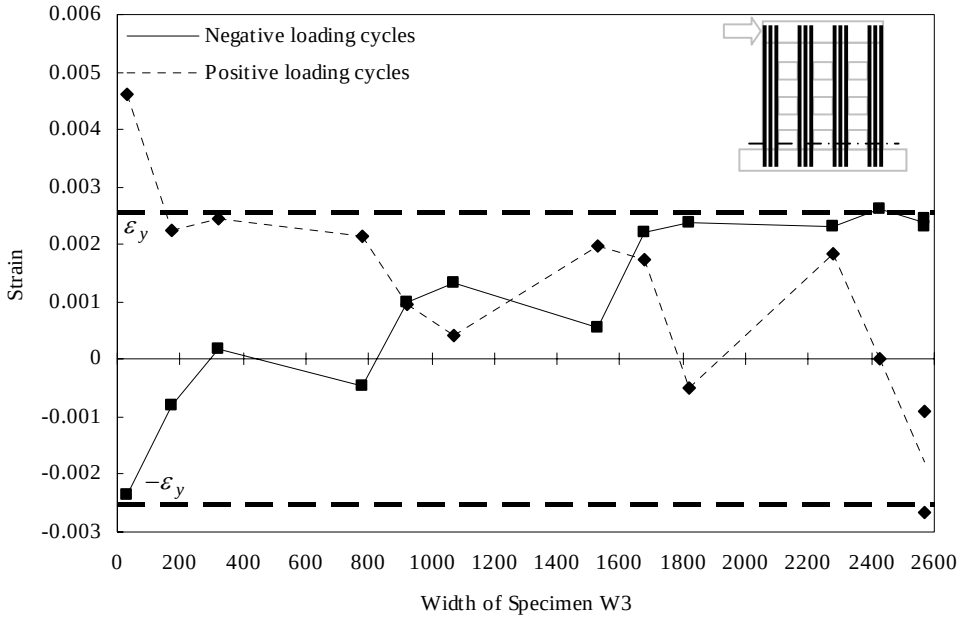

Figure 5.60: Strain profiles of reinforcing bars along the bottom of web

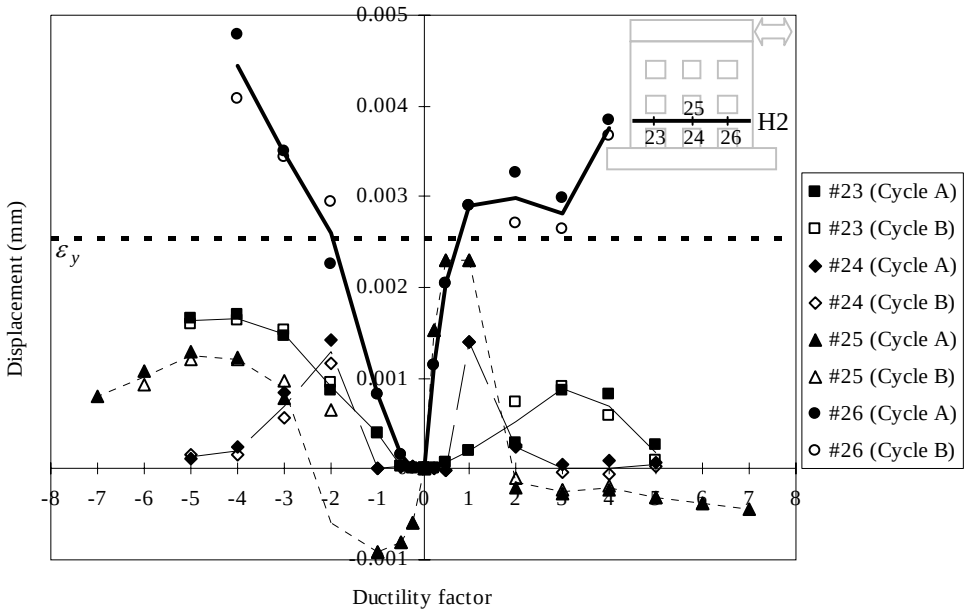

(a) Bar H2

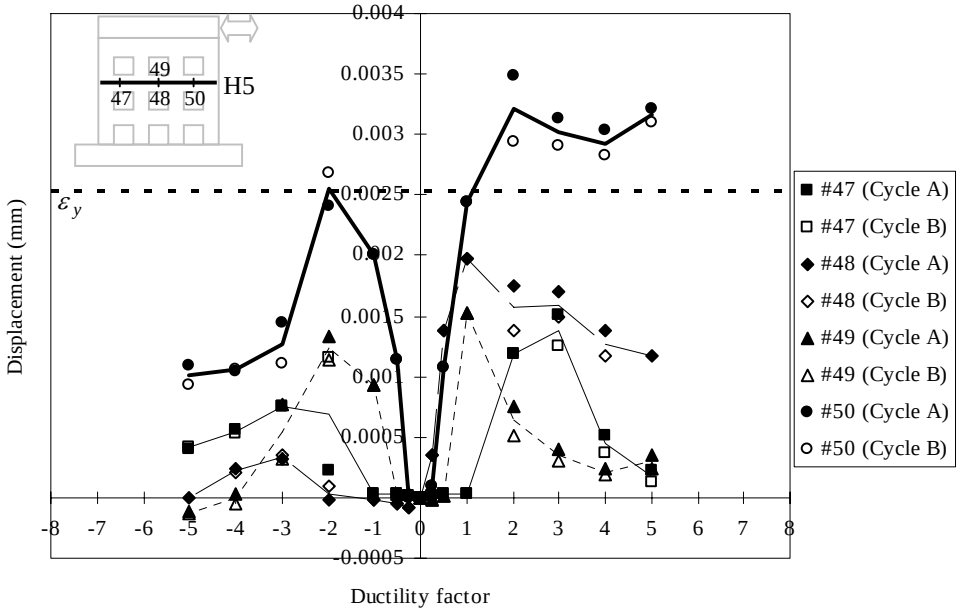

(b) Bar H5

Figure 5.61: Strain distributions of some horizontal reinforcing bars

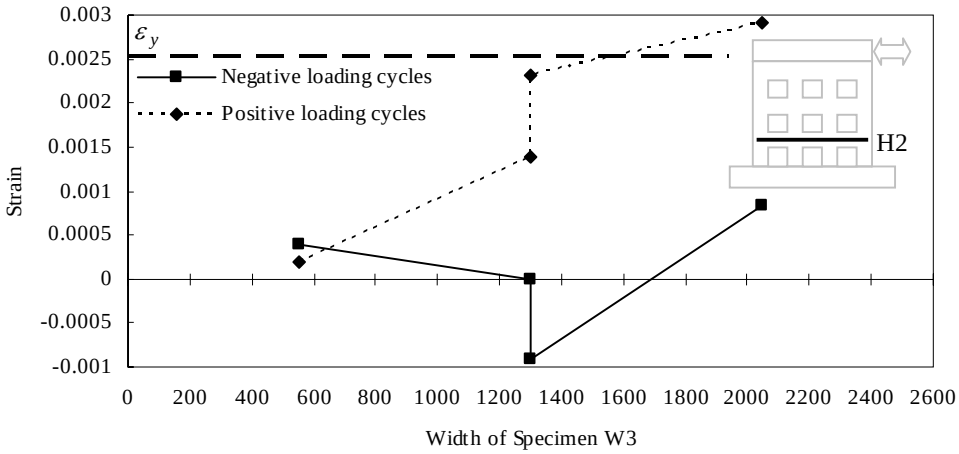

(a) Bar H2

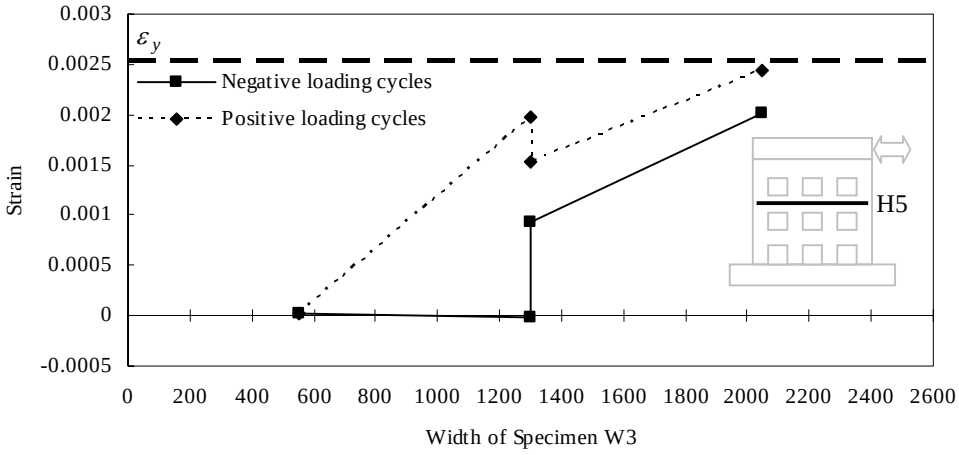

(b) Bar H5

Figure 5.62: Strain profiles along some horizontal reinforcing bars

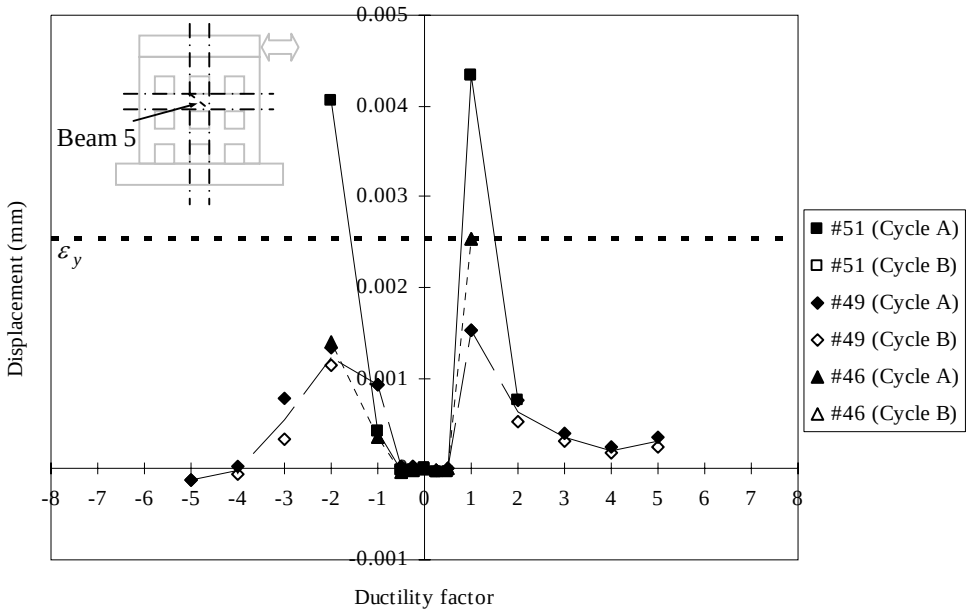

(a) Along the top right to the bottom left diagonal

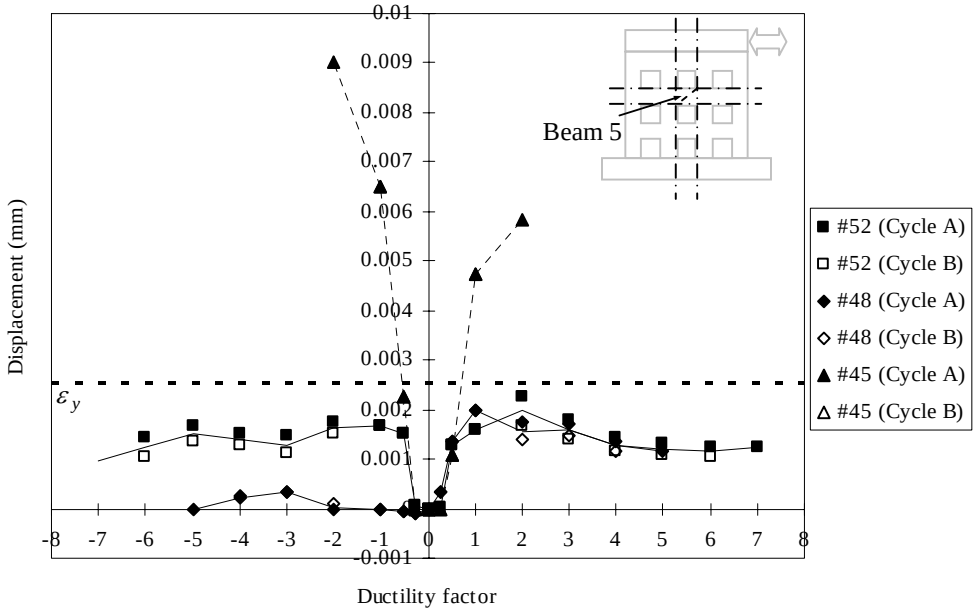

(b) Along the top left to the bottom right diagonal

Figure 5.63: Strains along diagonals of Beam 5

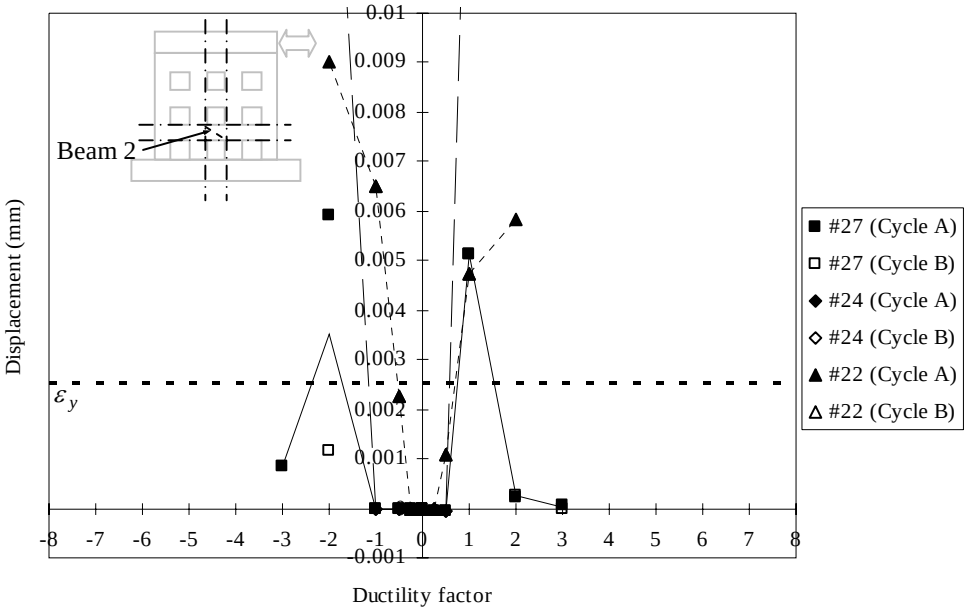

(a) Along the top right to the bottom left diagonal

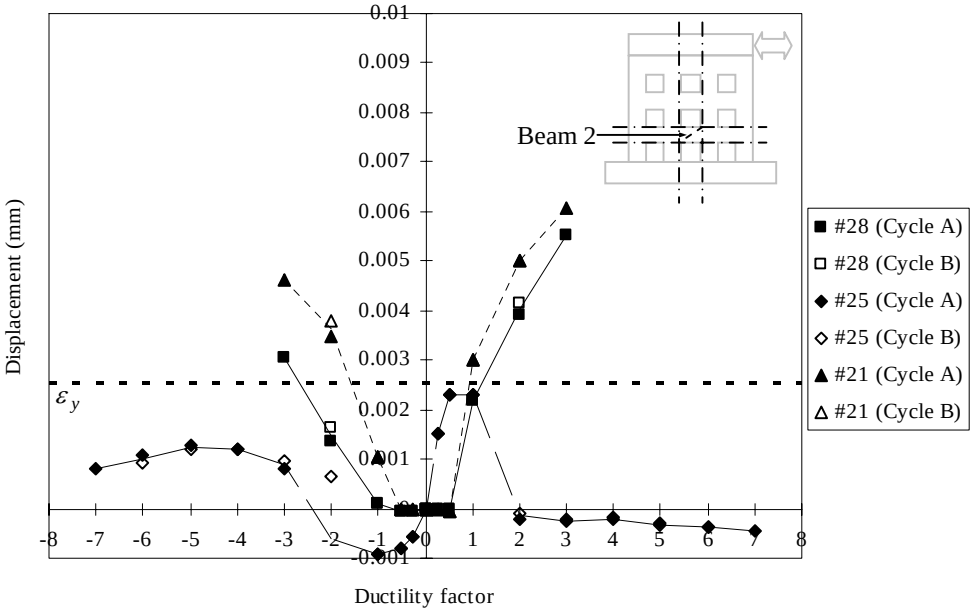

(b) Along the top left to the bottom right diagonal

Figure 5.64: Strains along diagonals of Beam 2

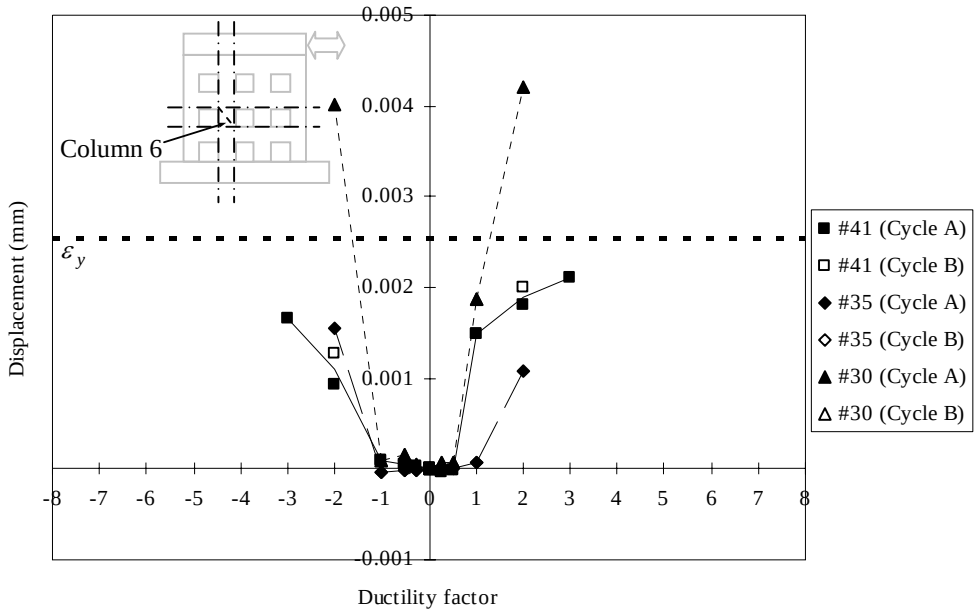

(a) Along the top right to the bottom left diagonal

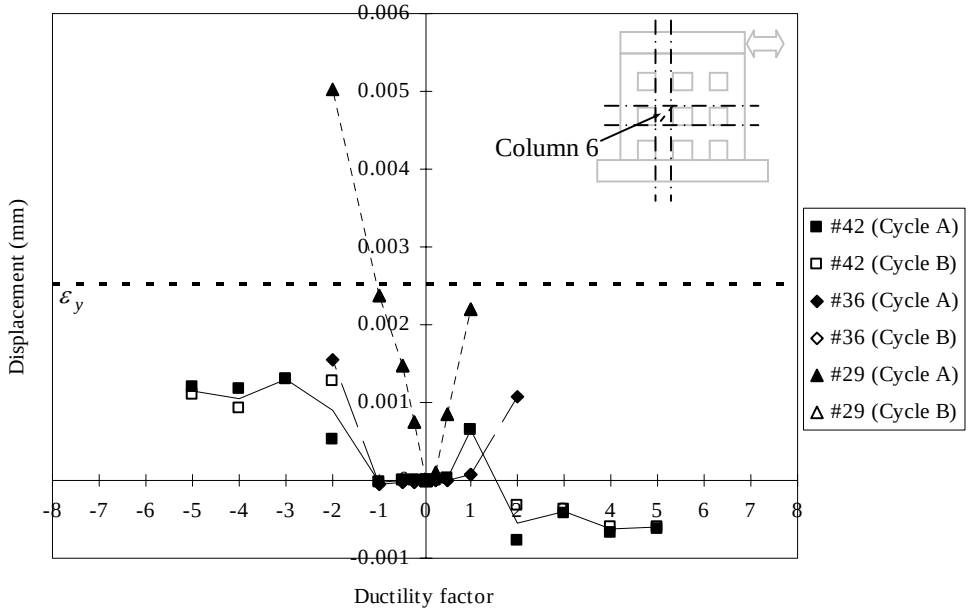

(b) Along the top left to the bottom right diagonal

Figure 5.65: Strains along diagonals of Column 6

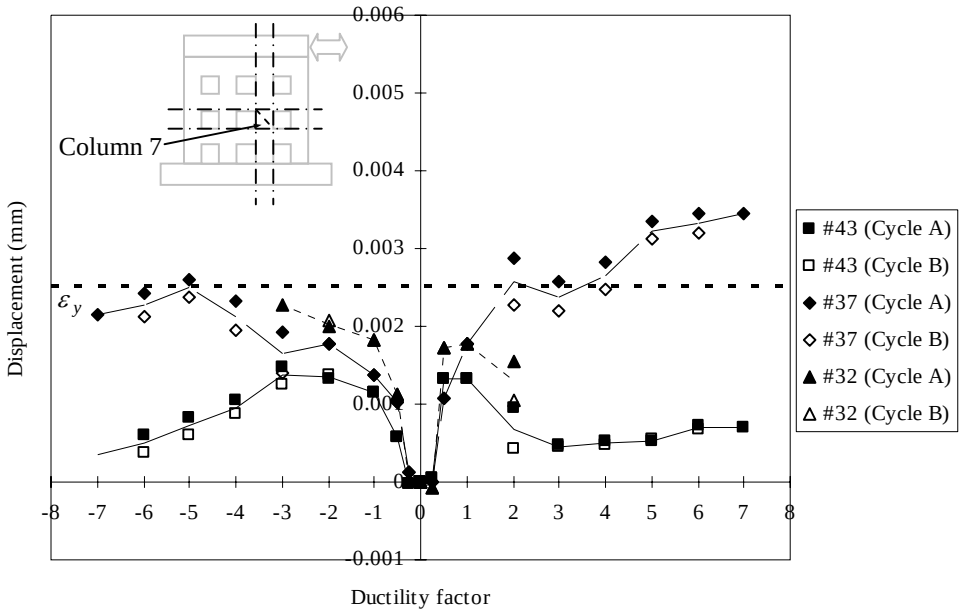

(a) Along top right to bottom left diagonal

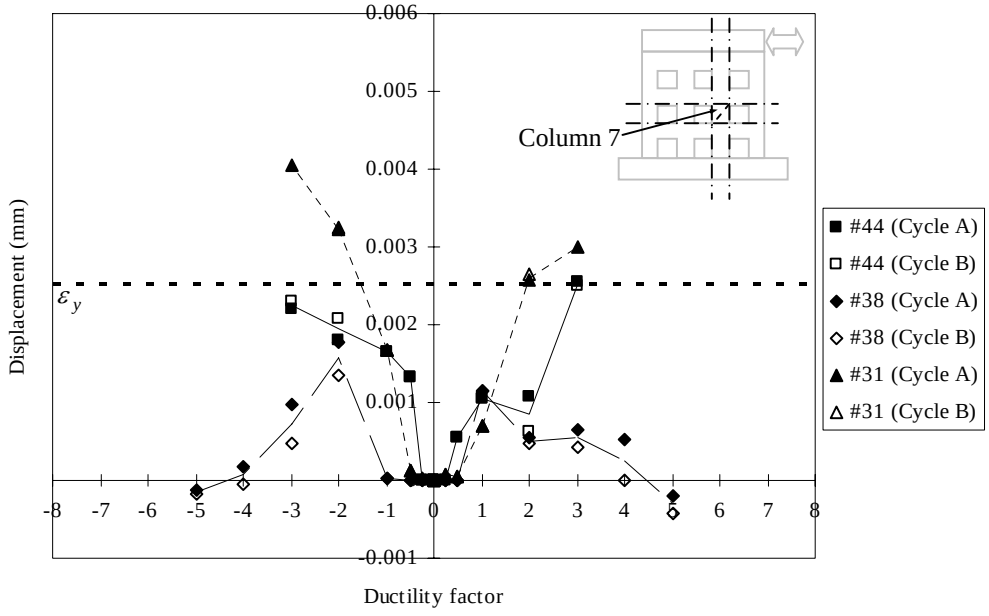

(b) Along the top left to the bottom right diagonal

Figure 5.66: Strains along diagonals of Column 7

5.10 Summary

In this chapter, a detailed knowledge about behaviour of reinforced concrete walls with opening under reversed cyclic loading has been obtained. Importantly, possible force transfer mechanism of each tested specimen has been seen through the experimental observation, especially the crack pattern. These understandings will help to develop the strut-and-tie model later. Hysteretic response, LVDT readings, and strain gauge readings of each wall specimen will be used in comparison with the analytical results to verify the validity of the strut-and-tie models.

CHAPTER 6

STRUT-AND-TIE ANALYSIS OF TESTED REINFORCED CONCRETE WALLS WITH OPENINGS

6.1 Introduction

This chapter aims to develop two different types of strut-and-tie models to analyze the wall specimens that have been tested in the experimental program. First all, a nonlinear finite element analysis is conducted upon each specimen to visualize more clearly and confirm the load paths that have been demonstrated through the crack patterns in the experiment. Then a comprehensive strut-and-tie model that utilizes the entire web of each specimen is developed to predict the overall response of the tested walls. Next, more refined strut-and-tie models are derived from the major load paths of the wall specimens with openings and capable of explaining the force transfer mechanism. Lastly, some recommendations are proposed regarding design using the strut-and-tie approach for reinforced concrete shear walls with openings.

6.2 Nonlinear Finite Element Analysis of the Tested Specimens

The Finite Element Method is frequently used in engineering and research investigations. Plenty of study has proved that it can successfully predict a wide range of behavior of reinforced concrete structures. However, a Finite Element Method cannot simply replace some other methods such as the strut-and-tie method, particularly in the design of reinforced concrete structures. This is because the Finite Element Method mainly focuses on giving the stress and strain distribution with a known structural configuration and reinforcement layout. So the finite element analysis has been used as a tool for analysis, rather than a tool for design as pointed out by Cook & Mitchell [C4]. The purpose of the finite element analysis in this research is to obtain more visible stress flow patterns to compare to the experimental observations of the reinforced concrete walls under the reverse cyclic loading. In turn these stress flow patterns will be used to identify

main load paths of the specimens which will help in setting up strut-and-tie models in later sections in this chapter.

6.2.1 Introduction the finite element analysis

Three tested reinforced concrete walls are analyzed with a nonlinear finite element program named UC-WIN/MESH & UC-WIN/WCOMD, which was developed by the University of Tokyo. This program consists of two sections: the interface section and the analysis solver section. The former is a tool for creating mesh and editing material property and the latter deals with the calculations of the two-dimensional nonlinear dynamic/static response of reinforced concrete structures. As this program is verified with accurate performance in the path-dependent two-dimensional static nonlinear analysis of various reinforced concrete structures, it is selected in this research as the tested walls are two-dimensional elements with significant nonlinearity.

The meshes of the finite element models of the reinforced concrete walls are generated by UC-WIN/MESH automatically. However, a few general principles should be followed when defining the properties of the elements in the mesh.

1) Different elements must be placed in accordance to different physical properties;
2) It is recommended that rectangular mesh should be used;
3) The side length of the rectangular mesh is around 100 mm to 300 mm. If the mesh size is too large, the analysis may become unstable;
4) Finer mesh size should be defined in regions with stress concentration. Larger elements would be adequate in low stress areas;
5) In reinforced concrete plates, the meshes must be defined depending on the density of the reinforcement ratio. It is also expected that the centre of gravity of the mesh would coincide with that of the reinforcing bars in the mesh, especially for main reinforcing bars.

By taking these principles into consideration, the mesh of the three specimens were generated as shown in **Figures 6.1** to **6.3**.

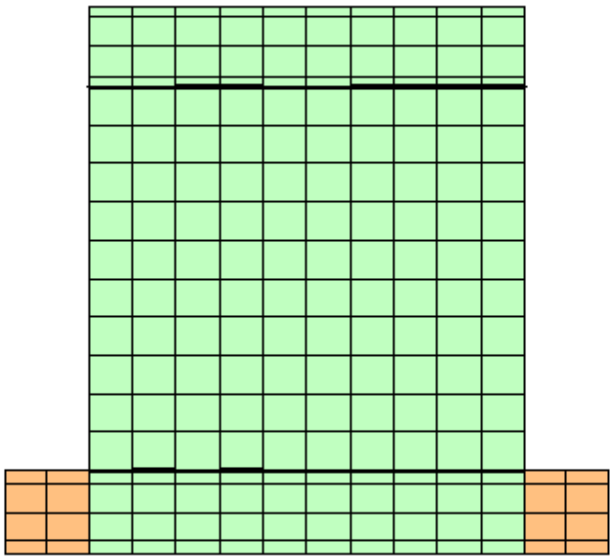

Figure 6.1: Mesh of Specimen W1

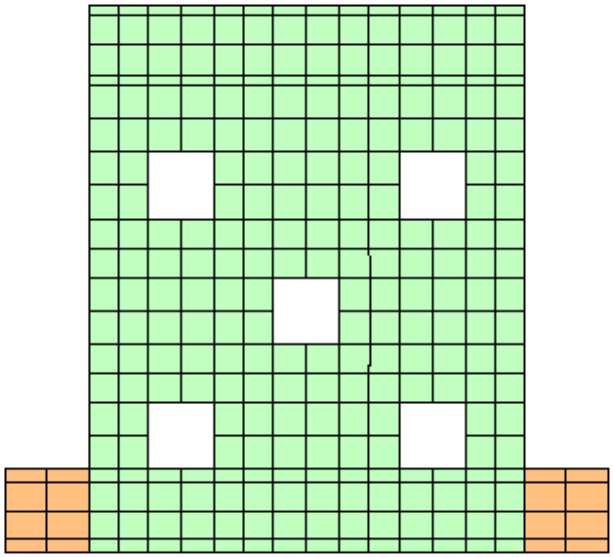

Figure 6.2: Mesh of Specimen W2

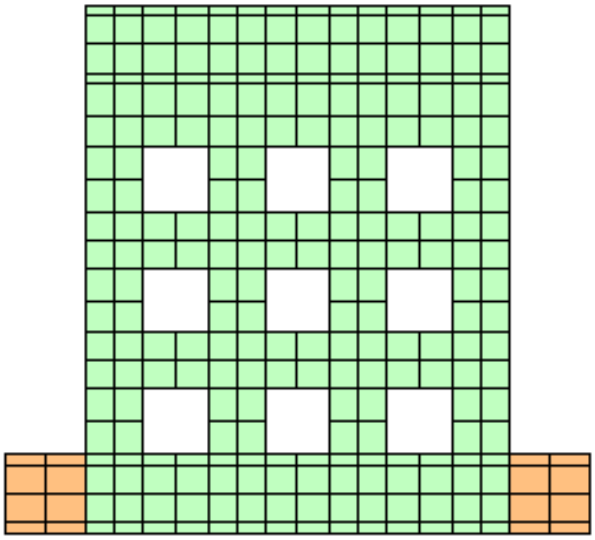

Figure 6.3: Mesh of Specimen W3

Every mesh generated should be matched with one plate type as defined by UC-WIN/MESH. There are four plate types available: Reinforced Concrete Plate, Plain Concrete Plate, Elastic Plate, and Soil Plate. The use of each plate is based on the actual physical properties of the reinforced concrete walls.

The advanced mode of the UC-WIN/MESH provides three criteria to determine the failure of the meshes. These failure criteria are maximum tensile strain normal to crack, maximum compressive strain parallel to crack, and maximum shear strain parallel to crack. These can be applied by the user according to the material properties. When one of the criteria is exceeded, the mesh is considered failed and the correspondent mode is presented for failure judgment.

6.2.2 Load-displacement responses of the tested specimens

The finite element analysis must be verified before the results of stress flows are used for further strut-and-tie models. Among all the parameters, the lateral load versus lateral displacement response is the most important measurement. So the finite element analysis for each specimen was loaded cyclically in the same way as it has experienced during the test. Due to the limitation of the program, the first three load-controlled cycles

were converted to the displacement-controlled ones. The comparison between the finite element analytical result and the experimental result of the load-displacement response for each wall specimen is shown and explained individually.

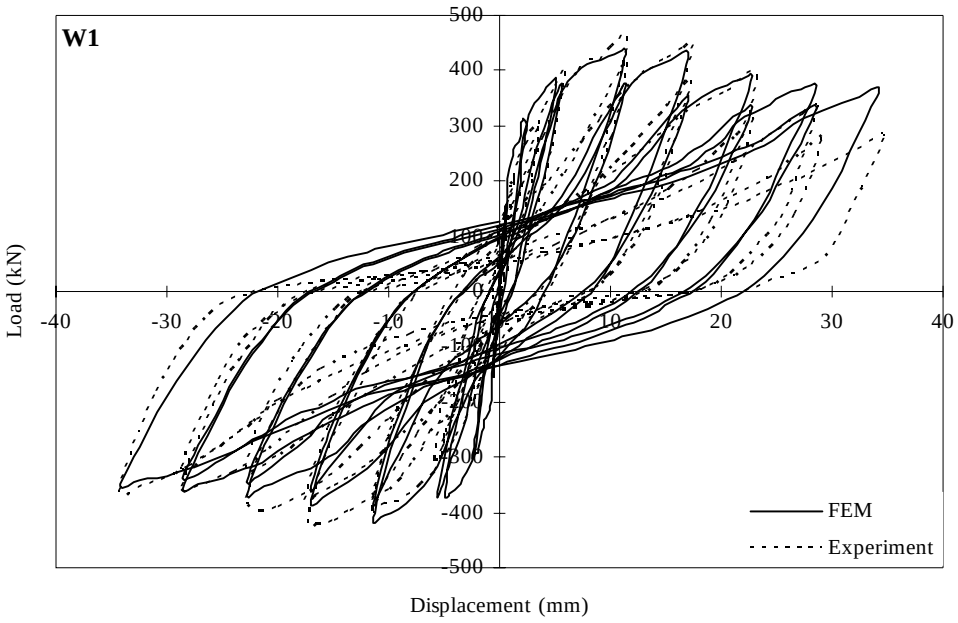

Figure 6.4: Comparison of finite element analytical and experimental load-displacement responses for Specimen W1

From Specimen W1, it is clearly seen that the analytical result is very close to the experimental one. The maximum strength achieved is at 5% tolerance to the experiment. The initial stiffness from the finite element analysis is 65.8 kN/mm, which is 8.5% larger than that from the experiment. A trend of strength degradation is observed in the finite element analysis which was also true from the experimental findings. Some discrepancies however also exist for the finite element analysis. The stiffness of the wall for the last three cycles, especially for the positive loading direction, is found to be larger than the experiment and as a result the energy absorption and dissipation capacity differed.

The comparison between the finite element analytical result and the experimental result of the load-displacement response for Specimen W2 is shown in **Figure 6.5**.

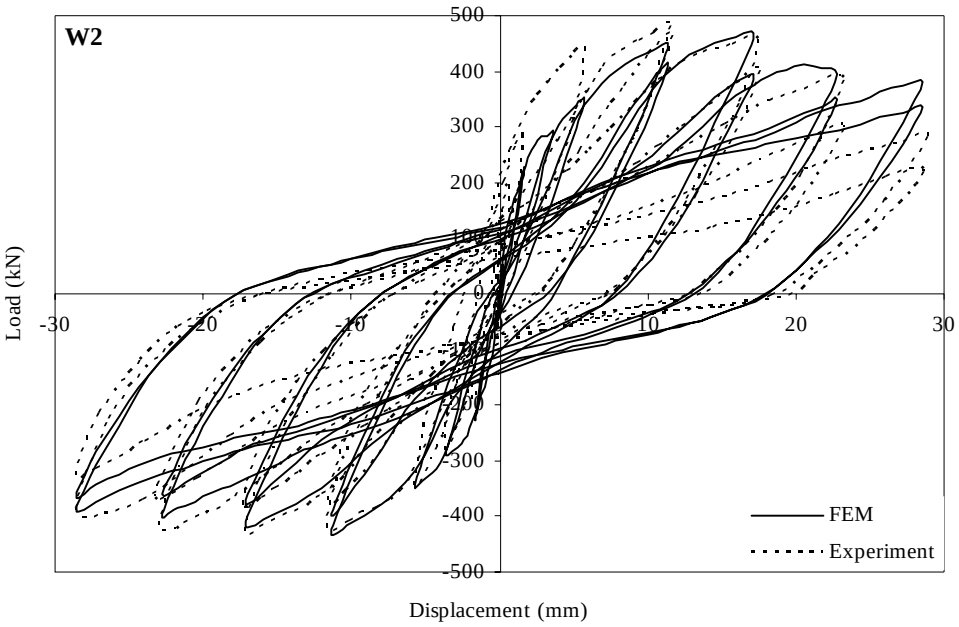

Figure 6.5: Comparison of finite element analytical and experimental load-displacement responses for Specimen W2

From this plot, it is clearly seen that the analytical result is very close to the experimental one. The maximum strength achieved is at 3% tolerance to the experiment. The initial stiffness from the finite element analysis is 61.6 kN/mm, which is 9.8% smaller than that from the experiment. The trend of strength degradation in the finite element analysis follows very closely to that in the experiment. Similar discrepancies in the analysis as Specimen W1 are also observed here. The stiffness of the wall for the cycles in the last two ductility factors is found to be larger than that in the experiment. Also then the energy absorption and dissipation capacity is different for the last two ductility levels.

The comparison between the finite element analytical result and the experimental result of the load-displacement response for Specimen W3 is shown in **Figure 6.6**.

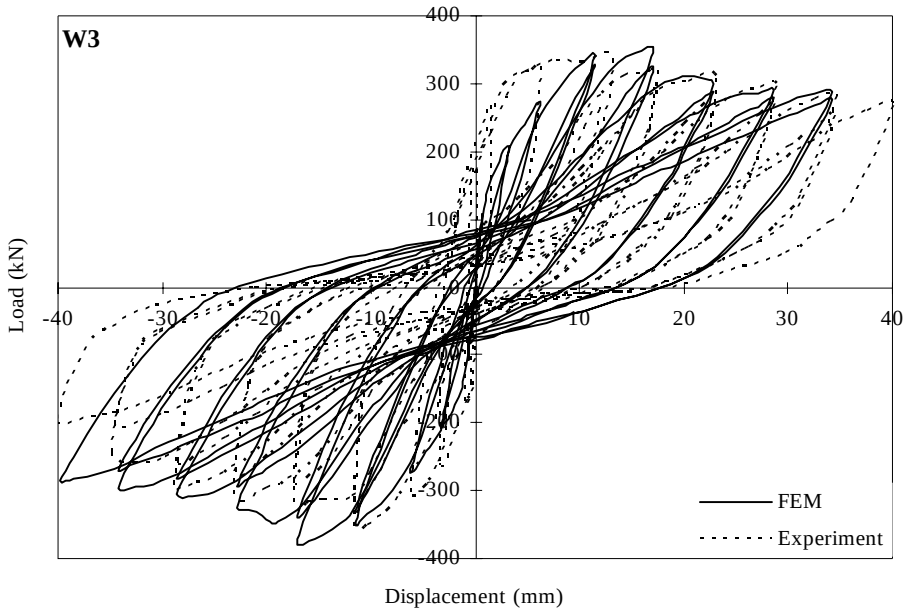

Figure 6.6: Comparison of finite element analytical and experimental load-displacement responses for Specimen W3

From **Figure 6.6**, it is seen that the analytical results match well with the experimental ones although the finite element analysis failed before the completion of the last cycle in the positive direction. The analytical result has larger strength as compared to the experiment, especially for the negative loading cycles, however the tolerance is only at 8%. The initial stiffness from the finite element analysis is 44.1 kN/mm, which is 13.2% smaller than that from the experimental one. A favorable trend of strength degradation is again observed in the finite element analysis and the stiffness discrepancy for the last a few cycles is improved in Specimen W3 as compared with the other two specimens. As a result, the energy absorption and dissipation capacity is closer to the actual conditions.

However, the validity of the finite element analysis results is sufficiently proved from the load-displacement response.

6.2.3 Crack patterns of the tested specimens

The crack pattern of the specimen is essential in indicating the possible internal stress flow during the experiment. In this section, the cracks predicted by the finite element analysis are compared with the experimental ones. **Figures 6.7** to **6.9** show that the analytical crack pattern of each specimen is similar to the experimental one. As the analytical crack pattern corresponds to the maximum negative displacement, the experimental crack pattern only shows the cracks from the negative loading cycles. It should be noted that in the program UC-WIN/WCOMD the cracks are dispersed spatially into each gauss point, and they do not represent the cracking location or the crack opening width exactly because they are based on the smeared crack model.

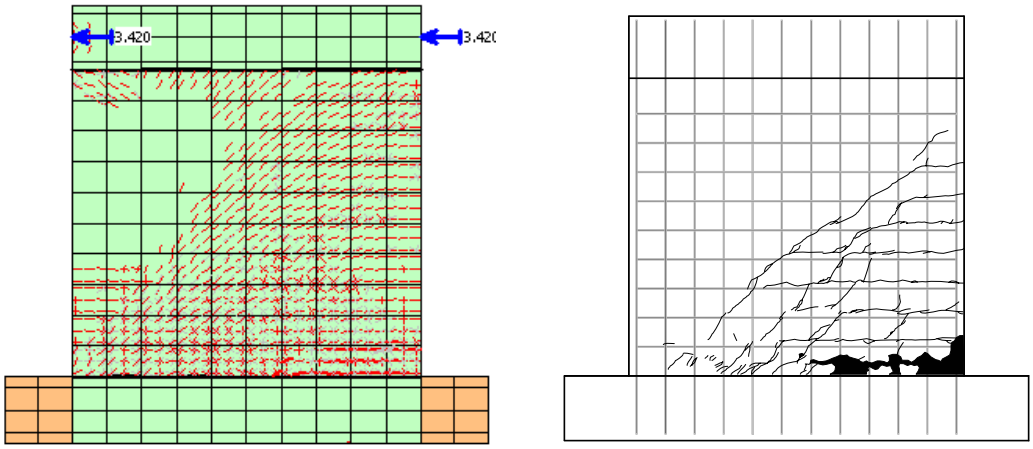

Figure 6.7: Analytical and experimental crack patterns of Specimen W1

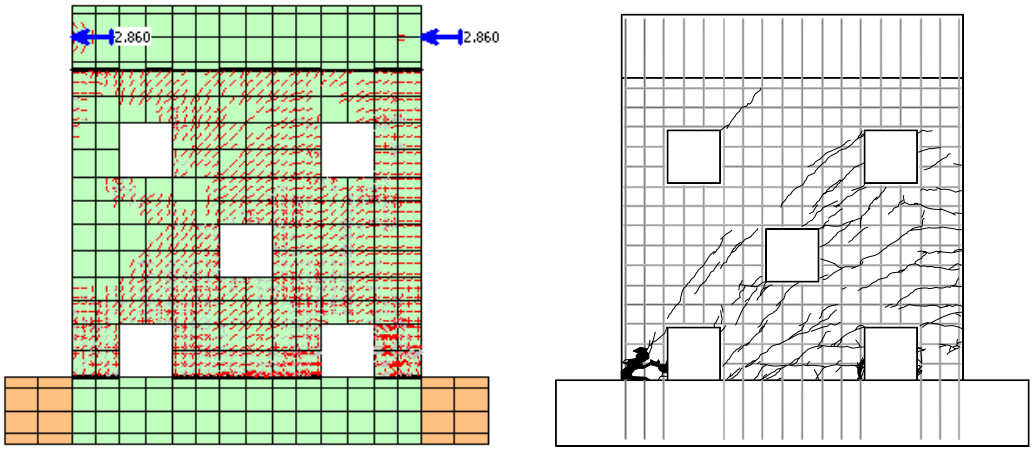

Figure 6. 8: Analytical and experimental crack patterns of Specimen W2

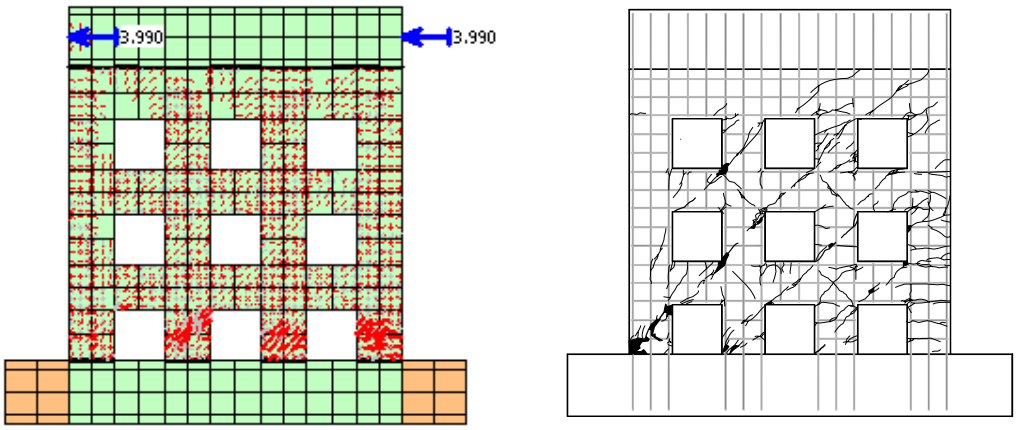

Figure 6.9: Analytical and experimental crack patterns of Specimen W3

6.2.4 Analytical stress flow patterns of the tested specimens

As demonstrated through the analytical load-displacement responses and crack patterns, the proposed finite element method generates reliable results, thus the visualized stress flow pattern of each specimen from the finite element analysis can be taken as further indications for possible strut-and-tie models. **Figure 6.10** shows the principle tensile and compressive stress flow of Specimen W1. It is found that the principle stress flow varies for different ductility levels. **Figure 6.10 (a)** is the stress flow pattern after the first loading cycle. It can be seen the compressive and tensile stresses are linearly distributed along the horizontal section on the web of the wall specimen. However, at $DF = \pm 1$ as shown in **Figure 6.10 (b)**, the compressive stress flow gives a distinct strut mechanism that directly transfers the load from the loading point to the support. The pattern of stress flow developed further at failure as shown in **Figure 6.10 (c)**. The compressive stress flow is obviously fan-shaped, dispersing out from the bottom edge of the web. Later the strut-and-tie model for Specimen W1 will try to capture this behavior.

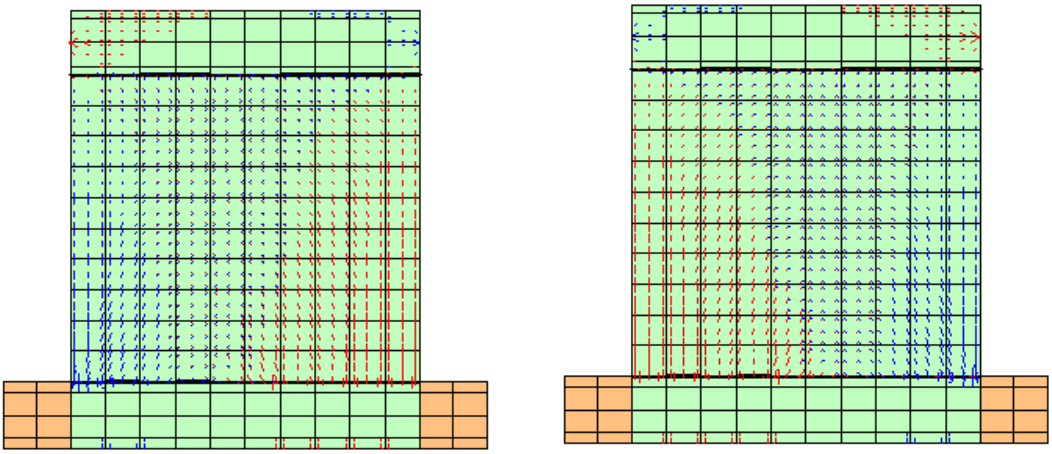

(a) At $0.25P_i$

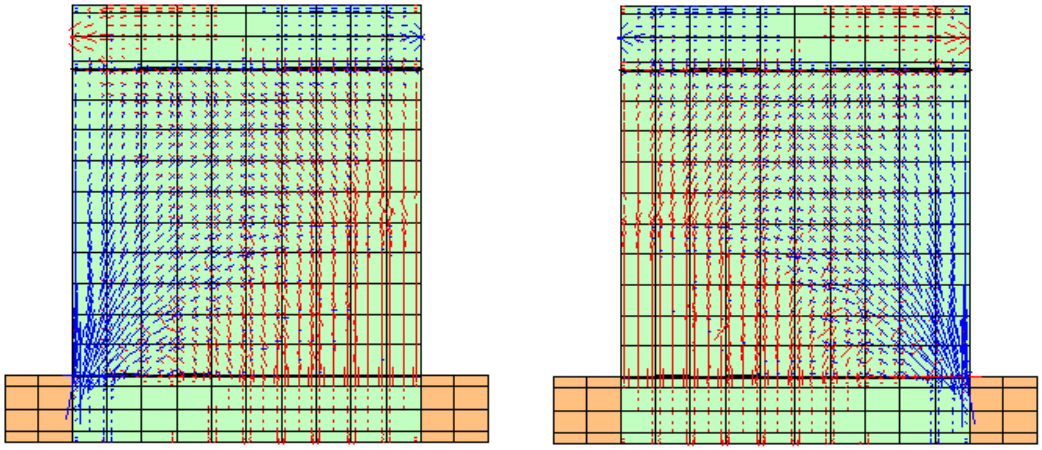

(b) At $DF = \pm 1$

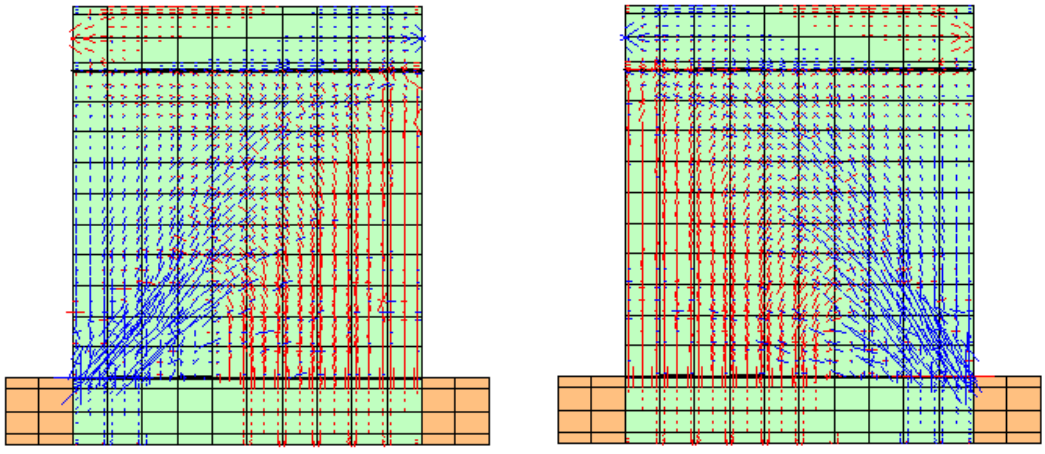

(c) At $DF = \pm 6$

Figure 6.10: Stress flow patterns of Specimen W1

Figure 6.11 shows the principle tensile and compressive stress flow of Specimen W2. Five regularly placed openings in Specimen W2 regulate the stress flow in the web so that ever since the beginning of the loading, the stress flow follows a definite pattern. Throughout the loading history, the stress flow only intensifies and grows in width. A stream compressive stress flows through Panel 1 and Panel 2 and further extends into the right bottom column zone for the negative loading direction. An identical pattern of compressive stress flow happens in Panel 1 and Panel 3 and then into the left bottom column zone for the positive loading direction. The two paths of stress flow in the respective loading direction should be the main mechanism that transfers the lateral load to the foundation beam. Stress flow patterns in the panel zones on the web are of major importance. It can be seen that bottle-shaped compressive stress flow patterns are developed in the three panel zones. Another minor compressive stress flow is observed at Panel 4 at the bottom of the web for both loading directions. This stress flow is a fan-shaped pattern and connected to a stream of vertical tensile stress flow in the middle of the web. These bottle-shaped and fan-shaped stress flow patterns will have their respective representation in the strut-and-tie model proposed for Specimen W2 later.

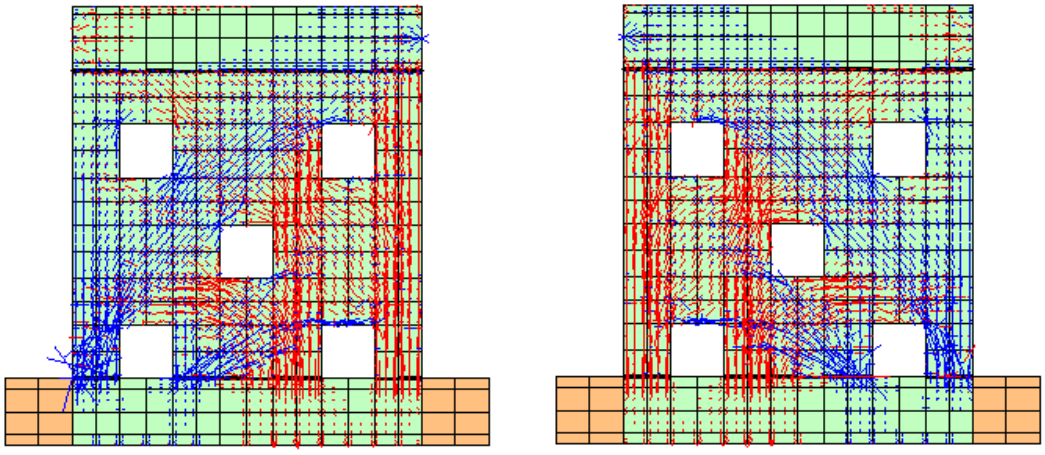

Figure 6.11: Stress flow patterns of Specimen W2

Figure 6.12 shows the principle tensile and compressive stress flow patterns of Specimen W3. The nice evenly distributed openings in the web further regulate the stress flow of Specimen W3 as compared to Specimen W2. In this specimen, sophisticated fan-shaped and bottle-shaped compressive stress flow patterns are not

found. Instead a very simple pattern of stress flow prevails directly along the diagonals of the beam and column zones. These stress flows along the diagonals connects to each other and three very obvious paths of load transfer are shown thus corresponding well with the experimental crack pattern. This pattern of stress flow indicated a direct strut mechanism along the diagonals of the beam and column zones, which will be modeled later in the strut-and-tie models of Specimen W3.

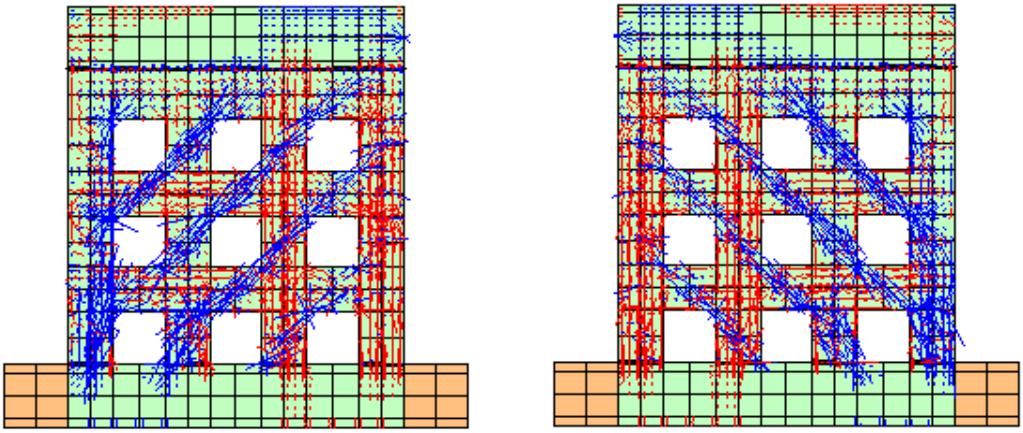

Figure 6.12: Stress flow patterns of Specimen W3

6.3 The Strut-and-Tie Models to Predict the Overall Responses of the Specimens

In the previous section, stress flow patterns of all the specimens have been visualized more clearly and compared with experimental evidences to prove their reliability after which the strut-and-tie approach is then used to analyze the specimens in this section. The strut-and-tie model is developed to predict the overall response of each specimen, especially their displacement and stiffness as well as reflecting the actual stress flow pattern that has been demonstrated in the finite element analysis as closely as possible towards better prediction of each specimen. Members in the models will be assigned with physical properties that are identical to the experiment. Then the strut-and-tie models will be analyzed with the DRAIN-2DX, which has been used previously in Chapter 3 and the analytical results are compared with experimental ones to verify the strut-and-tie approach.

6.3.1 Model setup

The purpose of the strut-and-tie models is to predict the overall response of all the specimens. Thus, the model should utilize the entire web section of each specimen that has participated in the force transfer mechanism. That is to say the web of each wall should be carefully modeled as a strut-and-tie system and the top and foundation beams should be modeled as boundary conditions that provide the restrains. The strut-and-tie model in the web should be a realistic reflection of the stress flow pattern of each specimen which was induced by the reverse cyclic loading. The stress flow pattern that corresponds to the ultimate stage for the negative loading cycles of each specimen from the finite element analysis is shown here again with one main path being identified.

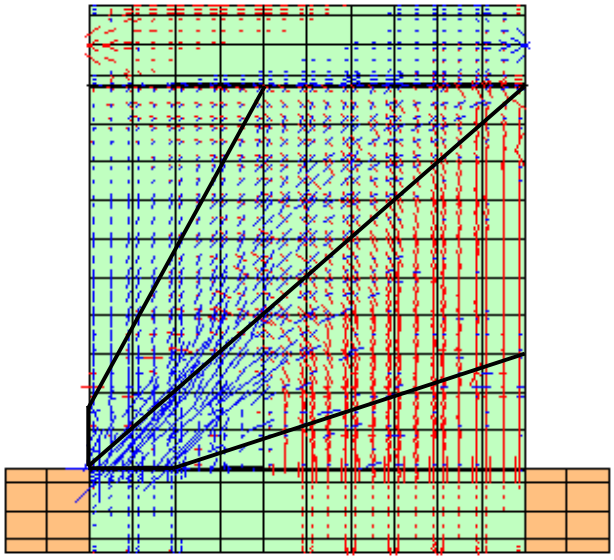

Figure 6.13: Identification of the main path in stress flow pattern of Specimen W1

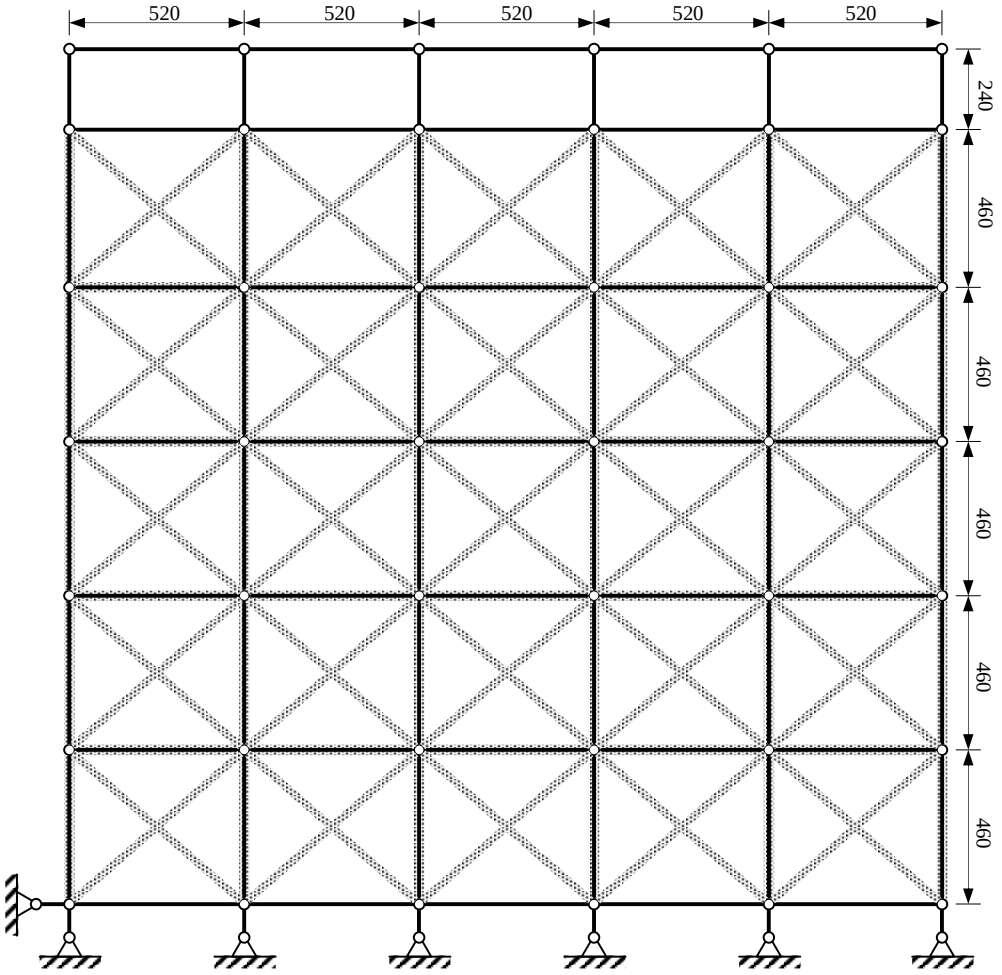

Figure 6.14: The strut-and-tie model of Specimen W1

For Specimen W1, the fan-shaped stress flow is highlighted. Moreover, it also experienced changes in the pattern of the stress flow. Therefore, the strut-and-tie model for it should capture all the three main patterns of stress flow so that the model is expected to be a comprehensive one that is able to give all these options. Hence, the strut-and-tie is proposed as shown in the **Figure 6.14**. The web of Specimen W1 is divided into small strut-and-tie units and configured to offer more possible paths to transfer the lateral load. Besides the direct strut mechanism, the fan-shaped stress flow is included in as much as possible.

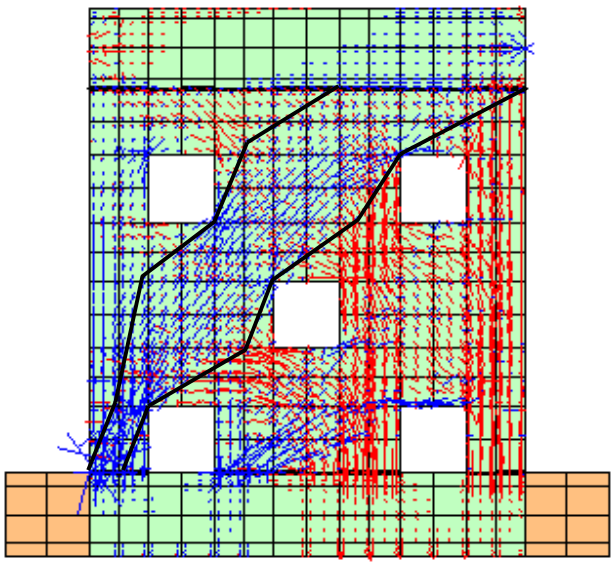

Figure 6.15: Identification of the main paths in stress flow patterns of Specimen W2

In Specimen W2, the five regularly placed openings naturally zone the web of the wall into four panels and the stress flow in each panel is regulated as shown in **Figure 6.15**. The two bottle-shaped stress flows in the panel zones are highlighted, hence the configuration of the developed strut-and-tie model is restrained to have the form as shown in **Figure 6.16**. It can be seen that the bottle-shaped compressive stress flow pattern in the upper three panel zones is well represented in the model and that the minor fan-shaped compressive stress flow at the bottom panel is also considered. Importantly, the area and the position of each opening are maintained.

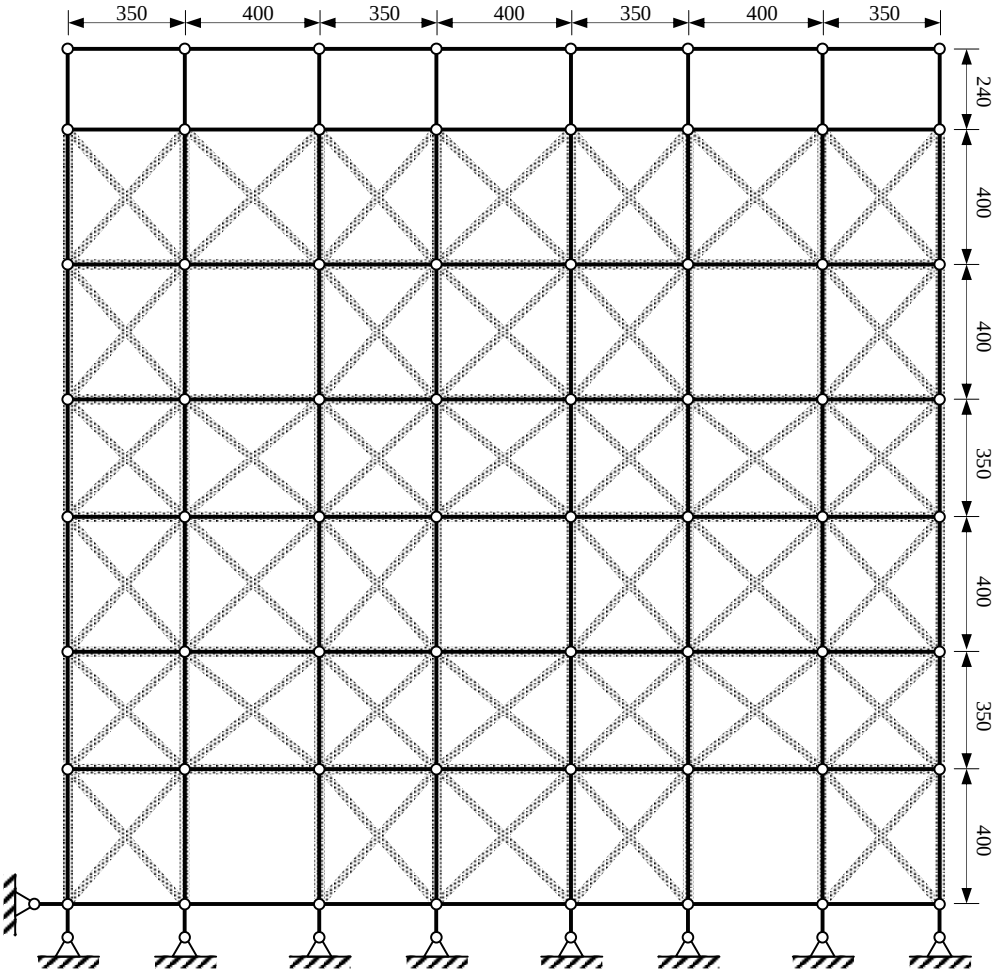

Figure 6.16: The strut-and-tie model of Specimen W2

.In Specimen W3, the nine evenly distributed openings zone the web of the wall into the small beam zones, column zones, and joint zones connecting them. The pattern of stress flow is very regular to be along the diagonals of the beam and column zones and can be recognized as nearly prismatic in shape. The strut-and-tie model for this specimen is conveniently established as shown in **Figure 6.18**. As can be seen, a diagonal strut mechanism is used to represent the stress flow pattern in each beam and column zone and thus the three main paths of stress flow are accurately outlined in this way.

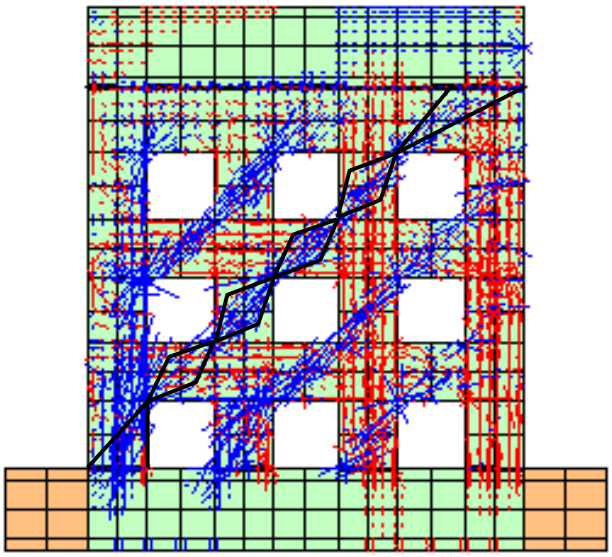

Figure 6.17: Identification of the main paths in stress flow pattern of Specimen W3

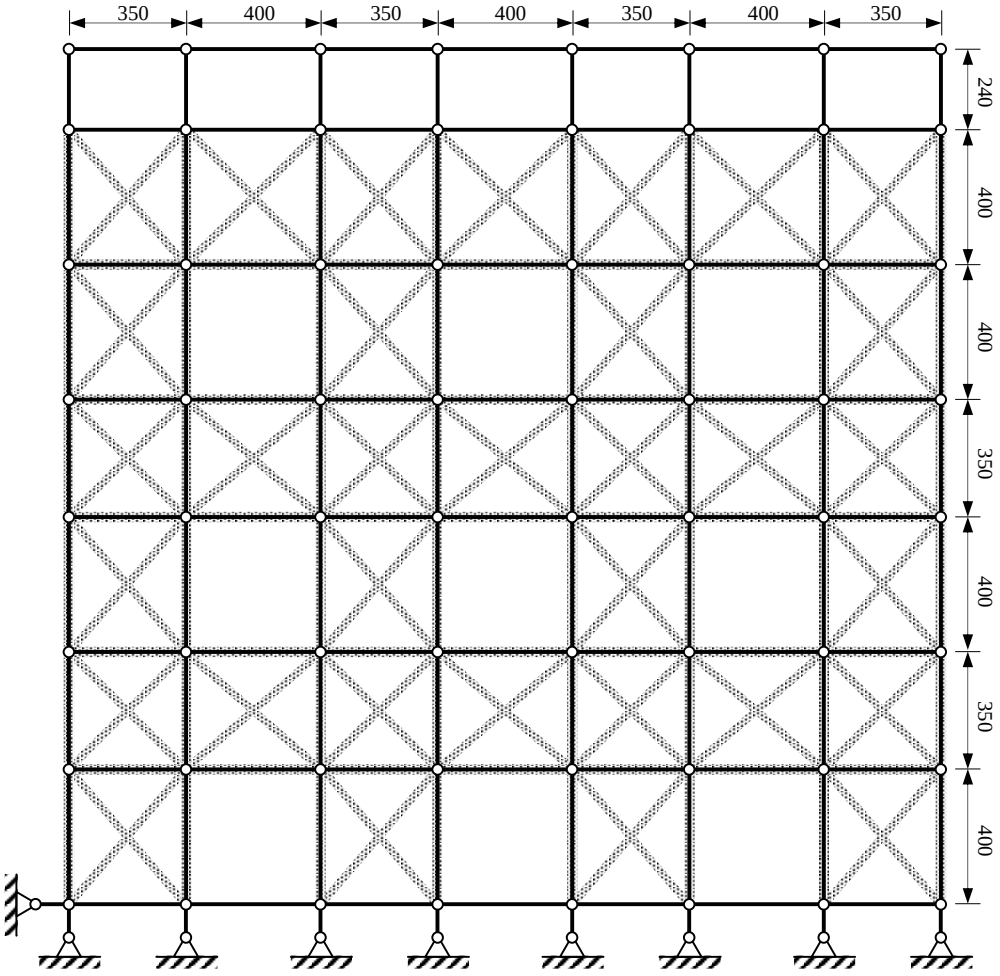

Figure 6.18: The strut-and-tie model of Specimen W3

In all the drawings of the strut-and-tie models, full lines are ties which represent reinforcement and are tensile members whereas dotted lines are struts which represent concrete and are compressive members. The ties are all vertical and horizontal which is according to the orthogonal reinforcement layout of the specimens. Some struts are diagonal with different inclination angles and designed to transfer the imposed lateral load. There are some vertical and horizontal struts which intend to take the concrete contribution in flexure into account wherever applicable. The top beam is simplified as a few two-dimensional elastic panels which are designed for loading and have strong stiffness to avoid unnecessary deformation there. The foundation beam is equivalent to a few auxiliary members that provide the restrains to the model. These auxiliary members are very short in length and strong in stiffness. One end of each member is fixed in translation for both the x-axis and the y-axis and the other end is pin-connected to members in the strut-and-tie model of the web. The restrain conditions provided in this way are found to be sufficient as the analytical results later shown.

Physical properties, including material strength and geometry, are assigned to various members in the model. For the strut, the constitutive relationship of concrete follows **Figure 3.2**. The area of each diagonal strut is half of the available area along its transverse direction. For every vertical or horizontal strut, its area is determined by the spacing between the members. As explained in Chapter 3, the concept of "effective compressive stress of concrete" still applies to the strut in the strut-and-tie model for reinforced concrete walls. Thus, $0.72 f_c^{'}$ is taken for vertical and horizontal struts and $0.68 f_c^{'}$ is taken for diagonal struts. Ties consist of reinforcement in their nearby region according to the reinforcement layout. For Specimen W1, each tie is standardized to have the area of 4T10 bars, while for Specimens W2 and W3 each tie has the area of 3T10 bars. Furthermore, secondary reinforcement has been provided in Specimen W2. Those R10 bars are of large areas and should be lumped into nearby tie members. The stress-strain relationship of the reinforcement is shown in **Figure 3.3**. The short auxiliary members are ties which have a strong stiffness (infinite when compared to other ties). The elastic panels are taken to be steel and with infinite stiffness for

elongation, bending, and shear. All the information is formatted into the text input files of DRAIN-2DX. The analytical results will be shown below.

6.3.2 Analytical results of the strut-and-tie models

In DRAIN-2DX, each strut-and-tie model is loaded in a similar way as that of each specimen in the experiment. The difference is that the models are only loaded for one cycle for each ductility level from $DF = \pm 2$. The analytical results are presented individually for each specimen.

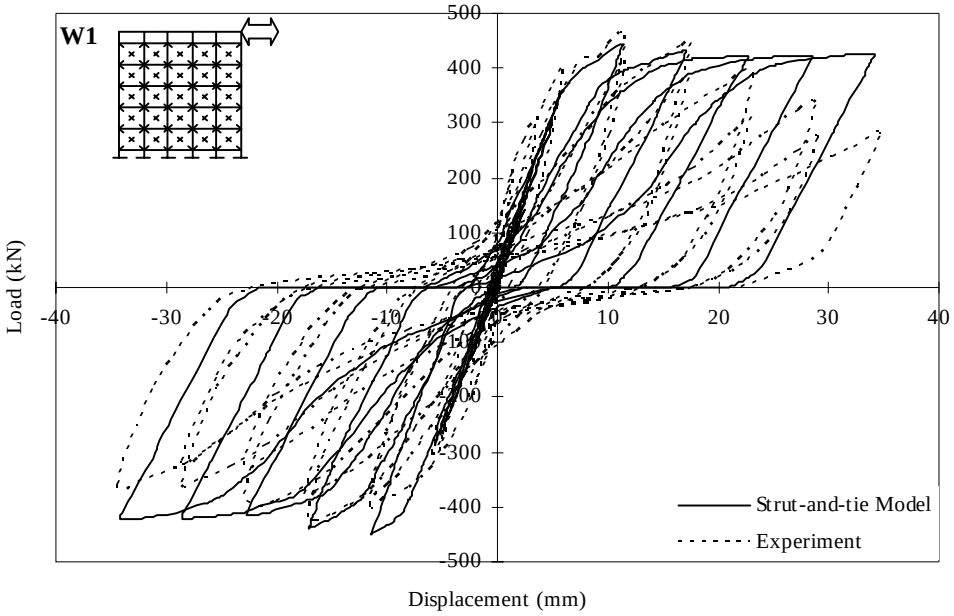

Figure 6.19: Comparison of strut-and-tie analytical and experimental load-displacement responses of Specimen W1

Generally, a smooth analytical lateral load versus lateral displacement response for Specimen W1 is obtained by the strut-and-tie model and compares well with the experimental one. The maximum strength prediction is accurate with a small discrepancy of 3%. The initial stiffness of the strut-and-tie model is 56.7 kN/mm, which is only 6.4% smaller than that from the experiment The strut-and-tie model tends to have a constant peak strength for each ductility level and the strength degradation is not observed as in the experiment. As a result, for the last two ductility factors, the

stiffness of the strut-and-tie model is larger than the actual specimen and the energy absorption and dissipation capacity is obviously different.

Next, the strains of a few ties in the strut-and-tie model of Specimen W1 are examined. These strains are plotted and compared with strain gauge readings in the similar locations as recorded during the tests. These plots can give a general trend of how these ties behave in the model and whether the behavior is reasonable against the experiment, but it should be noted that any particular tie strain from the strut-and-tie model is the average strain of the whole member, whereas the strain gauge in the test only measured the strain at a localized point along a reinforcing bar. To begin, the ties along the right and left edges of the strut-and-tie model will be shown in **Figure 6.20**.

These comparisons are made at $DF = \pm 2$. It is found that the tie strains in the strut-and-tie model follow a decreasing trend in magnitude along their height but remain relatively invariant. The analytical tensile strains achieved are of the similar magnitude to the readings from the experiment and show yielding of some ties at the bottom. However, the compressive strains are smaller than the experiment, especially at the right edge for the negative loading cycles.

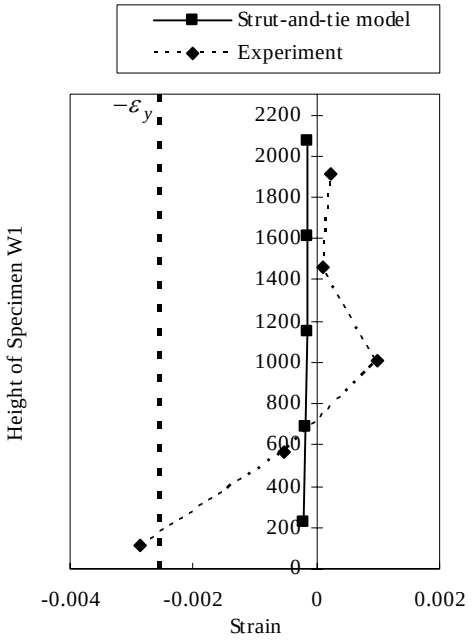

(a) Right edge in negative loading cycles

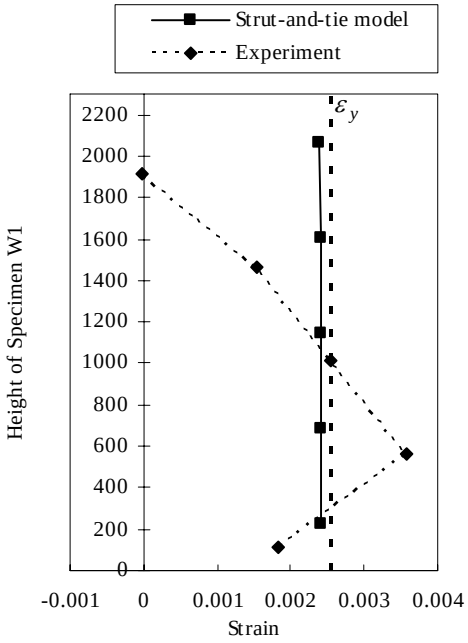

(b) Right edge in positive loading cycles

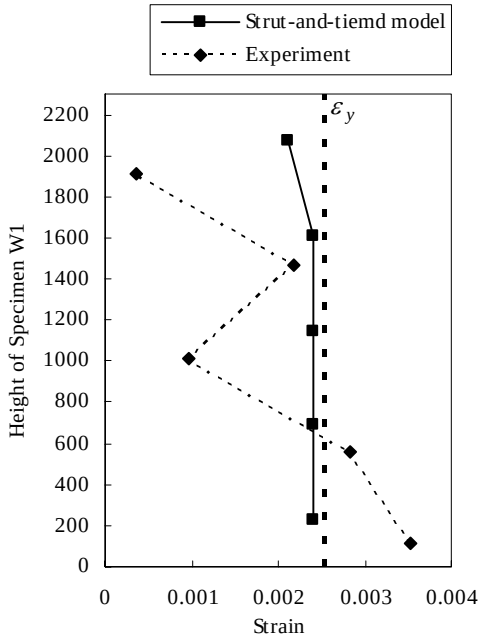

(c) Left edge in negative loading cycles

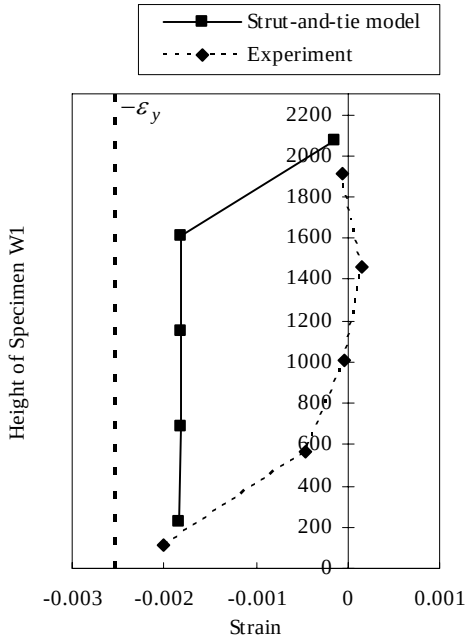

(d) Left edge in negative loading cycles

Figure 6.20: Comparison of strut-and-tie analytical and experimental vertical strain profiles of Specimen W1

Secondly, **Figure 6.21** shows the strain profile along the bottom horizontal section of the strut-and-tie model as compared to the experiment.

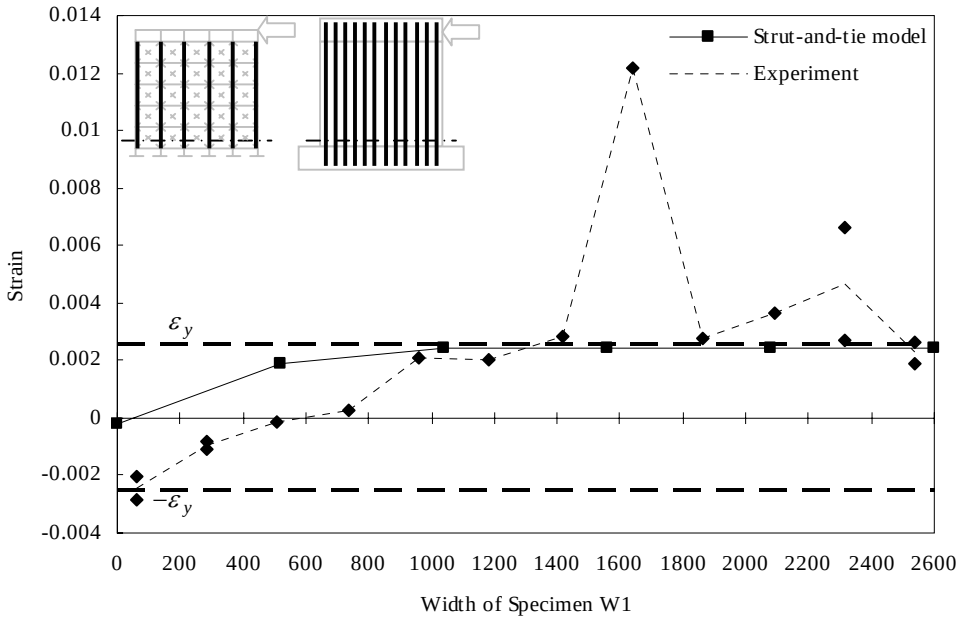

(a) For negative loading cycles

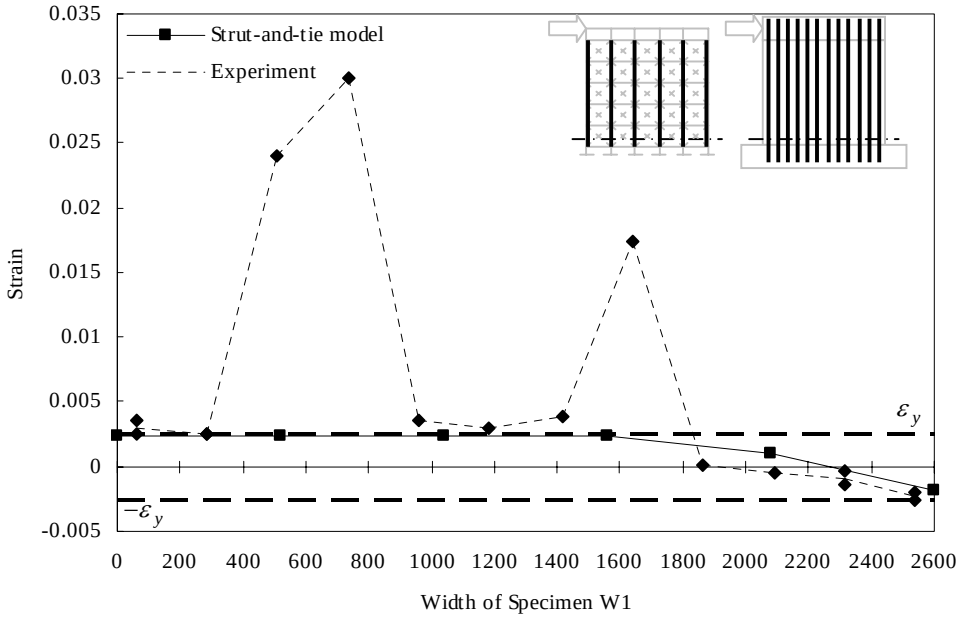

(b) For positive loading cycles

Figure 6.21: Comparison of strut-and-tie analytical and experimental bottom strain profiles of Specimen W1

The bottom strain profile from the strut-and-tie model of Specimen W1 matches well with the experimental trends except for four variant readings found for the experiment. For most of the area along the horizontal section of the web, the strut-and-tie model gives a similar strain magnitude as the experiment. The tensile strains maintain a relatively constant level in the tensile zone of the web. Discrepancies of this comparison could be from the small compressive strains that are given by the strut-and-tie model.

Lastly, strains of a few horizontal ties are compared with readings from strain gauges on the horizontal reinforcing bars.

The comparisons show that the horizontal tie strains in the strut-and-tie model deviate considerably from the experimental readings, especially for bar H1 and H3. The main reason for these unfavorable results is that the vertical positions of the horizontal reinforcing bars do not match those of the horizontal ties exactly. For any particular bar, its strains only compared with the strains from the nearest horizontal ties in the vertical position. However, these comparisons are indicative and show that the strains in the bars and the strains in the ties are of similar magnitude.

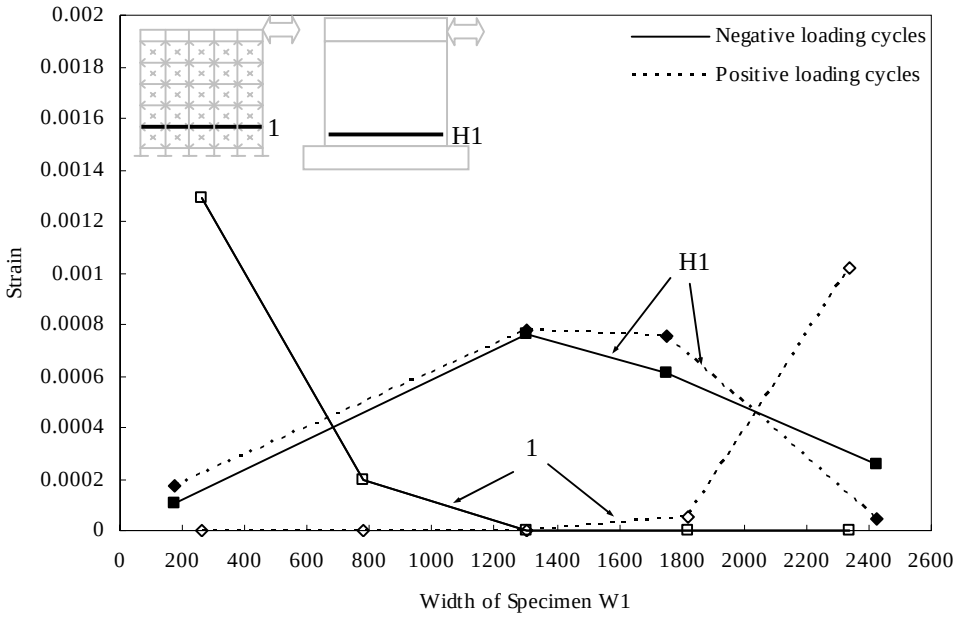

(a) At the position of Bar H1

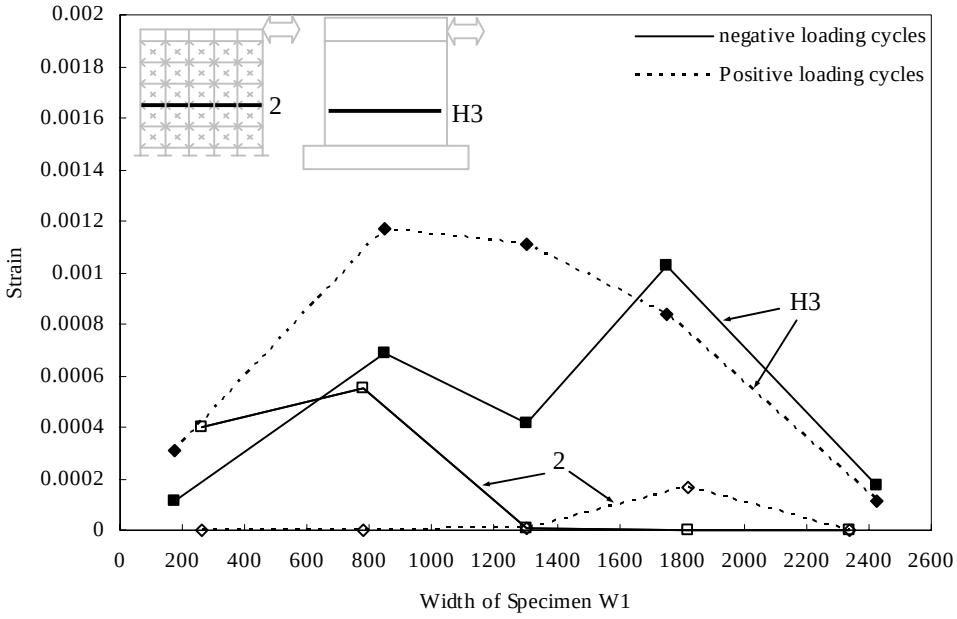

(b) At the position of Bar H3

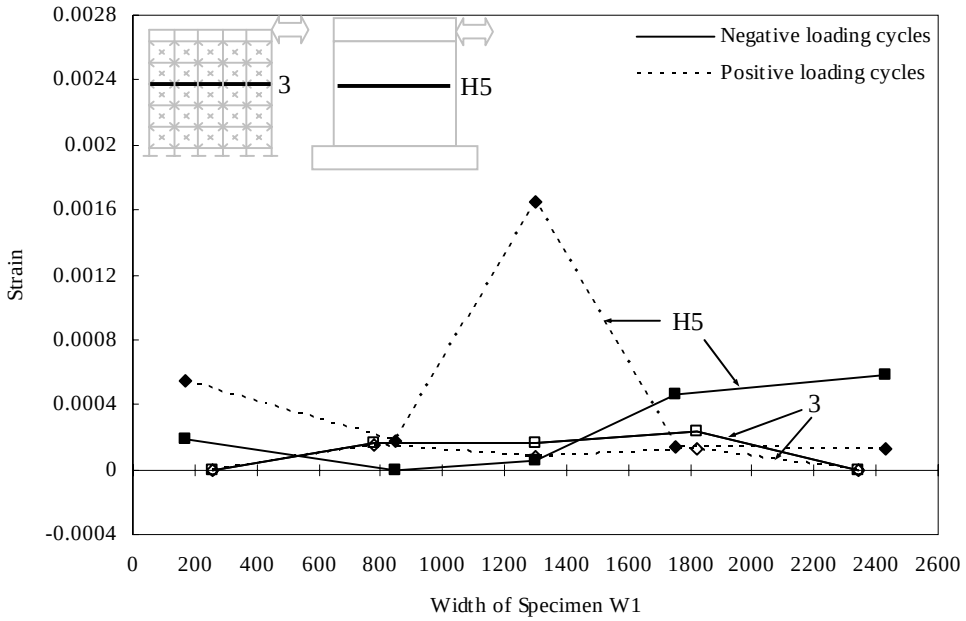

(c) At the position of Bar H5

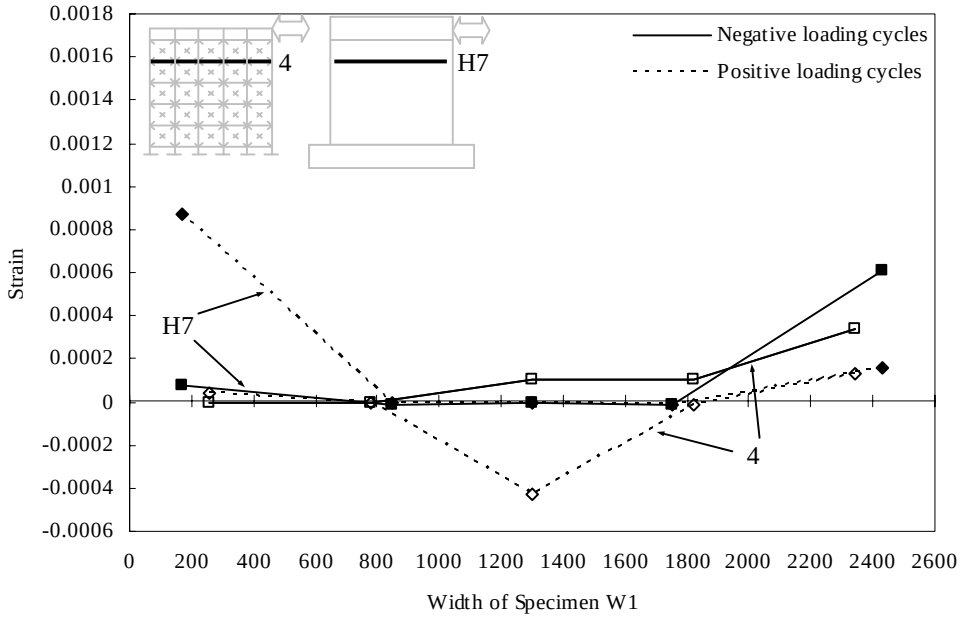

(d) At the position of Bar H7

Figure 6.22: Comparison of strut-and-tie analytical and experimental horizontal strain profiles of Specimen W1

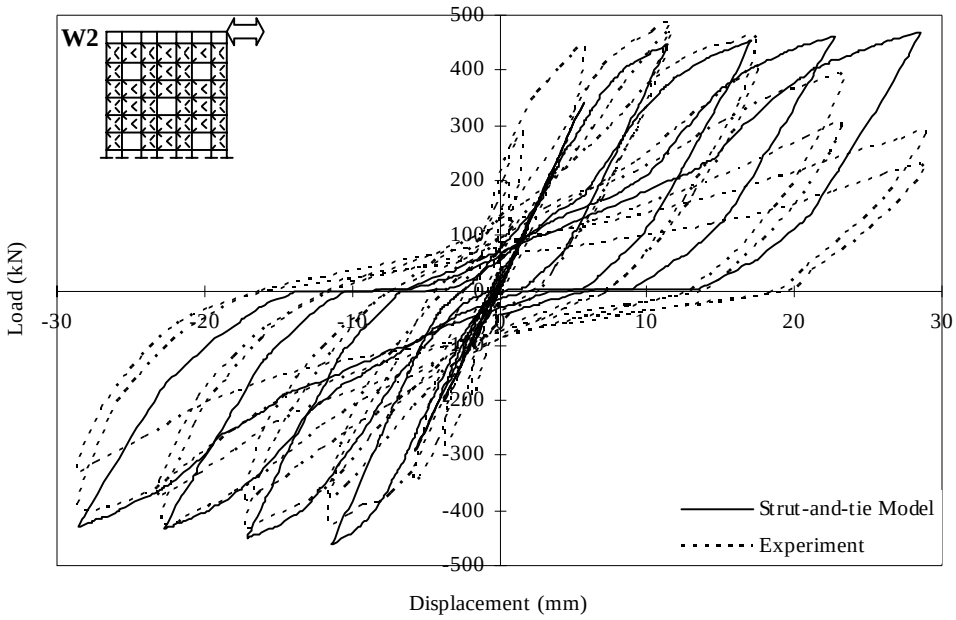

Figure 6.23: Comparison of strut-and-tie analytical and experimental load-displacement responses of Specimen W2

For Specimen W2, a very smooth, and in fact is more refined than Specimen W1, analytical lateral load versus lateral displacement response loop is obtained by the strut-and-tie model and compares well with the experiment. The maximum strength prediction is fairly accurate with a small discrepancy of 3%. The strut-and-tie model demonstrated considerable strength degradation in the negative loading cycles and matches very well with the experimental loops. However, for the positive loading cycles, the strength degradation is not observed. As a result, the strength achieved at the last two ductility factors is much higher than the experiment. A discrepancy occurs at the initial stiffness of the strut-and-tie model when compared with the actual conditions for it is only 55.5 kN/mm and is 18.7% smaller than the experiment. This undesirable situation mainly originates from the positive loading direction and means that the current strut-and-tie model underestimates the stiffness of the specimen. However, the stiffness for the following cycles is very close to that recorded in the experiment, even for the last a few cycles. This represents an improvement upon Specimen W1.

Comparisons of strain profiles are also conducted for Specimen W2. Firstly, the ties along the right and left edges of the strut-and-tie model will be shown in **Figure 6.24**.

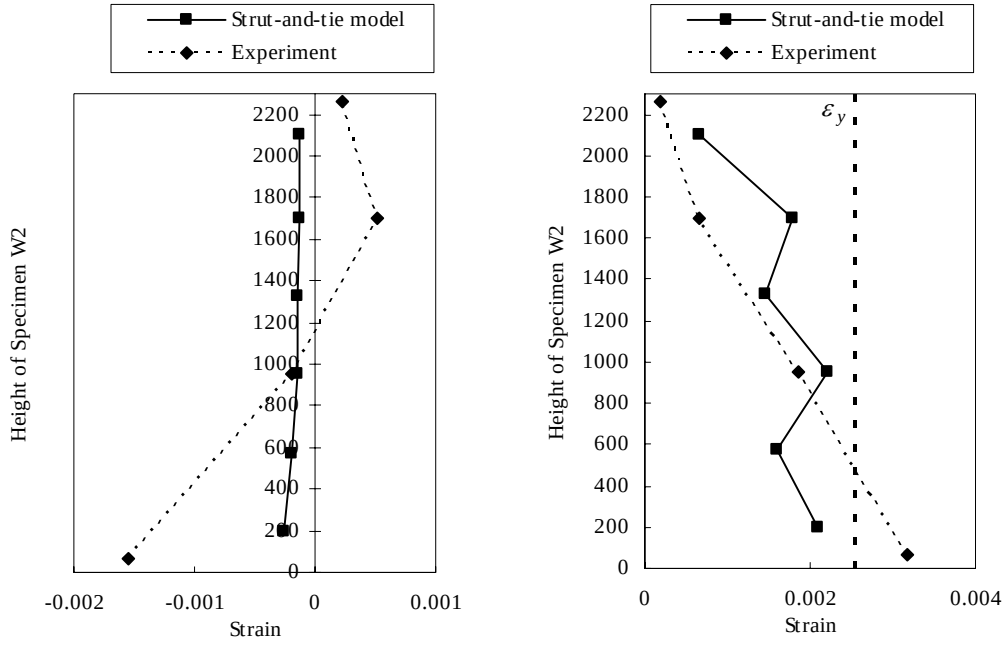

(a) Right edge in negative loading cycles (b) Right edge in positive loading cycles

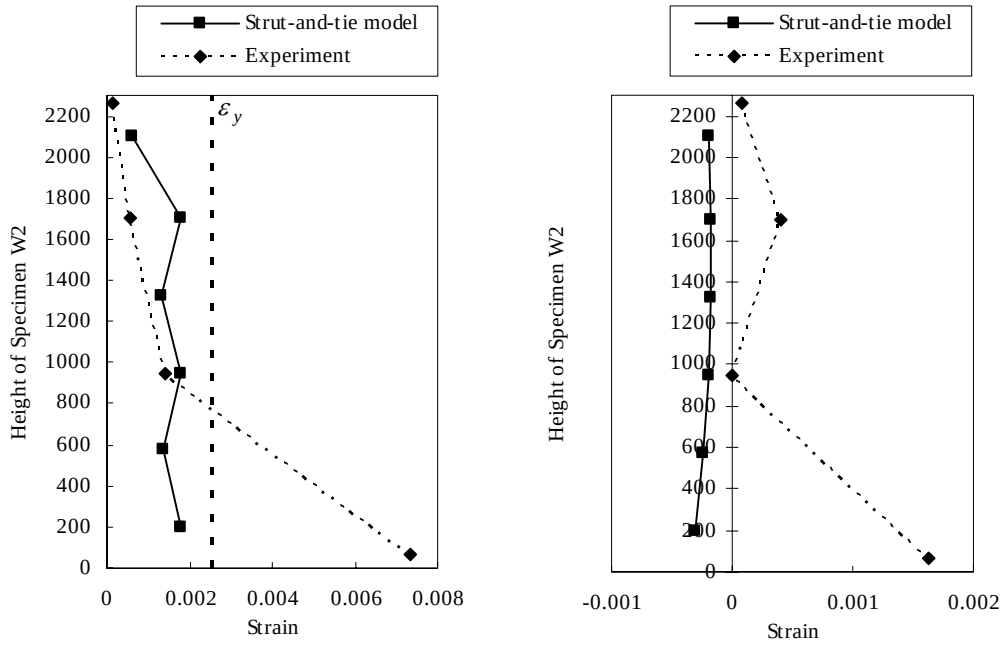

(c) Left edge in negative loading cycles (d) Left edge in negative loading cycles

Figure 6.24: Comparison of strut-and-tie analytical and experimental vertical strain profiles of Specimen W2

These comparisons are made at $DF = \pm 1$. As in the model for Specimen W1, it is found that the strains of the strut-and-tie model follow a decreasing trend in magnitude along their height, but are relatively invariant. The analytical tensile strains fluctuate considerably along their height and larger strains occur in the ties beside the openings. However, this trend was not observed for the experimental data. Similarly to Specimen W1, the compressive strains are still smaller than the experiment, which could be due to the large area that assigned to the vertical concrete strut in those positions.

Secondly, **Figure 6.25** shows the strain profile along the bottom horizontal section of the strut-and-tie model as compared to the experiment.

The bottom strain profiles from the strut-and-tie model match very well the experimental trends except for two unusual readings found from the experiment. For the most of the section along the width of the web, the strut-and-tie model gives a similar strain magnitude as that of the experiment with the tensile strains maintaining a relatively constant level and the compressive strains given by the strut-and-tie model being still smaller than the experiment.

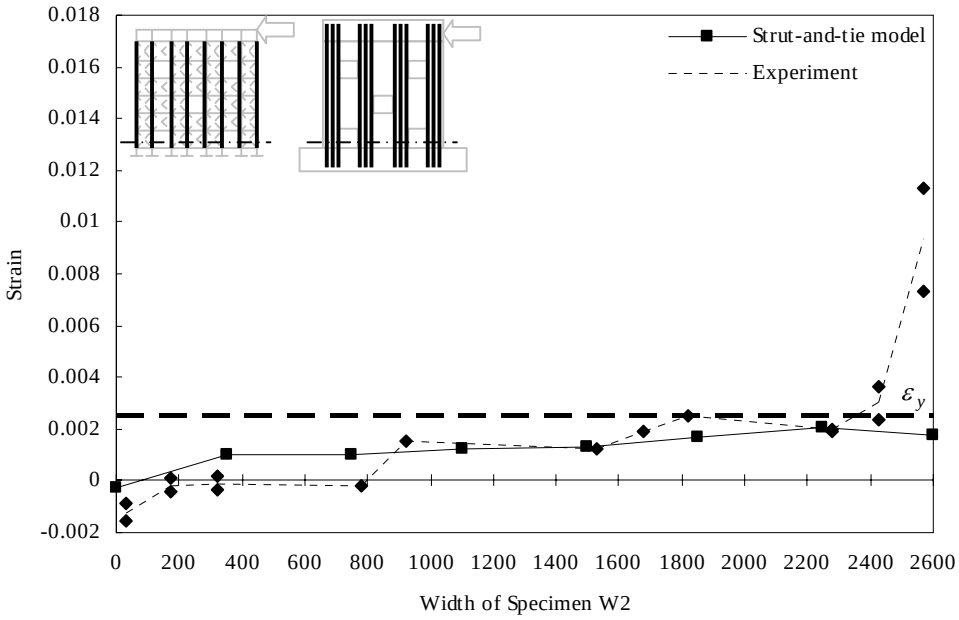

(a) For negative loading cycles

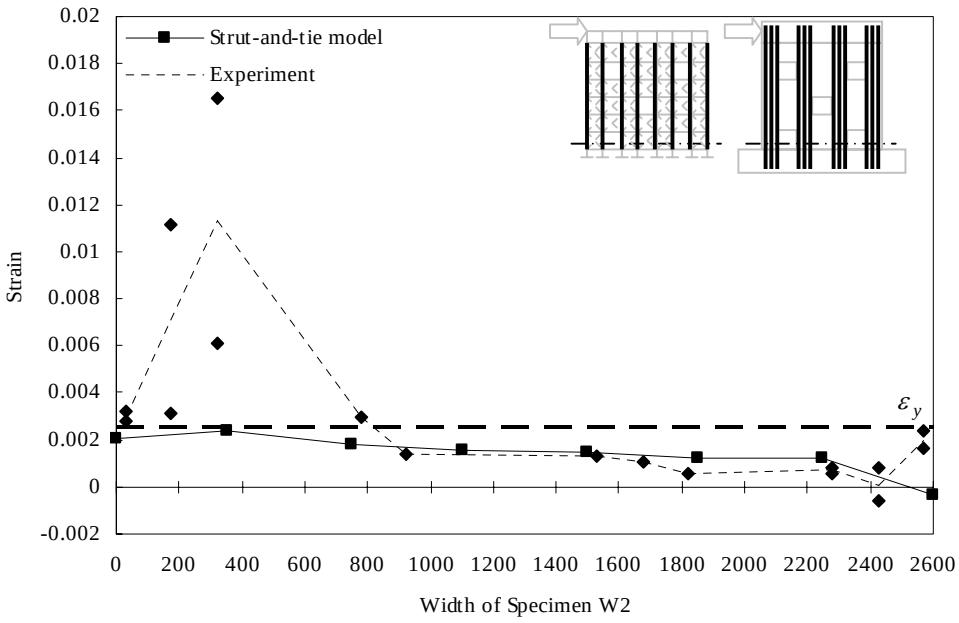

(b) For positive loading cycles

Figure 6.25: Comparison of strut-and-tie analytical and experimental bottom strain profiles of Specimen W2

Lastly, strains of a few horizontal ties are compared with readings from strain gauges on the horizontal reinforcing bars.

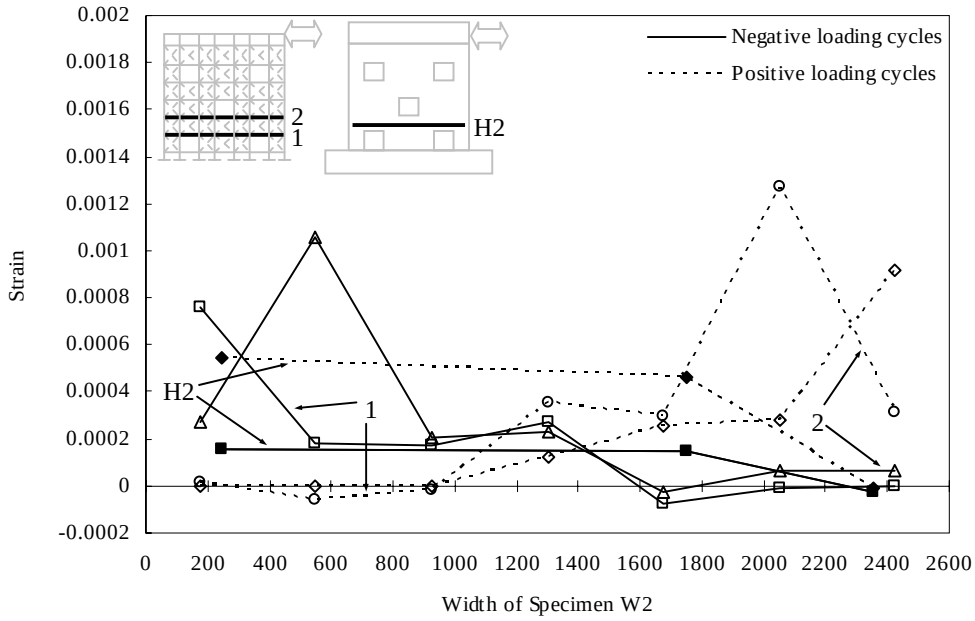

(a) At the position of Bar H2

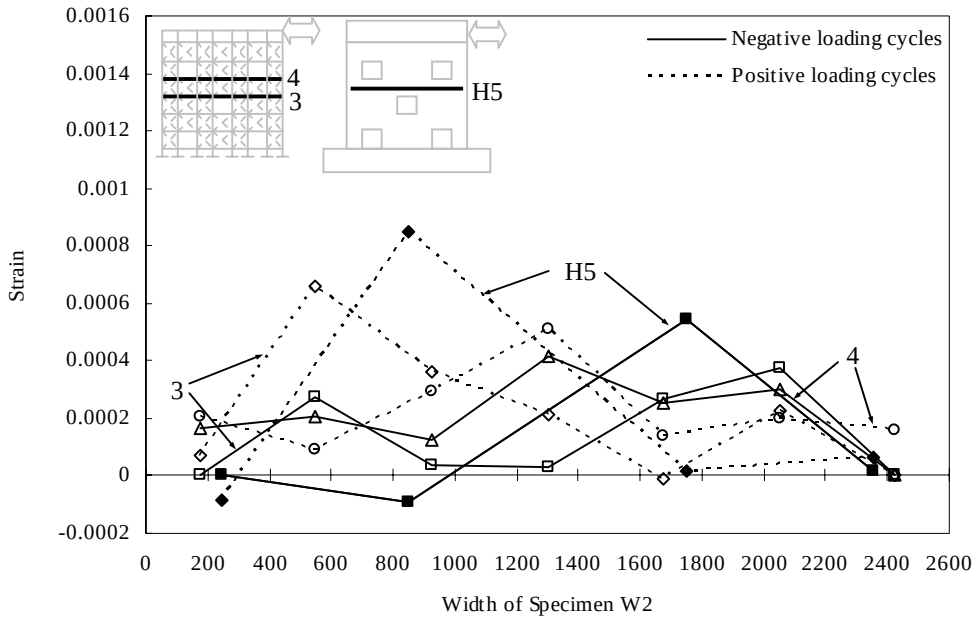

(b) At the position of Bar H5

Figure 6.26: Comparison of strut-and-tie analytical and experimental horizontal strain profiles of Specimen W2

For Specimen W2, bar H2 and H5 are compared to the nearest horizontal ties on both sides of them respectively according to the reinforcement layout and the configuration of the strut-and-tie model. The comparisons here are more regular than those of the Specimen W1. The strains in the ties are of similar magnitude with the strain gauge readings on the bars. The horizontal strain profiles in the strut-and-tie model follow quite closely to those in the experiment, especially along H5 bar.

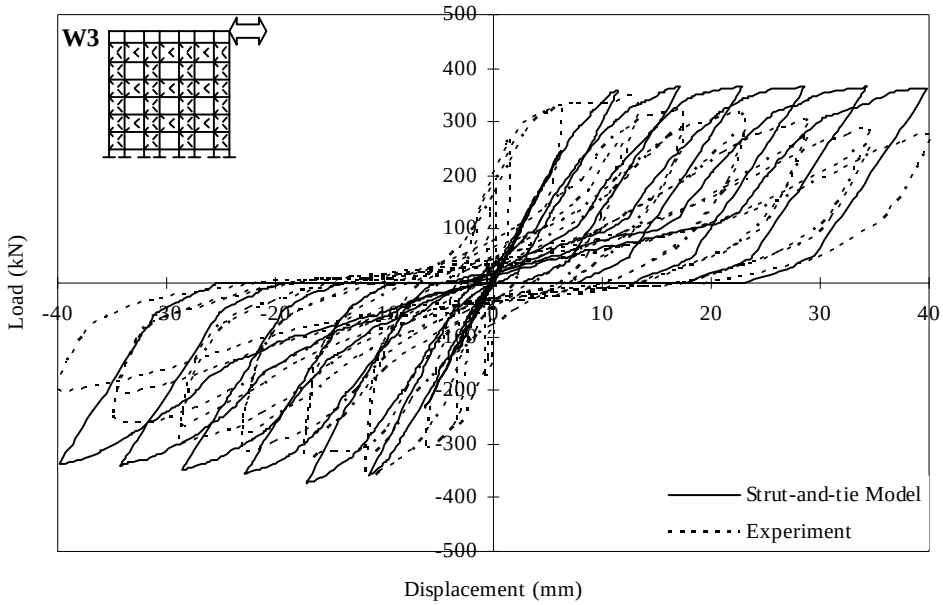

Figure 6.27: Comparison of strut-and-tie analytical and experimental load-displacement responses of Specimen W3

The analytical results for the lateral load versus lateral displacement response of Specimen W3 are compared to the experimental ones in **Figure 6.27**. A good analytical load-displacement response is obtained by the strut-and-tie model and compares satisfactorily with the experiment. The analytical results give s larger peak strength for every ductility level which is the same for the finite element analysis of this specimen. But the discrepancy in maximum strength is as small as 5% here. The strut-and-tie model of Specimen W3 again has no sign of strength degradation for both loading directions and the peak strength of each loading cycle remains at a constant level with the increase of the ductility factor. As with Specimen W2, a discrepancy occurs at the initial stiffness of the strut-and-tie model when compared with the actual condition. It is

only 38.5 kN/mm, which is 24.4% smaller than that from the experiment. Together with the findings in Specimen W2, it is concluded that the current strut-and-tie approach underestimates the initial stiffness of the reinforced concrete walls with openings.

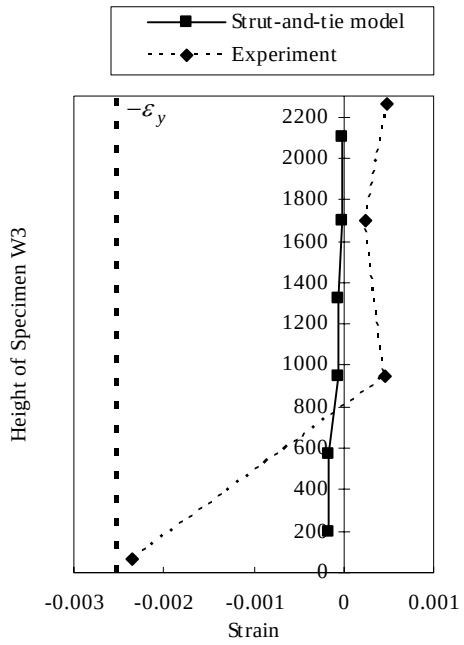

(a) Right edge in negative loading cycles

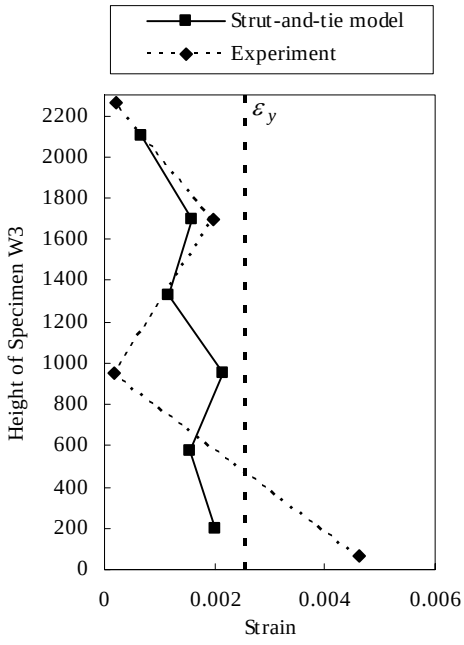

(b) Right edge in positive loading cycles

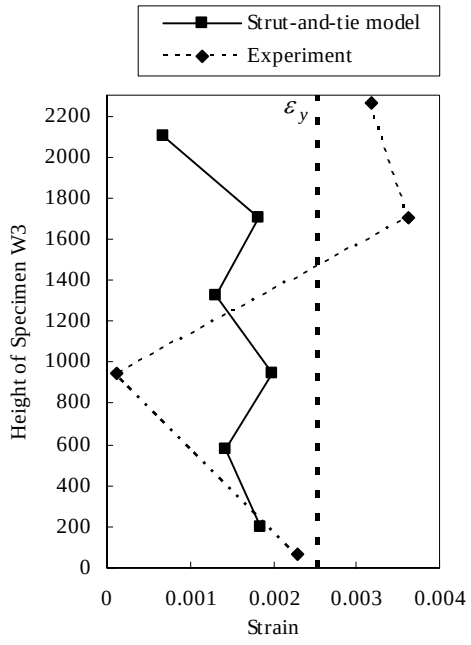

(c) Left edge in negative loading cycles

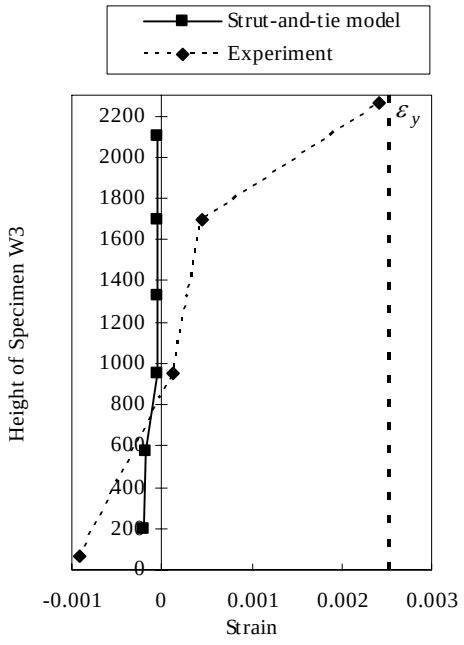

(d) Left edge in negative loading cycles

Figure 6.28: Comparison of strut-and-tie analytical and experimental vertical strain profiles of Specimen W3

Then strain profile comparisons for Specimen W3 are also conducted. Firstly, the ties along the right and left edges of the strut-and-tie model will be shown in **Figure 6.28**.

These comparisons are made at $DF = \pm 1$. The analytical tensile strains fluctuate obviously along the height. The larger strains occur in the ties beside the openings. The experimental strain gauge readings also fluctuated due to the openings, but not as regularly as in the strut-and-tie model. The compressive strains in the ties are still relatively invariant and the magnitude at the bottom section is smaller than the readings from the experiment. This could be due to the large concrete area that is assigned to the vertical struts in these positions.

Secondly, **Figure 6.29** shows the strain profile along the bottom horizontal section of the strut-and-tie model as compared to the experiment.

The bottom strain profiles from the strut-and-tie model match very well the experimental trends. Along the entire horizontal section of the web, the strut-and-tie model of Specimen W3 gives a similar strain magnitude as that of the experiment and for this specimen the strains in the tensile zone are not at a constant level, which is different from Specimens W1 and W2. The fluctuation of the member strains is due to the localized deformations of the four bottom column zones, moreover the manner of strain fluctuation in the strut-and-tie model is exactly the same as recorded in the experiment. Any discrepancy between these comparisons could be due to the small compressive strains that are given by the strut-and-tie model.

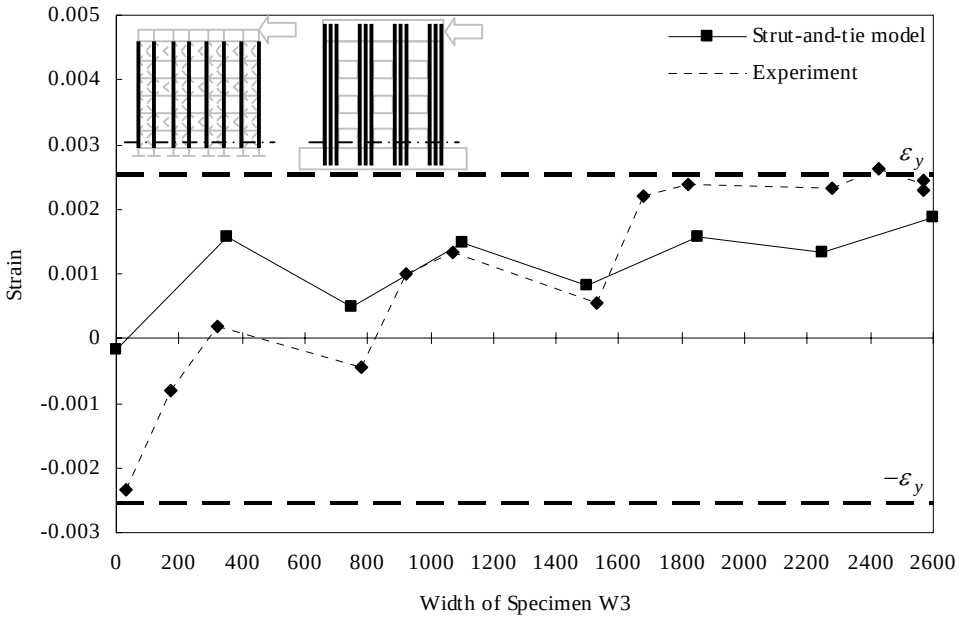

(a) For negative loading cycles

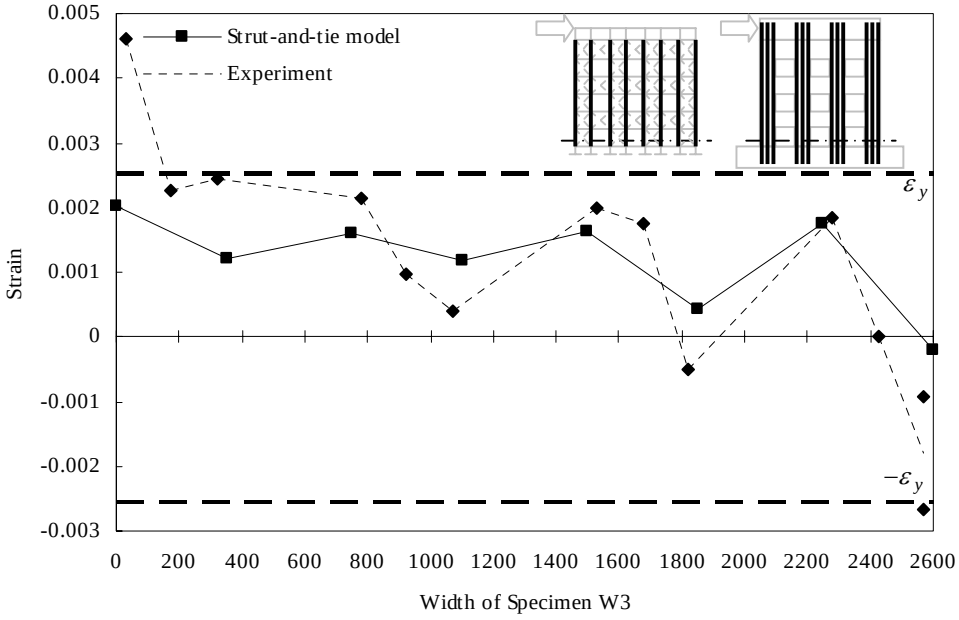

(b) For positive loading cycles

Figure 6.29: Comparison of strut-and-tie analytical and experimental bottom strain profiles of Specimen W3

Lastly, strains of a few horizontal ties are compared with readings from strain gauges on the horizontal reinforcing bars.

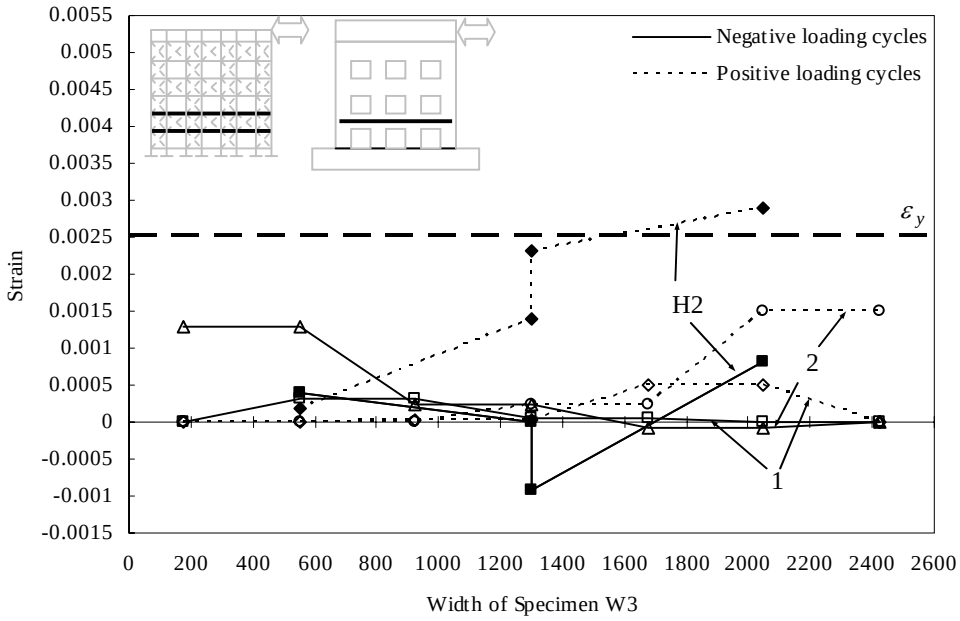

(a) At the position of Bar H2

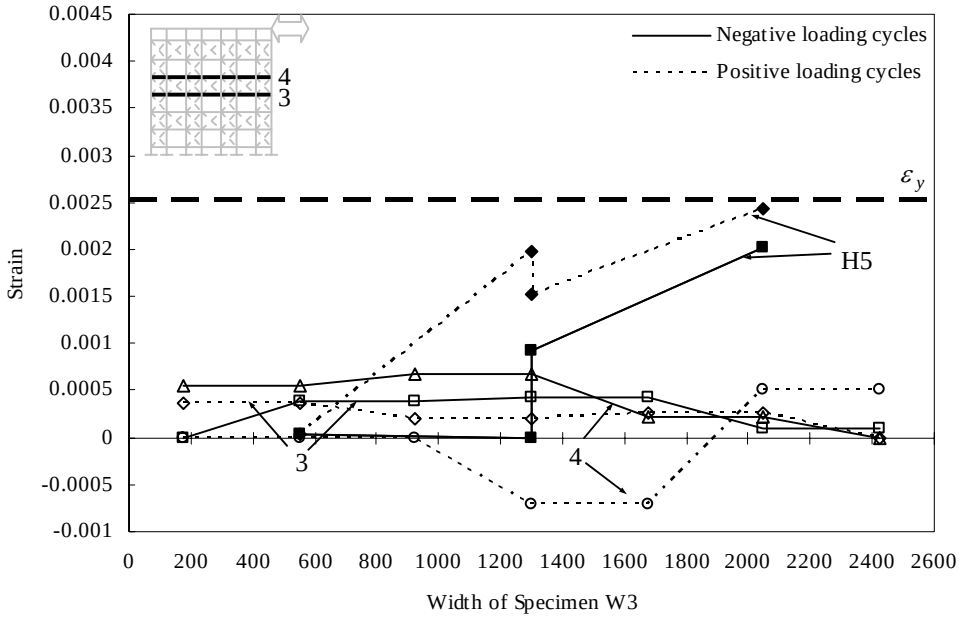

(b) At the position of Bar H5

Figure 6.30: Comparison of strut-and-tie analytical and experimental horizontal strain profiles of Specimen W3

The comparisons in horizontal strain profiles between the strut-and-tie model and the experiment for Specimen W3 are less meaningful than the other two specimens. In the two strain profiles of bar H2 and H3, each of them here is only marked out by strain gauges at three positions only and therefore the information obtained may not be complete for further judgment. The results are merely indicative.

As a whole, from the comparisons of the lateral load versus lateral displacement response and strain profiles, the strut-and-tie models proposed have performed satisfactorily.

6.4 The Refined Strut-and-Tie Models to Demonstrate Force Transfer Mechanisms of the Tested Specimens with Openings

In the previous section in this chapter, the strut-and-tie approach is used to predict the overall response of the wall specimens. Under that approach, the strut-and-tie models developed are sophisticated as full details of the specimens need to be considered for successful predictions. Although all the possible paths in each stress flow pattern are included in the models, major ones are not clearly indicated. And due to the complicated nature of the models, application of these models in engineering problems is limited. Therefore, this section will aim to develop a refined strut-and-tie model so that the main load paths in the stress flow pattern of each specimen are highlighted and the resulting model can be directly applied to engineering design works. The discussion here will be focused on Specimens W2 and W3 which have openings.

In the nonlinear finite element analysis, the principle stress flow pattern of each wall specimen is shown. The principle compressive stress flow of each specimen can be taken as the mechanism of how the imposed lateral load is transferred and various strut mechanisms can be used as the representation of it. Principle tensile stress flow indicates the concentration of the tensile stress and so ties should be placed in those locations. Specimens W2 and W3 have different opening configurations and thus different stress flow patterns and will be treated separately.

Figure 6.31 (a) shows again the principle stress flow of Specimen W2 at the ultimate state for a positive loading cycle. It can be seen that a stream of compressive stress goes through the Panel 1 and Panel 3 and then extended into the bottom right column zone. The stress flow patterns developed in the two panel zones are bottle-shaped. This path of stress flow should be the main mechanism that transfers the imposed lateral load to the foundation beam. Another minor compressive stress flow is observed at the bottom Panel 4 which has a fan-shaped pattern and connected to a stream of tensile stress flow in the middle of the web. The Crack pattern of Specimen W2 for the positive loading cycles is shown in **Figure 6.31 (b)**. The cracks in the Panel 1 and Panel 3 were not so extensive, but the developing directions were the same as the stress flows shown there. Cracks in the bottom Panel 4 dispersed out from the right bottom corner, indicating an exact fan-shaped stress flow pattern there.

If dash lines are used to show the direction of the compressive stress flow and full line are for the tensile stress flow, the main stress flow paths in Specimen W2 can be simplified into the form of **Figure 6.31 (c)** which clearly illustrates the force transfer mechanism of Specimen W2 for the positive loading cycles. One can further extend this philosophy by considering the dash lines are struts and the full lines are ties, where the force transfer mechanism can be well represented by a simple strut-and-tie model. In the strut-and-tie model, the imposed lateral load is solely transferred into Panel 1 at the top before going into Panel 3 which eventually is directed to the foundation beam through the right bottom column. Another minor path is through the bottom Panel 4. This stream of compressive stress flow can be taken to be transferred from the Panel 2, where a tie is connected horizontally for equilibrium.

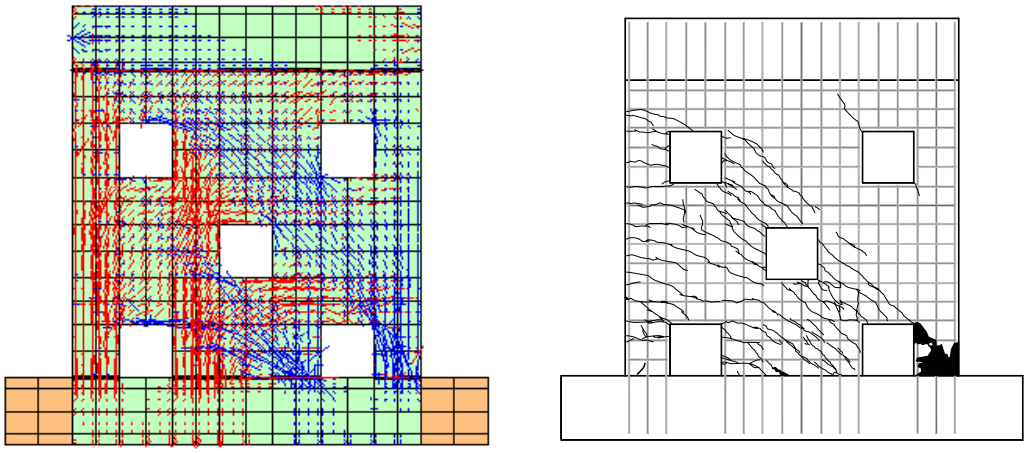

(a) Stress flow pattern (b) Crack pattern

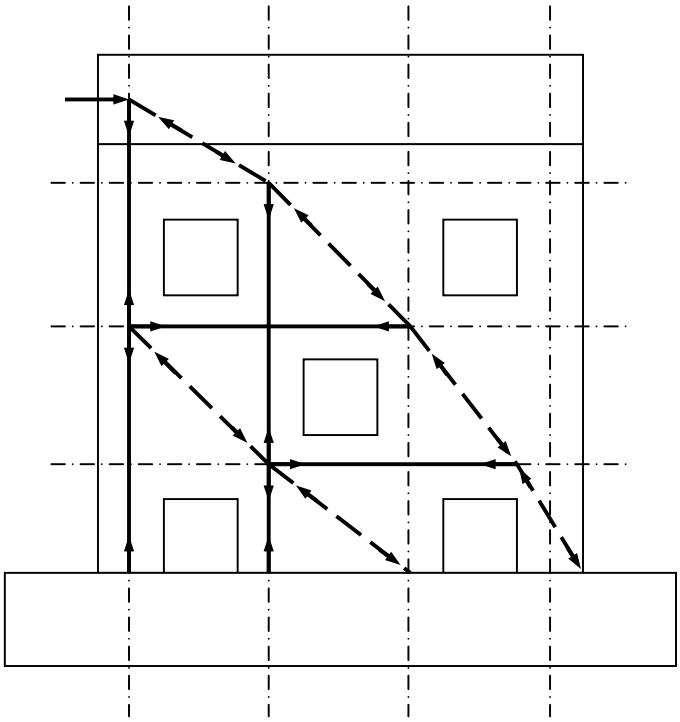

(c) Identified load paths

Figure 6.31: Force transfer mechanism of Specimen W2 in strut-and-tie model

Obviously, the developed strut-and-tie model for Specimen W2 from the principle stress flow pattern is much simpler than that in the previous section. From the finite element analysis results, the principle stress flow pattern is the same for all the ductility levels. Hence the strut-and-tie model at the ultimate stage is actually a good representation throughout the discussion. Moreover, this strut-and-tie model is statically determinate

for any particular imposed load at various loading stage, the force taken by each individual member in the model is readily calculated. The percentage of the imposed lateral load shared by each load path is defined and fixed. Therefore, the force transfer mechanism among the paths is made visible. The stress in the tie and average stress in the strut are accessible if the allowable areas of the ties and struts are defined. Failure mechanism of the specimen can be justified based on the information obtained. When a lateral load 450 kN (maximum strength from the average of the negative and positive loading cycles in the experiment) is applied to the strut-and-tie model, the forces developed in each member is shown in **Figure 6.32**. From this result, it is confirmed that the path that goes through Panel 1 and Panel 3 is the major one and transfers 63% of the lateral load to the foundation beam. The path that goes through the bottom Panel 4 is the minor one carrying only 37% of the lateral load to the foundation beam. For the reinforcement layout of the Specimen W2, the left bottom vertical tie with a member force of 357.5 kN goes beyond the force that can be provided by the reinforcement there at yielding. The calculation relates well to the experimental observations that

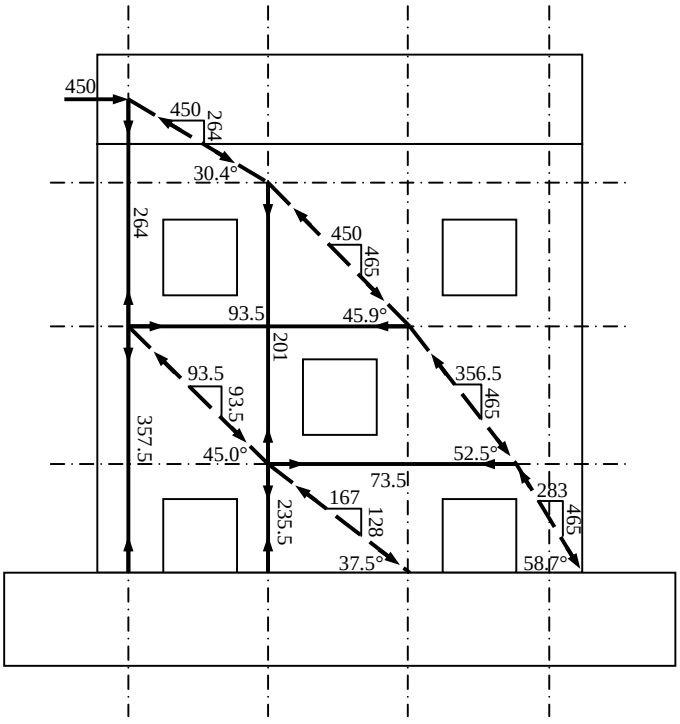

Figure 6.32: The refined strut-and-tie model of Specimen W2 at the ultimate state

reinforcing bars at that location were fractured at the ultimate stage. Thus it can be concluded that the failure of Specimen W2 was due to the fracture of the reinforcing bar at the bottom column.

The strut-and-tie model can also be used to predict a theoretical strength of the specimen. The theoretical strength is based on the criterion that the tie at the bottom left corner fails first as indicated in the previous figure. The calculation is illustrated in **Figure 6.33**. The strut-and-tie model gives a theoretical strength 284.7 kN, which is 63.2% of the maximum strength developed by Specimen W2 in the test. This low theoretically predicted strength is due to the strut-and-tie model developed selects only two of the most representative stress flow paths and other possibilities are omitted. Consequently, the shared imposed load by each path is increased. Also, the static determinate nature of the model makes the forces in the two vertical ties heavily rely on the angle of inclination of the path that transfers the imposed lateral load to Panel 1. However, this angle is very much defined with less variation as that can be observed from the finite element stress flow pattern. As a result, the tie in the left bottom column zone is subjected to a very

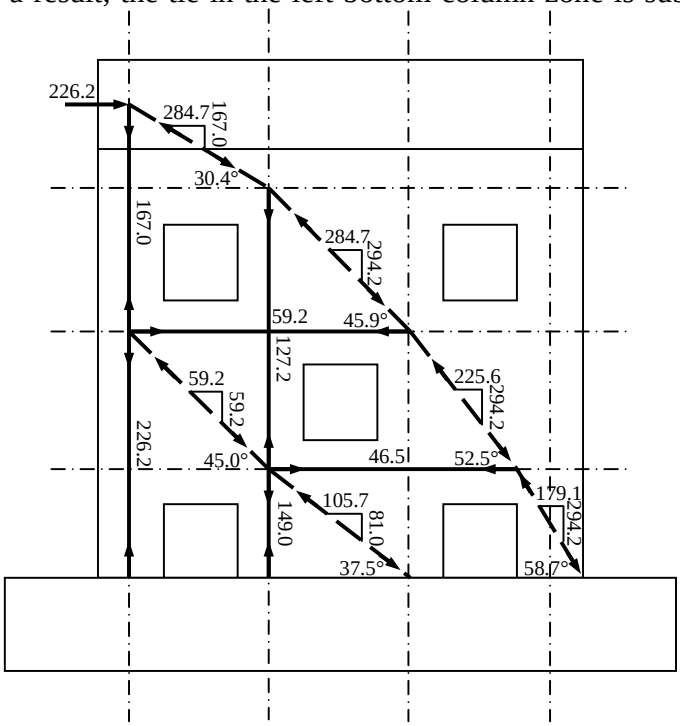

Figure 6.33: The strut-and-tie model to predict a theoretical strength of Specimen W2

large force under the current configuration of the strut-and-tie model.

The stress flow of Specimen W3 is more regular than that of Specimen W2 due to the nine evenly distributed openings in the web as shown in **Figure 6.34 (a)**. In this specimen, sophisticated fan-shaped and bottle-shaped compressive stress flows are not found. Instead, a very simple pattern of stress flow, which is directly along the diagonals of the beam and column zones, prevails. Three very obvious paths of principle compressive stress flow are shown. The crack pattern developed during the positive loading cycles in **Figure 6.34 (b)** proved this finding from the finite element analysis. Three sets of long diagonal cracks appeared at the same locations as the paths of compressive stress flow. The pattern of stress flow for Specimen W3 indicates a direct strut mechanism along the diagonals of the beam and column zones. Again if dash lines are used to mark out the direction of these compressive stress flow and full lines are for the direction of tensile stress flow, the force transfer mechanism with main load paths in this wall specimen is shown as in **Figure 6.34 (c)**. Besides the three load paths that have been described above, there is a minor path in the left bottom region. Thus all together four paths transfer the imposed lateral load to the foundation beam.

A strut-and-tie model can be derived from the force transfer mechanism. This strut-and-tie model is slightly more complicated than that of Specimen W2 due to the fact that more paths are available to transfer the lateral load. From the finite element analysis results, it can be seen that the path that each stress flow goes through is invariant with respect to the ductility level. Although the strut-and-tie model is developed at the ultimate stage, it is also applicable to other ductility levels. The multiple force transfer paths also make the model to be statically indeterminate. Thus, a solution of the member forces at any particularly stage is not feasible by hand calculation. To overcome this indeterminacy in the strut-and-tie model, finite element analysis results can be used. For any horizontal section along the web of the wall, the total amount of shear is equal to the imposed lateral load which is known. The finite element analysis with UC-WIN/MESH& UC-WIN/WCOMD can show the detailed shear and normal forces that pass through the column zones. The percentage of total lateral force shared by one

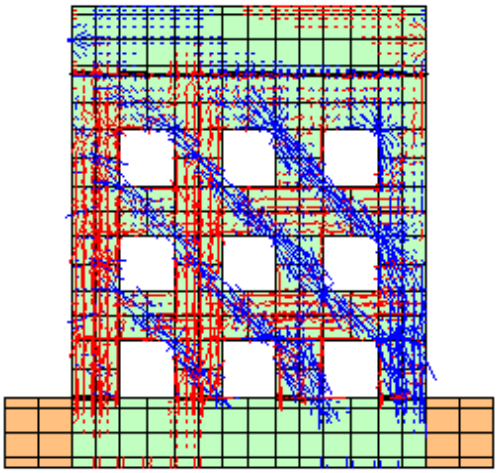

(a) Stress flow pattern

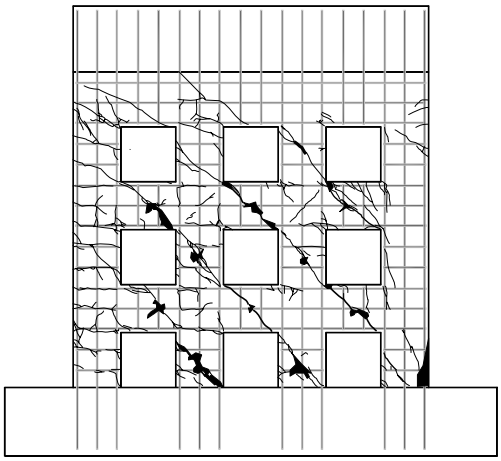

(b) Crack patterns

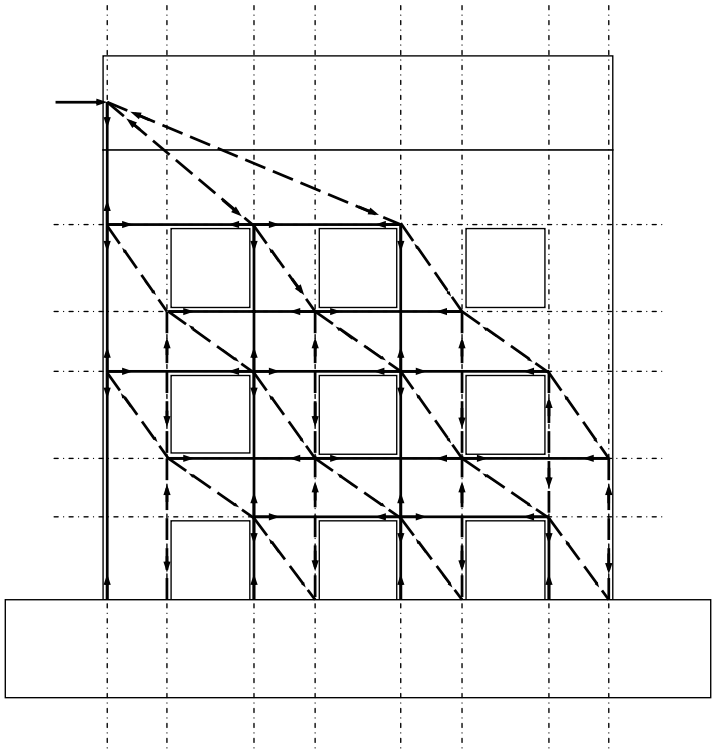

(c) Identified load paths

Figure 6.34: Force transfer mechanism of Specimen W3 in strut-and-tie model

column zone along a horizontal section is known at any loading stage. This condition can help to remove enough redundancy while the remaining member forces can be calculated from equilibrium conditions at the nodes. Each load path in the force transfer mechanism may take a different share of the imposed lateral load at different stages in

the cyclic loading process as the redistribution of the internal stress is likely to occur. Therefore, the analysis of member forces is conduced at three ductility levels, typically at $DF = \pm 1$, $DF = \pm 4$, and $DF = \pm 7$. All the results are shown below in **Figure 6.35**.

From the three sets of results, it is firstly found that the nature (being a strut or tie) of the vertical and horizontal members are determined by the calculation from equilibrium. Some members could be the opposite type as in the postulated force transfer mechanism in **Figure 6.29** which is one result of the internal stress redistribution. Secondly, the percentage of the imposed lateral load shared by each load path is different for the three ductility levels. For the current configuration of the strut-and-tie model, the uppermost load path only transfers a vertical force into the bottom Column 4 and the portion of the lateral load initially taken by it is redistributed to other load paths. Meanwhile the other three load paths, they transfer 12.7%, 29.7%, and 57.6% of the lateral load respectively from the left to the right to the foundation beam at $DF = \pm 1$. At this ductility level, the path that goes through Column 4 diagonally takes the more than half of the lateral load. At $DF = \pm 4$, this percentage for each one of them changes to 20.3%, 47.7%, and 31.9%. The amount of the lateral load shared by the path that goes through Column 4 diagonally is reduced more than 25% while among the other paths, the path that goes through Column3 increases 18% and becomes the critical one. At $DF = \pm 7$, the Specimen W3 reached its ultimate stage and the shared percentage of each load path is 20.3%, 47.5%, and 32.2%. It is noticed that the percentage shared by each load path is almost the same at $DF = \pm 4$ and $DF = \pm 7$. The force transfer mechanism of Specimen W3 is determined after $DF = \pm 4$. Thirdly, it is found that the horizontal members in the strut-and-tie model normally vary significantly at the three different ductility levels. This proves that the horizontal members play the major role in the redistribution process. The redistribution by the horizontal members is also responsible for the fact that the percentage of the imposed lateral load shared by each load path varies along different horizontal sections at the same ductility level.

When the strut-and-tie model is set up according to the reliable stress flow pattern, the model can be used to predict a theoretical strength of the specimen. For Specimen W3

here, if the proportion of the lateral load shared by each column zone along one horizontal section is taken to be that at the ultimate stage, the theoretical strength predicted by the model is 229.6 kN, which is 65.6% of the maximum lateral load applied to the specimen in the experiment. The member forces developed for the prediction are very close to those at $DF = \pm 7$ and the prediction for Specimen W3 is of the similar accuracy level to that of Specimen W2.

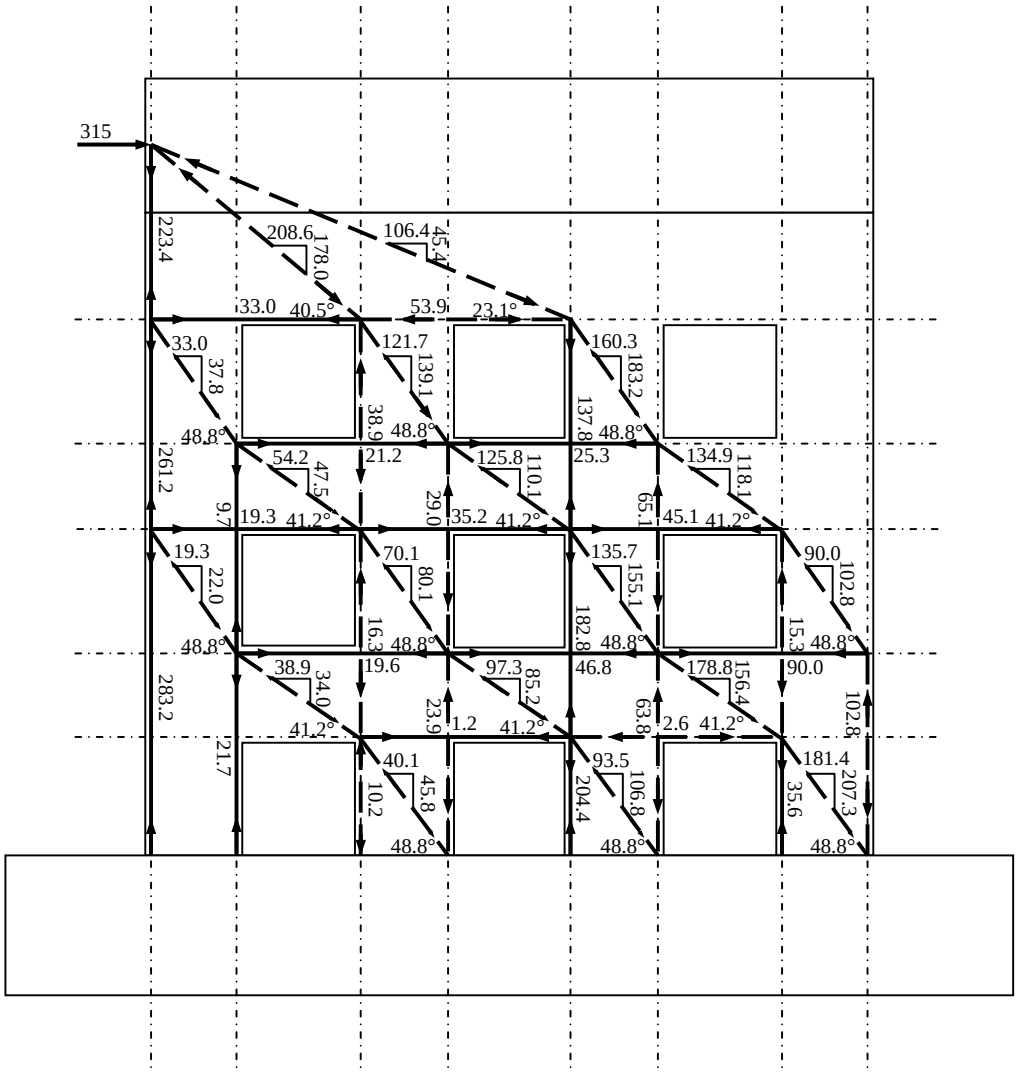

Figure 6.35 (a) The refined strut-and-tie model of Specimen W3 at $DF = \pm 1$

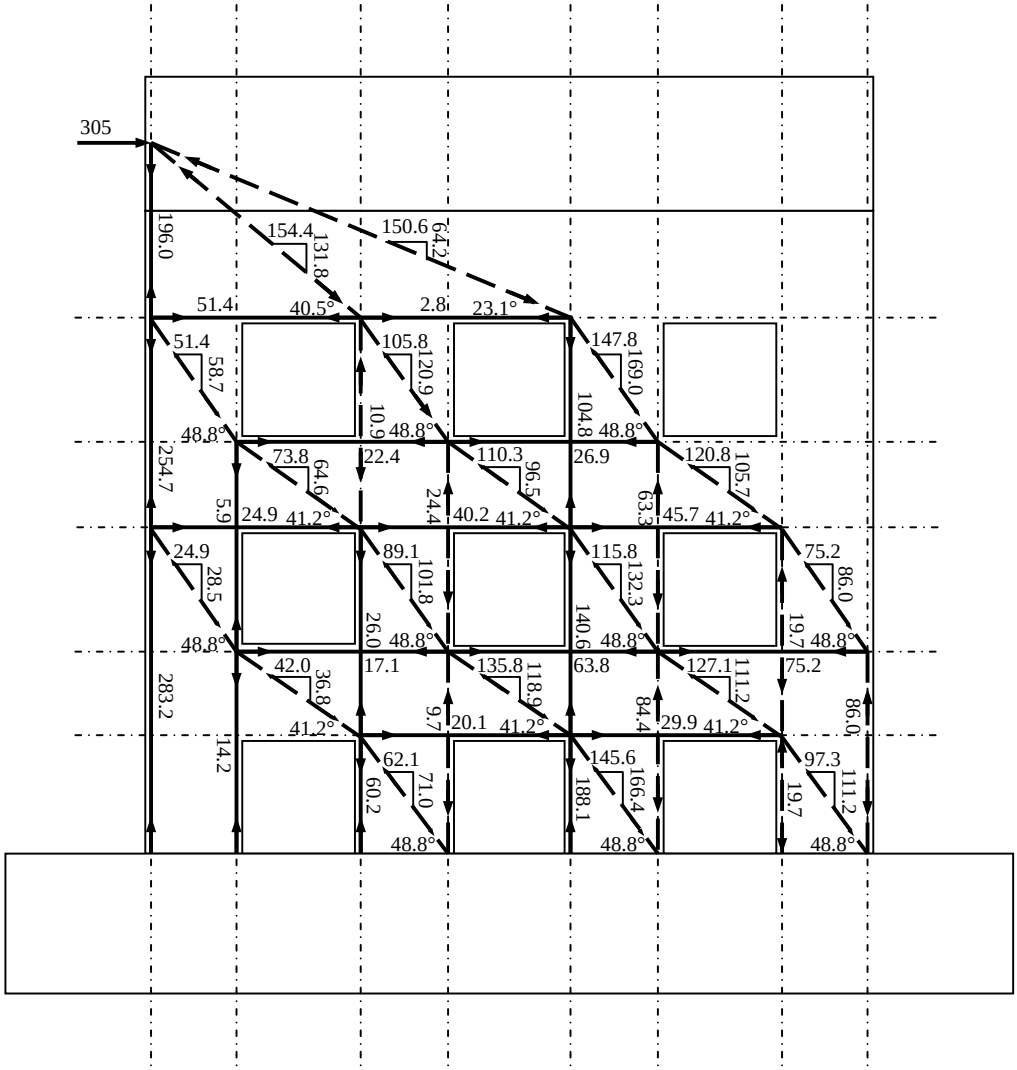

Figure 6.35 (b) The refined strut-and-tie model of Specimen W3 at $DF = \pm 4$

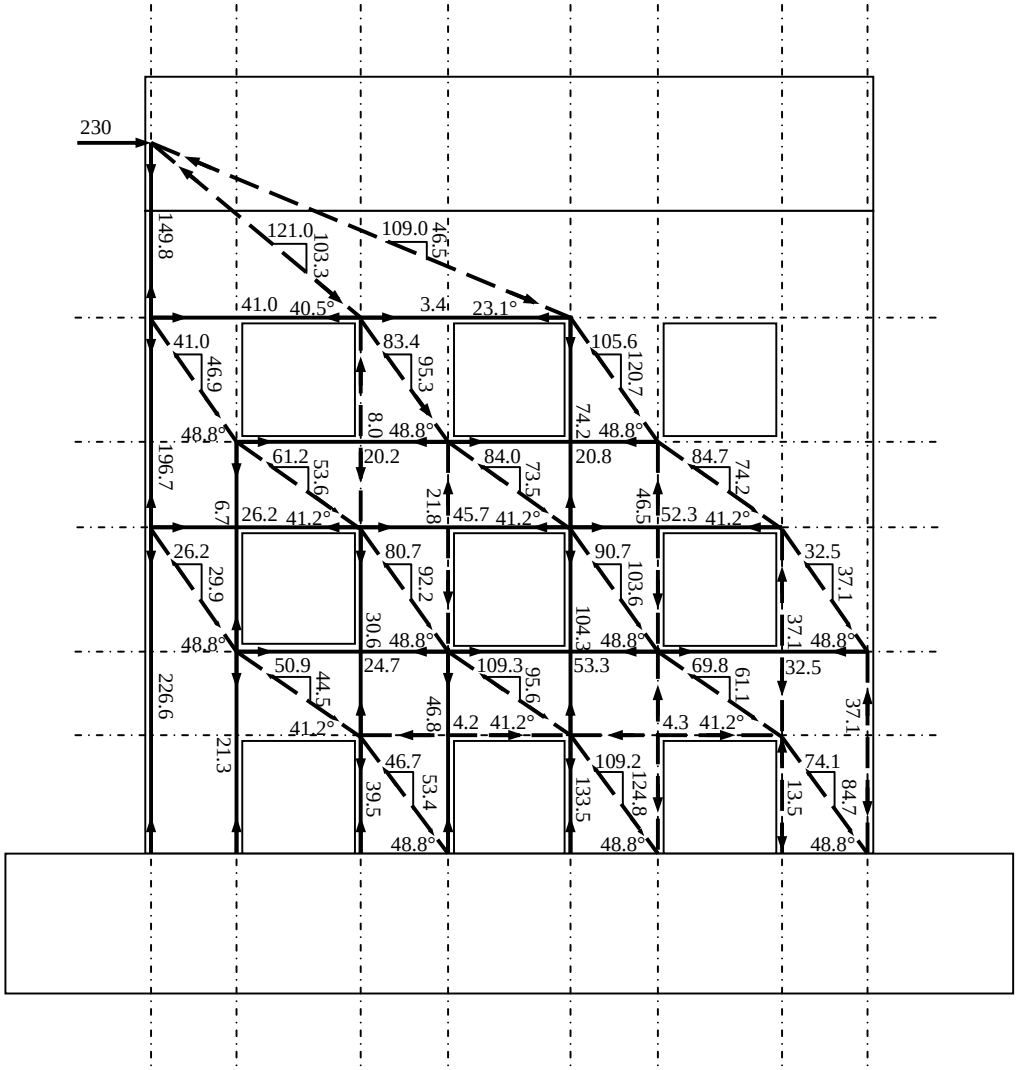

Figure 6.35 (c) The refined strut-and-tie model of Specimen W3 at $DF = \pm 7$

Figure 6.35: The refined strut-and-tie models of Specimen W3

6.5 Recommendations for Application and Design

In this chapter, a lot of effort has been made to visualize the internal stress flow patterns of the wall specimens subjected to the imposed lateral load. Then comprehensive strut-and-tie models, which intend to capture all the possible paths of the stress flow patterns of the tested specimens, have been developed to predict the overall response of the walls. Further than that, the refined strut-and-tie models, which only show the main paths in stress flow patterns, gives the force transfer mechanisms of the walls with openings. The refined strut-and-tie model is much simpler than the model for overall

response and enables hand calculations for member forces with some manipulations. Therefore, the refined strut-and-tie model can be used to predict the theoretical strength of the wall specimens.

The application of the two sets of strut-and-tie models is different. The strut-and-tie model developed for overall response of the wall specimen is an analytical tool for given specimen configuration and reinforcement detail, this type of strut-and-tie model can be set up and analyzed for strength, displacement, and stiffness. The analytical results from it have a satisfactory degree of accuracy in terms of predicted load-displacement responses, the internal stresses, and strains of individual members. The analytical process of this strut-and-tie model with the program DRAIN-2DX is much faster than a normal finite element program and can be used as a quick indicator, especially when displacement and stiffness properties are demanded.

The refined strut-and-tie model is derived from the main paths of stress flow of the specimens. Hence, it actually represents the force transfer mechanism of the modeled specimen. This type of strut-and-tie model is much simpler and can normally calculate member forces by hand. Finally, the force distribution among different paths and possible failure mechanisms is clearly depicted. On this basis, this model can be a tool to predict the theoretical strength of the wall specimen with openings. However, because of the fact that some force transfer paths are omitted, the predicted strength is on the lower side when compared to the experimental ultimate value. Moreover, in the refined strut-and-tie model, only member forces are involved in the calculation and nothing is said about the displacement and stiffness.

Design of reinforced concrete walls with openings is more complicated and early design codes provide little guidance towards a rational approach. The strut-and-tie model, especially the refined model used in this research, is a transparent tool that is derived from the force transfer mechanism. ACI 318-02 [A1] now gives some provisions on the application of the strut-and-tie modeling of structural members. A systematic design procedure for reinforced concrete walls with opening using the strut-and-tie approach is

summarized as follow:

Firstly, the likely paths in the stress flow patterns should be identified. In simple cases, this can be achieved on the basis of engineering judgment and so long as the resulting model from this judgment satisfies equilibrium and the struts are not over-stressed, the wall should develop the ultimate strength required. However, if the estimated stress flow deviates significantly from the actual distribution, the structure will have extensive cracking as it has to deform to redistribute the loading according to the designed reinforcement layout. Therefore, for complicated cases, a finite element analysis can be performed to offer a better indication of the stress flow. Moreover, a complicated stress flow may incur a statically indeterminate strut-and-tie model. To solve this type of model, a section result from the finite element analysis will be helpful.

Secondly, when a reliable stress flow is found, the main paths that transfer the applied load to the foundation can be identified as forming the force transfer mechanism of the structure. Then the positions of the struts and ties can be determined and the equilibrium condition must be satisfied at any nodal point. If the resulting strut-and-tie model is statically determinate, the member forces can be solved directly with hand calculations. If the strut-and-tie model is statically indeterminate, it requires eliminating enough redundant forces so that remaining member forces may be calculated by equilibrium only. Proportionately distributing the imposed load among all possible paths of stress flow serves this purpose. For preliminary design, this can be done by engineering judgment and refined later or section result in finite element analysis can be the guide in this distribution. After all the member forces are obtained, reinforcement can be designed according to the position and force magnitude of each tie.

Thirdly, when the reinforcement design is done, if there is a requirement to check the serviceability or stiffness properties of the designed reinforced concrete wall, the strut-and-tie model described in Section 6.3 can be used for a quick result. The strut-and-tie model can be developed in accordance to the designed wall configuration and reinforcement layout following the provisions in Section 6.3. The model can then be

analyzed by DRAIN-2DX to obtain the desired result.

The development of the strut-and-tie model for design in the second step is critical. A few recommendations are made here to establish the best performance. Generally, there is a choice between a statically determinate and a statically indeterminate strut-and-tie model. A statically determinate model has an advantage in its simple hand calculation and the statically indeterminate model can always be transformed into a determinate one by omitting certain members or stress paths. If some members are omitted, especially the ties, severe cracking can be expected in that region, even under service conditions. If some load paths are not taken into account, the model will become less efficient as members in other paths will be more stressed. Thus, although the use of a statically indeterminate strut-and-tie model increases the design complexity, it can improve the efficiency and serviceability.

6.6 Summary

In this chapter, the tested three wall specimens are analyzed in three ways. Firstly, nonlinear finite element analysis is conducted to obtain the reliable stress flow pattern of each specimen under the reversed cyclic loading. This is confirmed by the well-behaved analytical load-displacement response of all three specimens. Then a strut-and-tie model is developed to predict the overall response of each specimen. The results are within good accuracy and the internal member stress and strain are reasonable as compared with experimental data. Next, the refined strut-and-tie models, which are based on the stress flow patterns derived in the finite element analysis, show the force transfer mechanism of the walls with opening. The refined model is force based and used to predict the theoretical strength of specimens. Finally, a systematic of design procedure for reinforced concrete walls with openings, which revolves around the refined strut-and-tie model, is summarized as a recommendation from this research.

CHAPTER 7

CONCLUSIONS AND RECOMMENDATIONS

7.1 Conclusions

The main objectives of this study were to investigate the applicability of the modified truss model and the strut-and-tie method to the analysis and design of reinforced concrete beams and structural walls with opening that had complicated internal stress flow and to develop a design procedure for these beams and walls based on such models. The following conclusions were reached on the grounds of experimental and analytical works in this research:

The modified truss model for reinforced concrete beams

1. The modified truss model proposed in this thesis was essentially a variable angle truss model with concrete contribution in shear incorporated. After proper properties were assigned to members in the model, it could be analyzed for strength and deformation of reinforced concrete beams with the aid of a computer program. The strength and deformation of analyzed beams were compared reasonably well to the experimental data, proving that the truss model analogy could be successfully extended into the analysis of stiffness and deformation of reinforced concrete element.

2. In the modified truss model, construction of the model and the treatment of the concrete contribution in shear were still very much empirical. A more rigorous procedure could be developed to determine the exact solution. But due to its indeterminate nature, it can only have limited use in design.

The theoretical approach to determine strut angles in a variable angle truss model

1. The theoretical approach improved the formation of a truss model in three critical aspects. To begin with, the strut angles were determined mathematically according to the detail of reinforced concrete beams with the principle of virtual work. Next, the strut angle evaluated in each truss unit varied due to the changes in available span length. Similarly, the strut angle also changed with the applied shear level. Hence this method successfully developed a variable angle truss model for reinforced concrete beams subjected to shear. Stiffness and deformation were both readily defined in the variable angle truss model.

2. The theoretically approach proposed in this thesis also provided a possible solution to cater for the concrete contribution in shear. A rational method from the strain compatibility condition of each truss unit was used to relate transverse tensile strain to the concrete contribution.

3. When deformation and concrete contribution in shear were determined in the theoretical approach, load versus displacement response of several reinforced concrete beams were predicted with satisfactory correlation to the experimental data which verified the approach. The testing of two reinforced concrete beams in this research also supplemented the approach.

Experimental program of reinforced concrete walls with openings

1. Three reinforced concrete walls, in which two had openings in the web, were tested under reversed cyclic loading. Large opening percentage in the web of wall reduced strength and stiffness of the wall and the failure mode could also change accordingly. More significantly, the openings regulated the internal stress flow patterns and the force transfer mechanisms of the walls. Crack patterns displayed helped to develop strut-and-tie models for the wall specimens.

The strut-and-tie analysis of reinforced concrete walls with openings

1. The nonlinear finite element analysis was supplementary and focused on obtaining a clearly visible stress flow pattern of each wall specimen tested. The reliability of the stress flow patterns obtained was confirmed through well behaved analytical lateral load versus lateral displacement responses. The compressive stress flows of the two walls with openings were compared favourably with the experimental crack patterns.

2. The first type of the strut-and-tie model constructed for the tested wall specimens was a comprehensive model for overall responses. The aim of this model was to predict the displacement of reinforced concrete walls with the strut-and-tie approach. The analytical hysteretic responses of the wall were reasonable when compared to the experimental ones. Internal member stress and strain were also in good correlations to the experimental data at critical regions.

3. The second type of the strut-and-tie model developed for reinforced concrete walls with opening was based on the stress flow patterns. It represented the major paths in each stress flow pattern and was essentially the force transfer mechanism of each respective wall specimen. The model quantified the distribution among and main load paths and effectively explained the force transfer mechanism of each specimen. Nevertheless, it was a sort of strut-and-tie model with great transparency to analyze elements with complicated stress conditions.

4. A systematic design proposal was made for reinforced concrete walls with openings. Although the design brought finite element analysis into the picture, the proper construction of the strut-and-tie model and the solutions of member forces were the main aim. The philosophy could be extended to other reinforced concrete elements with static or geometrical discontinuities.

7.2 Recommendations for Design with the Strut-and-Tie Approach

The theoretical approach to determine strut angles in a variable angle truss model

The theoretical approach has been developed into a design procedure as shown in the flowchart in **Appendix A**. This design procedure is developed mainly for shear design. As a result, the design of the longitudinal reinforcement can be done from the normal flexural theory in various codes. The design for shear strength and the displacement could be checked following the method described in Chapter 4. Again it should be pointed out that the design was dependent on the formulation of the concrete contribution and other reliable ones that could replace the one used here. It emphasizes the region near the loading point by having quite closely spaced shear reinforcement. The truss unit formed near the support has a flat strut angle indicating the spacing of the shear reinforcement was sparse. Even though it corresponded well with the crack patterns, but it deviated considerably from current design codes and was subjected to further study.

The strut-and-tie design of reinforced concrete walls with openings

The design of reinforced concrete walls with openings was illustrated with in **Appendix C**. It was an iterative procedure between the finite element analysis and a strut-and-tie model. The finite element analysis used should generate a clear internal stress flow pattern. The key of the design however was construction of the strut-and-tie model which should represent the major paths in the stress flow patterns. When more paths were included in the model, the percentage of the imposed load shared by each path could be reduced with higher design strength was expected in the end result. However, the use of more load paths in the model would increase the complexity and the amount of the work in the calculation of member forces. Therefore, the choice of the strut-and-tie model should be based on the accuracy requirement set by the engineers.

REFERENCES

[A1] **ACI Committee 318 (2002)**, "Building Code Requirements for Structural Concrete (ACI 318-95) and Commentary (ACI 318R-02)," American Concrete Institute, Farming Hills, Mich.

[A2] **Adebar, P., Kuchma, D. and Collins, M. P. (1990)** "Strut-and-Tie Models for the Design of Pile Caps: An Experimental Study", *ACI Structural Journal*, V. 87, No. 1, January-February, pp. 81-92.

[A3] **Alshegeir, A., and Ramirez, J. A. (1992)** "Strut-Tie Approach in Pretensioned Deep Beams", *ACI Structural Journal*, V. 89, pp. 296-304.

[A4] **Al-Nahlawi, K. A., and Wight, J. K. (1992)** "Beam Analysis Using Concrete Tensile Strength in Truss Model", *ACI Structural Journal*, V. 89, No. 3, May-June, pp. 284-289.

[A5] **Al-Nahlawi, M. K. A.**, "An Experimental and Analytical Study of Shear Strength of Lightly Reinforced Concrete Beams," Doctor of Philosophy thesis, University of Michigan.

[A6] **Anderson, N. S.**, "Effect of the Detailing of Stirrup Reinforcement on the Ultimate Strength and Behavior of Reinforced Concrete Members Failing in Shear," Master of Engineering thesis, Purdue University.

[A7] **AS 3600-Supplementary 1 (1990)** "Concrete Structures-Commentary (Supplement to AS 3600-1988)", Standard Association of Australia, Sydney.

[B1] **Bresler, B., and MacGregor, J. G.**, "Review of Concrete Beams Failing in Shear," *ACI Journal, Proceedings*, V. 93, No. 1, February, 1967, pp. 343-372.

[B2] **Bresler, B., and Scordelis, A. C. (1963)** "Shear Strength of Reinforced Concrete Beams," *ACI Journal, Proceedings*, V. 60, No. 1, January, pp. 51-72.

[C1] **Canadian Standards Association (1994)** "Design of Concrete Structures", CSA A23.3-94, Rexdcale, Ontario, December, pp. 200

[C2] **CEB-FIP, (1978)** "Model Code for Concrete Structures", 3rd Edition, Comite-Euro-International du Beton/Federation Internationale de la Precontrainte, Paris.

[C3] **Collins, M. P. and Mitchell, D. (1991)** *Prestressed Concrete Structures*, Prentice-Hall, Inc.

[C4] **Cook, W. D. and Mitchell, D. (1988)** "Study of Disturbed Regions near Discontinuities in Reinforced Concrete Members", *ACI Structural Journal*, Vol.85, pp. 206-216.

[C5] **Cook, W. D. and Mitchell, D. (1988)** "Study of Disturbed Regions near Discontinuities in Reinforced Concrete Members", *ACI Structural Journal*, Vol.85, pp. 206-216.

[D1] **Dilger, W. (1966)** "Veränderlichkeit der Biege- und Schubsteifigkeit bei Stahlbetontragwerken und ihr Einfluβ auf Schnittkraftverteilung und Traglast bei statisch undestimmter Lagerung," Deutscher Ausschuss für Stahlbeton, Heft 179, Berline, Germany.

[E1] **Elfgren, L. (1972)** "Reinforced Concrete Beams Loaded in Combined Torsion, Bending and Shear", *Publication 71:3*, Division of Concrete Structures, Chalmers University of Technology, Göteborg, Sweden.

[E2] **Elzanaty, A. H., Nilson, A. H., and Slate, F. O. (1986)** " Shear Capacity of reinforced Concrete Beams Using High-Strength Concrete", *ACI Journal, Proceedings*, V. 81, No. 2, March-April, pp. 290-296.

[E3] **Eurocode No. 2 (1991)** "Design of Concrete Structures. Part 1: General Rules and Rules for Buildings", Commission of the European Communities, ENV 1992-1-1, December, pp. 253

[F1] **Foser, S. J., and Gilbert, R. I. (1997)** "Strut and Tie Modeling of Non-flexural Members", *Australian Civil/Structural Engineering*, University of New South Wales.

[H1] **Hong, S. G. (1996)** "Truss Model for Tension Bars in Reinforced Concrete Beams: Tension-Tension-Compression Regions", *ACI Structural Journal*, V. 93, No. 6, November-December, pp. 729-738.

[H2] **Hong, S. G., Ha, T. (2000)** "Shear-friction Truss Model for Reinforced Concrete Beams",

[H3] **Hsu, T. T. C. (1988)** "Softened Truss Model Theory for Shear and Torsion", *ACI Structural Journal*, V. 85, pp. 624-635.

[H4] **Hsu, T. T. C. (1993)** *Unified Theory of Reinforced Concrete*, CRC, Boca Raton, Fla.

[H5] **Hsu, T. T. C. (1996)** "Toward a Unified Nomenclature for Reinforced Concrete Theory", *Journal of Structural Engineering*, ASCE, Vol.122, No.3 March, pp. 275-283.

[H6] **Hwang, S. J. and Lee, H. J. (1999)** "Analytical Model for Predicting Shear Strengths of Exterior Reinforced Concrete Beam-Column Joints for Seismic Resistance", *ACI Structural Journal*, V. 96, No. 5, September-October, pp. 846-857.

[H7] **Hwang, S. J. and Lee, H. J. (2000)** "Analytical Model for Prediction Shear Strengths of Interior Reinforced Concrete Beam-Column Joints for Seismic Resistance", *ACI Structural Journal*, V. 97, No. 1, January-February, pp. 35-44.

[H8] **Hwang, S. J., Lu, W. Y. and Lee, H. J. (2000)** "Shear Strength Prediction for Deep Beams", *ACI Structural Journal*, V. 97, No. 3, May-June, pp. 367-376.

[H9] **Hwang, S. J., Fang, W. H., Lee H. J. and Yu, H. W. (2001)** "Analytical Model for Predicting Shear Strength of Squat Walls", *Journal of Structural Engineering*, ASCE, V. 127, No. 1, January, pp. 43-50.

[I1] **Ito, A., Niwa, J., and Tanabe, T. (1999)** "Lattice Model Analysis of RC Columns Subjected to Cyclic Loading", *Transaction of the Japan Concrete Institute*, V. 21, pp. 371-376.

[I2] **Ito, A., Niwa, J., and Tanabe, T. (2000)** "Non-Linear Dynamic Analysis of RC Columns Using the Lattice Model", *Transaction of the Japan Concrete Institute*, V. 22, pp 299-304.

[K1] **Kent, D. C. and Park, R. (1971)** "Flexural Members with Confined Concrete", *Journal of the Structural Division*, V. 97, No. 7, July, pp. 1969-1990.

[K2] **Kim, J. H. (1996)** "Seismic Evaluation of Shear-Critical Reinforced Concrete Columns and Their Connections", PhD Dissertation, State University of New York, Buffalo, New York.

[K3] **Kim, J. H. and Mander, J. B. (2000)** "Seismic Detailing of Reinforced Concrete Beam-Column Connections", *Structural Engineering and Mechanics*, V. 10. No. 6, pp. 589-601.

[K4] **Kong, P. Y. L. and Rangan, B. V. (1998)** "Shear Strength of High-Performance Concrete Beams", *ACI Structural Journal*, V. 95, No. 6, November-December, pp. 677-687.

[L1] **Lampert, P., and Thurlimann, B. (1968)** "Torsion Tests of Reinforced Concrete Beams (Torsionsversuche an Stahlbetonbalken)", *Bericht No. 6506-2*, Institute fur Baustatik, ETH, Zruich, Switzerland (in German).

[L2] **Lampert, P. and Thurlimann, B, (1971)** "Ultimate Strength and Design of Reinforced Concrete Beams in Torsion and Bending", International Association for Bridge and Structural Engineering, *Publications*, V. 31-1, pp. 107-131.

[L3] **Leonhardt, F. (1965)** "Reducing the Shear Reinforcement in Reinforced Concrete Beams and Slabs", *Magazine Concrete Research*, V. 17, No. 53.

[L4] **Li, B., Maekawa, K., and Okamura, H. (1989)** "Contact Density Model for Stress Transfer Across Cracks in Concrete", *Journal of the Faculty of Engineering*, the University of Tokyo(B), V. XL, No. 1, pp. 9-52.

[M1] **Marti, P. (1980)** "Zur Plastischen Berechnung von Stahlbeton (On Plastic Analysis of Reinforced Concrete)", Institute of Structural Engineering, *Report* No. 104, ETH, Zurich, pp. 176.

[M2] **Marti, P. (1985)** "Basic Tools of Reinforced Concrete Beam Design", *American Concrete Institute Journal*, V. 7, No. 1, Jan-Feb, pp. 46-56.

[M3] **Marti, P. (1985)** "Truss Models in detailing", *Concrete International: Design & Construction*, V. 83, pp. 46-83.

[M4] **Marti, P. (1986)** "Staggered Shear Design of Concrete Bridge Girders", *Proceedings*, International Conference on Short and Medium Span Bridges, Ottawa, V. 1, pp. 139-149.

[M5] **Marti, P. (1991)** "Dimensioning and detailing", *IABSE report*, V. 62, pp. 411-443.

[M6] **Marti, P. (1999)** "How to Treat Shear in Structural Concrete", *ACI Structural Journal*, V. 96, No. 3, May-June, 1999, pp. 408-414.

[M7] **MacGregor, J. G., and Bartlett, F. M. (2000)** "Reinforced Concrete: Mechanics and Design (First Canadian Edition)", Prentice-Hall Canada Inc., Scarborough, Ontario.

[M8] **Morsch, E. (1902)** *Der Eisenbetonbau seine Theorie und Anwendung* (Theory and Applications of Reinforced Concrete), Verlag Konrad Wittwer, Stuttgart.

[M9] **Muttoni, A., Schwartz, J. and Thürlimann, B. (1997)** *Design of Concrete Structures with Stress Fields*, Birkaühser Verlag, Basel, Switzerland.

[N1] **Nielson, M. P. (1984)** "Limit Analysis and Concrete Plasticity", Prentice-Hall Inc., Eaglewood Cliff, N. J.

[P1] **Pang, X. B. and Hsu, T. T. C. (1996)** "Fixed-Angle Softened-Truss Model for Reinforced Concrete", *ACI Structural Journal*, V. 93, No. 2, March- April, pp. 197-207.

[P2] **Park, R. and Paulay, T. (1975)** *Reinforced Concrete Structures*, John Wiley and Sons, New York.

[P3] **Paulay, T. (1971)** "Coupling Beams of Reinforced Concrete Shear Walls", *Journal of the Structural Division*, ASCE, V. 97, ST3, March, pp. 843-862.

[P4] **Paulay, T. (1971)** "Simulated Seismic Loading of Spandrel Beams", *Journal of the Structural Division*, ASCE, V. 97, ST9, September, pp. 2407-2419.

[P5] **Paulay, T. and Priestley, M. J. N. (1992)** *Seismic Design of Reinforced Concrete and Masonry Buildings*, John Wiley, New York.

[P6] **Pendyala, R. S., and Mendis, P. (2000)** "Experimental Study on Shear Strength of High-Strength Concrete Beams", *ACI Structural Journal*, V. 97, No. 4, July-August, pp. 564-571.

[P7] **Powell, G. H. (1993)** *DRAIN-2DX Element Description and User Guide For Element Type01, Type02, Type04, Type06, Type 09, and Type15 Version1.10*, Department of Civil Engineering, University of California, Berkeley, California. Report No. UCB/SEMM-93/18.

[P8] **Prakash, V., Powell, G. H., and Campbell. S. (1993)** *DRAIN-2DX Base Program Description and User Guide Version 1.01*, Department of Civil

Engineering, University of California, Berkeley, California. Report No. UCB/SEMM-93/17.

[P9] **Priestley, M. J. N., Verma, R., and Xiao, Y. (1994)** "Seismic Shear Strength of Reinforced Concrete Columns," *Journal of Structural Engineering*, V. 120, No. 8, ASCE, August, pp 2310-2329.

[R1] **Ramirez, J. A., and Breen, J. E. (1991)** "Evaluation of a Modified Truss-Model Approach for Beams in Shear", *ACI Structural Journal*, V. 88, No. 5, September-October, pp. 562-571.

[R2] **Rausch, E, (1929)** *Berechnung des Eisenbetons gegen Verdrehung und Abscheren* (Design of reinforced concrete for torsion and shear), Julius Springer Verlag, Berlin.

[R3] **Regan, P. E. (1969)**, "Shear in Reinforced Concrete Beams," Magazine of Concrete Research, V. 21, No. 66, pp. 31-42.

[R4] **Ritter, W. (1899)** "Die Bauwerise hennebique", *Schweritzerische Bauzeritung*, Zurich, Switzerland (in German).

[R5] **Robinson, J. R., and Demorieux, J. M. (1968)** "Essais de Traction-compression sur Modèles D'âme de poutre en Béton Armé." *IRABA Rep.*, Institut de Recherches Appliquées du Bvton de l'Ame, Paris, France.

[R6] **Robinson, J. R., and Demorieux, J. M. (1972)** "Resistance Ultimate du béton de l' âme de Poutres en Double te en Béton Armé" *IRABA Rep.*, Institut de Recherches Appliquées du Bvton de l'Ame, Paris, France.

[R7] **Rogowsky, D. M., and MacGregor, J. G. (1986)** "Design of Reinforced Concrete Deep Beams", *Concrete International: Design and Construction*, 8(8), pp. 49-58.

[S1] **Schlaich, J., Schäfer, K. and Jennewein, M. (1987)** "Toward a Consistent Design of Structural Concrete", *PCI Journal*, V. 32, No. 3, May-June, pp. 74-150.

[S2] **Schlaich, J., Schäfer, K. (1991)** "Design and Detailing of Structural Concrete Using Strut-and-Tie Models", *The Structural Engineer*, V. 69, No. 6, pp. 113-125.

[S3] **Schlaich, M., and Anagnostou, G. (1990)** "Stress Fields for Nodes of Strut-and-Tie Models", *Journal of Structural Engineering*, ASCE, V. 116, No. 1, January, pp. 13-23.

[S4] **Sritharan, S., Ingham, J. M. and Priestley, M. J. N. (2000)** "Strut-and-Tie Model Concepts for Seismic Design and Assessment of Concrete Bridge Joints", *Proceedings of 12WCEE*, pp. 1448.

[S5] **Su, R. K. L., and Chandler, A. M. (2001)** "Design Criteria for Unified Strut and Tie Models", *Prog. Structural Engineering Mater*: 3: pp. 288-298.

[T1] **Thurlimann, B. (1977)** "Shear Strength of Reinforced and Prestressed Concrete Beams CEB Approach", *Technical Report*, ACI Symposium 1976, February, Revised Copy, pp. 33.

[T2] **Thurlimann, B., Grob, J. and Luchinger, P., (1975)** "Torsion, Biegung und Schub in Stahlhbetontragern (Torsion, Flexure an Shear in Reinforced Concrete Girders)", Institute of Structural Engineering, ETH, Zruich, pp. 170.

[T3] **To, N. H. T., Ingham, J. M. and Sritharan, S. (2000)** "Cyclic Strut & Tie Modeling of Simple Reinforced Concrete Structures", *Proceedings of 12WCEE*, pp. 1249.

[V1] **Vecchio, F. J., and Collins, M. P. (1981)** "Stress-strain Characteristics of Reinforced Concrete in Pure Shear", *Final Rep.*, IABSE Colloquium on Advanced Mechanics of Reinforced Concrete, Delft, Netherland, pp. 211-225.

[V2] **Vecchio, F. J. and Collins, M. P. (1986)** "The Modified Compression-Field Theory for Reinforced Concrete Elements Subjected to Shear", *ACI Journal*, V. 83, No. 2, March-April, pp. 219-231.

[V3] **Vecchio, F. J. (2000)** "Disturbed Stress Field Model for Reinforced Concrete: Formulation", *Journal of Structural Engineering*, ASCE, V. 126, No. 9, September, pp.1070-1077.

[W1] **Walraven, J. C. (1981)** "Fundamental Analysis of Aggregate Interlock," *Proceedings*, ASCE, V. 107, ST11, November, pp 2245-2270.

[W2] **Warwick, W., and Foster, S. J. (1993)** "Investigation into the Efficiency factor Used in Nonflexural Member Design", *UNICIV Report*, No. R-320, School of Civil Engineering, University of New South Wales, Kensington, July.

[X1] **Xiao, Y., Priestley, M. J. N and Seible F. (1996)** "Seismic Assessment and Retrofit of Bridge Column Footings", *ACI Structural Journal*, V. 93, No. 1, January-February, pp. 79-93.

[Y1] **Yanez, F. V., Park, R. and Paulay, T. (1992)** "Seismic Behavior of Walls with Irregular Openings", *Earthquake Engineering Tenth World Conference*, Balkema, Rotterdam.

[Z1] **Zsutty, T. (1968)** "Beam Shear Strength Predicting by Analysis of Existing Data', ACI Journal, V. 65, No. 11, November, pp. 942-951

APPENDIX B

EVALUATION OF FLEXURAL AND SHEAR DEFORMATIONS IN REINFORCED CONCRETE WALLS

B.1 Evaluation of Flexural Deformation of Reinforced Concrete Walls

Based on the Bernoulli hypothesis that plane sections remain plane after deformation, the wall flexural deformations can be obtained from the rotation of each segment in the wall measured from a pair of left and right LDVTs located at each side of the web. With the reference to **Figure B.1**, the change of slope of region i is given by:

$$\theta_i = \frac{\delta_{Ri} - \delta_{Li}}{L_T} \tag{B-1}$$

Where θ_i is the change of slope occurring in the region i, δ_{Ri} and δ_{Li} are the extension and shortening of the right and left side of the web measured by a pair of LVDTs in the region i, and L_T is the horizontal distance between left and right LVDTs. The average curvature in region i can be evaluated as:

$$\phi_i = \frac{\theta_i}{S_i} \tag{B-2}$$

where S_i is the gauge length of the LVDT in this region. The top drift obtained from the change of slope in this region is:

$$\Delta_{fi} = \theta_i (h_W - h_i) = \theta_i H_i \tag{B-3}$$

where h_i is the vertical distance between the center line of region i to the wall foundation beam and H_i is the vertical distance from the center line to the loading point. Thus, the top drift induced by flexural distortion Δ_f can be obtained from the sum of

Δ_{fi} based on this discrete model. As shown in **Figure B.2**, assuming that three pairs of LVDTs are used to measure the flexural distortions of the Region 1, 2, and 3, the top drift caused by flexural then can be obtained by:

$$\Delta_f = \Delta_1 + \Delta_2 + \Delta_3 \tag{B-4}$$

It should be noted that the slope change in the Region 1, just adjunct to the joint between the web and the foundation beam, may include distortion due to joint opening. The slope change obtained here is averaged into the slope change of the Region i. The curvature of this region is possibly overestimated by Equation (B-4).

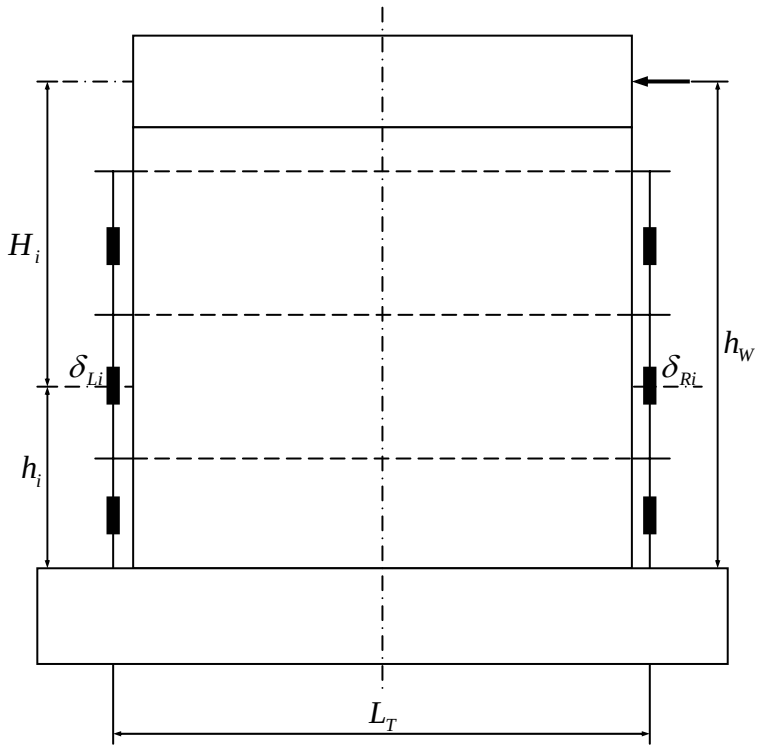

Figure B.1: Evaluation of flexural deformation

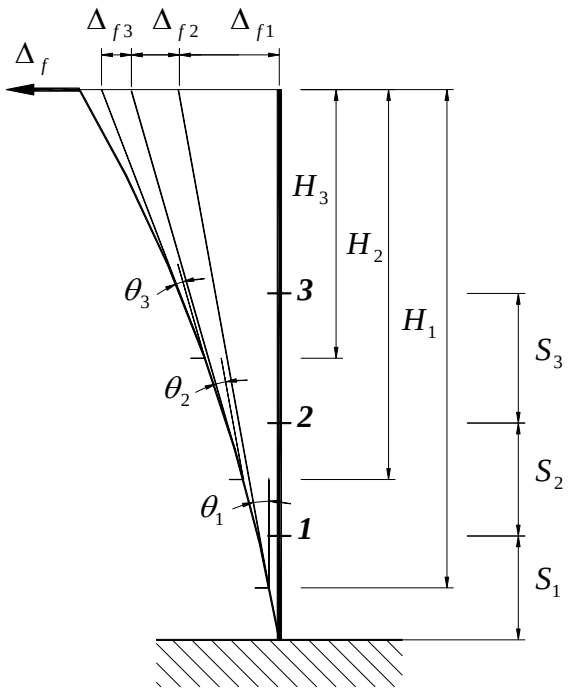

Figure B.2: Relationship of flexural deformations to top drift

B.2 Evaluation of Shear Deformation of Reinforced Concrete Walls

The shear distortion of a rectangular panel can be evaluated based on the length variations of its two diagonals as shown in **Figure B.3**. the deformation is given by:

$$\gamma = \gamma_1 + \gamma_2 = \frac{\Delta_1 - \Delta_2}{2L}(\tan\alpha + \cot\alpha) \qquad \text{(B-5)}$$

where Δ_1 and Δ_2 are the deformations of the panel diagonals, L is the length of the diagonal, and α is the angle between the diagonal and the side of rectangular. Δ_1 and Δ_2 are positive when they are in extension. The top drift due to shear distortion Δ_V can be calculated by:

$$\Delta_V = \gamma h_W \qquad \text{(B-6)}$$

where h_W is the distance from foundation beam of the wall up to lateral loading point.

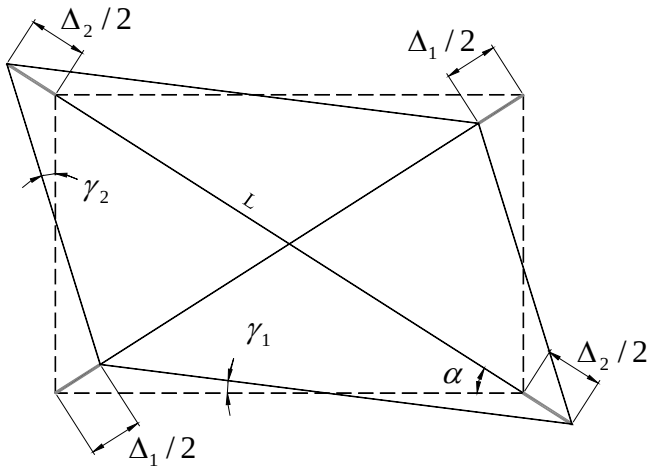

Figure B.3: Evaluation of rectangular panel shear distortion

APPENDIX A

DESIGN EXAMPLE OF REINFORCED CONCRETE BEAM SUBJECTED TO SHEAR

Verified by past and current experimental data, it can be seen that the proposed theoretical approach to determine strut angles of a variable angle truss model in Chapter 4 is a sufficient method in the analysis of reinforced concrete beams, particularly for any shear problem. This approach is able to be further developed in a shear design procedure for reinforced concrete beams which is organized in the flowchart shown in **Figure A.1**. The design begins from the loading point in the shear span. With assumed shear reinforcement spacing, Equation (4-12) can then give the strut angle of the truss unit and hence the strength contribution V_s from the shear reinforcement. Then compatibility analysis can give the concrete contribution V_c from Equation (4-21). The assumed shear reinforcement spacing is acceptable for this truss unit if it can be shown that V_s plus V_c is just greater than the applied ultimate load. Next, the variable l can be updated for the following truss units; the design stops when the left span length is not enough to form a truss unit.

The shear reinforcement of the beam with point load shown in **Figure A.2 (a)** will be design with the above procedure for the given ultimate load $450\,\text{kN}$ with $f_y = 460$ MPa for longitudinal deformed bars, $f_y = 250$ MPa for stirrup plain bars, $f_c' = 30$ MPa, and a cover of 20 mm. The beam cross section is taken to be 300 mm for width and 500 mm for depth. Followed from the design flowchart in **Figure A.1**, truss units can be formed in the shear span of the beam as shown in **Figure A.2 (b)**. The shear reinforcement required from the design is also

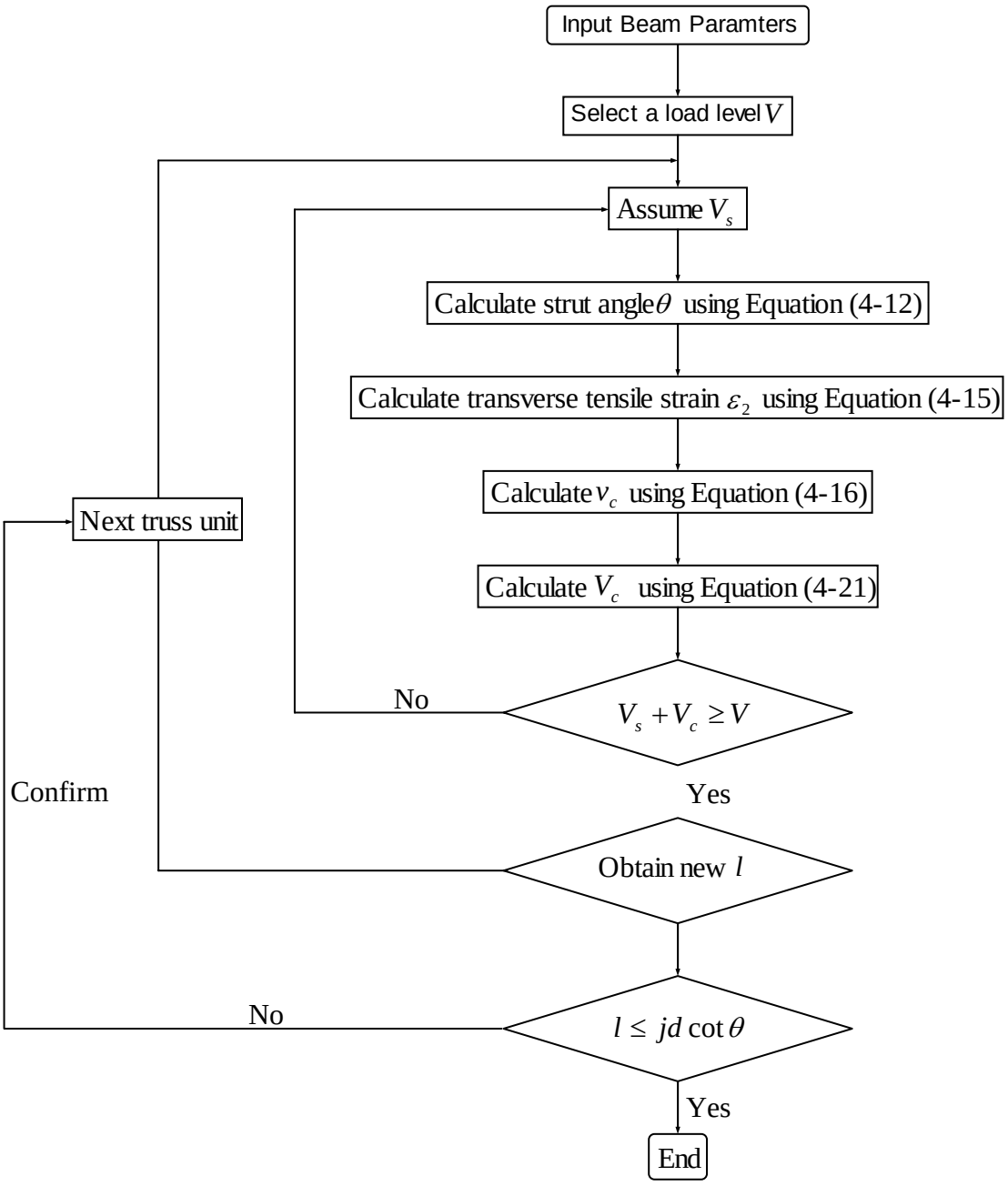

Figure A.1: Design flowchart

given. In the design, considering the plain bars used for the shear reinforcement, a safety factor of 0.9 is applied to the yielding strength. The shear reinforcement spacing is controlled to be no less than 200 mm with the actual shear reinforcement detailing can be made from **Figure A.2 (b)** based on engineering judgments. The final design is given in **Figure A.2 (c)**.

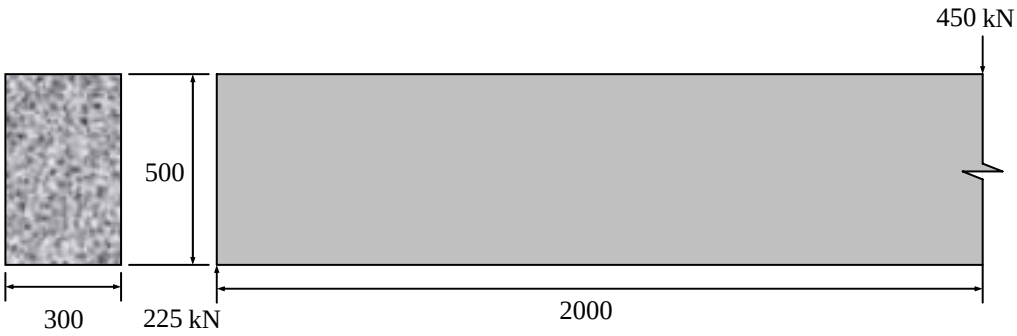

(a) Geometry and loading

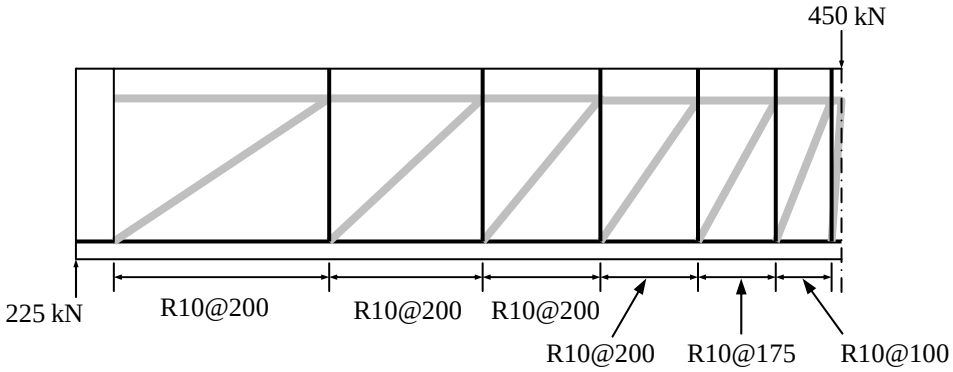

(b) Formed variable angle truss model in the shear span

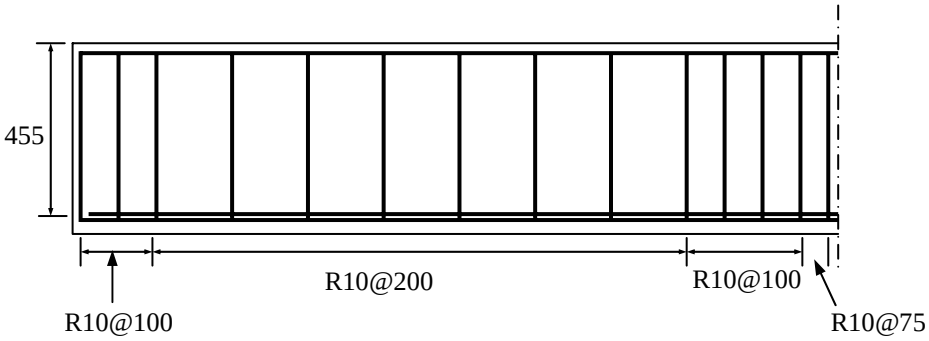

(c) Reinforcement detailing

Figure A.2: Design Example of reinforced concrete beam subjected to shear

This design procedure is developed mainly for shear and so the design of the longitudinal reinforcement can be done from the normal flexural theory in various codes. It emphasizes the region near the loading point by having quite closely spaced shear reinforcement. The truss unit formed near the support has a flat strut angle indicating the spacing of the shear reinforcement is sparse. And special treatment is given to the leftover region at the support end. Shear reinforcement with similar spacing to that of the region near the loading point can be provided.

APPENDIX C

DESIGN EXAMPLE OF REINFORCED CONCRETE WALL WITH OPENINGS

At the end of Chapter 6, a systematic design approach for reinforced concrete walls with openings using the strut-and-tie method has been proposed. In this appendix, a design example will be given to illustrate how the approach works. Let us consider an 120 mm thick reinforced concrete wall with a height of 2000 mm and width of 2000 mm and which has four openings as shown in **Figure C.1**. $f_c^{'} = 30$ MPa, $f_y = 460$ MPa for high yield steel bar, and $f_y = 250$ MPa for mild steel bar is used.

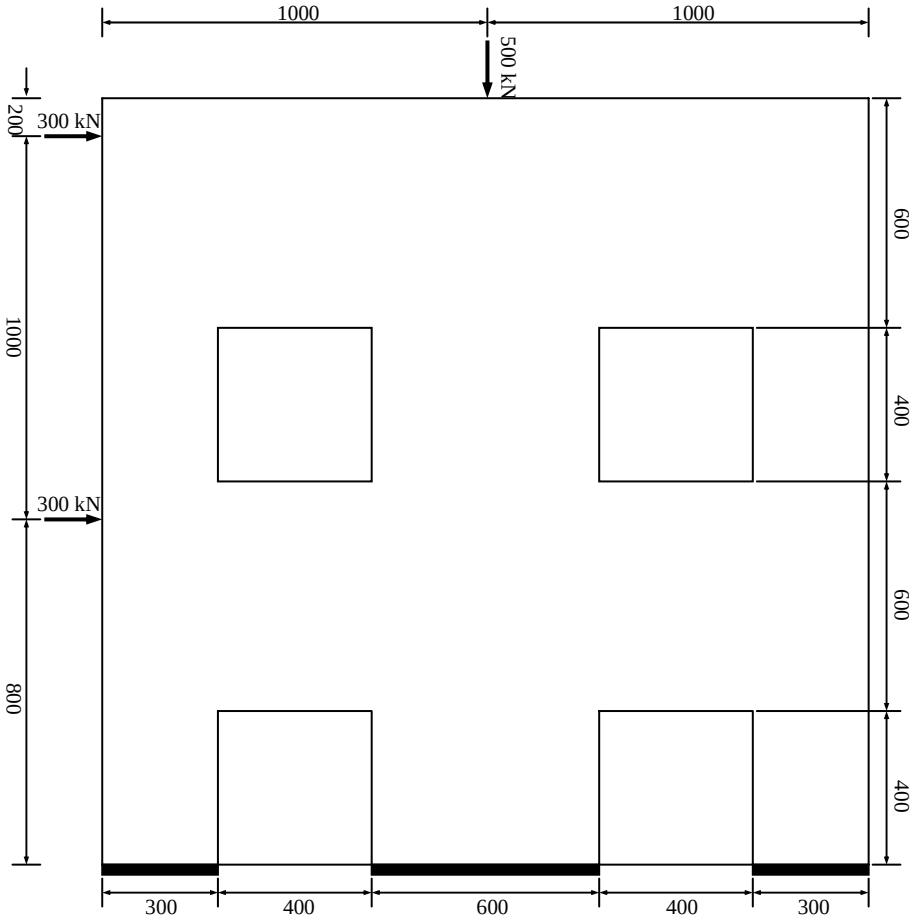

Figure C.1: Geometry and loads of the reinforced concrete wall

The wall is to be designed for two factored load cases:

Load Case 1: two lateral loads of 300 kN;

Load Case 2: two lateral loads of 300 kN and one axial load of 500 kN.

As pointed out in Chapter 6, the strut-and-tie model for each load case is developed according to the stress flow pattern in the force transfer mechanism. In the preliminary design, the stress flow caused by any particular load case is not directly visible. The development of the strut-and-tie model should be largely based on engineering judgment from the wall configuration and load cases. Two aspects can be considered: the likely paths of the loads being transferred to support and the orthogonal reinforcement pattern. Therefore, the strut-and-tie model for Load Case 1 can be established as **Figure C.2**.

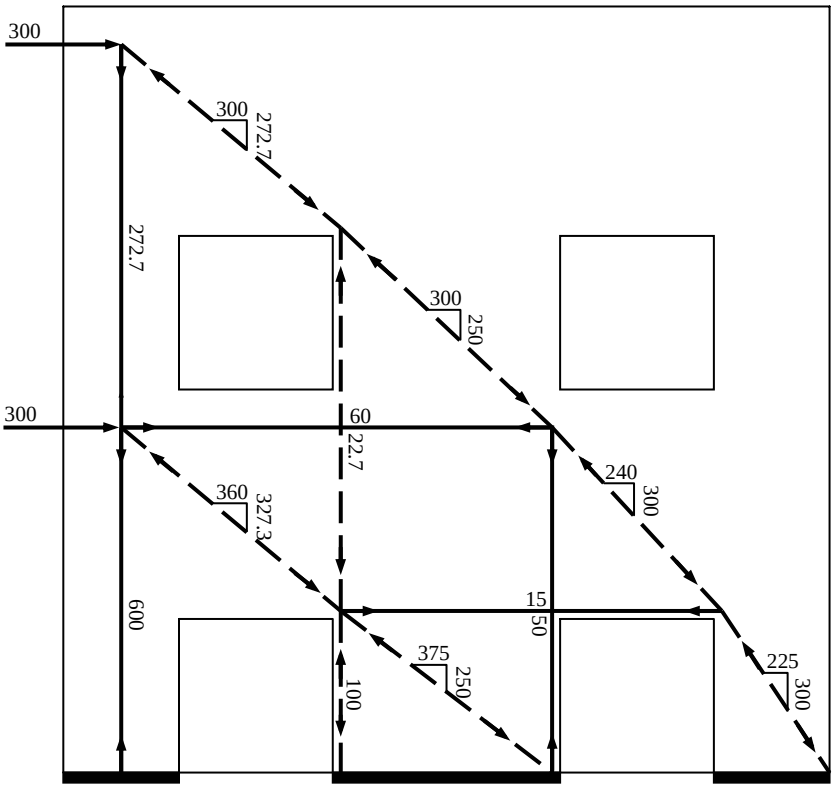

Figure C.2: The preliminary strut-and-tie model for Load Case 1

The strut-and-tie model for Load Case 1 is statically indeterminate at the upper horizontal tie. A reasonable portion of lateral load can be assigned to it in the preliminary design and verified it later and thus the member forces in the preliminary strut-and-tie model can be solved. The area of steel required for each tie can be calculated from the

expression:

$$A_{s,req} = \frac{F_u}{\phi f_y} \tag{C-1}$$

where ϕ is the material safety factor and can be taken as 0.85. Then a reinforcement layout satisfying the tie requirement for Load Case 1 is shown in Figure C.3.

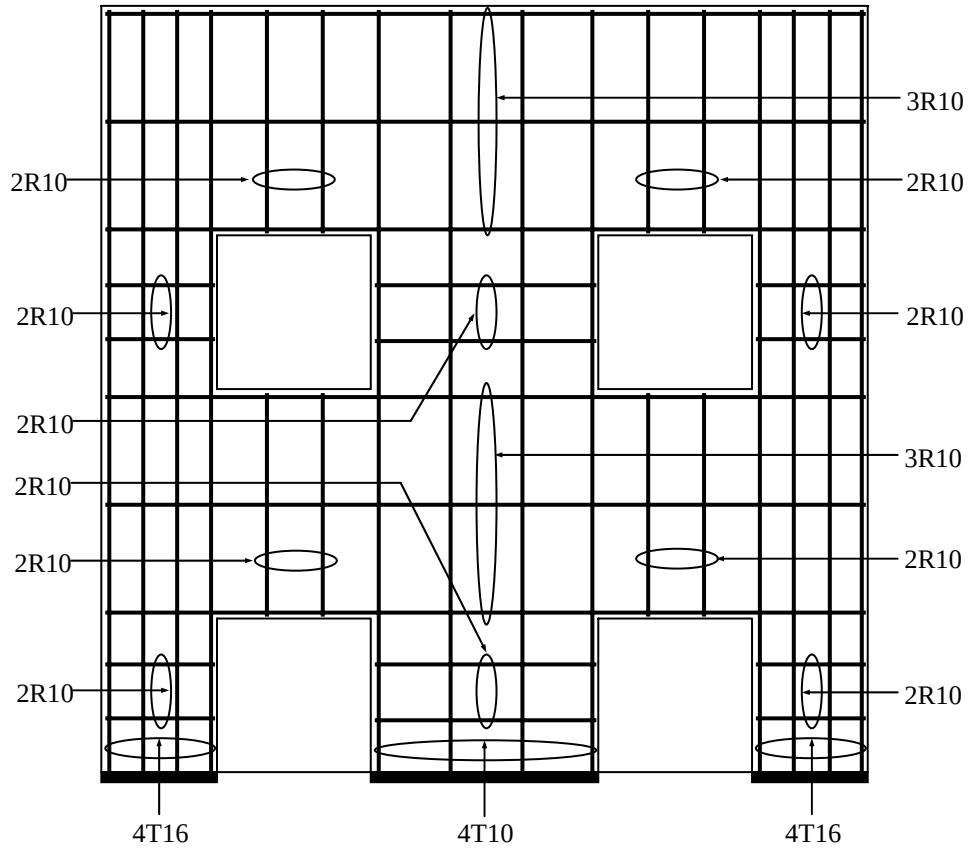

Figure C.3: Preliminary reinforcement layout of Load Case 1

Next, Load Case 1 can be analyzed by the finite element method with the reinforcement detail to verify the preliminary strut-and-tie model. This finite element analysis is still conducted with UC-WIN/MESH & UC-WIN/WCOMD for clear visualization of stress flow pattern. The results of Load Case 1 are in **Figure C.4**.

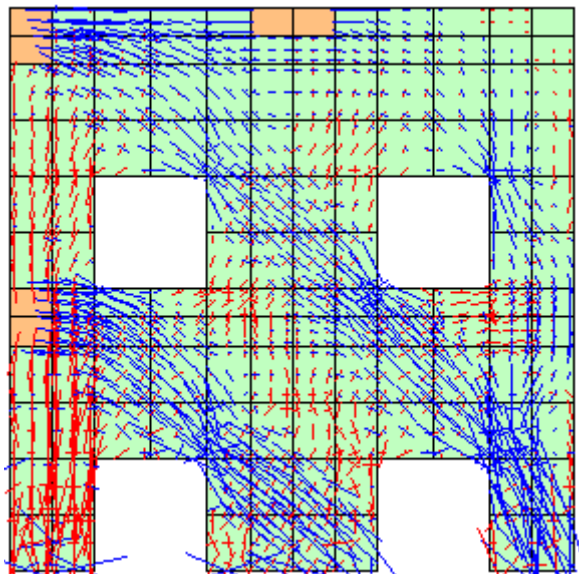

Figure C.4: Preliminary finite element analysis of Load Case 1

From the finite element analysis on the preliminarily designed reinforcement layout, it is verified that the assumed stress flow pattern, upon which the preliminary strut-and-tie model is based, is the same as that in the finite element analysis. This proves that developed the strut-and-tie model is valid. As the strut-and-tie model is statically indeterminate, sectional results in the finite element analysis can be used to re-calculate the member forces. In this case, the re-calculated member forces are only of 5% tolerance at maximum to those in the preliminary design and therefore it is confirmed that the reinforcement layout designed previously is final to Load Case 1.

The design procedure for Load Case 2 is similar as the Load Case 1 where for the particular load configuration in this load case, the preliminary strut-and-tie model could have the form as shown in **Figure C.5**.

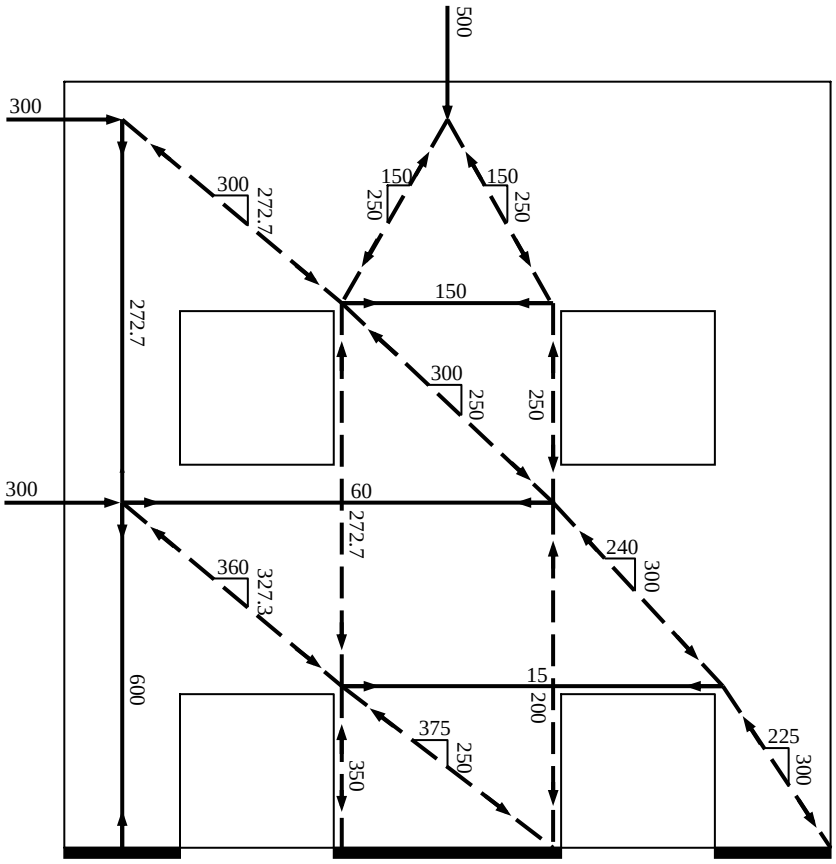

Figure C.5: The preliminary strut-and-tie model for Load Case 2

This model is more complicated than that in Load Case 1 as the axial load induced more paths. The strut-and-tie model is again statically indeterminate. To solve all the member forces, assumptions must be made and therefore for this model configuration, it is assumed that the second horizontal tie from the bottom takes 20% of the lateral load transfer at its ends. After the member forces being solved, the reinforcement can be designed and detailed according to the force of each tie. In the regions without ties, nominal reinforcement should be provided. Then the preliminary reinforcement layout can be designed as shown in **Figure C.6**.

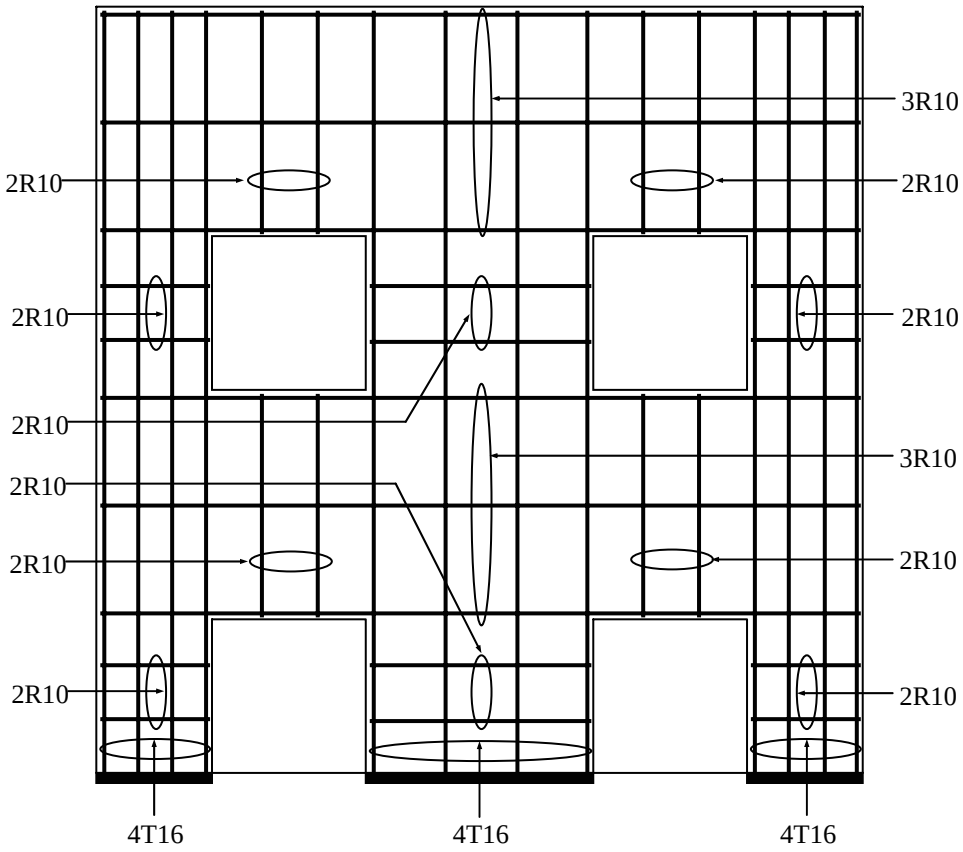

Figure C.6: Preliminary reinforcement layout of Load Case 2

The designed reinforcement layout can become input in the finite element program to obtain a stress flow pattern for Load Case 2 with the results shown in **Figure C.7**.

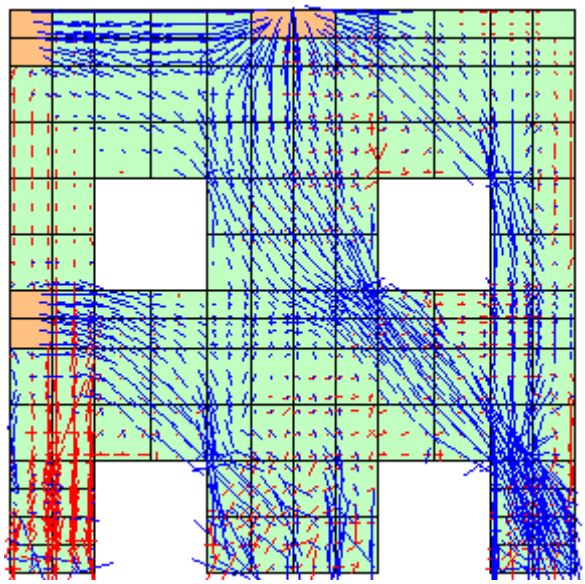

Figure C.7: Preliminary finite element analysis of Load Case 2

It is found that the strut-and-tie model in the preliminary analysis deviates considerably from the stress flow pattern of the preliminary finite element analysis. Thus, the strut-and-tie model needs to be refined. It can be seen that the upper lateral load is connected to the axial load with a stream of compressive stress flows and that a stream of compressive stress from the axial load goes through the top right portion of the wall. From here the refined strut-and-tie model can be developed as shown in **Figure C.8**.

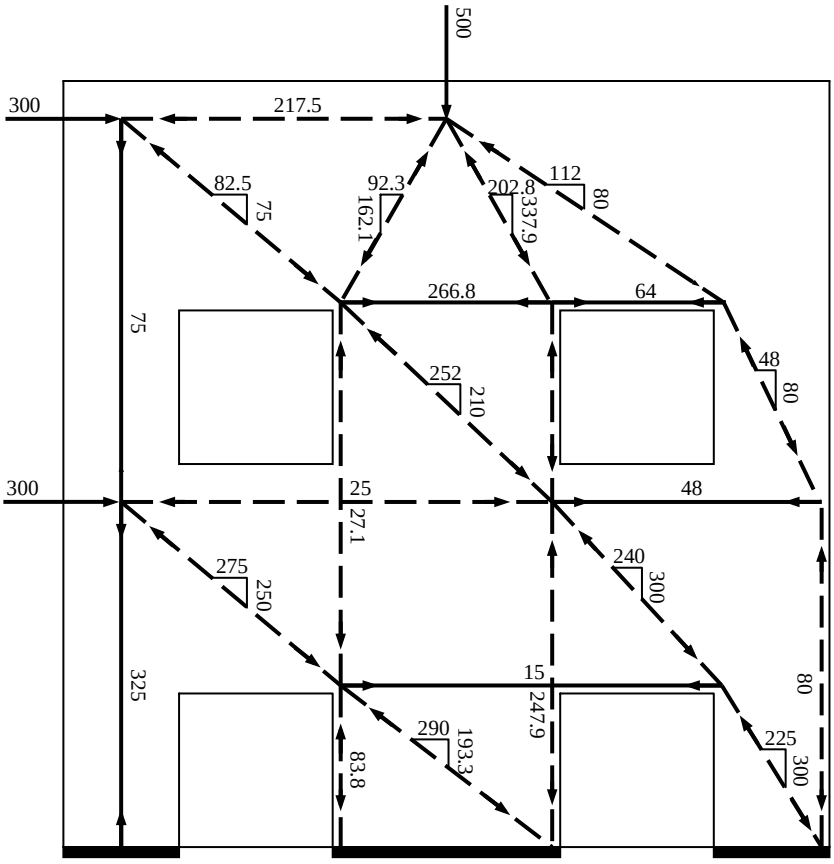

Figure C.8: The revised strut-and-tie model for Load Case 2

The refined strut-and-tie model is still statically indeterminate with the solution for member forces to be achieved through sectional result in the preliminary finite element analysis. The calculated member forces are also shown in **Figure C.8** with the major differences compared to the preliminary strut-and-tie model being that the two left vertical ties have much smaller member forces, indicating the reinforcement provided there could be reduced. Thus from the member forces in the refined strut-and-tie model, the preliminary reinforcement layout should be improved from the current tie forces.

The improved reinforcement layout is shown in **Figure C.9**.

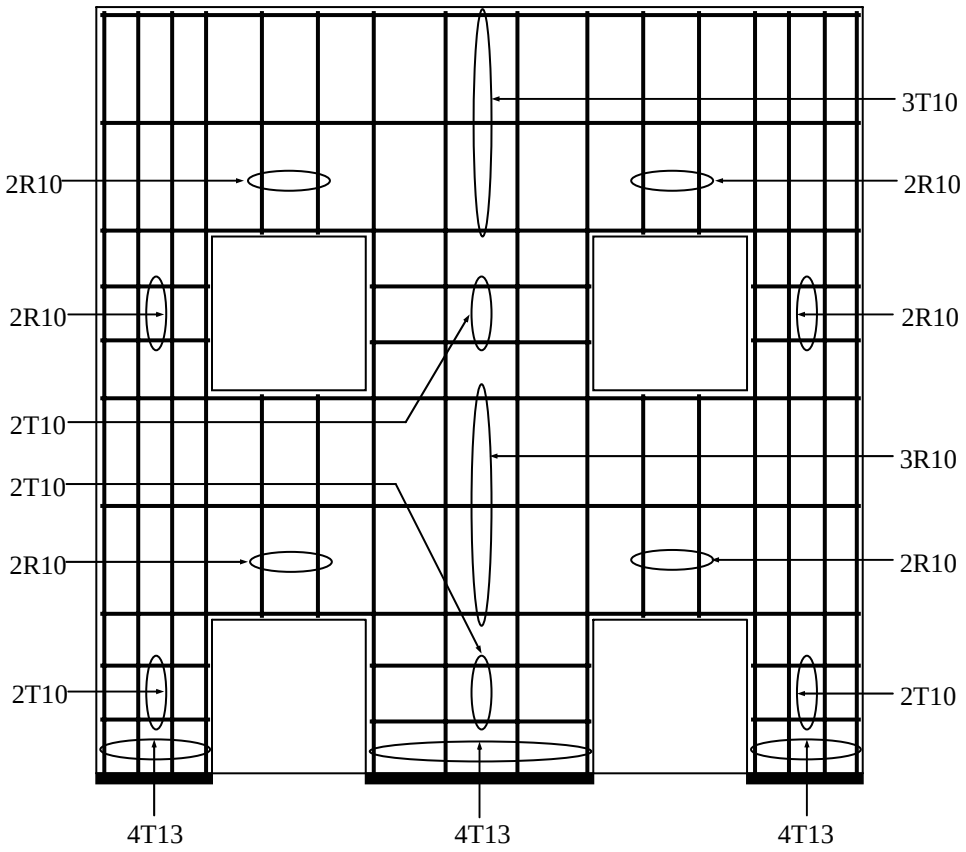

Figure C.9: The revised reinforcement layout of Load Case 2

The new reinforcement layout reduces the vertical reinforcement at the two sides of the wall. The lateral confinement provided to the two bottom columns is increased to prevent possible crushing failure there. The lateral reinforcement provided between the upper two openings is also enhanced to cater for the large member force of the tie there. Then, this reinforcement layout is analyzed again by the finite element method and the updated stress flow pattern from the finite element analysis is shown in **Figure C.10**.

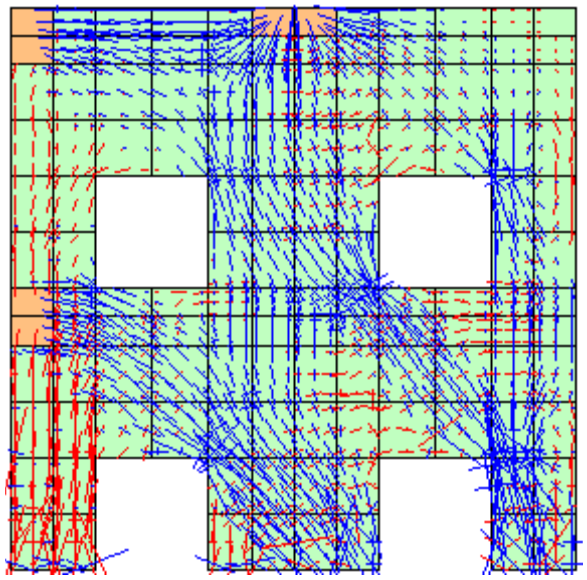

Figure C.10: The revised finite element analysis of Load Case 2

The updated stress flow pattern indicates the same load transfer mechanism as that in the preliminary analysis. Then the sectional results in the new finite element analysis are examined to check the member forces calculated in the refined design. It is found that the maximum difference now is within 5% which leads to the conclusion that the member forces shown in the refined strut-and-tie model are realistic. The reinforcement layout designed according to it is acceptable.

To summarize, the design procedure developed in Chapter 6 is an iteration process between the strut-and-tie model and the finite element analysis. However, the emphasis is really on the strut-and-tie model as the configuration of the model and the member forces are the keys to design the final reinforcement details.